In Vitro Characterisation of Melanoma Progression in a Melanoma Skin Equivalent Model

In vitro Characterisation of Melanoma Progression in a Melanoma Skin Equivalent Model

Parvathi Haridas
Bachelor of Science (Biotechnology)
Master of Science (Biotechnology, Advanced)

Principal Supervisor: Professor Matthew J Simpson

Associate Supervisor: Dr Jacqui A McGovern

A thesis submitted in fulfilment of the requirements for the degree of

Doctor of Philosophy

School of Mathematical Sciences

Faculty of Science and Engineering

Tissue Repair and Translational Physiology Program

Institute of Health and Biomedical Innovation

Queensland University of Technology

2017

QUT ihbi
Institute of Health and Biomedical Innovation

Keywords

Melanoma, cell migration; cell proliferation; cell invasion; 2D model; 3D model; human skin equivalent; melanoma skin equivalent; stages of melanoma; radial growth phase; vertical growth phase; metastasis; melanoma-associated markers; histology; immunohistochemistry; Western blotting; real time PCR; nests.

Abstract

Melanoma is a fatal form of skin cancer which progresses in an orchestrated pattern in human skin. In this thesis, we focus on three phases of melanoma progression: radial growth phase (RGP) where melanoma cells are generally confined to the epidermis of the skin; vertical growth phase (VGP) where melanoma cells invade into the dermis of the skin; and the metastatic phase where melanoma cells enter the blood stream and spread to other parts of the body. Characterising these phases of melanoma *in vitro* is important to investigate disease progression. The principal aim of this thesis is to quantify key features of melanoma progression, these include: melanoma cell migration; melanoma cell proliferation; melanoma cell invasion; and melanoma nest formation using two-dimensional (2D) and three-dimensional (3D) assays. We first investigate a reliable melanoma-specific marker and provide evidence that S100 is a sensitive marker that identifies melanoma cell lines: WM35 (RGP); WM793 (VGP); and SK-MEL-28 (metastatic) used in this project. Also included in this thesis is a demonstration of the difficulty of identifying a certain melanoma cell line, MM127. The most commonly used melanoma-associated markers failed to identify this cell line. We further investigate the rates of melanoma cell migration and cell proliferation using 2D co-culture assays. Since fibroblasts are thought to play an important role in cancer progression, the result from the cross-talk between melanoma cells and primary fibroblast cells could provide insightful information about their influence on the rates of spatial expansion. However, results from this study provide evidence that a more multicellular, heterogeneous, 3D environment might be necessary to examine the cross-talk between skin cells and melanoma cells. Since, cell-cell interactions are known to differ in an environment with more than two cell types, we characterise melanoma progression by constructing a 3D melanoma skin equivalent (MSE) model which resembles human skin *in vivo* and present our quantitative results of melanoma invasion in a time course pattern. Lastly, we use the 3D MSE model to identify and report our findings that proliferation and increased initial cell number drives melanoma nest formation. The outcomes of this project provide a foundation for 3D melanoma research and future *in vitro* assays are essential to fully understand the potential of this 3D model for clinical purposes.

Table of Contents

List of Publications

Manuscripts related to this thesis

1. **P. Haridas,** A.P. Browning, J.A. McGovern, D.L.S. McElwain and M.J. Simpson (2017). Three-dimensional experiments and individual based simulations show that cell proliferation drives melanoma nest formation in human skin tissue. <u>*BMC Systems Biology*</u> 12: 34 (doi: 10.1186/ s12918-018-0559-9)

2. **P. Haridas**, J.A. McGovern, D.L.S. McElwain and M.J. Simpson (2017). Quantitative comparison of the spreading and invasion of radial growth phase and metastatic melanoma cells in a three-dimensional human skin equivalent model. <u>*PeerJ*</u>. 5: e3754. (doi: <u>10.7717/peerj.3754</u>)

3. **P. Haridas**, C.J. Penington, J.A. McGovern, D.L.S. McElwain and M.J. Simpson (2017). Quantifying rates of cell migration and cell proliferation in co-culture barrier assays reveals how skin and melanoma cells interact during melanoma spreading and invasion. <u>*Journal of Theoretical Biology*</u>.423: 13-25. (doi: <u>10.1016/j.jtbi.2017.04.017</u>)

4. **P. Haridas**, J.A. McGovern, A.S. Kashyap, D.L.S. McElwain and M.J. Simpson (2016). Standard melanoma-associated markers do not identify the MM127 metastatic melanoma cell line. <u>*Scientific Reports*</u>. 6: 24569. (doi: <u>10.1038/srep24569</u>)

vi

Statement of Original Authorship

The work contained in this thesis has not been previously submitted to meet requirements for an award at this or any other higher education institution. To the best of my knowledge and belief, the thesis contains no material previously published or written by another person except where due reference is made.

Signature: _____

Date: _____20th December, 2017_____

Acknowledgment

Chapter 1: Introduction

1.1 BACKGROUND

To provide an understanding of the project, we first outline the background information about melanoma progression. The introduction summarises: melanoma disease statistics; an overview of human skin; the skin environment that can influence melanoma progression; and finally the importance of three-dimensional (3D) studies to understand melanoma progression.

1.1.1 Melanoma Statistics

Melanoma is a deadly form of skin cancer and is the fourth most common cancer in Australia (Sneyd & Cox 2013; Sidhu *et al*., 2017). Australia has one of the highest rates of melanoma incidence in the world (Jelineck *et al*., 2016; Karimkhani *et al*., 2017) and accounts for majority of skin cancer-related mortality, with over 1500 melanoma-related deaths reported in 2015 alone (AIWH 2016). Additionally, the reports of the Australian Institute of Health and Welfare (AIHW) indicate that skin cancer costs approximately AUD $400 million per year causing a significant burden on the healthcare system of Australia (AIWH 2014; AIWH 2016). Therefore, there is an urgent need to improve our understanding of melanoma progression, which still remains unclear. Addressing the knowledge gaps will identify improved melanoma treatment options and prevent disease advancement. Melanoma originates from the malignant transformation of melanocytes present in the skin (Shay 2017). To understand the underlying features of melanoma and its progression, it is essential to understand the structure of the human skin.

1.1.2   Human Skin

Human skin constitutes 16% of the total body mass and comprises of two main regions, epidermis and dermis separated by a basement membrane (Olsen *et al*., 1995; Wickett & Visscher, 2006). Both these regions of the skin work synergistically to provide physical protection and maintain the internal body homeostasis (Wegner *et al*., 2016). The multilayer epidermis predominantly comprises of keratinocytes (Klar *et al*., 2017). The keratinocytes proliferate and stratify from the basal layer called the *stratum basal*, situated adjacent to the underlying dermis (Natarajan *et al*., 2014). Within this basal layer are the melanocytes that produce and distribute the melanin pigment. Cells in the basal layer of the skin proliferate and form the *stratum spinosum*, *stratum granulosum* and finally the apical cornified *stratum corneum*, which works as the first barrier to the external environment (Natarajan *et al*., 2014; Klar *et al*., 2017). Transforming keratinocytes in the basal region of stratum corneum also form the *stratum lucidum*, found only on palms of hands and soles of feet (Lai-Cheong & McGrath 2009).

The basement membrane lies at the epidermal-dermal interface, plays a key role in skin homeostasis and is important for a synchronized epithelialisation (Wegner *et al*., 2016; Klar *et al*., 2017). The basement membrane anchors and supports the structural organisation of the epidermis (Breitkreutz *et al*., 2013). Beneath the continually renewing epidermis is the collagen-rich dermal layer. This layer of connective tissue is divided into papillary dermis just below the epidermis, and a deeper reticular dermis (Shirshin *et al*., 2017). Fibroblasts from mesenchymal origin predominantly appear in the dermis and produce collagen which constitutes 70% of the structural dermal matrix (Shirshin *et al*., 2017). Skin is a significant barrier that protects the body from the harmful external environment, compromising the skin integrity through disease or injury would damage the protective barrier (Wegner *et al*., 2016).

1.1.3   Melanoma in Human Skin

The neural crest derived melanocytes (Figure 1.1) synthesise and transfer melanin pigment to neighbouring keratinocytes through the cell's dendritic protrusions to an average of 36 keratinocytes in vesicles called melanosomes (Haass *et al*., 2005; Bandarchi *et al*., 2010; Zocco & Blanpain 2017). The melanocytes maintain a stable ratio of 1:5 to keratinocytes in the basal layer of epidermis through proliferation and migration to form epidermal–melanin units (Haass *et al*., 2005). Melanocyte morphology, cellular migration, proliferation and overall growth are regulated by keratinocyte-derived hormones, growth factors and cytokines (Hsu *et al*., 2002; Zocco & Blanpain 2017).
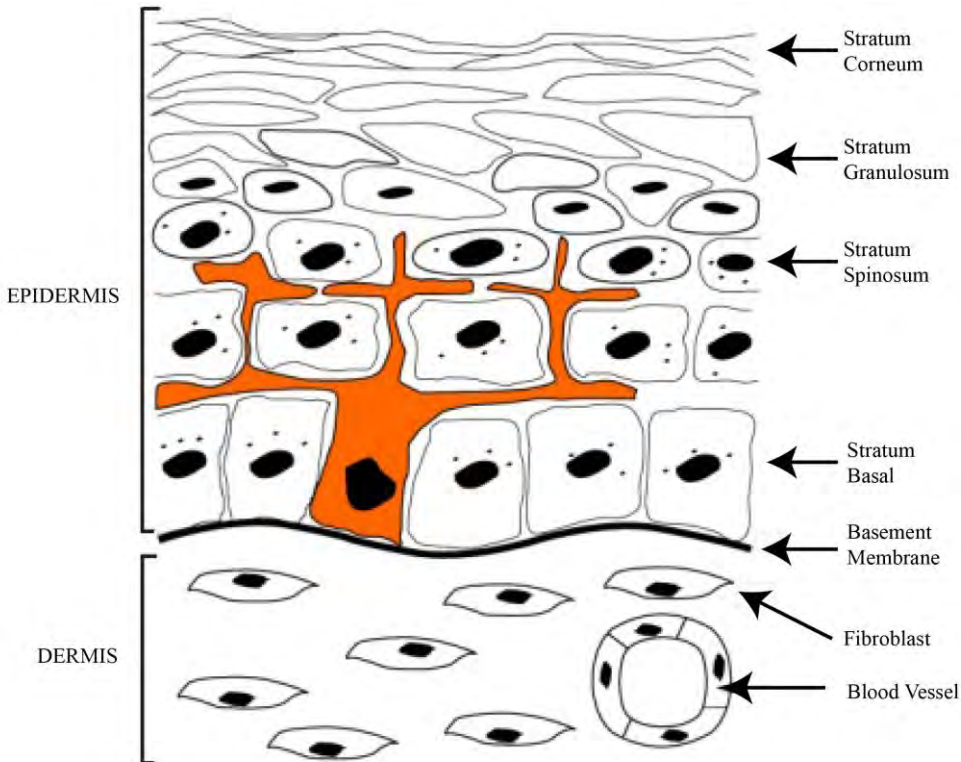
Figure 1.1: *Melanocyte in the epidermis.* Schematic illustration of the human skin layers showing a melanocyte in the basal epidermal layer (orange). The figure is adapted from Balois & Amar (2014).

Disruption to the epidermal-melanocyte unit interrupts the normal melanocyte homeostasis causing continuous melanocyte proliferation which is thought to eventually lead to melanoma (Haass *et al*., 2005; Zocco & Blanpain 2017). The transition of melanocytes to melanoma includes production of their own growth factor cascade, continuous proliferation of cells, with reduced apoptosis and loss of keratinocyte dominance by the down-regulation of cell-cell adhesion molecules (Haass *et al*., 2005; Xiao *et al*., 2016). This escape of melanocytes from the keratinocyte control allows invasion of the transformed melanocytes, from now on referred to as *melanoma cells*. These melanoma cells invade into the dermis, permitting cellular communication with fibroblasts, endothelial cells in the dermis and subsequent recruitment of neovasculature (Hanahan *et al*., 2011; Izar *et al*., 2016).

In human skin, keratinocytes and fibroblasts play a vital role in melanoma progression. Wang *et al*. (2011) show that keratinocyte-derived extracellular matrix proteins enhance melanoma spreading. Additionally, the keratinocytes promote survival and invasion of the melanoma cells into the dermal region. Proteolytic enzymes such as MMPs secreted by keratinocytes degrade the basement membrane enabling melanoma cells to invade into the dermis (Chung *et al*., 2011). Additionally, previous studies show that the extracellular matrix components secreted by epidermal keratinocytes promote the adhesion and migration of melanoma cells (Chung *et al*., 2011). Furthermore, research by Aberty *et al*. (2012) show that dermal fibroblasts also enhances melanoma cell proliferation paralleled with reduced melanoma apoptosis. Overall the fibroblasts and keratinocytes, from now on referred to as *skin cells*, interact with the surrounding melanoma cells and are responsible for melanoma cell growth, adhesion and survival (Kilsdonk *et al*., 2010; Flach *et al*., 2011; Zhou *et al*., 2015). Melanoma is associated with different stages and these are classified in the following section.

1.1.4   *Classification of Melanoma Progression*

Pathological findings based on genomics, epigenomics and proteomics have led to molecular reclassification of melanoma (Kalia 2015). There are five prominent stages of melanoma development and progression (Figure 1.2). The first stage of melanoma is

indicated by the formation of proliferative melanocytic nevus or clusters of cells in the epidermis (Clark *et al*., 1984; Gray-Schopfer *et al*., 2007). However, not all nevi become melanoma but are associated with the risk of melanoma formation (Kalia 2015). The melanocytic nevi further develop into precursors of melanoma called dysplastic nevi. These cells have a finite life-span due the interplay of genetic and environmental factors (Meier *et al*., 1998; Goldstein & Tucker 2013). Further, these nevi acquire sequential genetic alterations accompanied by the influence of various growth factors and transform into malignant melanoma (Balois & Amar 2014).
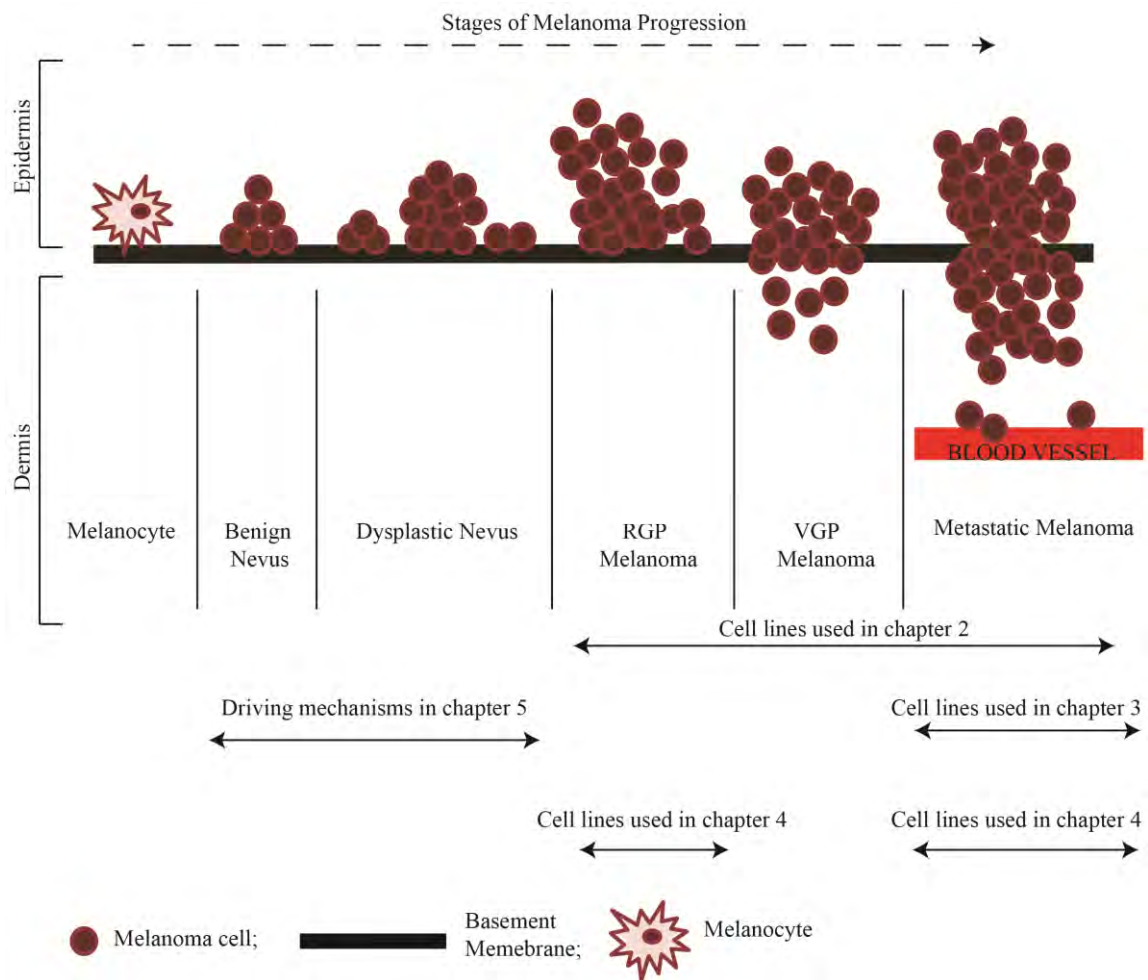
Figure 1.2: *Stages of melanoma progression*. The schematic illustrates melanoma progression, showing the localisation of nevi and clusters of melanoma cells. The chapters in this thesis that include the corresponding stage of melanoma are indicated

respectively. The mechanism that drives nevi and nest formation are investigated in Chapter 5 while, radial growth phase (RGP), vertical growth phase (VGP) and metastatic cell lines are used in the study detailed in Chapters 2, 3 and 4, as indicated using arrows.

After nevi, the *radial growth phase* (RGP) is considered the first step of malignant melanoma, where the melanoma nests grow in size and are confined to the epidermis (Balois & Amar 2014; Beaumont *et al*., 2014). The next stage is the *vertical growth phase* (VGP) wherein melanoma nests, accompanied through the action of proteolytic enzymes, disrupt the basement membrane and invade into the dermis (Bennett 2016; Meier *et al*., 1998). Lastly, the melanoma cells acquire metastatic properties that facilitate melanoma cell invasion into the lymphatic system or haematogenous route, thereby spreading to other tissues (Eves *et al*., 2003; Damsky *et al*., 2014; Piskounova *et al*., 2015; Garbe *et al*., 2016). It is essential to emulate these stages *in vitro* to further our understanding about the various mechanisms that influence and promote melanoma progression. In particular, to study the invasion of melanoma cells *in vitro*, a three-dimensional (3D) platform is required. The details of these 3D models is summarised below.

1.1.5   *Three-Dimensional Human Skin Equivalent Model in Melanoma Progression*

Melanoma is widely researched on a two-dimensional (2D) platform. These 2D assays are simple to perform, relatively inexpensive and are ideal for pre-clinical, preliminary melanoma research investigations (Beaumont *et al*., 2014; Beaumont *et al*., 2016). Previous 2D research studies about melanoma progression have focused on examining the radial migration of cell populations, cell proliferation, cell-cell adhesion as well as protein-expression of melanoma cells (Alexaki *et al*., 2010; Simpson *et al*., 2013; Treloar *et al*., 2013; Das *et al*., 2015). However these 2D studies do not re-capitulate an environment similar to human skin *in vivo.* The 2D models do not demonstrate the complex architecture of native human skin where a diverse array of intercellular interactions, cell-extracellular matrix interactions and cell signalling takes place (Vorsmann *et al*., 2013; Beaumont *et al*., 2014; Shannan *et al*., 2016).

Studies show that melanoma cells communicate with the surrounding skin cells and tissues and this cross-talk influences melanoma progression (Hill *et al*., 2015; Wang *et al*., 2016; Ferrarelli 2017). Additionally, to study the invasive properties of melanoma cells a 3D environment is required. Extensive research on melanoma has been carried out using animal models, 3D models with dermal substitutes, as well as 3D skin models. Animal models overcome most of the 2D limitations but animal skin biology does not replicate properties observed in human skin (Wang *et al*., 2016; Day *et al*., 2017). There are commercially available skin equivalent models where the dermal scaffold is developed using biomaterials like collagen and fibrin (Brohem *et al*., 2011; Vorsmann *et al*., 2013; Zoschke *et al*., 2016). However, skin substitutes may fail to mimic native skin architecture and generally do not have a basement membrane which is proven essential in melanoma progression studies (Schafer *et al*., 1989; Halim *et al*., 2010). There is also evidence in the literature that suggests skin substitutes comprising both epidermal and dermal components such as biopolymers and animal-derived dermal components like rat tail collagen alter the environment (El *et al*., 2009). Commercially available human skin equivalent models without human cells do not need ethics approval but they incur high purchase costs. They need to go through vigilant Australian quarantine that limits the entry of human cell-based materials (Poumay *et al*., 2004).

Therefore construction of human skin equivalents *in vitro* using primary (human derived) skin cells that retain structural and cellular organisation of native skin is an excellent research tool (Figure 1.3). These human skin equivalent (HSE) models are extensively used for research purposes for example, to study burn treatments (Topping *et al*., 2006), wound healing progression (Xie *et al*., 2011) as well as other skin-related diseases (Dekker *et al*., 2000; Fernandez *et al*., 2014). Furthermore, the HSE retains the basement membrane necessary for keratinocyte attachment *in vitro* allowing the formation of a stratified epidermis. Hence the HSE model can be used to emulate the stages of melanoma as observed in human skin *in vivo* and study the key properties of melanoma progression.
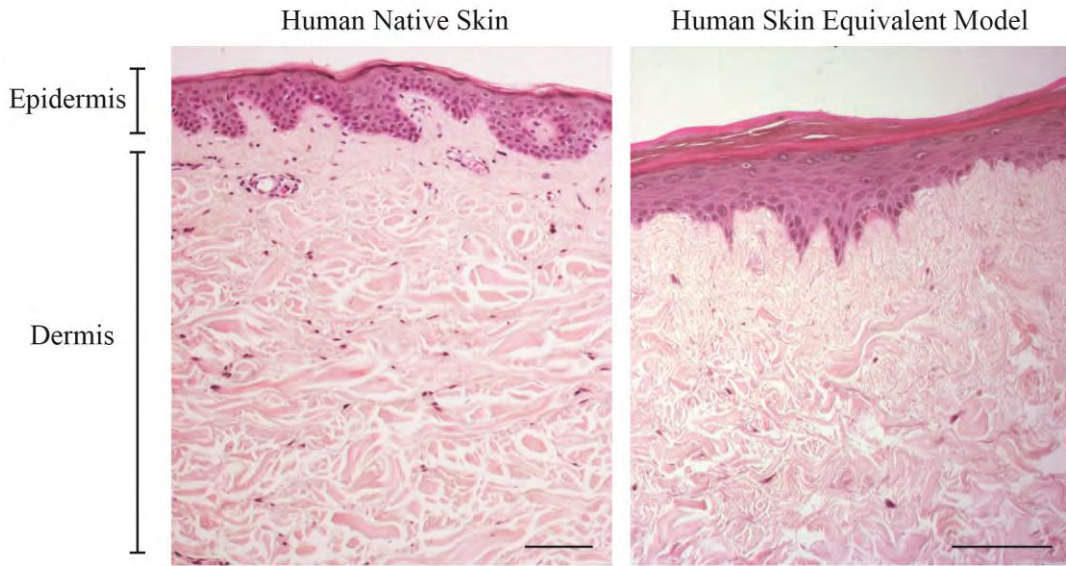
Figure 1.3: *Comparison of human native skin and the human skin equivalent (HSE) model.* The cross-sectional image of haematoxylin and eosin stained human native skin and HSE model show the physiological organisation of epidermal and dermal layers. Scale bar on each image corresponds to 100 μm. Images are generated as part of this thesis.

There are a limited number of melanoma studies that construct a melanoma skin equivalent (MSE) model using basic concepts of the HSE model (Eves *et al.*, 2000; Meier *et al.*, 2000; Marques & Mac Neil 2016). Among these restricted number of studies only Dekker *et al.* (2000) compare stages of melanoma by constructing an MSE model incorporating cell lines associated with the RGP, VGP and metastatic phases. Most studies focus mainly on the metastatic phase of melanoma (Damsky *et al.*, 2011; Tiwary *et al.*, 2014). Additionally, there are no time course studies using 3D MSE models which would provide an improved understanding of intricate aspects of the model. For example, additional information about the distribution of cells over time, the durability of the model, the difference in behaviour of cells at an early time-point compared to later time-points, are a few concepts that can be addressed using time-course studies. After careful consideration of the concepts associated with melanoma progression, we infer a set of aims to further our understanding about the key features of the disease advancement that have not been examined previously.

1.2 AIMS OF THE PROJECT

The principal aim of this project is to construct a melanoma skin equivalent (MSE) model to further our understanding about melanoma progression. This project specifically aims to quantify key features of melanoma progression, such as: melanoma cell migration; melanoma cell proliferation; melanoma cell invasion; and melanoma nest formation, using experimental and mathematical techniques.

1.2.1 Specific Aims of the Project

    (i) Reliably detect melanoma cell lines used within this project

    (ii) Quantify key features of melanoma growth, such as cell migration and proliferation

    (iii) Construct a melanoma skin equivalent model (MSE) and examine nest formation in the early and late phases of melanoma

    (iv) Identify the dominant mechanism that drives melanoma nest formation

1.3 SIGNIFICANCE OF THE PROJECT

Melanoma is associated with improved prognosis when detected at an earlier stage but the prognosis varies significantly depending upon the stage of the disease (Balch *et al*., 2009). The five-year survival rate of patients with an advanced metastatic stage of melanoma is 5-15% while the survival rate of patients with melanoma at an early stage, such as RGP is 95% (Carter *et al*., 2016). Hence, the severity of melanoma is not only associated with the alarming incidence rates of the disease but also to the limited diagnosis as well as effective treatment options available when the melanoma has progressed to an advanced stage. This highlights the need for accurate melanoma diagnosis and an in-depth understanding of the different individual features of melanoma progression, which could eventually be targeted to control the spread of the disease. Here we elaborate on the knowledge gaps significant to each aim and provide a brief description about how the aim is addressed.

1.3.1 Knowledge gap and significance of aim 1

An effective treatment of early melanoma is surgical excision but this requires accurate early detection (Guerra-Rosas *et al.*, 2017). Histological identification of melanoma cells is a standard diagnostic method (March *et al.*, 2015a; March *et al.*, 2015b). Identification of melanoma cells is proven to be challenging due to the cellular heterogeneity. Melanoma cells are morphologically diverse and studies show that these cells are difficult in histopathological diagnosis. From a research perspective, accurate identification of melanoma cells within a population of normal cells is proven essential for further downstream analysis.

Since preliminary studies document challenges in melanoma identification, this project aims to use a reliable marker to accurately identify melanoma cell lines used within this study. In this chapter, melanoma cell lines used in this project are detailed. Different experimental approaches that are used to identify a reliable melanoma-associated marker are described followed by the challenges faced using a particular metastatic melanoma cell line. The study reports S100 as a reliable melanoma-associated marker that successfully identifies all of the melanoma cell lines used further in this project. The findings of this chapter also highlight the rationale for omitting the particular metastatic cell line, MM127 in further studies.

1.3.2 Knowledge gap and significance of aim 2

In human skin, individual melanoma cells cluster to form nests, which is a prominent feature in melanoma progression. Cell migration and cell proliferation are two known mechanisms that promote the growth of melanoma nests. Examining these underlying features independently would emphasise their contribution to the progression of the disease and enable their effective control measures. Previous studies by Justus *et al.* (2014); Gallinaro *et al.* (2013); and Treloar *et al.* (2013) examine cell migration and cell proliferation and highlight the importance of these processes in melanoma progression. These studies use melanoma monocultures in scratch assays, barrier assays as well as

Transswell® assays to investigate these underlying melanoma processes. However, melanoma progresses in a multicellular environment *in vivo* and individual melanoma cells are known to cross-talk with the surrounding skin cell populations (Kilsdonk *et al*., 2010; Flach *et al*., 2011; Zhou *et al*., 2015). Therefore, this project extends previous studies, and aim to mimic the spreading of individual melanoma cells as observed in human native skin, using 2D *in vitro* co-culture models. Furthermore, this novel study is combined with mathematical modelling to quantify cellular mechanisms and provide additional information.

Previous studies show mathematical models to provide insight into the experimental results (Maini *et al*., 2004; Gallinaro *et al*., 2013; Morais *et al.,* 2017). Here, the tandem use of mathematical modelling with experimental investigations further quantify these underlying mechanisms by extracting detailed information about cell migration and cell proliferation. Thus by cataloguing these mechanisms of melanoma progression we aim to highlight potential targets for future effective melanoma therapeutics. Here, we quantify the rate of melanoma cell proliferation and melanoma cell migration in the presence and absence of skin cells, which has not been identified previously.

Melanoma cell line, SK-MEL-28 that is successfully detected in Chapter 2 of this thesis is used in this study. In this 2D co-culture model, melanoma cells are cultured alongside primary fibroblast cells that are previously reported to influence melanoma cell migration and proliferation (Aberty *et al*., 2012). A suite of barrier assays are performed with varying cell densities of both the cell types in this 2D co-culture model. The rates of cell migration and cell proliferation are examined. The main purpose of this study is to report the influence of fibroblasts on melanoma cell migration and cell proliferation in using the 2D co-culture model. The outcomes does not show any influence of fibroblasts on melanoma cells as hypothesised, however there can be a number of explanations to this result. The rationale of the study along with the experimental methods and the mathematical modelling is described in this chapter.

1.3.3 Knowledge gap and significance of aim 3

Co-culture models provide excellent preliminary data. However, melanoma cells embedded within the human skin behave differently to melanoma cells grown two-dimensionally (Beaumont *et al*., 2014). In a 2D environment the melanoma cells do not form colonies, and do not display invasive properties, therefore 2D monocultures and co-cultures of melanoma cells do not accurately represent the physiology of human skin *in vivo* (Xu *et al*., 2015). Typically melanoma cells are known to reside within a complex multicellular environment, containing extracellular matrix and producing a suite of signalling molecules which collectively contribute to melanoma progression (Beaumont *et al*., 2014). Moreover, previous research demonstrates that promising 2D results can be altered when translated into *in vivo* situations as both, 2D and 3D environments are entirely different (Zanoni *et al*., 2016). Therefore, a 3D model is essential for investigating melanoma development, progression and melanoma associated therapeutics.

While mice models are widely used in melanoma research, they have their limitations as the skin architecture varies significantly from human skin. The early invasion of melanoma cells through the basement membrane cannot be investigated using mice models as the melanocytes reside in dermal hair follicles while in human skin the melanocytes are found in the basal epidermal layer (Wang *et al*., 2016). Furthermore, there are organotypic models constructed using bovine or rat tail collagen, however untimely contraction of these dermal substitutes may effect in extrapolating accurate results (Hill *et al*., 2015). Overall, there is a growing need for more advanced, biologically representative and reproducible *in vitro* models, which closely resemble human skin to better investigate melanoma progression. There are limited studies using 3D human skin equivalent models that compare the early and late stages of melanoma (Bergers *et al*., 2016). Here, we not only construct a 3D melanoma skin equivalent model, but address concepts that have not been investigated previously such as examining and quantifying melanoma cell invasion as a function of time.

To further investigate the features of melanoma progression described in Chapter 4, a 3D MSE model is constructed. Melanoma progresses in a 3D environment surrounded by skin cells. This chapter describes the method used to construct a 3D melanoma human skin model incorporating melanoma cells from the early and late phase of the disease (cell lines from the RGP and metastatic phase of melanoma). These cell lines are characterised in Chapter 2 and the melanoma nests are identified accurately using S100.

1.3.4 Knowledge gap and significance of aim 4

While the underlying mechanisms of cell migration, cell proliferation and cell invasion are investigated, it is also important to understand and examine the mechanism that drives melanoma nest formation. These processes could lead to potential therapeutic targets that can be used for efficient melanoma treatment. Nest formation is a concept recently researched using individual melanoma cells by Wesssls *et al*. (2017) however, the model used in their investigations is entirely different to this projects' 3D MSE model. The 3D MSE model used in this study provides a multicellular environment, where the cross-talk of melanoma cells with the surrounding skin cells re-create a more realistic *in vivo* like situation. Moreover, this project highlights results as a function of time, varying initial cell density and identifying for the first time that both, the role of cell number, and cell proliferation drive melanoma nest formation.

To address aim 4, the 3D MSE model developed in Chapter 4 is used to examine the mechanisms that drive melanoma nest formation. Two mechanisms are prominent in melanoma nest formation, these include: cell migration; and cell proliferation. The metastatic melanoma cell line, SK-MEL-28, is used in this study. This melanoma cell line is aggressive in nature and forms noticeably large nests as described in Chapter 4. The proliferation of the melanoma cells are inhibited to independently observe the role of cell migration. This study extends previous Matrigel studies using a multicellular 3D model and using varying initial number of melanoma cells. Furthermore, addressing this aim, demonstrates the 3D MSE model as a suitable platform to research melanoma progression.

Overall, this thesis will address the above described knowledge gaps resulting in the development of a durable 3D MSE model that can potentially be used as a pre-clinical *in vitro* model to successfully study melanoma progression.

1.4   THESIS BY PUBLICATION OUTLINE

The outcomes of this project highlight the importance of understanding the underlying key features of melanoma progression. It mainly focusses on the identification of melanoma cells and their interaction with the surrounding skin cells. Moreover, the 3D MSE model demonstrates its potential as a reproducible *in vitro* research platform which can be further utilised for pre-clinical melanoma research. Furthermore, this is an interdisciplinary project where the PhD candidate is from the Faculty of Health and the principal supervisor is from the School of Mathematical Sciences. In this project the PhD candidate performed all the experimental investigations and analysed the results. However, the experimental data is further verified using mathematical models by members from the School of Mathematical Sciences: Dr Catherine Penington – Post Doctoral Research Fellow; and Mr Alex Browning-Masters' Student. The PhD candidate interacted with mathematicians to provide experimental data that is sufficient to extrapolate mathematical models and verify the experimental outcomes. Out of the four manuscripts, two manuscripts are entirely experimental. The other two manuscripts detail the experimental outcomes and are further interpreted using mathematical models. Please also note that the results in this thesis do not include statistical analysis as the experimental data is extrapolated and corroborated using mathematical models.

This thesis is presented by publications. It comprises of three published peer-reviewed manuscripts and one manuscript currently undergoing peer review. At the end of each chapter a set of references are listed for the ease of the reader. Also the numbering of the figures is changed and is not in accordance to the original publication. The figures and tables in this thesis are numbered by first assigning the chapter number which is followed by the appearance of the respective table or the figure in that chapter. For example, (Figure 1.1)

corresponds to the figure in Chapter 1 and it is the first figure in that chapter. The appearance of each chapter is outlined below describing the individual details.

1. Chapter 1: Introduction

This chapter introduces the background and literature necessary to understand the objectives of this project. Following the literature review the thesis provides specific aims of the study and the significance of each aim. Lastly the structure of the thesis is outlined providing an overview of each chapter.

2. Chapter 2: Research Paper 1

Standard melanoma-associated markers do not identify the MM127 metastatic melanoma cell line. (2016). *Scientific Reports*. 6: 24569. (doi: 10.1038/srep24569)

3. Chapter 3: Research Paper 2

Quantifying rates of cell migration and cell proliferation in co-culture barrier assays reveals how skin and melanoma cells interact during melanoma spreading and invasion. (2017). *Journal of Theoretical Biology*. 423: 13-25 (doi: 10.1016/j.jtbi.2017.04.017)

4. Chapter 4: Research Paper 3

Quantitative comparison of the spreading and invasion of radial growth phase and metastatic melanoma cells in a three-dimensional human skin equivalent model. (2017). *PeerJ*. 5:e3754 (doi: 10.7717/peerj.3754)

5. Chapter 5: Research Paper 4

Three-dimensional experiments and individual based simulations show that cell proliferation drives melanoma nest formation in human skin. (2018). *BMC Systems Biology*. 12: 34 (doi: 10.1186/s12918-018-0559-9)

6.   Chapter 6: Conclusion and Future Work

In this chapter, the overall findings of this thesis are summarised followed by potential future work that can extend the current findings creating new avenues for melanoma research.

1.5 REFERENCES

1. Abety AN, Fox JW, Schonefub A, Zamek J, Landsberg J, Krieg T, Blobel C, Mauch C, Zigrino P. 2012. Stromal fibroblast–specific expression of ADAM-9 modulates proliferation and apoptosis in melanoma cells *in vitro* and *in vivo*. *The Journal of Investigative Dermatology*. 132: 2451-2458.

2. AIHW & AACR (Australasian Association of Cancer Registries) 2014. Cancer in Australia: an overview 2014. Cancer series no. 90. Cat. no. CAN 88. Canberra: AIHW.

3. Alexaki VI, Javelaud D, Van-Kempen LCL, Mohammed KS, Dennler S, Luciani F, Hoek KS, Juarez P, Goydos JS, Fournier PJ *et al*. 2010. GL12-mediated melanoma invasion and metastasis. *Journal of the National Cancer Institute* 102: 1148-1159.

4. Australian Institute of Health and Welfare. *Skin cancer in Australia. Cat. no. CAN 96.* Canberra, Australia: AIHW; 2016 [cited 2016 Oct 5] Available from: http://www.aihw.gov.au/publication-detail/?id=60129555786.

5. Balch CM, Gershenwald JE, Soong SJ, Thompson JF, Atkins MB, Byrd DR, *et al*. 2009. Final version of 2009 AJCC melanoma staging and classification. *Journal of Clinical Oncology*. 27: 6199-206.

6. Balois T, Amar MB. 2014. Morphology of melanocytic lesions *in situ*. *Scientific Reports*. 4: 3622.

7. Bandarchi B, Ma L, Navab R, Seth A, Rasty G. 2010. From melanocyte to metastatic malignant melanoma. *Dermatology Research and Practice*. 2010: e583748.

8. Beaumont KA, Mohana-Kumaran N, Haass NK. 2014. Modelling melanoma *in vitro* and *in vivo*. *Healthcare* 2: 27-46.

9. Beaumont KA, Hill DS, Daignault SM, Lui GYL, Sharp DM, Gabrielli B, Weninger W, Haass NK. 2016. Cell cycle phase-specific drug resistance as an escape mechanism of melanoma cells. The Journal of Investigative Dermatology. 136: 1479-1489.

10. Bennett DC. 2015. Genetics of melanoma progression: the rise and fall of cell senescence. *Pigment Cell and Melanoma Research*. 29: 122-140.

11. Bergers LIJC, Reijnders CMA, van den Broek LJ, Speikstra SW, de Gruijl TD, Weijers EM, Gibbs S. 2016. Immuno-competent human skin disease models. *Drug Discovery Today*. 21: 1479-1488.

12. Breitkreutz D, Koxholt I, Thiemann K, Nischt R. 2013. Skin basement membrane: the foundation of epidermal integrity-BM functions and diverse roles in bridging molecules nidogen and perlecan. *Biomed Research International*. 2013: 179784.

13. Brohem CA, Cardeal LBS, Tiago M, Soengas MS, Barros SBM, Maria-Engler SS. 2011. Artificial skin in perspective: concepts and applications. *Pigment Cell and Melanoma Research*. 24: 35-50

14. Carter JH, Deddens JA, Spaulding NRIV, Lucas D, Colligan BM, Lewis TG, Hawkins E, Jones J, Pemberton JO, Doughlass LE, Graff JR. 2016. Phosphorylation of eIF4E serine 209 is associated with tumour progression and reduced survival in malignant melanoma. *British Journal of Cancer*. 114: 444-453.

15. Chung H, Suh EK, Han IO, Oh ES. 2011. Keratinocyte-derived laminin-332 promotes adhesion and migration in melanocytes and melanoma. *The Journal of Biological Chemistry*. 286: 13438-13447.

16. Damsly WE, Rosenbaum LE, Bosenberg M. 2011. Decoding melanoma metastasis. *Cancers*. 3: 126-163.

17. Damsky WE, Theodosakis N, Bosenberg M. 2014. Melanoma metastasis: new concepts and evolving paradigms. *Oncogene*. 33: 2413-2422.

18. Das AM, Eggermont AMM, Hagen TLM. 2015. A ring barrier–based migration assay to assess cell migration *in vitro*. *Nature Protocols*. 10: 904-915.

19. Day C, Marchalik R, Merlino G, Michael H. 2017. Mouse models of UV-induced melanoma: genetics, pathology, and clinical relevance. *Laboratory Investigation*. 97: 698-705.

20. El GA, Commandeur S, Rietveld MH, Mulder AA, Willemze R. 2009. Replacement of animal-derived collagen matrix by human fibroblast-derived dermal matrix for human skin equivalent products. *Biomaterials*. 30: 71-78.

21. Eves P, Katerinaki E, Simpson C, Layton C, Dawson R, Evans G, Mac Neil S. 2003. Melanoma invasion in reconstructed human skin is influenced by skin cells-investigation of the role of proteolytic enzymes. *Clinical and Experimental Metastasis*. 20: 685-700.

22. Fernandez TL, Lonkhuyzen DR, Dawson RA Kimlin MG, Upton Z. 2014. In vitro investigations on the effect of dermal fibroblast on keratinocyte responses to ultraviolet B radiation. *Photochemistry and Photobiology*. 90: 1332-1339

23. Ferrarelli LK. 2017. Melanoma cells talk to keratinocytes. *Science*. 355: 1169-1171.

24. Flach EH, Rebecca VW, Herlyn M, Smalley KSM, Anderson ARA. 2011. Fibroblasts contribute to melanoma tumour growth and drug resistance. *Molecular Pharmaceutics*. 8: 2039-2049.

25. Foth M Wouters J, Chaumont C, Dynoodt P, Gallagher WM. 2015. Prognostic and predictive biomarker in melanoma: an update. *Expert Review of Molecular Diagnosis*. 16: 223-237.

26. Garbe C, Peris K, Hauschild A, SaiagP, Middleton M, Bastholt L, Grob JJ, Malvehy J, Newton-Bishop J, Strtigos A *et al*., 2016. Diagnosis and treatment of melanoma. European consensus-based interdisciplinary guideline – Update 2016. *European Journal of Cancer*. 63: 201-217.

27. Gallinaro JV, Marques CMG, Azevedo FM, Suzuki DOH. 2013. Mathematical Modeling of Melanoma Cell Migration with an Elastic Continuum Model for the Evaluation of the Influence of Tumor Necrosis Factor-Alpha on Migration. *Journal of Computational Medicine*. 2013: 534073.

28. Goldstein AM, Tucker MA. 2013. Dysplastic nevi and melanoma. *Cancer Epidemiology, Biomarkers and Prevention*. 22: 528-532.

29. Guerra-Rosas E, Alvarez-Borrego J, Angulo-Molina A. 2017. Identification of melanoma cells: a method based in mean variance of signatures via spectral densities. *Biomedical Optic Express*. 8: 2185.

30. Haass NK, Smalley KSM, Li L, Herlyn M. 2005. Adhesion, migration and communication in melanocytes and melanoma. *Pigment Cell and Melanoma Research.* 18: 150-159.

31. Halim AS, Khoo TL, Mohd Yussof SJ. 2010. Biologic and synthetic skin substitutes: An overview. *Indian Journal of Plastic Surgery*. 43: S23-28.

32. Hanahan D, Weinberg RA. 2011. Hallmarks of Cancer: The next generation. *Cell*. 144: 646-674.

33. Hill DS, Robinson NDP, Caley MP, Chen M, O'Toole EA, Armstrong JL, Przyborski S, Lovat PE. 2015. A novel fully-humanised 3D skin equivalent to model early melanoma invasion. *Molecular Cancer Therapies.* 14: 2665-2673.

34. Izar B, Joyce CE, Goff S, Cho NL, Shah PM, Sharma G, Li J, Ibrahim N, Gold J, Hodi FS, Garraway LA, Novina CD, Bertagnolli MM, Yoon CH. 2016. Bidirectional cross talk between patient-derived melanoma and cancer-associated fibroblasts promotes invasion and proliferation. *Pigment Cell and Melanoma Research*. 29: 656-658.

35. Jelineck S, Bettles S, Bright P, Jakel A. 2016. Osteopaths in the United Kingdom and Australia: attitudes, practice, confidence and knowledge with regard to melanoma recognition- an observational questionnaire study. *International Journal of Osteopathic Medicine.* 20: 18-30.

36. Justus CR, Leffler N, Ruiz-Echevarria M, Yanh LV. 2014. *In vitro* cell migration and invasion assays. *Journal of Visualised Experiments.* 88: 51046.

37. Karimkhani C, Green AC, Nijsten T, Weinstock MA, Dellavalle RP, Naghavi M, Fitzmaurice C. 2017. The Global burden of melanoma: Results from global burden of disease study 2015. *British Journal if Dermatology*. 177: 134-140.

38. Kilsdonk JWJV, Bergers M, Kempen LCLTV, Schalkwijk J, Swart GWM. 2010. Keratinocytes drive melanoma invasion in a reconstructed skin model. *Melanoma Research.* 20: 372-380.

39. Klar AS, Michalak K, Bottcher-Haberzeth S, Reichmann E, Meuli M, Biedermann T. 2017. The expression pattern of keratin 24 in tissue-engineered dermo-epidermal human skin substitutes in an in vivo model. *Pediatric Surgery International*. [Ahead of print] doi: 10.1007/s00383-017-4198-9

40. Lai-Cheong JE, McGrath JA. 2009. Structure and function of skin, hair and nails. *Medicine*. 37: 223-226.

41. Maini PK, McElwain DLS, Leavesley DI. 2004. Traveling wave model to interpret a wound–healing cell migration assay for human peritoneal mesothelial cells. *Tissue Engineering*. 10: 475–482.

42. March J, Hand M, Truong A, Grossman D. 2015a. Practical application of new technologies for melanoma diagnosis: Part II. Molecular approaches. *Journal of the American Academy of Dermatology*. 72: 943–958.

43. March J, Hand M, Grossman D. 2015b. Practical application of new technologies for melanoma diagnosis: Part I. Non-invasive approaches. *Journal of the American Academy of Dermatology*. 72: 929–941.

44. Meier F, Satyamoorthy K, Nesbit M, Hsu MY, Schittel B, Garbe C, Herlyn M. 1998. Molecular events in melanoma development and progression. *Frontiers of Bioscience*. 3: D1005-1010.

45. Morais MCC, Stuhl I, Sabino AU, Lautenschlager WW, Queiroga AS, Tortelli TC, Chammas R, Suhov Y, Ramos AF. 2017. Stochastic model of contact inhibition and the proliferation of melanoma *in situ*. *Scientific Reports*. 7: 8026.

46. Muller M, Beck IM, Gadesmann J, Karschuk N, Paschen A, Proksch E, Djonov V, Reiss K, Sedlacek R. 2016. MMP 19 is upregulated during melanoma progression and increases invasion of melanoma cells. *Modern Pathology*. 23: 511-52.

47. Olsen LO, Takiwaki H, Serup J. 1995. High-frequency ultrasound characterization of normal skin. Skin thickness and echographic density of 22 anatomical sites. *Skin Research and Technology*. 1: 74-80.

48. Ordonez NG. 2014. Value of melanocytic-associated immunohistochemical markers in the diagnosis of malignant melanoma: a review and update. *Human Pathology*. 45: 191-205.

49. Poumay Y, Dupont F, Marcoux S, Leclercq-Smekens M, Herin M, Coquette A. 2004. A simple reconstructed human epidermis: preparation of the culture model and utilization in in vitro studies. *Archives of Dermatological Research*. 296: 203-211.

50. Piskounova E, Agathocleous M, Murphy MM, Hu Z, Huddlestun SE, Zhao Z, Leitch AM, Johnson TM, De Berardinis RJ, Morrison SJ. 2015. Oxidative stress inhibits distant metastasis by human melanoma cells. *Nature*. 527: 186-191.

51. Schafer IA, Shapiro A, Kovach M, Lang C, Fratianne RB. 1989. The interaction of human papillary and reticular fibroblasts and human keratinocytes in the contraction of three-dimensional floating collagen lattices. *Experimental Cell Research*. 183: 112-125.

52. Shannan B, Chen Q, Watters A, Perego M, Krepler C, Thombre R, Li L, Rajan G, Peterson S, Gimotty PA, Wilson M, Nathanson KL, Gangadhar TC, Schuchter LM, Weeraratna AT, Herlyn M, Vultur A. 2016. Enhancing the evaluation of PI3K inhibitors through 3D melanoma models. *Pigment Cell Melanoma Research*. 29: 317–328.

53. Shay JW. 2017. New insights into melanoma development. *Science*. 357: 1358-1359.

54. Shirshin EA, Gurfinkel YI, Priezzhev AV, Fadeev VV, Lademann J, Darvin ME. 2017. Two-photon autofluorescence lifetime imaging of human skin papillary dermis *in vivo*: assessment of blood capillaries and structural proteins localization. *Scientific Reports*. 7: 1171.

55. Simpson MJ, Treloar KK, Binder BJ, Haridas P, Manton KJ, Leavesley DI, McElwain DLS, Baker RE. 2013. Quantifying the roles of cell motility and cell proliferation in a circular barrier assay. *Journal of the Royal Society Interface*. 10: 20130007.

56. Sidhu P, Menzies AM, Long G, Carlino M, Lorens S, Kapoor R. 2017. Radiological manifestations of immune-related adverse effects observed in patients with melanoma undergoing immunotherapy. *Journal of Medical Imaging and Radiation Oncology*. 61: 759-766.

57. Sneyd MJ, Cox B. 2013. A comparison in trends of melanoma mortality in New Zealand and Australia: the two countries with the highest melanoma incidence and mortality in the world. *BMC Cancer*. 13: 372.

58. Tiwary S, Preziosi M, Rothberg PG, Zeitouni N, Corson N, Xu L. 2014. ERBB3 is required for metastasis formation of melanoma cells. *Oncogenesis*. 3:e110.

59. Topping G, Malda J, Dawson R, Upton Z. 2006. Development and characterisation of human skin equivalents and their potential application as a burn wound model. *Primary Intention*. 14: 16-18.

60. Treloar KK, Simpson MJ, Haridas P, Manton KJ, Leavesley DI, McElwain DLS, Baker RE. 2013. Multiple types of data are required to identify the mechanisms influencing the spatial expansion of melanoma cell colonies. *BMC Systems Biology*. 7: 137.

61. Wang JX, Fukunaga-Kalabis M, Herlyn M. 2016. Crosstalk in skin: melanocytes, keratinocytes, stem cells, and melanoma. *Journal of cell communication and signalling*. 10: 191-196.

62. Wegner J, Loser K, Apsite G, Nischt R, Eckes B, Krieg T, Werner S, Sorokin L. 2016. Laminin α5 in the keratinocyte basement membrane is required for epidermal-dermal intercommunication. *Matrix Biology*. 56: 24-41.

63. Wessels D, Lusche DF, Voss E, Kuhl S, Buchele EC, Klemme MR, Russell KB, Ambrose J, Sol BA, Bossler A *et al*. 2017. Melanoma cells undergo aggressive coalescence in a 3D Matrigel model that is repressed by anti-CD44. *PLoS ONE*.12: e0173400.

64. Wickett RR, Visscher MO. 2006. Structure and function of the epidermal barrier. *American Journal of Infection Control*. 34: s98-s110.

65. Xiao D, Barry S, Kmetz D, Egger M, Pan J, Rai SN, Qu J, McMasters KM, Hao H. 2016. Melanoma cell–derived exosomes promote epithelial–mesenchymal

transition in primary melanocytes through paracrine/autocrine signaling in the tumor microenvironment. *Cancer Letters*. 376: 318-327.

66. Xie Y, Rizzi SC, Dawson R, Lynam E, Richards S, Leavesley DI, Upton Z. 2011. Development of a three-dimensional human skin equivalent wound model for investigating novel wound healing therapies. *Tissue Engineering Part C: Methods*. 16: 1111-1123.

67. Xu X, Farach-Carson MC, Jia X. 2014. Three-dimensional *in vitro* tumor models for cancer research and drug evaluation. *Biotechnology Advances*. 32: 1256-1258.

68. Zanoni M, Piccinini F, Arienti C, Zamagni A, Santi S, Polico R, Bevilacqua A, Tesei A. 2016. 3D tumor spheroid models for *in vitro* therapeutic screening: a systematic approach to enhance the biological relevance of data obtained. *Scientific Reports*. 6:19103.

69. Zhou L, Yang K, Andl T, Wickett RR, Zhang Y. 2015. Perspective of targeting cancer-associated fibroblasts in melanoma. *Journal of Cancer*. 6: 717-726.

70. Zocco M, Blanpain C. 2017. Identifying the niche controlling melanocyte differentiation. *Genes and Development*. 31: 721-723.

71. Zoschke C, Ulrich M Sochorova M, Wolff C, Vavrova K, Ma N, Ulrich C, Brandner JM, Schafer-Korting M. 2016. The barrier function of organotypic non-melanoma skin cancer models. *Journal of Controlled Release*. 233: 10-18.

Chapter 2: Standard melanoma-associated markers do not identify MM127 metastatic melanoma cell line

Statement of Contribution of Co-Authors for
Thesis by Published Paper

The following is the suggested format for the required declaration provided at the start of any thesis chapter which includes a co-authored publication.
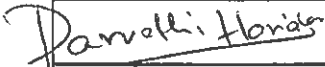
The authors listed below have certified that:

1. they meet the criteria for authorship in that they have participated in the conception, execution, or interpretation, of at least that part of the publication in their field of expertise;
2. they take public responsibility for their part of the publication, except for the responsible author who accepts overall responsibility for the publication;
3. there are no other authors of the publication according to these criteria;
4. potential conflicts of interest have been disclosed to (a) granting bodies, (b) the editor or publisher of journals or other publications, and (c) the head of the responsible academic unit, and
5. they agree to the use of the publication in the student's thesis and its publication on the QUT's ePrints site consistent with any limitations set by publisher requirements.

In the case of this chapter:

Haridas P, McGovern JA, Kashyap AS, McElwain DLS, Simpson MJ. (2016). Standard melanoma-associated markers do not identify the MM127 metastatic melanoma cell line. *Scientific Reports*. 6: 24569. (doi: 10.1038/srep24569)

Published online 18 April 2016.

Contributor	Statement of contribution*
Parvathi Haridas	Designed experiments, performed all laboratory experiments, analysed data, wrote the manuscript, prepared figures and/tables and reviewed drafts of the manuscript
06/11/2017	
Jacqui A. McGovern	Designed experiments, reviewed data analysis and reviewed drafts of the manuscript
Abhishek S. Kashyap	Designed experiments, reviewed data analysis and reviewed drafts of the manuscript
D. L. Sean McElwain	Designed experiments, reviewed data analysis and reviewed drafts of the manuscript
Matthew J. Simpson	Designed experiments, reviewed data analysis and reviewed drafts of the manuscript

Principal Supervisor Confirmation

I have sighted email or other correspondence from all Co-authors confirming their certifying authorship.
(If the Co-authors are not able to sign the form please forward their email or other correspondence confirming the certifying authorship to the RSC).

Matthew J Simpson

Name _____   Signature _____   Date 10|11|2017

2.1   ABSTRACT

Reliable identification of different melanoma cell lines is important for many aspects of melanoma research.   Common markers used to identify melanoma cell lines include: S100; HMB-45; and Melan-A. We explore the expression of these three markers in four different melanoma cell lines: WM35; WM793; SK-MEL-28; and MM127. The expression of these markers is examined at both the mRNA and protein level.   Our results show that the metastatic cell line, MM127, cannot be detected using any of the commonly used melanoma-associated markers.   This implies that it would be very difficult to identify this particular cell line in a heterogeneous sample, and as a result this cell line should be used with care.

2.2   INTRODUCTION

Melanoma is an aggressive form of skin cancer that has the highest incidence rate in Australia[1]. Since many aspects of melanoma research rely on the use of various types of melanoma cell lines[2,3], the reliable identification of different melanoma cell lines is very important.

A range of melanoma-associated markers are used to identify different types of melanoma cell lines[4]. The three most frequently used markers are: S100; HMB-45 and Melan-A[5, 6]. A common feature of many experimental investigations is that some melanoma cell lines are unable to be detected using certain markers[7]. To address this limitation, many studies use two different markers to ensure reliable identification[8]. MM127 is a metastatic melanoma cell line of human origin, isolated in 1970[9]. Since then, MM127 melanoma cells have been used in many published investigations. For example, MM127 cells have been used in ultraviolet radiation studies[10], gene-based studies[11], drug-response studies[12] and in other melanoma-associated research.

Some of our previous work involves investigating how the balance of the rate of cell migration and the rate of cell proliferation affects the collective spreading of a population of MM127 melanoma cells[13]. In this previous study we describe results from an *in vitro* monoculture circular barrier assay[14,15], and we use a discrete random walk mathematical model to quantify the rates of cell migration and cell proliferation in the experiment. Because this previous study involves a monoculture assay with just one cell type present, we did not attempt to identify the MM127 cells using any melanoma-associated markers. One way to extend this previous work would be to perform more complicated co-culture experiments. Such an extension would require the identification of the MM127 melanoma cells amongst the total population of cells in the assay. To meet this aim we first need to establish whether we can reliably identify MM127 melanoma cells using standard melanoma-associated markers. The focus of the present study is to explore whether MM127 cells can be reliably identified using standard approaches.

This work is organised in the following way. In the Results section we describe the outcomes of three different experimental techniques for identifying different melanoma cell lines using S100, HMB-45, and Melan-A. These techniques include immunofluorescence, Western blotting, and quantitative reverse transcription-polymerase chain reaction (qRT-PCR) assays. These techniques are applied to four different melanoma cell lines, and the results for the metastatic melanoma cell line, MM127, are not as expected. We find that this cell line is not identifiable using any of the three markers.

2.3 METHODS

2.3.1 Cell culture

Melanoma cell culture: Melanoma cell lines WM35 and WM793 are cultured in MCDB 153 medium (Sigma Aldrich, Australia) containing 20% Leibovitz L-15 medium (Life Technologies, Australia), 4% Foetal Calf Serum (FCS) (Hyclone, Australia), 7.5% w/v sodium bicarbonate (Life Technologies), 5μg/ml insulin (Sigma Aldrich), 1.68mM calcium chloride, 50U/ml of penicillin and 50μg/ml of streptomycin (Life Technologies). Melanoma cell lines MM127 and SK-MEL-28 are maintained in RPMI1640 medium (Life Technologies) supplemented with 10% FCS, 2mM L-glutamine (Life Technologies), 23mM HEPES (Life Technologies), 50U/ml of penicillin and 50μg/ml of streptomycin. The HaCaT cell line is cultured in Dulbecco's Modified Eagle's Medium (DMEM) (Life Technologies) with 10% FCS and 50U/ml of penicillin and 50μg/ml of streptomycin. All cells are routinely screened for *mycoplasma*.

2.3.2 Primary Cell Culture

Keratinocyte culture: Human keratinocytes are isolated from skin discards collected after abdominoplasty and breast reduction surgery. All skin collections are obtained with written informed patient consent. All experimental protocols used in this study are approved by the Queensland University of Technology (QUT) research ethics committee

(approval number QUT 3865H) and the St Andrew's Hospital ethics committee (approval number: 200 4/46). The experimental methods carried out in this study are in accordance with the approved guidelines. Keratinocytes are collected from the underside of the epidermis and papillary side of the dermis from surgical skin discards that are placed, overnight, in 0.25% trypsin (Life Technologies) diluted in a 1:1 ratio with phosphate buffered saline (PBS) (Life Technologies). Keratinocytes are grown in a 2:1 ratio on an irradiated feeder layer of 3T3 (i3T3) in full Green's medium containing DMEM with Ham's F12 (Life Technologies) in a 3:1 v/v ratio, 10% FCS, 2mM L-glutamine, 50U/ml of penicillin, 50μg/ml of streptomycin, 180mM adenine (Sigma Aldrich), 1μg/ml insulin, 0.1μg/ml cholera toxin (Sigma Aldrich), 0.01% non-essential amino acid solution (Life Technologies), 5μg/ml transferrin (Sigma Aldrich), 0.2μM triiodothyronine (Sigma Aldrich), 0.4μg/ml hydrocortisone (Sigma Aldrich) and 10ng/ml human recombinant EGF (Life Technologies). Cells are cultured at 37°C, in 5% CO_2 and 95% air.

Melanocyte culture: Melanocytes are grown from an epidermal cell suspension (keratinocyte cell suspension). Isolated epidermal cell suspensions are seeded into T25cm² tissue culture flasks (Nunc®, Australia) with 254 Medium (Life Technologies) together with Human Melanocyte Growth Supplement (Life Technologies). Epidermal cells, at a density of 8×10^4 cells/cm², are seeded and incubated at 37°C in 5% CO_2 and 95% air. If the melanocyte culture is contaminated with fibroblasts it is treated with 100μg/ml of Geneticin® (Life Technologies) for 2-3 days.

Fibroblast culture: The dermis, obtained after keratinocyte isolation, is finely minced and placed in a 0.05% collagenase A type I (Life Technologies) solution prepared in DMEM at 37°C, in 5% CO_2 and 95% air for 24 hours. The dermal cell solution is centrifuged at 212g for 10 minutes and the cells are seeded into T75cm² flasks (Nunc®) in DMEM with 10% FCS, 2mM L-glutamine, 50U/ml of penicillin and 50μg/ml of streptomycin at 37° C in 5% CO_2 and 95% air.

2.3.3 Immunofluorescence

Cells are grown on glass coverslips and fixed with 4% paraformaldehyde (Electron Microscopy Sciences, Australia) for 30 minutes at room temperature. Cells are permeabilised with 0.1% Triton-X in PBS for 10 minutes, washed with 0.5% w/v bovine serum albumin (BSA) (Life Technologies) in PBS and the non-specific binding sites are blocked using 0.5% BSA for 30 minutes. This is followed by the addition of primary antibody (S100-1:2500, HMB-45-1:100 and Melan-A-1:200) (Dako, Australia) on cells for an hour, and the secondary antibody (Alexa Fluor® 480-1:400 and Alexa Fluor 555®-1:400) (Life Technologies) for an hour. Before proceeding with our experiments, we perform a series of experiments to determine the optimal dilution for each antibody. The optimal dilution was determined by starting with the manufacturer's recommended dilution and then increasing the dilution to find an optimum result. Cells are washed three times with 0.5% BSA, the nucleus is stained with DAPI – 1:1000 (Sigma Aldrich) and f-actin is stained with Alexa Fluor® 488-1:200 (Life Technologies) for 10 minutes. Coverslips are mounted on glass slides using ProLong® Gold Antifade mountant (Life Technologies).

2.3.4 Western blotting

Melanoma cell lines (WM35, WM793, MM127, SK-MEL-28) and non-melanoma cells (HaCaT, fibroblasts, melanocytes) are lysed by adding lysis buffer containing 80% Radio Immuno-Precipitation Assay (RIPA) buffer (Thermo Fisher Scientific, Australia), 10% protease inhibitor (Roche Diagnostics, Australia) and 10% phosphatase inhibitor (Thermo Fisher Scientific). Cells are collected in Eppendorf tubes, vortexed every 5 minutes for half an hour and passed through a 27.5 gauge needle three to four times. Cell lysates of keratinocytes are obtained following removal of the feeder layer. The cell pellet is washed twice with PBS, and the cells are lysed by adding the lysis buffer. Cell lysates are centrifuged at 18000 x g for 15 minutes at 4°C. The proteins are separated using sodium dodecyl sulphate polyacrylamide gel electrophoresis (SDS-PAGE) and transferred onto nitrocellulose membranes (BioTrace®NT, Pall Corporation, USA).

Membranes are blocked in Tris-buffered saline containing 0.05% Tween-20 (TBST) and 5% skim milk (TBST/milk 5%). All additional immunostaining washes are performed using TBST at room temperature. The corresponding primary antibody is used to incubate membranes overnight at 4°C; (S100-1:2000 (Dako), HMB-45-1:100 (Thermo Fisher Scientific) and Melan-A-1:1000 (Dako)) in TBST containing 5% BSA (TBST/BSA 5%), and with a secondary antibody, horseradish peroxidase-conjugated anti mouse (1:5000) (R&D Systems, USA); anti-rabbit (1:5000) (R&D Systems, USA); in TBST containing 5% skim milk for 1 hour. We use GAPDH (1:100) (Cell Signalling, USA) as an internal loading control. These optimal dilutions for each antibody are determined with a series of dilution assays. Membranes are washed five times in TBST and developed with enhanced chemiluminescence, ECL solution (GE Healthcare Life Sciences, Life Technologies). Images are compiled using Adobe Illustrator® and the auto colour balance is adjusted in all figures.

2.3.5 *Quantitative reverse transcription-polymerase chain reaction (qRT-PCR)*

Total cellular RNA is extracted from melanoma (WM35, WM793, MM127, SK-MEL-28) and non-melanoma cell lines (HaCaT) using Trizol Reagent (Life Technologies) following the manufacturer's protocol. One µg of RNA is reverse transcribed and cDNA is synthesised using SuperScript® III First-Strand (Life Technologies). The qRT-PCR is performed using an ABI Prism 7500 Sequence Detection System (Applied Biosystems, USA) and SYBR Green (Life Technologies). PCR cycle parameters are the same for all primers: 40 cycles of denaturing at 94°C for 30 seconds, annealing at 60°C for 40 seconds and extension at 72°C for 50 seconds. To quantify the expression of mRNA in each cell line the cycle threshold (Ct) value of each cell line is subtracted from the corresponding Ct value for the internal control, *RPL32*. The main results are presented here [Fig. 2.1(*d*)] and additional results are given in the supplementary material document (Supplementary Information). Each qRT-PCR assay is performed in triplicate. Data are reported as the sample mean obtained by averaging over the three identically-prepared replicate ± the sample standard error.

2.4 RESULTS

2.4.1 *Short tandem repeat profiling*

All melanoma cell lines: WM35; WM793; SK-MEL-28 and MM127, are validated using short tandem repeat (STR) profiling (Cell Bank, Australia. January 2015). The STR profiling results confirm that all these melanoma cell lines are identical to the reference samples held at Cell Bank. Therefore, all melanoma cell lines in this study are identical to the reference samples held at Cell Bank.

The alleles obtained from STR profiling are analysed using the DMSZ database (http://www.dsmz.de/fp/cgi-bin/str.html) to give the closest match to each cell line we consider. The results from this analysis confirm that WM35, WM793 and SK-MEL-28 are as expected (Supplementary Information). Conversely, the results for MM127 are not as expected since there is no match identified using the MM127 alleles [Fig. 2.1(*a*)]. This preliminary result suggests that further investigation is warranted.

2.4.2 *Immunofluorescence*

Immunofluorescence is used on fixed cell preparations for S100, HMB-45 and Melan-A. The cell nuclei, f-actin and three standard melanoma-associated markers are highlighted [Fig. 2.1(*b*)]. S100 is localised to the nucleus and cytoplasm, and is observed in WM35, WM793 and SK-MEL-28 cells. HMB-45 is detected in the cytoplasm of WM35, WM793 and SK-MEL-28 cells [Fig. 2.1(*b*)]. Melan-A staining is present in both the WM35 and SK-MEL-28 cells, whereas it is absent from WM793 cells. Interestingly, MM127 is the only melanoma cell line that is negative for all three melanoma-associated markers in the immunofluorescence investigations. To confirm the immunofluorescence results, Western blotting analysis is *performed.*

2.4.3 Western blotting

The expression of S100 (10kDa), HMB-45 (27 and 100kDa), and Melan-A (18kDa) proteins in the WM35, WM793, SK-MEL-28, MM127 and HaCaT cell lines are analysed using Western blots. The expression of these markers is also examined in primary cells, including keratinocytes and fibroblasts, showing that both keratinocytes and fibroblasts are negative for S100, HMB-45 and Melan-A [Fig. 2.1(*c*)]. The expression of these markers is also examined in primary melanocytes, showing that they are positive for S100, HMB-45 and Melan-A [Fig. 2.1(*c*)].

In the SK-MEL-28 and WM35 cell lines, HMB-45 is detected as two bands, which is consistent with previous results[16]. The cell lines WM793 and MM127 are negative for Melan-A and HMB-45 [Fig. 2.1(*c*)]. The absence of HMB-45 in WM793 cells in the Western blots does not coincide with the immunofluorescence analysis [Fig. 2.1(*b*)]. This is an interesting result that has not been reported previously. It is possible that HMB-45 could be detected by prolonging the exposure of the blot because HMB-45 is observed in the immunofluorescence results [Fig. 2.1(*b*)]. Discrepancies in protein expression among individual melanoma cells have been previously reported[17], and this is consistent with the results presented here, since some individual WM793 cells are positive for HMB-45 [Fig. 2.1(*b*)] while other individual WM793 cells are negative for HMB-45. However, most importantly for our work, the expression of all three markers are absent from the MM127 cells. The Western blotting results for the MM127 cell line concur with the immunofluorescence results [Fig. 2.1(*b*)] and suggest that the MM127 cell line does not express the same antigens as the other melanoma cell lines investigated. To provide additional confirmation of the immunofluorescence and Western blot data, qRT-PCR assays are also performed.

2.4.4 Quantitative reverse transcription-polymerase chain reaction (qRT-PCR)

The presence of genes that encode specific proteins associated with melanoma cell lines are quantified using qRT-PCR. The HaCaT cell line is used as a negative control because this cell line does not express any melanoma-associated markers as observed in immunofluorescence [Fig. S2.1], Western blotting [Fig. 2.1(*c*)] and qRT-PCR [Fig. S2.2] experiments. All qRT-PCR results are reported relative to the housekeeping gene (*RPL32*).
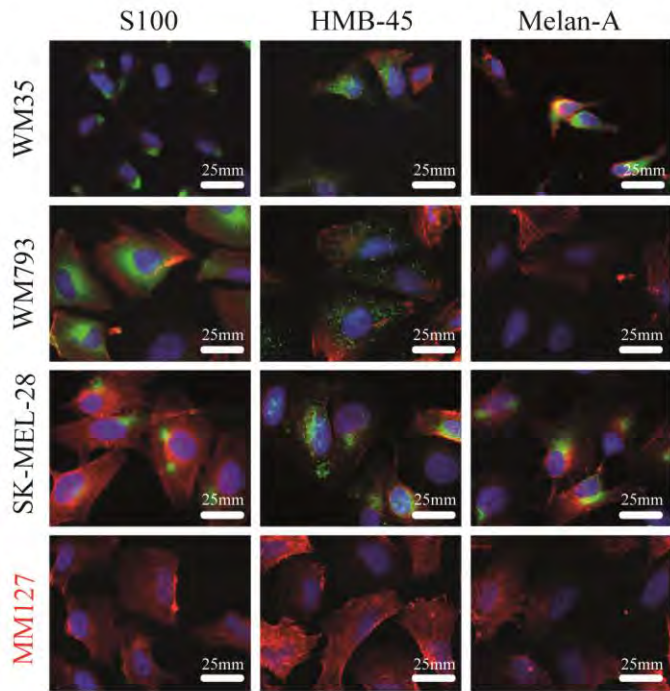
The qRT-PCR results indicate that the expression of S100 (*S100β)*, Melan-A (*MLANA)* and HMB-45 (*PMEL*) in MM127 is very similar to the negative control [Fig. 2.1(*d*)]. The gene level for S100 in the HaCaT and MM127 cell lines is below the detectable limit (BDL). Overall, these qRT-PCR results are consistent with the Western blotting and immunofluorescence analysis, and confirm that these three standard melanoma-associated markers are not detected in the MM127 cell line.

To further verify the qRT-PCR results, the gene expression of two other commonly-used melanoma markers: microphthalmia-associated transcription factor (*MITF*); and tyrosinase (*TYR*)[18] are also examined. Again, the expression of *MITF* and *TYR* in the MM127 cells are very similar to the negative control (Supplementary Information).
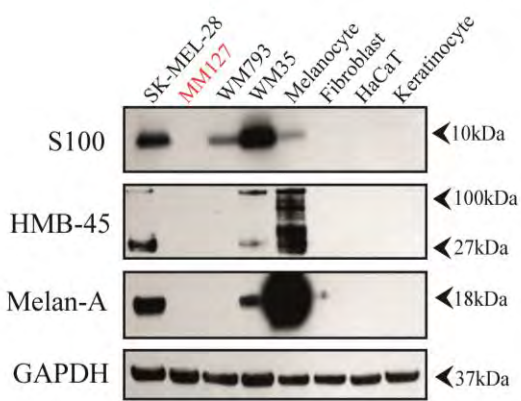
(*a*)

D3S1358	TH01	D21S11	D18S51	Penta E	D5S818	D13S317	D7S820	D16S539	CSF1PO	Penta D	Amel	vWA	D8S1179	TPOX	FGA
15,17	8,9	29	15,20	5,10	11,12	12,13	10,11	10,13	10,11	10	X,Y	16,18	14,15	11,12	14,15

(*b*)

(*c*)

(*d*)
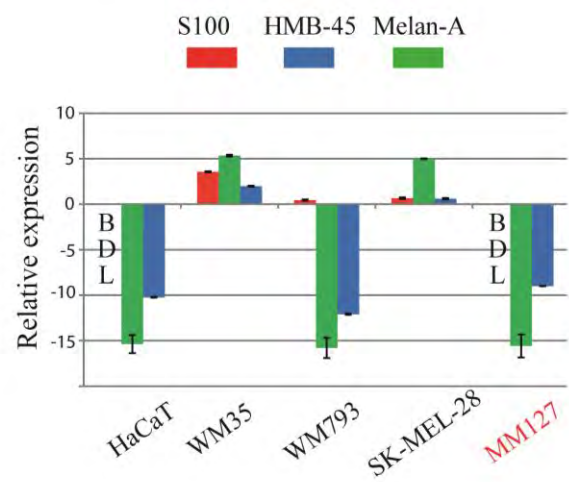
Figure 2.1: MM127 cell line does not express three standard melanoma-associated markers. (*a*) STR analysis of the MM127 cell line. Upper row shows the allele names. Lower row describes the location of the allele on the chromosome. (*b*) Immunofluorescence results for four melanoma cell lines (WM35, WM793, SK-MEL-28, MM127). Cells are fixed in 4% paraformaldehyde and stained for S100 (green), HMB-45 (green) and Melan-A (green). The nucleus (blue) and f-actin (red) are highlighted. Results for the negative control (HaCaT) are given in the supplementary information [Fig. S2.1]. (*c*) Melanoma (WM35, WM793, SK-MEL-28 and MM127) and negative controls (primary cells: keratinocytes, fibroblasts, and cell line: HaCaT) are analysed by Western blotting for S100, HMB-45 and Melan-A. GAPDH is used as loading control and detected at 37kDa. (*d*) qRT-PCR results show the difference between the expression of melanoma-associated genes for the negative control (HaCaT) and various cell lines. Values correspond to the mean ΔCt (n=3), where ΔCt = Ct (*RPL32*) – Ct (*target gene*). Error bars indicate the standard error (n=3). Results below the detectable limit are given as BDL.

2.5   DISCUSSION

Our group, and several other research groups, have previously worked with the metastatic melanoma cell line, MM127[13, 19-21]. Our previous work involves performing and analysing two-dimensional barrier assays with MM127 cells in monoculture[13,21]. Since these previous studies involve a monoculture experiment, there was no need to identify the cells within the experiment since all cells are known to be MM127 cells. If these monoculture experiments are to be extended to co-culture conditions, with multiple cell types present, we would be interested in identifying the MM127 cells within the total heterogeneous population. The results of the present study indicate that making this kind of distinction using standard melanoma-associated markers would be very difficult because MM127 cells cannot be identified using S100, Melan-A, HMB-45, MITF or tyrosinase.

Immunofluorescence on WM35, WM793 and SK-MEL-28 show positive expression of all the melanoma–associated markers considered, while the negative control, HaCaT cells, and the metastatic melanoma cell line MM127 did not express any of the markers we consider. All antibodies are used at an optimal dilution which we determined using a series of sensitivity assays specifically optimised for each marker prior to proceeding with the experiments. The Western blot analysis also shows the presence of all markers in WM35 and SK-MEL-28, and S100 in WM793. In contrast, all melanoma-associated markers considered are absent in the negative control and the MM127 cell line.

We find that the WM793 cell line does not express all the melanoma markers considered. One possible explanation for a variation between the immunofluorescence and Western blot analysis for WM793 cells is that a longer period of time might be needed to expose the blot. However, using a longer period of time might cause an over expression of proteins in the other lanes. We are not concerned by this variation since WM793 cells reliably express S100, and so can be identified using this marker. On the contrary, MM127 cells cannot be identified using any of the commonly used markers we consider.

Collectively, our findings indicate that the standard melanoma-associated markers we consider are not detected in the MM127 cell line. Although the MM127 cell line has been used in several previous studies[13,19-21], we find that this cell line cannot be detected using standard melanoma-associated markers. Therefore, we suggest that other metastatic melanoma cell lines that express standard markers, such as the SK-MEL-28 cell line, ought to be used in preference to the MM127 cell line.

Since the MM127 cells we use in this study and the MM127 cells available from Cell Bank Australia are sourced from the same institution, it is not surprising that the cell validation results confirm that the cells we use are 100% identical to those available from Cell Bank (Supplementary Information). However, since the MM127 cell line was first discussed in 1979[9], it is possible that the MM127 cells currently available from Cell

Bank are somehow different to the cells originally reported in 1979. Given that MM127 cells are primarily in use at one research institution, it is impossible to for us to repeat our investigations using samples of MM127 cells sourced from multiple institutions. Certain recent investigations have shown that MM127 cells are positive for the *NRAS* mutation which is consistent with the idea that these cells are melanoma[22-23]. Regardless of their *NRAS* status, our observation that MM127 cells cannot be detected using standard melanoma-associated markers is an important finding.

Although our study explores the presence of five different melanoma-associated markers in MM127 cells, it is always possible to extend our work by repeating the immunofluorescence, Western blotting and qRT-PCR experiments with additional markers. For example, recently it has been suggested that SOX10 is a sensitive marker for melanoma cells[24], and so it would be interesting to repeat our work using SOX10. We have chosen not to use SOX10 in the present work because other authors suggest that S100 is a very sensitive marker for melanoma cells[5].

2.6   ACKNOWLEDGEMENTS

2.7 REFERENCES

1. Sneyd MJ, Cox BA. 2013. Comparison in trends of melanoma mortality in New Zealand and Australia: the two countries with the highest melanoma incidence and mortality in the world. *BMC Cancer*. 13: 372.

2. Yu X, Ambrosini G, Roszik J, Eterovic AK, Stempke-Hale K, Seftor EA, Chattopadhyay C, Grimm E, Carvajal RD, Hendrix MJ. *et al*. 2015. Genetic analysis of the 'uveal melanoma' C918 cell line reveals atypical *BRAF* and common *KRAS* mutations and single tandem repeat profile identical to the cutaneous melanoma C8161 cell line. *Pigment Cell and Melanoma Research*. 28: 357-359.

3. Tsao SC, Weiss J, Hudson C. 2015. Monitoring response to therapy in melanoma by quantifying circulating tumour DNA with droplet digital PCR for *BRAF* and *NRAS* mutations. *Scientific Reports*. 5: 11198.

4. Behren A, Anaka M, Lo PH, Vella LJ, Davis ID, Catimel J, Cardwell T, Gedye C, Hudson C, Stan R. *et al*. 2013. The Ludwig Institute for Cancer Research Melbourne melanoma cell line panel. *Pigment Cell and Melanoma Research*. 26: 597-600.

5. Viray H, Bradley WR, Schalper KA, Rimm DL, Rothberg BEG. 2013. Marginal and joint distributions of S100 HMB-45 and Melan-A across a large series of cutaneous melanomas. *Archives of Pathology and Laboratory Medicine*. 137: 1063-1073 (2013).

6. Eves P, Katerinaki E, Simpson C, Layton C, Dawson R, Evans G, Mac Neil S. 2003. Melanoma invasion in reconstructed human skin is influenced by skin cells – investigation of the role of proteolytic enzymes. *Clinical and Experimental Metastasis*. 20: 685-700.

7. Guo R, Franco-Palacios M, Russell M. 2013. Micropthalmia Transcription Factor (MITF) as a diagnostic marker for metastatic melanomas negative for other melanoma markers. *International Journal of Clinical and Experimental Pathology*. 6: 1658-1664.

8. Weinstein D, Leininger J, Hamby C, Safai B. 2013. Diagnostic and prognostic biomarkers in melanoma. *The Journal of Clinical and Aesthetic Dermatology*. 7: 13-24.

9. Pope JH, Morrison L, Moss DJ, Parsons PG, Mary SR. 1979. Human malignant melanoma cell lines. *Pathology*. 11: 191-195.

10. Chalmers AH, Lavin M, Atisoontornkul S, Mansbridge J, Kidson C. 1976. Resistance of human melanoma cells to ultraviolet radiation. *Cancer Research*. 36: 1930-1934.

11. Chenevix-Trench G, Martin NG, Ellem KAO. 1990. Gene expression in melanoma cell lines and cultured melanocytes: correlation between levels of c-src-1, c-myc and p53. *Oncogene*. 5: 1187-1193.

12. Cozzi SJ, Parsons PG, Ogbourne SM. 2006. Induction of senescence in diterpene ester-treated melanoma cells via protein kinase c- dependent hyperactivation of the mitogen-activated protein kinase pathway. *Cancer Research*. 66: 10083-10091.

13. Treloar KK, Simpson MJ, Haridas P, Manton KJ, Leavesley DI, McElwain DLS, Baker RE. 2013. Multiple types of data are required to identify the mechanisms influencing the spatial expansion of melanoma cell colonies. *BMC Systems Biology*. 7: 137.

14. Simpson MJ, Treloar KK, Binder BJ, Haridas P, Manton KJ, Leavesley DI, McElwain DLS, Baker RE. 2013. Quantifying the roles of ell motility and cell proliferation in a circular barrier assay. *Journal of the Royal Society Interface* 10:20130007.

15. Treloar KK, Simpson MJ, McElwain DLS, Baker RE. 2014. Are *in vitro* estimates of cell diffusivity and cell proliferation rate sensitive to assay geometry? *Journal of Theoretical Biology*. 356: 71-84.

16. Kawakami A, Sakane F, Imai S, Yasuda S, Kai M, Kanoh H, Jin HY, Hirosaki K, Yamashita T, Fisher DE. *et al*. 2008. Rab7 regulates maturation of melanosomal matrix protein gp100/Pmel17/Silv. *Journal of. Investigative Dermatology*. 128: 143-150.

17. Kim JE, Leung E, Baguley BC, Finlay GJ. 2013. Heterogeneity of expression of epithelial-mesenchymal transition markers in melanocytes and melanoma cell lines. *Frontiers of Genetics*. 4: 97.

18. Sheffield MV, Yee H, Dorvault CC, Weilbaecher KN, Eltoum IA, Siegal GP, Fisher DE, Chhieng DC. 2002. Comparison of five antibodies as markers in the diagnosis of melanoma in cytologic preparations. *American Journal of Clinical Pathology*. 118: 930-936.

19. Cozzi SJ, Parsons PG, Ogbourne SM, Pedley J, Boyle GM. 2006. Induction of senescence in diterpene ester-treated melanoma cells via protein kinase C-dependent hyperactivation of the mitogen-activated protein kinase pathway. *Cancer Research*. 66: 10083-10091.

20. Goss P, Parsons PG. 1977. The effect of hyperthermia and melphan on survival of human fibroblast strains and melanoma cell lines. *Cancer Research*. 37: 152-156.

21. Treloar KK, Simpson MJ, Binder BJ, McElwain DLS, Baker RE. 2014. Assessing the role of spatial correlations during collective cell spreading. *Scientific Reports*. 4: 5713.

22. Yang Y, Wu J, Demir A, Castillo-Martin M, Melamed RD, Zhang G, Fukunaga-Kanabis M, Perez-Lorenzo R, Zheng B, Silvers DN. *et al*. 2013. GAB2 induces tumor angiogenesis in NRAS-driven melanoma. *Oncogene*. 32: 3627-3637.

23. Perez-Lorenzo R, Gill KZ, Shen CH, Zhao FX, Zheng B, Schulze HJ, Silvers DN, Brunner G, Horst BA. 2014. A tumor suppressor function for the lipid phosphatase INPP4B in melanocytic neoplasms. *Journal of Investigative Dermatology*. 134: 1359-1368.

24. Willis BC, Johnson G, Wang J, Cohen C. 2015. SOX10: A useful marker for identifying metastatic melanoma in sentinel lymph nodes. *Applied Immunohistochemistry and Molecular Morphology*. 23: 109-112.

2.8 SUPPLEMENTARY INFORMATION

2.8.1 *Immunofluorescence*

Results for the negative control (HaCaT) confirm that the HaCaT cell line is negative for S100, HMB-45 and Melan-A (Figure S2.1)].
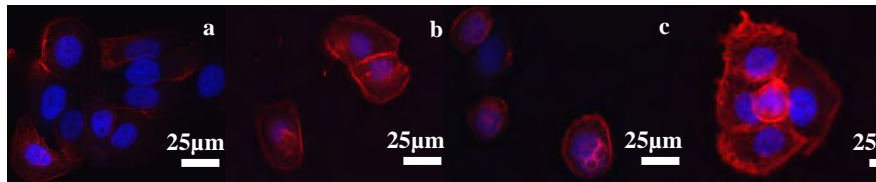
Figure S2.1: Immunofluorescence analysis for the negative control (HaCaT) do not express melanoma-associated proteins. Cells are fixed in 4% paraformaldehyde and stained for (a) S100 (green), (b) HMB-45 (green) and (c) Melan-A (green). The nucleus (blue) and f-actin (red) are highlighted. (d) Shows results for the secondary antibody only.

Additional results confirm that some of the primary cells we consider (fibroblasts and keratinocytes) are also negative for S100, HMB-45 and Melan-A. Alternatively, primary melanocytes are positive for all the three melanoma-associated markers. As a result, we do not use primary keratinocytes and fibroblasts as negative controls as they are always at risk of being contaminated with melanocytes, which could lead to false positive results. Therefore, we use the HaCaT cell line as the negative control.

2.8.2 *Quantitative reverse transcription-polymerase chain reaction (qRT-PCR)*

Total cellular RNA is extracted from melanoma cell lines (WM35, WM793, MM127, SK-MEL-28), and the non-melanoma control cell line (HaCaT) using Trizol Reagent (Life Technologies) following the manufacturer's protocol. One µg of RNA is reverse transcribed and cDNA is synthesised using SuperScript® III First-Strand (Life

Technologies). The gene-specific primers (Sigma Aldrich) used in qRT-PCR are given in Table S2.1

Gene Symbol	Primer Sequence	Gene Bank Accession Number
MLANA	Forward:5' CACGGCCACTCTTACACCAC 3' Reverse: 5' GGAGCATTGGGAACCACAGG 3'	NM_006272.2
S100β	Forward: 5' TGGCCCTCATCGACGTTTTC 3' Reverse: 5' ATGTTCAAAGAACTCGTGGCA 3'	NM_005511.1
PMEL	Forward: 5' AGTTCTAGGGGGCCCAGTGTCT 3' Reverse: 5' GGGCCAGGCTCCAGGTAAGTAT 3'	NM_006928.4
MITF	Forward: 5' CATTGTTATGCTGGAAATGCTAGAA 3' Reverse: 5' GGCTTGCTGTATGTGGTACTTGG 3'	NM_198178.2
TYR	Forward: 5' GGCTGTTTTGTACTGCCTGCT 3' Reverse: 5' AGGAGACACAGGCTCTAGGGAA 3'	NM_000372.4
RPL32	Forward: 5' CCCCTTGTGAAGCCCAAGA 3' Reverse: 5' GACTGGTGCCGGATGAACTT 3'	NM_001007073.1

Table S2.1: Gene and primer sequences.

The expression of *MITF* and *TYR* in the MM127 cell line is very similar to the negative control (Figure S2.2).
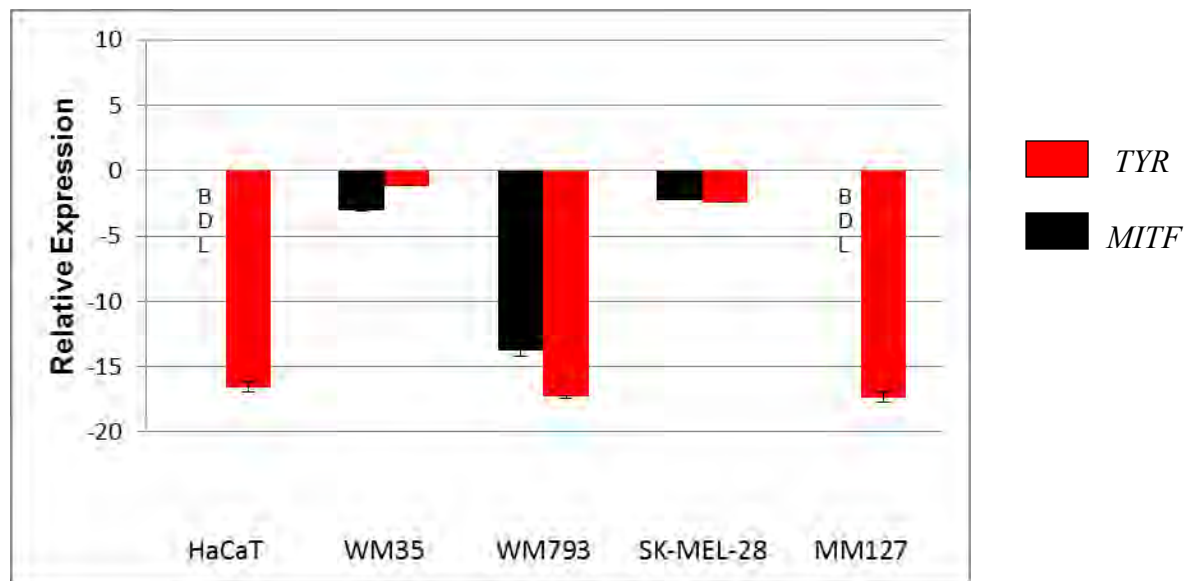
Figure S2.2: Gene expression of *MITF* and *TYR* relative to *RPL32*. Results for *TYR* and *MITF* in the HaCaT and MM127 cell lines are below the detectable limit (BDL). qRT-PCR results are reported as the difference between the expression of melanoma-associated genes for the negative control (HaCaT) and various cell lines. Values correspond to the mean ΔCt (n=3), where ΔCt = Ct (*RPL32*) – Ct (*target gene*). Error bars indicate the standard error (n=3).

2.8.3 *DSMZ database matching the melanoma cell lines used in this project*

CellBank Australia

CellBank Australia is operated by the Children's Medical Research Institute
ABN 47 002 684 737
Street: 214 Hawkesbury Rd Westmead NSW 2145 Australia
Postal: Locked Bag 23 Wentworthville NSW 2145 Australia
Tel 02 8865 2850
Fax 02 8865 2801
www.cellbankaustralia.com.au

Certificate of Analysis, Identification testing (Human cell line)

REPORT NO. 14-243

Sender

Name:	Parvathi Haridas
Laboratory/Organisation:	Queensland University of Technology
Client No.:	CN19
Phone No.:	3138 6229
Email:	p.haridas@qut.edu.au

Cell Line Sample

Sample Name:	WM35
Sender ID Number (if used):	p22
Collection Date:	07/12/2014
Analysis Request:	Human Cell Line Identification, Promega PP16HS kit
CellBank ID Number:	14-243
Reference Sample[1]:	WM35 (COSMIC Cell Lines Project: COSS1299080)

[1]You may wish to compare this sample to another potential match; this is referred to as a reference sample. CellBank may also supply a matching repository sample during testing.

Testing Performed

Test Method	Protocol No.	Test Date	Analysis Date	Lane
PCR - PP16HS	325v01	16/12/2014	23/12/2014	12-15

Test Result (see following pages for STR Profile)

Full profile, known match, repository sample

Identification of human cell lines is primarily performed using short tandem repeat (STR) profiling. This method uses tetranucleotide or pentanucleotide repeats within a set of established loci to build up a profile for each cell line; the result can be compared to other holdings of the same cell line. STR profiles may vary with passage number due to intrinsic genetic instability in some cell lines; we cannot guarantee that samples from the same cell line will produce identical profiles. From the literature, cell lines are normally considered to match if their profiles are more than 80% identical.

The results included here relate only to the sample tested. This test report shall not be reproduced except in full, without full written approval of the testing laboratory.

This test is for research use only and is not appropriate for human clinical or diagnostic samples.

322v03_Form02_Certificate of Analysis Human Cell Line (30/07/2014)   Page 1 of 2

CellBank Australia
Certificate of Analysis, Identification Testing
(Human cell line)

STR Profile – Sample

Sample Name	WM35
Source	14-243
D3S1358	16,18
TH01	9.3
D21S11	29,32.2
D18S51	14,15
Penta E	13,15
D5S818	11,12
D13S317	11
D7S820	10,13
D16S539	12,13
CSF1PO	10
Penta D	11,14,15
Amel	X
vWA	17
D8S1179	11,13
TPOX	8
FGA	19,24

– Reference/Repository Sample

Sample Name	WM35
Source	COSMIC Cell Lines Project: COSS1299080
D3S1358	
TH01	9
D21S11	
D18S51	
Penta E	
D5S818	11,12
D13S317	11
D7S820	10,13
D16S539	12,13
CSF1PO	10
Penta D	
Amel	X
vWA	17
D8S1179	
TPOX	8
FGA	

Comments

Full profile generated:
- out of 9 loci, 22/24 (91%) alleles were identical to WM35 (COSMIC Cell Lines Project: COSS1299080)
- within the scientific literature samples are usually thought to match if >80% of alleles are identical, so we conclude that this result is consistent with correct identity

Authorisation

Authorised by:	George Theodosopoulos
Date:	08/01/2015

CellBank Australia

Certificate of Analysis, Identification testing (Human cell line)

REPORT NO. 14-244

Sender

Name:	Parvathi Haridas
Laboratory/Organisation:	Queensland University of Technology
Client No.:	CN19
Phone No.:	3138 6229
Email:	p.haridas@qut.edu.au

Cell Line Sample

Sample Name:	WM793
Sender ID Number (if used):	p23
Collection Date:	06/12/2014
Analysis Request:	Human Cell Line Identification, Promega PP16HS kit
CellBank ID Number:	14-244
Reference Sample[1]:	WM793B (COSMIC Cell Lines Project: COSS1299081)

[1]You may wish to compare this sample to another potential match; this is referred to as a reference sample. CellBank may also supply a matching repository sample during testing.

Testing Performed

Test Method	Protocol No.	Test Date	Analysis Date	Lane
PCR - PP16HS	325v01	16/12/2014	23/12/2014	16-19

Test Result (see following pages for STR Profile)

Full profile, known match, repository sample

Identification of human cell lines is primarily performed using short tandem repeat (STR) profiling. This method uses tetranucleotide or pentanucleotide repeats within a set of established loci to build up a profile for each cell line; the result can be compared to other holdings of the same cell line. STR profiles may vary with passage number due to intrinsic genetic instability in some cell lines; we cannot guarantee that samples from the same cell line will produce identical profiles. From the literature, cell lines are normally considered to match if their profiles are more than 80% identical.

The results included here relate only to the sample tested. This test report shall not be reproduced except in full, without full written approval of the testing laboratory.

This test is for research use only and is not appropriate for human clinical or diagnostic samples.

CellBank Australia
Certificate of Analysis, Identification Testing
(Human cell line)

STR Profile – Sample

Sample Name	WM793
Source	14-244
D3S1358	14,16
TH01	6,8
D21S11	28,29
D18S51	14,15
Penta E	5,12
D5S818	10,12
D13S317	8,14
D7S820	10,12
D16S539	12
CSF1PO	11
Penta D	13
Amel	X,Y
vWA	17
D8S1179	11,14
TPOX	8
FGA	20,21

– Reference/Repository Sample

Sample Name	WM793B
Source	COSMIC Cell Lines Project: COSS1299081
D3S1358	
TH01	6,8
D21S11	
D18S51	
Penta E	
D5S818	10,12
D13S317	8,14
D7S820	10,12
D16S539	12
CSF1PO	11
Penta D	
Amel	X,Y
vWA	17
D8S1179	
TPOX	8
FGA	

Comments

Full profile generated:
- out of 9 loci, 28/28 (100%) alleles were identical to WM793B (COSMIC Cell Lines Project: COSS1299081)

Authorisation

Authorised by:	George Theodosopoulos
Date:	08/01/2015

The Lady Mary Fairfax CellBank Australia
Established by a joint venture of the Children's Medical Research Institute,
Cure Cancer Australia Foundation, and National Breast Cancer Foundation,
and by an Enabling Grant of the National Health and Medical Research Council of Australia
Operated by CMRI from July 2007

CellBank Australia

Certificate of Analysis, Identification testing (Human cell line)

REPORT NO. 14-245

Sender

Name:	Parvathi Haridas
Laboratory/Organisation:	Queensland University of Technology
Client No.:	CN19
Phone No.:	3138 6229
Email:	p.haridas@qut.edu.au

Cell Line Sample

Sample Name:	SK-MEL-28
Sender ID Number (if used):	p5
Collection Date:	11/12/2014
Analysis Request:	Human Cell Line Identification, Promega PP16HS kit
CellBank ID Number:	14-245
Reference Sample[1]:	SK-MEL-28 (ATCC: HTB-72)

[1]You may wish to compare this sample to another potential match; this is referred to as a reference sample. CellBank may also supply a matching repository sample during testing.

Testing Performed

Test Method	Protocol No.	Test Date	Analysis Date	Lane
PCR - PP16HS	325v01	19/12/2014	23/12/2014	32-37

Test Result (see following pages for STR Profile)

Full profile, known match, repository sample

Identification of human cell lines is primarily performed using short tandem repeat (STR) profiling. This method uses tetranucleotide or pentanucleotide repeats within a set of established loci to build up a profile for each cell line; the result can be compared to other holdings of the same cell line. STR profiles may vary with passage number due to intrinsic genetic instability in some cell lines; we cannot guarantee that samples from the same cell line will produce identical profiles. From the literature, cell lines are normally considered to match if their profiles are more than 80% identical.

The results included here relate only to the sample tested. This test report shall not be reproduced except in full, without full written approval of the testing laboratory.

This test is for research use only and is not appropriate for human clinical or diagnostic samples.

CellBank Australia
Certificate of Analysis, Identification Testing
(Human cell line)

STR Profile – Sample

Sample Name	SK-MEL-28
Source	14-245
D3S1358	16,18
TH01	7
D21S11	28,29
D18S51	12,16
Penta E	8,12
D5S818	11,13
D13S317	11,12
D7S820	10
D16S539	9,12
CSF1PO	10,12
Penta D	9,10
Amel	X,Y
vWA	16,19
D8S1179	13
TPOX	8,12
FGA	19

– Reference/Repository Sample

Sample Name	SK-MEL-28
Source	ATCC: HTB-72
D3S1358	
TH01	7
D21S11	
D18S51	
Penta E	
D5S818	11,13
D13S317	11,12
D7S820	9.3,10
D16S539	9,12
CSF1PO	10,12
Penta D	
Amel	X,Y
vWA	16,19
D8S1179	
TPOX	8,12
FGA	

Comments

Full profile generated:
- out of 9 loci, 32/33 (96%) alleles were identical to SK-MEL-28 (ATCC: HTB-72)
- within the scientific literature samples are usually thought to match if >80% of alleles are identical, so we conclude that this result is consistent with correct identity

Authorisation

Authorised by:	George Theodosopoulos
Date:	08/01/2015

The Lady Mary Fairfax **CellBank Australia**
Established by a joint venture of the Children's Medical Research Institute,
Cure Cancer Australia Foundation, and National Breast Cancer Foundation,
and by an Enabling Grant of the National Health and Medical Research Council of Australia
Operated by CMRI from July 2007

CellBank Australia

Certificate of Analysis, Identification testing (Human cell line)

REPORT NO. 14-242

Sender

Name:	Parvathi Haridas
Laboratory/Organisation:	Queensland University of Technology
Client No.:	CN19
Phone No.:	3138 6229
Email:	p.haridas@qut.edu.au

Cell Line Sample

Sample Name:	MM127
Sender ID Number (if used):	p7
Collection Date:	07/12/2014
Analysis Request:	Human Cell Line Identification, Promega PP16HS kit
CellBank ID Number:	14-242
Reference Sample[1]:	MM127 (CellBank Australia: CBA-1344)

[1]You may wish to compare this sample to another potential match; this is referred to as a reference sample. CellBank may also supply a matching repository sample during testing.

Testing Performed

Test Method	Protocol No.	Test Date	Analysis Date	Lane
PCR - PP16HS	325v01	16/12/2014	23/12/2014	08-11
—				
—				—

Test Result (see following pages for STR Profile)

Full profile, known match, repository sample

Identification of human cell lines is primarily performed using short tandem repeat (STR) profiling. This method uses tetranucleotide or pentanucleotide repeats within a set of established loci to build up a profile for each cell line; the result can be compared to other holdings of the same cell line. STR profiles may vary with passage number due to intrinsic genetic instability in some cell lines; we cannot guarantee that samples from the same cell line will produce identical profiles. From the literature, cell lines are normally considered to match if their profiles are more than 80% identical.

The results included here relate only to the sample tested. This test report shall not be reproduced except in full, without full written approval of the testing laboratory.

This test is for research use only and is not appropriate for human clinical or diagnostic samples.

CellBank Australia
Certificate of Analysis, Identification Testing
(Human cell line)

STR Profile – Sample

Sample Name	MM127
Source	14-242
D3S1358	15,17
TH01	8,9
D21S11	29
D18S51	15,20
Penta E	5,10
D5S818	11,12
D13S317	12,13
D7S820	10,11
D16S539	10,13
CSF1PO	10,11
Penta D	10
Amel	X,Y
vWA	16,18
D8S1179	14,15
TPOX	11,12
FGA	19,20

– Reference/Repository Sample

Sample Name	MM127
Source	CellBank Australia: CBA-1344
D3S1358	15,17
TH01	8,9
D21S11	29
D18S51	15,20
Penta E	
D5S818	11,12
D13S317	12,13
D7S820	10,11
D16S539	10,13
CSF1PO	10,11
Penta D	
Amel	X,Y
vWA	16,18
D8S1179	14,15
TPOX	11,12
FGA	19,20

Comments

Full profile generated:
- out of 14 loci, 54/54 (100%) alleles were identical to MM127 (CellBank Australia: CBA-1344)

Authorisation

Authorised by:	George Theodosopoulos
Date:	08/01/2015

Chapter 3: Quantifying rates of cell migration and cell proliferation in co-culture barrier assays reveals how skin and melanoma cells interact during spreading and invasion

Statement of Contribution of Co-Authors
for Thesis by Published Paper

The following is the suggested format for the required declaration provided at the start of any thesis chapter which includes a co-authored publication.

The authors listed below have certified that:

6. they meet the criteria for authorship in that they have participated in the conception, execution, or interpretation, of at least that part of the publication in their field of expertise;
7. they take public responsibility for their part of the publication, except for the responsible author who accepts overall responsibility for the publication;
8. there are no other authors of the publication according to these criteria;
9. potential conflicts of interest have been disclosed to (a) granting bodies, (b) the editor or publisher of journals or other publications, and (c) the head of the responsible academic unit, and
10. they agree to the use of the publication in the student's thesis and its publication on the QUT's ePrints site consistent with any limitations set by publisher requirements.

In the case of this chapter:

Haridas P*, Penington CJ*, McGovern JA, McElwain DLS, Simpson MJ. (2017). Quantifying rates of cell migration and cell proliferation in co-culture barrier assays reveals how skin and melanoma cells interact during spreading and invasion. *Journal of Theoretical Biology.* **5: e3754**

* Authors contributed equally
Published online 20 April 2017.

Contributor	Statement of contribution*
Parvathi Haridas *Parvathi Haridas* 06/11/2017	Designed experiments, performed all the laboratory experiments, analysed data, wrote the manuscript (50%), prepared figures and/tables and reviewed and edited drafts of the manuscript
Catherine J. Penington	Designed experiments, analysed data, wrote the manuscript (50%), prepared figures and/tables and reviewed drafts of the manuscript
Jacqui A. McGovern *signature*	Designed experiments, reviewed analysed data and reviewed drafts of the manuscript
D. L. Sean McElwain	Designed experiments, reviewed analysed data and reviewed drafts of the manuscript
Matthew J. Simpson	Designed experiments, reviewed analysed data and reviewed drafts of the manuscript

Principal Supervisor Confirmation

I have sighted email or other correspondence from all Co-authors confirming their certifying authorship.
(If the Co-authors are not able to sign the form please forward their email or other correspondence confirming the certifying authorship to the RSC).

Matthew J Simpson

Name _____   Signature *M Simpson*   Date 10 | 11 | 2017

3.1 ABSTRACT

Malignant spreading involves the migration of cancer cells amongst other native cell types. For example, *in vivo* melanoma invasion involves individual melanoma cells migrating through native skin, which is composed of several distinct subpopulations of cells. Here, we aim to quantify how interactions between melanoma and fibroblast cells affect the collective spreading of a heterogeneous population of these cells *in vitro*. We perform a suite of circular barrier assays that includes: (i) monoculture assays with fibroblast cells; (ii) monoculture assays with SK-MEL-28 melanoma cells; and (iii) a series of co-culture assays initiated with three different ratios of SK-MEL-28 melanoma cells and fibroblast cells. Using immunostaining, detailed cell density histograms are constructed to illustrate how the two subpopulations of cells are spatially arranged within the spreading heterogeneous population. Calibrating the solution of a continuum partial differential equation to the experimental results from the monoculture assays allows us to estimate the cell diffusivity and the cell proliferation rate for the melanoma and the fibroblast cells, separately. Using the parameter estimates from the monoculture assays, we then make a prediction of the spatial spreading in the co-culture assays. Results show that the parameter estimates obtained from the monoculture assays lead to a reasonably accurate prediction of the spatial arrangement of the two subpopulations in the co-culture assays. Overall, the spatial pattern of spreading of the melanoma cells and the fibroblast cells is very similar in monoculture and co-culture conditions. Therefore, we find no clear evidence of any interactions other than cell-to-cell contact and crowding effects. The outcomes of the cellular interactions between the two cell types shows no influence of the fibroblast cells on the melanoma cell migration and proliferation. The experimental observations are also quantified using mathematical models.

3.2 INTRODUCTION

Melanoma is the deadliest form of skin cancer and arises due to the malignant transformation of melanocytes (Geller and Annas, 2003). In Australia, melanoma is reported to be the third most common cancer (Melanoma Institute Australia, 2016), and it is associated with high rates of mortality (Sneyd *et al*., 2013). However, if melanoma is detected early, before significant spreading occurs, prognosis after surgery is very good (Erdei *et al*., 2010; Faries and Ariyan, 2011). Therefore, understanding the mechanisms that drive melanoma spreading and invasion is very important.

Melanoma spreading takes place in a complex environment that including the extracellular matrix and many different kinds of cell types including: endothelial cells; keratinocytes; fibroblasts and immune cells (Cornil *et al*., 1991; Flach *et al*., 2011). Melanoma spreading in the dermis involves the movement of individual melanoma cells through an environment that also contains fibroblast cells (Li *et al*., 2007; Sriram *et al*., 2015). Previous experimental work suggests that melanoma cells can interact with fibroblast cells through diffusible factors, such as growth factors and cytokines, or by cell-to-cell contact and crowding (Flach *et al*., 2011; Goldstein *et al*., 2005; Labrousse *et al*., 2004; Ruiter *et al*., 2002; Zhou *et al*., 2015). In the experimental literature, these kinds of interactions are often broadly referred to as *cross-talk* between different subpopulations (Dvorankova *et al*., 2016; Ye *et al*., 2014). Although experimental studies indicate that fibroblasts can play a role in cancer progression, the precise details of how melanoma cells and fibroblast cells interact are not well understood (Kalluri and Zeisberg, 2006; Li *et al*., 2003).

Metastatic melanoma cells are known to grow in colonies, that are sometimes called nests (Baraldi *et al*., 2013; Schwartz *et al*., 2008). The spatial expansion of these colonies is driven by the rate at which individual melanoma cells move, and the rate at which individual melanoma cells proliferate. Therefore, to understand how quickly a population of melanoma cells spreads through the surrounding environment, it is important to develop techniques that allow us to quantify the rates of cell migration and

cell proliferation (Treloar *et al*., 2013). Previous *in vitro* studies examining the spatial spreading of populations of melanoma cells have focused on monoculture experiments that contain only melanoma cells (Cornil *et al*., 1991; Im *et al*, 2012; Justus *et al*., 2014; Treloar *et al*., 2013). To make these kinds of *in vitro* studies more relevant to the *in vivo* environment, it is important to investigate, and quantify, how the spatial spreading of melanoma cells is affected by interactions with other cells types, such as fibroblasts.

In this study we perform a series of monoculture and co-culture barrier assays to examine the spatial and temporal patterns of the spreading of a heterogeneous cell population that is composed of both melanoma cells and primary fibroblast cells. All experiments in this work make use of the human metastatic melanoma cell line SK-MEL-28 (Fofaria and Srivastava, 2014), whereas the fibroblast cells are primary cells obtained from human donors. We first examine the spreading of melanoma cells and primary fibroblast cells separately, in a series of monoculture experiments. This allows us to quantify the rate of cell proliferation and the cell diffusivity for both melanoma cells and primary fibroblast cells, separately. Then, using our estimates of:

(i)   the melanoma cell diffusivity
(ii)   the primary fibroblast cell diffusivity
(iii)   the melanoma cell proliferation rate; and,
(iv)   the primary fibroblast cell proliferation rate,

we investigate whether the solution of an appropriate mathematical model describing the co-culture experiments, parameterised using data from the monoculture experiments, is able to predict the patterns of spreading in a suite of co-culture experiments where both cell types are present in varying ratios. The procedure that we describe can be used to quantify the extent to which the interactions between the two cell types affect the co-culture experiments.

In summary, we present a method that can be used to identify potential interactions between two different cell types. In particular, we focus on interactions between primary

fibroblast cells and SK-MEL-28 melanoma cells. Our hypothesis is that the rates at which these cells proliferate and migrate might be different when the cells are cultured in isolation to when the cells are cultured together. Overall, the results of our experimental and mathematical study supports the null hypothesis, since we find no clear evidence of any interactions other than cell-to-cell contact and crowding effects.

3.3 EXPERIMENTAL METHOD

3.3.1 Melanoma Cell Culture

The metastatic melanoma cell line, SK-MEL-28, is cultured as described previously (Haridas *et al.*, 2016). In brief, SK-MEL-28 melanoma cells are maintained in RPMI1640 medium (Thermo Scientific, Australia) supplemented with 10% fetal calf serum (FCS; Thermo Scientific), 2 mM L-glutamine (Thermo Scientific), 23 mM HEPES (Thermo Scientific), 50 U/ml of penicillin and 50 µg/ml of streptomycin (Thermo Scientific). The melanoma cell line is grown at 37 °C, in 5% CO_2 and 95% air, and the cell line is routinely screened for *mycoplasma* contamination.

3.3.2 Primary fibroblast culture

Human skin discards are obtained from abdominoplasty and breast reduction surgeries (Xie *et al.*, 2010). The epidermis is removed, discarded and the remaining dermis is used for fibroblast isolation. All experimental procedures are approved by the QUT research ethics committee (approval number QUT HREC #1300000063) and St Andrew's Hospital ethics committee (approval number: Uniting Care Health 2003/46). The dermis is finely minced with a scalpel blade and placed in a 0.05% w/v collagenase A type I (Thermo Scientific) solution prepared in Dulbecco's Modified Eagle's Medium (DMEM) (Thermo Scientific) at 37 °C, in 5% CO_2 and 95% air for 24 hours. The dermal cell solution is centrifuged at 212 g for 10 minutes, and cells are seeded into T75 cm^2 flasks (Nunc®, Australia) in DMEM with 10% FCS, 2 mM L-glutamine, 50 U/ml of penicillin and 50 µg/ml of streptomycin at 37 °C in 5% CO_2 and 95% air.

3.3.3   Circular barrier assay

The spreading and proliferation of both primary fibroblast cells and SK-MEL-28 melanoma cells are examined using a two-dimensional circular barrier assay (Treloar *et al*., 2014a; Treloar *et al*. 2014b). Two types of experiments are performed. Firstly, in the monoculture experiments, the barrier assays are initialised with approximately 20,000 primary fibroblast cells (Fb monoculture), or approximately 20,000 SK-MEL-28 melanoma cells (SK monoculture). Secondly, in the co-culture experiments, assays are performed using three ratios of melanoma to fibroblast cells with the total number of initial cells held constant at approximately 20,000. We use three different ratios, and refer to these experiments as: co-culture 1; co-culture 2; and co-culture 3. Co-culture 1 experiments are initialised with approximately 15,000 primary fibroblast cells and approximately 5,000 SK-MEL-28 melanoma cells; co-culture 2 experiments are initialised with approximately 10,000 primary fibroblast cells and approximately 10,000 SK-MEL-28 melanoma cells; and, co-culture 3 experiments are initialised with approximately 5,000 primary fibroblast cells and approximately 15,000 SK-MEL-28 melanoma cells. We note that all experiments are initialised with approximately 20,000 cells in total. This means that the initial density of cells is less than half of the carrying capacity density, and this allows the cell populations to spread as a monolayer (Treloar *et al*. 2013; Treloar *et al*. 2014a) instead of piling up to form three-dimensional structures.

Clean and dried metal-silicone barriers, 6 mm in diameter (Aix Scientifics, Germany), are placed in a 24 well tissue culture plate (Nunc®) over glass coverslips (ProSciTech, Australia) containing 500 µl of full Green's medium. The medium is made up of DMEM with Ham's F12 medium (Thermo Scientific) in a 3:1 v/v ratio, 10% FCS, 2 mM L-glutamine, 50 U/ml of penicillin, 50 µg/ml of streptomycin, 180 mM adenine (Sigma Aldrich, Australia), 1 µg/ml insulin, 0.1 µg/ml cholera toxin (Sigma Aldrich), 0.01% non-essential amino acid solution (Thermo Scientific), 5 µg/ml transferrin (Sigma Aldrich), 0.2 µM triiodothyronine (Sigma Aldrich), 0.4 µg/ml hydrocortisone (Sigma Aldrich) and 10 ng/ml human recombinant epidermal growth factor (EGF; Thermo Scientific). The cell suspension is carefully pipetted into the barrier to ensure the cells

are as evenly distributed as possible. Cells are allowed to attach to the plate for 2 hours in a humidified incubator at 37°C, 5% CO_2 and 95% air, before the barriers are carefully removed (Treloar *et al*., 2013). The cell layer is washed with serum free medium (SFM; culture medium without FCS) and the cells are cultured in full Green's medium. The culture plates are incubated at 37°C, 5% CO_2 and 95% air for $t = 0$, 24 and 48 hours. Each assay is performed in triplicates. Each assay is also repeated using primary fibroblast cells from three separate human donors.

3.3.4   *Crystal violet staining*

The cells grown on coverslips are washed with phosphate buffered saline (PBS; Thermo Scientific) and fixed for 20 minutes at room temperature using 10% neutral buffered formalin (United Biosciences, Australia), followed by staining the cells in 0.01% v/v crystal violet (Sigma Aldrich) in PBS. The coverslips are rinsed with PBS to remove excess stain and are air-dried. Images of the entire spreading cell population are acquired using a stereo microscope (Nikon SMZ 800) fitted with a Nikon digital camera.

3.3.5   *Immunofluorescence*

Cells grown on coverslips are fixed with 4% paraformaldehyde (Electron Microscopy Sciences, Australia) for 20 minutes at room temperature. Cell membranes are permeabilised with 0.1% v/v Triton X-100 (Merck Millipore, Australia) in PBS for 10 minutes, and the non-specific binding sites are blocked using 0.5% w/v bovine serum albumin (BSA) (Thermo Scientific) in PBS for 10 minutes. This is followed by the addition of primary antibody, *S100* in a ratio of 1:2000 (Dako, Australia) for an hour, and the secondary antibody *Alexa Fluor*® 555 in a ratio of 1:400 (Thermo Scientific) for an hour. Cells are washed with 0.5% BSA and the nuclei are stained with *dapi* in a ratio of 1:1000 (Sigma Aldrich) for 5 minutes. Coverslips are mounted on glass slides using ProLong® Gold Antifade mountant (Thermo Scientific).

3.4 MATHEMATICAL MODELLING METHODS

3.4.1 Model summary

One way of providing further information about cancer progression is to interpret experimental observations using a mathematical model (Byrne, 2010). To quantify the role of various mechanisms acting in the monoculture and co-culture experiments we will use a continuum partial differential equation (PDE) model describing the collective spreading, proliferation and cell-to-cell crowding in a heterogeneous population of cells that is composed of two distinct subpopulations (Simpson *et al.* 2014). The PDE model is given by,

$$\frac{\partial C_{Fb}}{\partial t} = \frac{D_{Fb}}{r}\frac{\partial}{\partial r}\left(r\left[\left[1-\frac{S}{K}\right]\frac{\partial C_{Fb}}{\partial r}+\frac{C_{Fb}}{K}\frac{\partial S}{\partial r}\right]\right)+\lambda_{Fb}C_{Fb}\left(1-\frac{S}{K}\right), \tag{1}$$

$$\frac{\partial C_{SK}}{\partial t} = \frac{D_{SK}}{r}\frac{\partial}{\partial r}\left(r\left[\left[1-\frac{S}{K}\right]\frac{\partial C_{SK}}{\partial r}+\frac{C_{SK}}{K}\frac{\partial S}{\partial r}\right]\right)+\lambda_{SK}C_{SK}\left(1-\frac{S}{K}\right), \tag{2}$$

where $C_{Fb}(r,t)$ and $C_{SK}(r,t)$ are the density of fibroblast and melanoma cells, respectively, as a function of radial position, r, and time, t. The total cell density is given by $S(r,t) = C_{Fb}(r,t) + C_{SK}(r,t)$, and the carrying capacity density is K. Since we consider circular barrier assays, in which the population of spreading cells always maintains a circular geometry over the entire duration of the experiment, Eq. (1)-(2) are written in terms of the radial coordinate, r, taking advantage of the axisymmetric geometry. Note that if there is just a single population present, Eq. (1)-(2) reduces to the standard Fisher-Kolmogorov equation in radial geometry (Treloar *et al.* 2014a).

3.4.2 Model parameters

There are five parameters in the co-culture model: (i) D_{Fb} is the diffusivity of the primary fibroblast cells; (ii) D_{SK} is the diffusivity of the SK-MEL-28 melanoma cells;

(iii) λ_{Fb} is the proliferation rate of the primary fibroblast cells; (iv) λ_{SK} is the proliferation rate of the SK-MEL-28 melanoma cells; and (v) K is the carrying capacity density. Since the cells in our experiments spread as a monolayer, and the diameter of both the primary fibroblast cells and the SK-MEL-28 melanoma cells is approximately 20 μm (Treloar *et al*. 2013; Treloar *et al*. 2014a), we estimate the carrying capacity density by assuming that the maximum density of cells corresponds to hexagonal packing of disks of diameter 20 μm, giving $K = 2.8 \times 10^{-3}$ cells/μm². With this assumption there are now four unknown parameters in Eq. (1)-(2).

3.4.3 Initial condition

The PDE model can be used to simulate both co-culture and a monoculture barrier assays. To simulate a co-culture assay we specify appropriate non-zero initial conditions for both $C_{Fb}(r,0)$ and $C_{SK}(r,0)$, chosen to match the initial cell density in the co-culture experiments. Alternatively, to simulate a fibroblast monoculture assay, we set $C_{SK}(r,0) = 0$ and specify some appropriate non-zero initial condition for $C_{Fb}(r,0)$. Similarly, to simulate a melanoma monoculture assay we set $C_{Fb}(r,0) = 0$ and specify some appropriate non-zero initial condition for $C_{SK}(r,0)$.

3.4.3 Numerical solution

Regardless of whether we use the PDE model to simulate a monoculture or co-culture assay, we always solve Eq.(1)-(2) numerically. Spatial derivatives are approximated using a central difference approximation on a uniformly-spaced finite difference mesh, with mesh spacing Δr. The resulting system of coupled nonlinear ordinary differential equations is solved using a backward Euler approximation, with time steps of duration Δt. The nonlinear ordinary differential equations are linearised using Picard iteration with a convergence tolerance of ε (Chapra and Canale, 1998).

3.4.4 Model background

Before applying Eq. (1)-(2) to our experimental data set, it is useful to briefly explain the origin of the PDE model and the underlying assumptions. The model was described and presented by us previously (Simpson *et al*. 2014). In that previous work we consider both a stochastic random walk process and the associated continuum limit PDE description. In brief, the lattice based random walk model describes the collective motion of a population of two potentially distinct subpopulations of cells. Cells in both subpopulations undergo nearest neighbour motility events, where cells attempt to step a distance of Δ, at some specified constant rate. Here, Δ corresponds to the average cell diameter. Potential motility events are unbiased so that the direction of movement is chosen with equal probability. Crowding effects are incorporated by ensuring that any potential motility event that would place a cell on an occupied site is aborted. The discrete model also allows cells to proliferate, at some other specified constant rate. A potential proliferation event will involve a cell placing a daughter cell, of the same subpopulation, on a randomly chosen nearest neighbour lattice site. Again, crowding effects are incorporated by ensuring that any potential proliferation event that would place a daughter cell on an occupied lattice site is aborted. The continuum limit description of this discrete model, in a radially symmetric geometry, is Eq. (1)-(2) (Simpson *et al*., 2014).

The system of PDEs, given by Eq. (1)-(2), corresponds to a coarse-grained description of the cell-to-cell crowding effects that are explicitly described in the discrete random walk model. For example, the nonlinear diffusion terms in Eq. (1)-(2) correspond to hard-core exclusion in the motility mechanism of the discrete model. Similarly, the nonlinear source terms in Eq. (1)-(2) correspond to the proliferation mechanism of the discrete model.

3.5 EXPERIMENTAL RESULTS AND DISCUSSION

3.5.1 *Diameter of the spreading population*

We first investigate the spatial expansion of the cell populations over time. Results in Fig. 3.1(a)-(i) show the spreading populations from $t = 0$ until $t = 48$ hours. To quantify the spatial spreading, we calculate the diameter of each spreading population at $t = 0$, 24 and 48 hours. To achieve this we use ImageJ (2016) to automatically detect the position of the leading edge of the spreading population using the Sobel method (Treloar and Simpson, 2013; Johnston *et al.* 2014). ImageJ also provides an estimate of the area contained within the leading edge of the spreading population. Using this estimate of area, we assume that the spreading population remains approximately circular, allowing us to convert the area estimate into an estimate of the equivalent circular diameter. The diameter of the spreading populations is shown in Fig. 3.1(j) where we see that there is an increase in the diameter with time in all cases. However, we observe that the rate of increase in the diameter in some experiments is different. For example, we observe that Fb monoculture experiments spread fastest, whereas the SK monoculture experiments spread slowest. In comparison, the co-culture experiments spread at an intermediate rate.
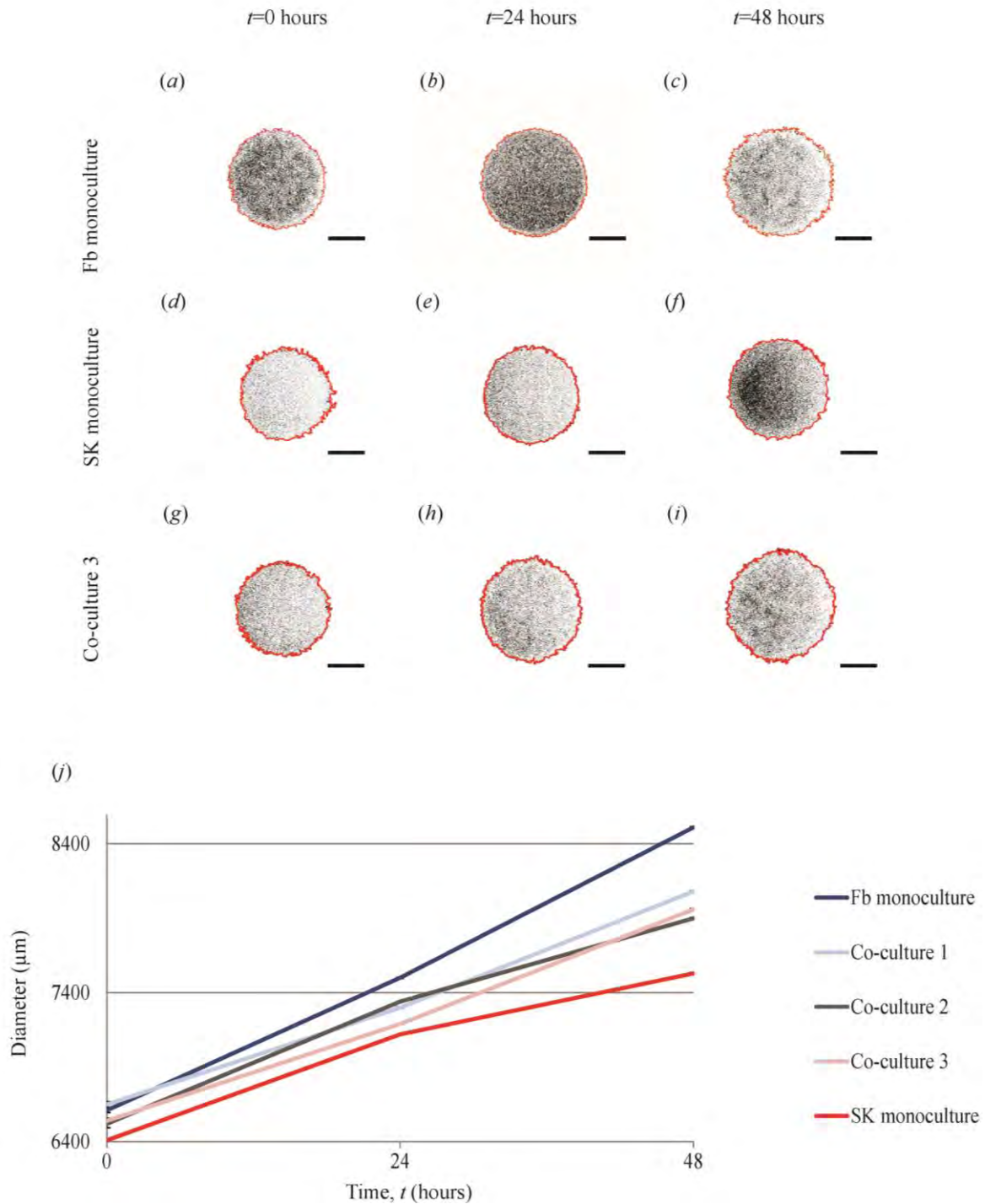
Figure 3.1: Spatial spreading of cell populations over 48 hours. Images in (*a*)-(*c*) show monoculture barrier assays initialised with approximately 20,000 primary fibroblasts (Fb monoculture), (*d*)-(*f*) show monoculture barrier assays initialised with approximately 20,000 SK-MEL-28 melanoma cells (SK monoculture), and (*g*)-(*i*) show

co-culture barrier assays initialised with approximately 10,000 SK-MEL-28 melanoma cells and approximately 10,000 primary fibroblast cells (co-culture 2). Images show the spreading of the population at $t = 0$, 24 and 48 hours, as indicated. The red outline shows the position of the leading edge detected using ImageJ. Each scale bar is 3000 μm. Data in (*j*) show the increase in average diameter of the spreading cell populations with time (n = 3). Each initial ratio of cells is shown using a different colour, as indicated. Co-culture 1 corresponds to experiments initialised with approximately 15,000 primary fibroblasts and approximately 5,000 SK-MEL-28 melanoma cells, co-culture 2 corresponds to experiments initialised with approximately 10,000 primary fibroblasts and approximately 10,000 SK-MEL-28 melanoma cells, and co-culture 3 corresponds to experiments initialised with approximately 5,000 primary fibroblasts and approximately 15,000 SK-MEL-28 melanoma cells.

Although these results focusing on the rate at which the leading edge of the populations spread is insightful, they do not provide any information about how the primary fibroblast cells and the SK-MEL-28 melanoma cells are distributed throughout the spreading populations. To provide this additional information, we use a more sophisticated experimental approach.

3.5.2   *Cell type identification in co-cultures*

To extend our initial investigation about the spatial expansion of the cell populations, we quantify the spatial distribution of primary fibroblast cells and SK-MEL-28 melanoma cells throughout the spreading populations. To achieve this we must distinguish the primary fibroblast cells from the SK-MEL-28 melanoma cells within these heterogeneous populations. The metastatic melanoma cell line, SK-MEL-28 can be reliably and exclusively identified using the *S100* marker (Haridas *et al*., 2016). However, it is challenging to identify primary fibroblast cells in a heterogeneous population because many because fibroblast markers, like *vimentin* and *alpha smooth muscle actin*, are also expressed by other migrating cell types present in the population (Kalluri and Zeisberg, 2006; Marsh *et al*., 2013; Sugimoto *et al*., 2006). To deal with

this complication we use *dapi* to stain the cell nuclei of all cells, capturing both the SK-MEL-28 melanoma cells and the primary fibroblast cells. By counting the number of *dapi*-positive cells and subtracting the number of *S100* positive cells, we are able to reliably estimate the number of primary fibroblast cells in each image.

Images showing the entire spreading populations are superimposed with an immunostained transect that passes through the centre of the cell population in Fig. 3. 2. These immunostained transects allow us to extract detailed information about the spatial distribution of primary fibroblast cells and SK-MEL-28 melanoma cells in each experiment. Greyscale images showing the entire spreading population at t = 24 and 48 hours are shown in Fig. 3. 2(*a*), (*c*), (*e*), (*g*), (*i*), (*k*), (*m*), (*o*), (*q*) and (*s*). The central region of the transect, as indicated, is magnified and shown in Fig. 3.2(*b*), (*d*), (*f*), (*h*), (*j*), (*l*), (*n*), (*p*), (*r*) and (*t*). Our results in Fig. 3.2 show that we are able to clearly and reliably identify the two different cell types in the experiments. We are confident in our results because there are no *S100* positive cells in the primary fibroblast monoculture experiment (Fig. 3.2(*b*), (*d*)), and we observe an increasing proportion of *S100* positive cells in co-culture 3 (Fig. 3.2(*m*)-(*p*)), compared to co-culture 2 (Fig. 3.2(*i*)-(*l*)). Similarly, we observe an increasing proportion of *S100* positive cells in co-culture 2 (Fig. 3.2(*i*)-(*l*)), compared to co-culture 1 (Fig. 3.2(*e*)-(*h*)).
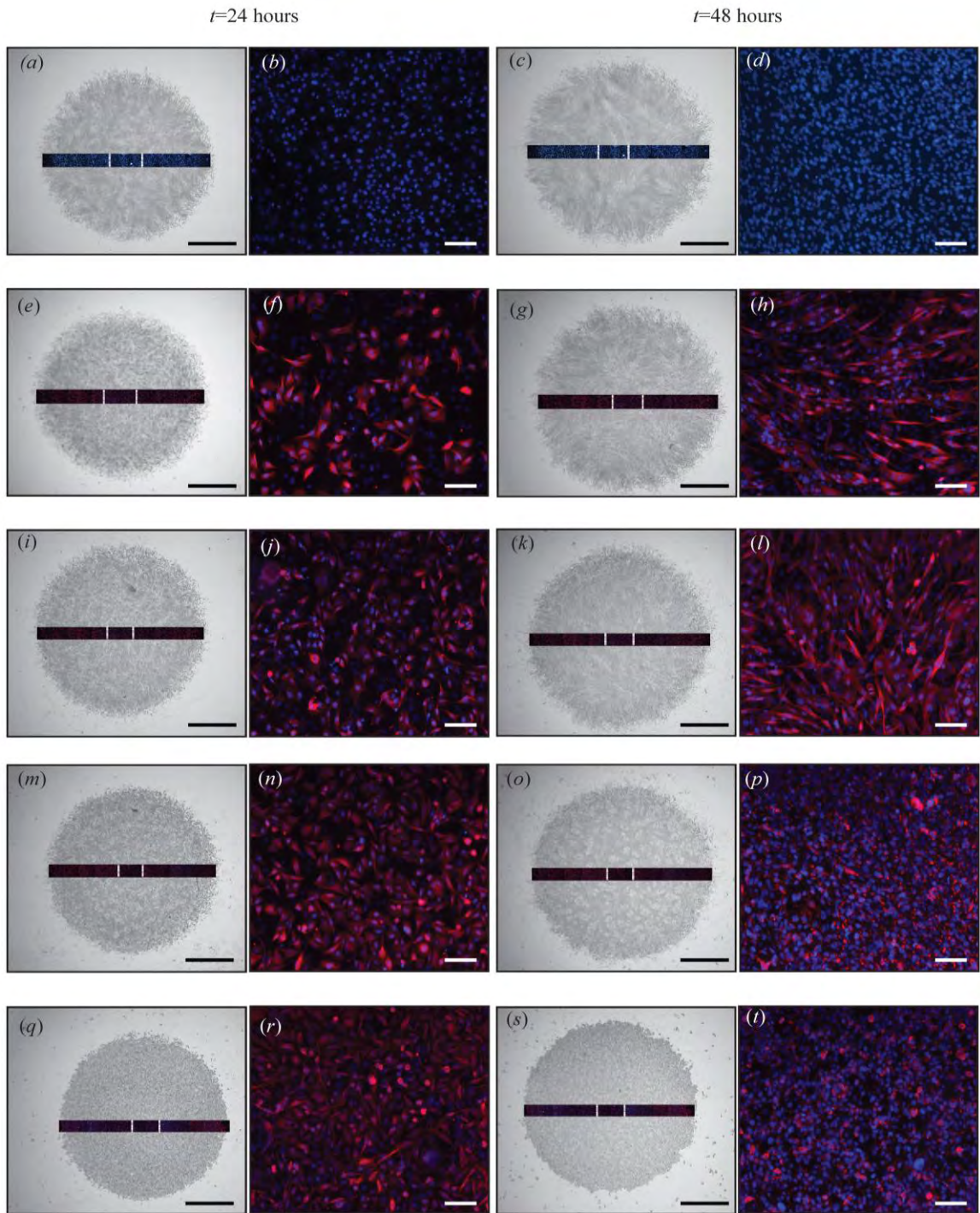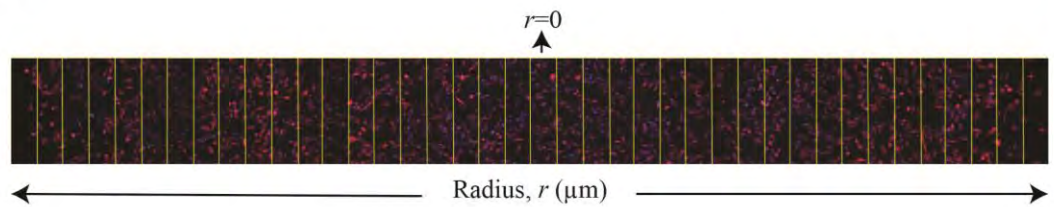
Figure 3.2: Experimental images of spreading cell populations and corresponding immunofluorescence images to detect the composition of the co-culture assays, at *t* = 24 and 48 hours. The two left-most columns of images correspond to *t* = 24 hours, and the two right-most columns of images correspond to *t* = 48 hours. Results in (*a*) and

(*c*) correspond to Fb monoculture; (*e*) and (*g*) correspond to co-culture 1; (*i*) and (*k*) correspond to co-culture 2; (*m*) and (*o*) correspond to co-culture 3; and (*q*) and (*s*) correspond to SK monoculture, as indicated. A transect showing immunofluorescence staining is superimposed on each greyscale image, and the transect passes through the centre of each spreading population. The vertical white lines on each transect indicates the central region of the transect, and the central regions in (*a*), (*c*), (*e*), (*g*), (*i*), (*k*), (*m*), (*o*), (*q*) and (*s*) are magnified, and shown in (*b*), (*d*), (*f*), (*h*), (*j*), (*l*), (*n*), (*p*), (*r*) and (*t*), respectively. In the immunofluorescence images, all cell nuclei (Fb + SK) are stained with *dapi* (blue), whereas just the SK-MEL-28 melanoma cells (SK) are stained with *S100* (red). The scale bar in all greyscale images is 2000 μm, and the scale bar in all immunofluorescence images is 100 μm.
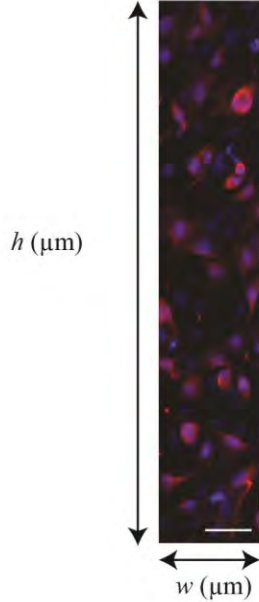
3.5.3 *Construction of cell density histograms*

To quantify how the two subpopulations of cells are spatially distributed within the heterogeneous spreading populations, we construct cell density histograms. To do this, we count the number of cells in many equally spaced subregions across each transect, as shown in Fig. 3.3(*a*). We use immunofluorescence to identify primary fibroblast cells and SK-MEL-28 melanoma cells as described in Section *3.4.2*, and as shown in Fig. 3.3(*b*)-(*d*). An estimate of the cell density for each cell type along the transect is calculated by counting the number of primary fibroblast cells and the number of SK-MEL-28 melanoma cells in each subregion, and dividing these numbers by the area of the subregion. A histogram showing cell density as a function of position is generated for each experimental replicate in each experimental condition. Averaging the histograms from each experimental replicate gives an averaged histogram, as shown in Fig. 3.3(*e*).

(a)

r=0

Radius, *r* (μm)

(b) (c) (d)

h (μm)

w (μm)

(e)

x10⁻³

Co-culture 2   *t*=0

Density

r (μm)
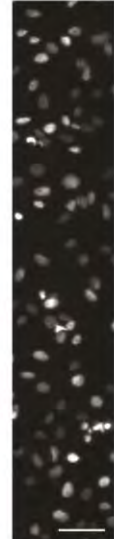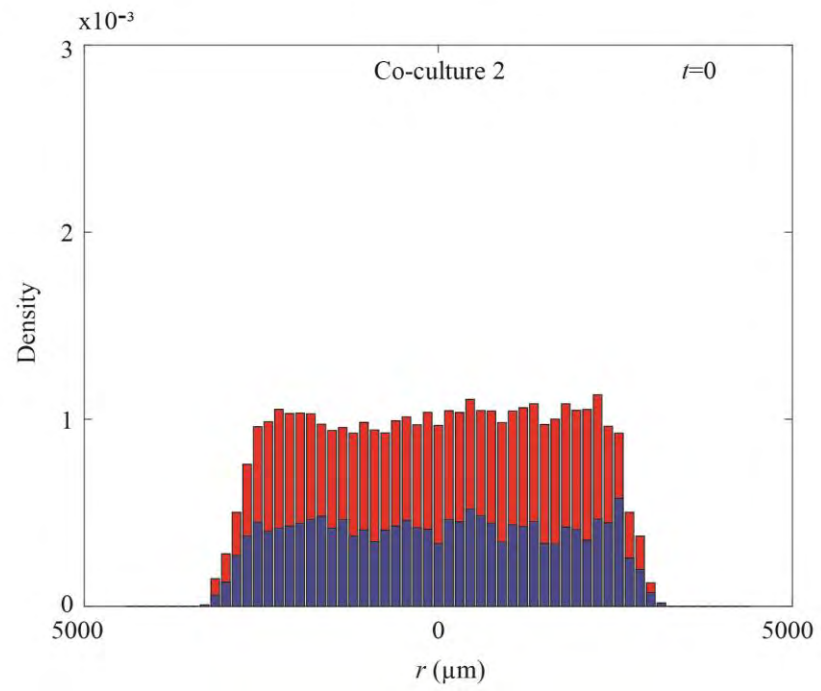
Figure 3.3: Immunofluorescence staining identifies the spatial and temporal patterns of cell spreading in the co-culture barrier assays. (*a*) Example transect through the centre of a spreading population. The centre of the population corresponds to $r = 0$, and the distance from the centre of the population is measured by the radial coordinate, $r > 0$. Each transect is divided into many equally-spaced subregions, each of width $w = 150$ µm and height h. The value of w is constant, fixed at 150 µm in all experiments. However, the height of the subregion, h, varied between 622-817 µm in different experiments, but the height is constant for each transect in each particular experiment. To quantify the density of cells across the transect, we count the number of cells of each type in each subregion, and divide by the area of the subregion to give an estimate of the density of each cell type, at each radial position, r. To count the number of cells in each subregion we use immunofluorescence staining, as shown in (*b*). The staining in (*c*) shows *dapi* staining (Fb + SK), whereas the staining in (*d*) shows *S100* (SK) staining. The number of primary fibroblast cells in each subregion is the difference between the total number of *dapi*-positive nuclei and the number of *S100*-positive cells in each subregion. The scale bar in (*b*)-(*d*) is 100 µm. Using these cell counts, we construct the cell density histogram, as shown in (*e*), illustrating the spatial variation in cell density at $t = 0$ in an experiment corresponding to co-culture 2. The blue section in the histogram shows the density of primary fibroblast cells, the red section shows the density of SK-MEL-28 melanoma cells, and the total height of the histogram shows the total cell density.

A series of averaged cell density histograms at $t = 0$, 24 and 48 hours are shown in Fig. 3.4. Each histogram shows the average density of cells across the entire transect. The radial position is given by $r > 0$. The centre of the spreading cell population corresponds to $r = 0$, and the population spreads in both directions, away from the centre. The blue section in the histograms indicate the average density of primary fibroblast cells, the red section shows the average density of SK-MEL-28 melanoma cells, and the total height of the histogram shows the average total cell density.
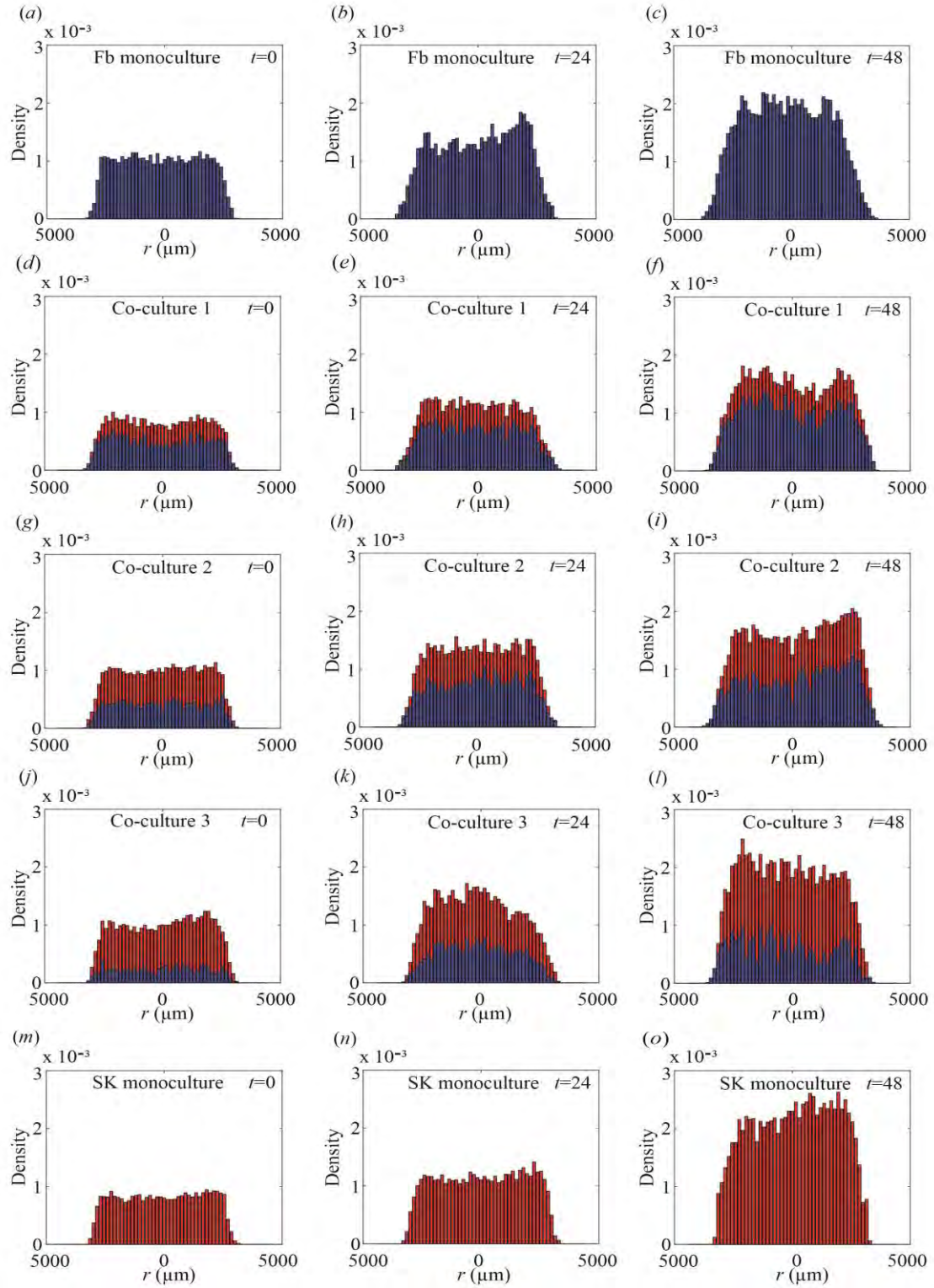
Figure 3.4: Summary of cell density profiles. Cell density histograms for individual experiments, constructed using the technique presented in Fig. 3.3, are averaged across three identically prepared experimental replicates (n = 3) to give a series of averaged cell density histograms. Averaged cell density histograms in (*a*)-(*c*) correspond to Fb monoculture; (*d*)-(*f*) correspond to co-culture 1; (*g*)-(*i*) correspond to co-culture 2; (*j*)-(*l*) correspond to co-culture 3; and (*m*)-(*o*) correspond to SK monoculture, at $t = 0$, 24 and 48 hours, as indicated. The blue section in the histogram shows the density of primary fibroblast cells, the red section shows the density of SK-MEL-28 melanoma cells, and the total height of the histogram shows the total cell density.

Results in Fig. 3.4(*a*), (*d*), (*g*), (*j*) and (*m*) show the histograms at $t = 0$. These results confirm that all barrier assays are initialised such that the total population of cells is approximately uniformly distributed across the transect, with a total cell density of approximately 1×10^{-3} cells/μm^2, which is less than half the carrying capacity density of these cells in a monolayer (Supplementary Material). However, the ratio of melanoma to primary fibroblast cells differs in Fig. 3.4(*a*), (*d*), (*g*), (*j*) and (*m*). For example, the profile in Fig. 3.4(*a*) contains only primary fibroblast cells, the prolife in Fig. 3.4(*m*) contains only melanoma cells, and the profiles in Fig. 3.4(*d*), (*g*) and (*j*) contain both melanoma and primary fibroblast cells with an increasing ratio of melanoma to fibroblast cells, respectively.

Our results in each row in Fig. 3.4 show how the cell density changes with time. The middle column of results corresponds to $t = 24$ hours, and the right-most column corresponds to $t = 48$ hours. Comparing results in Fig. 3.4(*c*) and Fig. 3.4(*o*) shows that the cells in the Fb monoculture experiments spread further than the cells in the SK monoculture experiments, and result this is consistent with the leading edge results in Fig. 3.1. Furthermore, comparing the shape of the cell density histograms in Fig. 3.4(*c*) and Fig. 3.4(*o*) shows that the leading edge of the cell density profile is sharper in the SK monoculture experiments than for the Fb monoculture experiments. While we observe differences in the rate of the spatial extent of the spreading of the two monoculture

experiments, we observe that the increase in cell density towards the centre of the population, at $r = 0$, is very similar. For example, at $t = 0$ the cell density at the centre of both monoculture experiments is approximately 1×10^{-3} cell/ μm^2, and after 48 hours the cell density at the centre of both monoculture experiments has approximately doubled to a density of $2 \times 10^{-3} - 2.5 \times 10^{-3}$ cells/μm^2.

Comparing the time evolution of the cell density patterns in the co-culture experiments with the monoculture experiments suggests that there are minimal differences in the behaviour of the monoculture and co-culture experiments. For example, co-culture 1 that is initiated with approximately 15,000 primary fibroblast cells and approximately 5,000 SK-MEL-28 melanoma cells behaves in a very similar way to the Fb monoculture experiment in terms of both the spatial extent of the spreading of the total population and the total increase in the cell density towards the centre of the spreading population. Similarly, co-culture 3, that is initiated with approximately 5,000 primary fibroblast cells and approximately 15,000 SK-MEL-28 melanoma cells behaves in a very similar way unto the SK monoculture experiment in terms of both the spatial extent of the spreading of the total population and the total increase in the cell density towards the centre of the spreading population. Results for co-culture 2 lie between co-culture 1 and co-culture 3. An interesting feature of co-culture 1 and co-culture 2 is that at both $t = 24$ and $t = 48$ hours, we see that the primary fibroblast cells dominate the total population right at the leading edge of the heterogeneous population of cells. This is consistent with our observation that the primary fibroblast cells spread faster than the SK-MEL-28 melanoma cells in the monoculture experiments.

Now that we have presented, and discussed, the cell density histograms for the monoculture and co-culture experiments, we will further explore the similarities and differences between the experiments by calibrating a mathematical model to these data. Combining our experimental results with a mathematical model will allow us to explore, in more detail, the question of whether the primary fibroblast cells and/or the SK-MEL-

28 melanoma cells behave differently when grown in monoculture or in co-culture conditions.

3.6 MATHEMATICAL RESULTS AND DISCUSSION

3.6.1 *Estimating parameters for the monoculture experiments*

Since fibroblast cells and melanoma cells are cultured separately in the monoculture experiments, the coupled model, given by Eq. (1)-(2), uncouples to give

$$\frac{\partial C_{Fb}}{\partial t} = \frac{D_{Fb}}{r} \frac{\partial}{\partial r}\left(r \frac{\partial C_{Fb}}{\partial r} \right) + \lambda_{Fb} C_{Fb}\left(1 - \frac{C_{Fb}}{K} \right), \tag{3}$$

$$\frac{\partial C_{SK}}{\partial t} = \frac{D_{SK}}{r} \frac{\partial}{\partial r}\left(r \frac{\partial C_{SK}}{\partial r} \right) + \lambda_{SK} C_{SK}\left(1 - \frac{C_{SK}}{K} \right). \tag{4}$$

Equations (3)-(4) are two, uncoupled, single-species Fisher-Kolmogorov equations in radial coordinates that we will use to describe the Fb monoculture and SK monoculture experiments, respectively. There are four parameters to be estimated: D_{Fb}; D_{SK}; λ_{Fb} and λ_{SK}. We now explain how these parameters can be estimated separately, using data in Fig. 3.4(*a*)-(*c*) for the Fb monoculture experiment, and using data in Fig. 3.4(*m*)-(*o*) for the SK monoculture experiment. Following the approach of Johnston *et al*. (2015), we note that in the central region of the monoculture experiments, where $r < 1425$ μm, the cell density profile is approximately spatially uniform in both the fibroblast monoculture and the melanoma monoculture (Fig. 3.4). This region approximately corresponds to the middle third of the spreading population, and hence this region is well away from the leading edge of the spreading populations. Since, locally in the centre of the fibroblast monoculture experiment we have $\partial C_{Fb}/\partial r \approx 0$, and locally in the centre of the melanoma monoculture experiment we have $\partial C_{SK}/\partial r \approx 0$,

the two uncoupled PDEs, Eq. (3)-(4), simplify to two uncoupled ordinary differential equations (ODE) that can be written as

$$\frac{dC_{Fb}}{dt} = \lambda_{Fb} C_{Fb} \left(1 - \frac{C_{Fb}}{K}\right), \tag{5}$$

$$\frac{dC_{SK}}{dt} = \lambda_{SK} C_{SK} \left(1 - \frac{C_{SK}}{K}\right). \tag{6}$$

The solutions of Eq. (5)-(6) are

$$C_{Fb}(t) = \frac{K C_{Fb}(0) \exp(\lambda_{Fb} t)}{K + C_{Fb}(0)[\exp(\lambda_{Fb} t) - 1]}, \tag{7}$$

$$C_{SK}(t) = \frac{K C_{SK}(0) \exp(\lambda_{SK} t)}{K + C_{SK}(0)[\exp(\lambda_{SK} t) - 1]}, \tag{8}$$

where $C_{Fb}(0)$ is the initial density of the fibroblast cells in the central region of the Fb monoculture experiments, and $C_{SK}(0)$ is the initial density of the melanoma cells in the central region of the SK monoculture experiments. Estimates of λ_{Fb} and λ_{SK} are obtained by choosing these parameters so that $C_{Fb}(t)$ and $C_{SK}(t)$, given by Eq. (7)-(8), match the experimental data from the central region of the fibroblast monoculture experiments and the melanoma monoculture experiments, respectively (Supplementary Material-2). In summary, matching these solutions to our experimental data gives us a range of estimates: $0.02 \leq \bar{\lambda}_{Fb} \leq 0.04$ /hour and $0.03 \leq \bar{\lambda}_{SK} \leq 0.05$ /hour. Here we use the overbar notation to indicate the least-squares estimates of the parameters, and the range of estimates corresponds to the sample mean plus or minus one sample standard deviation calculated using the three identically prepared experimental replicates of the monoculture experiments. It is interesting to note that these estimates of the proliferation rate for the melanoma cells and the fibroblast cells are approximately equal. Furthermore, the proliferation rates correspond to a doubling time of approximately 23 hours, and this is consistent with previous results (Treloar *et al.* 2013).

Given our estimates of λ_{Fb} and λ_{SK}, we solve Eq. (3)-(4) across the entire domain, $0 < r < 4350$ μm, and match the numerical solution of each uncoupled PDE with the averaged cell density profiles across the entire domain for both monoculture experiments. Setting the proliferation rates to be in the middle of the range previously identified ($\bar{\lambda}_{Fb} = 0.03$ /hour and $\bar{\lambda}_{SK} = 0.04$ /hour), we obtain estimates of $\bar{D}_{Fb} \approx 1200\,\mu\mathrm{m}^2$/hour, and $\bar{D}_{SK} \approx 170\,\mu\mathrm{m}^2$/hour (Supplementary Material). Unlike our estimates of the proliferation rates, the estimate of the cell diffusivity for the fibroblast cells is an order of magnitude higher than the estimate of the cell diffusivity for the melanoma cells. Our estimate for the cell diffusivity of the human primary fibroblast cells is very similar to previous estimates of the cell diffusivity for 3T3 mouse fibroblast cells, which have been reported to be approximately 800-2900 μm²/hour (Treloar *et al*. 2014a). Furthermore, our estimate of the cell diffusivity for the SK-MEL-28 melanoma cells is similar to previous estimates for other metastatic melanoma cell lines, which have been reported to be approximately 160-250 μm²/hour (Treloar *et al*. 2013).

3.6.2   *Predicting collective cell spreading in the co-culture experiments*

Given our parameter estimates from the monoculture experiments, we are interested to investigate whether the solution of the coupled co-culture model, Eq. (1)-(2), can accurately predict the spatial and temporal patterns of spreading in the co-culture experiments when parameterised in the same way. Examining this question will provide insight into whether the fibroblast and/or melanoma cells behave differently in monoculture than they do in co-culture. In summary, if we can find a unique choice of D_{Fb} ; D_{SK} ; λ_{Fb} and λ_{SK} for which:

(i)   the solution of the coupled system, Eq. (1)-(2), matches the experimental data for all three co-culture assays;

(ii)   the solution of Eq. (3) matches the experimental data for the fibroblast monoculture assay; and

(iii)   the solution of Eq. (4) matches the experimental data for the melanoma monoculture assay,

it would be reasonable to conclude that the migratory and proliferative behaviour of the melanoma and fibroblast cells appears to be independent of whether these two cell types are cultured separately or together. In contrast, if we must choose very different parameter values to match the monoculture experiments compared to the parameter values required to match the co-culture experiments, then our results would suggest that the cells behave very differently in monoculture and co-culture environments.

Results in Fig. 3.5 compare the spatial and temporal evolution of the two monoculture assays and the three co-culture assays together with the solution of the appropriately parameterised mathematical models. Using our parameter estimates from the monoculture experiments as an initial estimate, we manually adjusted the parameters and find that setting $D_{Fb} \approx 1200\,\mu\text{m}^2/\text{hour}$; $D_{SK} \approx 170\,\mu\text{m}^2/\text{hour}$; $\lambda_{Fb} = 0.03\,/\text{hour}$ and $\lambda_{SK} = 0.03\,/\text{hour}$ leads to a reasonably accurate match across both the two monoculture assays and the three co-culture assays (Supplementary Material). Given that we are able to match both the monoculture and co-culture experiments using a single combination of parameters, this suggests that the only interactions necessary to explain the experimental observations are cell-to-cell contact and crowding effects. In particular, no additional cross-talk mechanisms, such as interactions mediated by the production of signalling factors, is required to explain our experimental observations.
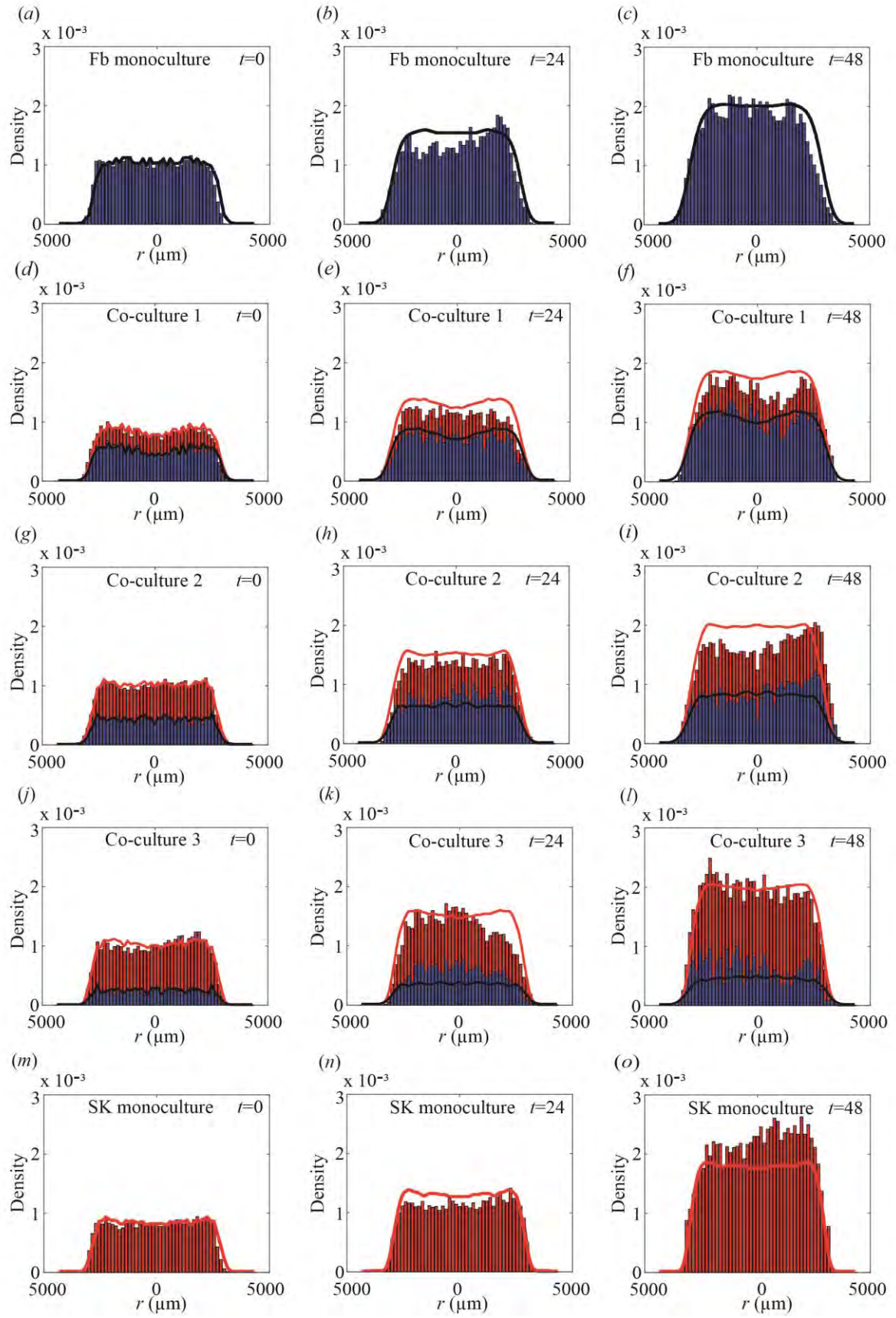
Figure 3.5: Comparison of average cell density profiles and the solution of the mathematical model, Eq. (1)-(2). The experimental data is presented in the same format as presented in Fig. 3.4. All experimental data are superimposed with appropriate numerical solutions of Eq. (1)-(2), with $C_{Fb}(r,t)$ shown in black, and $S(r,t)$ shown in red, and $C_{SK}(r,t)$ is the difference between the red curve and the black curve. The initial condition for $C_{Fb}(r,0)$ and $S(r,0)$, shown in (a), (d), (g), (j) and (m), are chosen to match the observed experimental data at $t = 0$. The parameters used to solve Eq. (1)-(2) are: $D_{Fb} = 1200 \, \mu\text{m}^2/\text{hour}$; $D_{SK} = 170 \, \mu\text{m}^2/\text{hour}$; $\lambda_{Fb} = 0.03 \, \text{hour}^{-1}$; $\lambda_{SK} = 0.03 \, \text{hour}^{-1}$ and $K = 2.8 \times 10^{-3} \text{cells}/\mu\text{m}^2$. The equations are solved on $0 < r < 4350 \, \mu\text{m}$. Zero flux boundary conditions are implemented at $r = 0 \, \mu\text{m}$ and $r = 4350 \, \mu\text{m}$. The numerical solutions of Eq. (1)-(2) are obtained with $\Delta r = 10 \, \mu\text{m}$, $\Delta t = 0.1$ hours and $\varepsilon = 1 \times 10^{-5}$.

Results in Fig. 3.4-3.5 indicate that cell density profile for co-culture 1 appears to contain a 'dip' in the central region, near $r = 0 \, \mu\text{m}$. Equivalent results for co-cultures 2, 3, and the monoculture experiments do not contain such a pronounced dip (Fig. 3.4-3.5). Since all experiments are prepared using the same procedure, we prefer not to offer an interpretation of this dip because it could be due to a statistical fluctuation rather than some underlying mechanism.

All of our results, so far, suggest that the diffusivity and proliferation rate of primary fibroblast cells and SK-MEL-28 melanoma cells are insensitive to whether the cell populations are grown in monoculture or co-culture. This implies that there are limited interactions or crosstalk between these two cell populations. If we were to observe some interactions, such as melanoma cell migration being stimulated by the presence of fibroblast cells, we can use our mathematical model to explore how these potential interactions might be best observed. To explore this we conduct a series of numerical experiments to investigate how the solutions of Eq. (1)-(2) depend on D_{SK}. Since we focus on altering D_{SK} alone, we find that the solution of Eq. (1)-(2) is most sensitive at the low-density leading edge of the population, as depicted in Fig. 3.6(a). Results in Fig.

3.6(b) compare the experimental density profile for co-culture 3 at $t = 48$ hours with the standard choice of parameters from Fig 3.5, showing that the solution of the mathematical model for $S(r,t)$ matches the experimental data quite well at the leading edge of the spreading population. We also show results where D_{SK} is increased by a factor of 5, where we see that the solution of the mathematical model predicts that the population spreads notably further than observed in the experiments. Similarly, we also show equivalent results where D_{SK} is increased by a factor of 20 and the differences are even more pronounced.
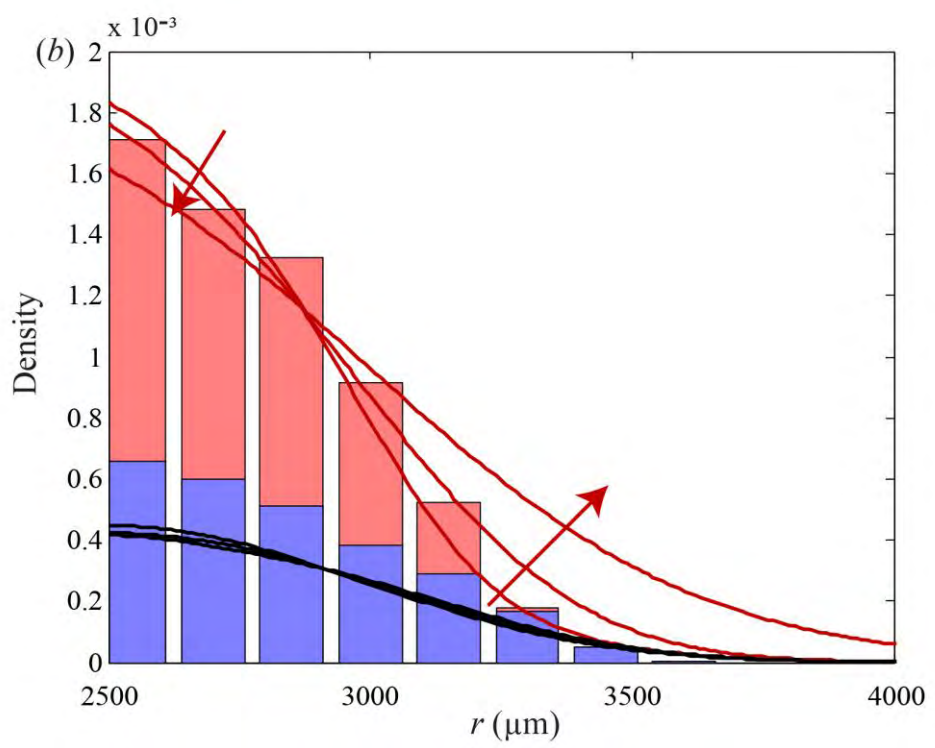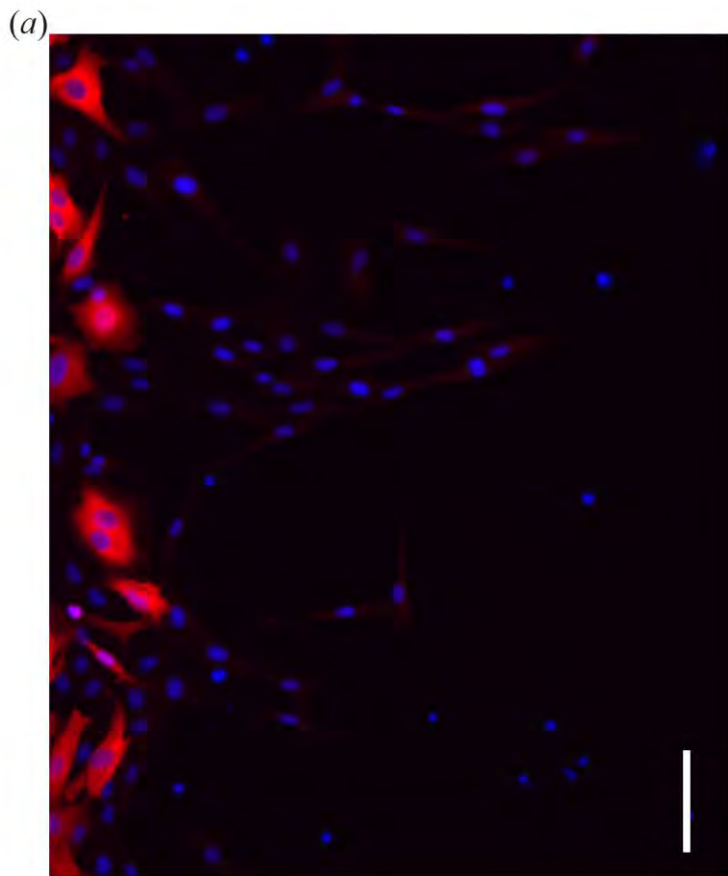
Figure 3.6: Focussing on the leading edge of the spreading population highlights the sensitivity of the spreading to the value of D_{SK}. (*a*) Immunofluorescence staining at the leading edge of the spreading population in co-culture 3 showing individual fibroblast cells (blue) ahead of the SK-MEL-28 melanoma cells (red). The scale bar is 100 μm. (*b*) The average experimental cell density profile for co-culture 3 after 48 hours near the leading edge of the spreading population is compared with three numerical solutions of Eq. (1)-(2). The solution for $C_{Fb}(r,t)$ is shown in black, $S(r,t)$ is shown in red and $C_{SK}(r,t)$ is the difference between the red and black curves. The parameters used to solve Eq. (1)-(2) are: $D_{Fb} = 1200$ μm²/hour; $\lambda_{Fb} = 0.03$ /hour; $\lambda_{SK} = 0.03$ /hour and $K = 2.8 \times 10^{-3}$ cells/μm² for all three profiles, while the value of D_{SK} includes 170, 850 and 3400 μm²/hour with the arrows showing the direction of increasing D_{SK}. The equations are solved on $0 < r < 4350$ μm, but the profiles are shown only at the leading edge where $2500 < r < 4000$ μm. The numerical solutions of Eq. (1)-(2) are obtained with $\Delta r = 10$ μm, $\Delta t = 0.1$ hours and $\varepsilon = 1 \times 10^{-5}$.

The additional results in Fig. 3.6 suggest that the comparison of the experimental cell density profile and the solution of the mathematical model at the leading edge of the spreading population is relatively sensitive to the value of D_{SK}. One way of interpreting the results in Fig. 3.6(*b*) is that our procedure could be used to detect potential interactions that would lead to a modest increase in D_{SK} when the two cell types are grown in co-culture.

3.7   CONCLUSION

Many *in vitro* studies examining the spatial spreading of cancer cells use monoculture experiments (Kramer *et al.*, 2013; Liao *et al.*, 2013; Treloar *et al.*, 2013; Treloar *et al.*, 2014b). However, these monoculture experiments are unrealistic in the sense that the spreading cancer cells are not subject to interactions with other cell types as would occur *in vivo*. To address this limitation, our approach to investigate the spatial spreading of a

melanoma cell population is to examine a suite of monoculture and co-culture circular barrier assays. Our monoculture experiments involve studying both primary fibroblast cells and SK-MEL-28 melanoma cells separately, while our co-culture experiments use three ratios of both cell types in the same experiment. All of our experiments are initialised by placing approximately 20,000 cells into the barrier, and we examine the collective spreading over a period of 48 hours. To quantify how these heterogeneous populations of cells spread over time we: (i) measure the diameter of each expanding cell population; (ii) identify individual cell types in each expanding population; (iii) count the number of primary fibroblast cells and SK-MEL-28 melanoma cells in a series of transects across each expanding cell population; and (iv) construct cell density histograms to show the spatial arrangements of each cell type in each expanding cell population.

Previous experimental studies suggest that interactions between fibroblast and melanoma cells can lead to an increase in rates of collective spreading when these two cell types are in contact (Cornil *et al*., 1991; Flach *et al*., 2011). However, these previous studies do not make detailed measurements of spatial and temporal arrangements of cells within the spreading population, and they do not consider varying the initial ratio of fibroblast cells to melanoma cells. To provide more information about the interaction between melanoma cells and fibroblast cells, we perform co-culture experiments using three different initial ratios of cells, and we make detailed measurements about the spatial and temporal arrangements of both subpopulations within the heterogeneous population as it spreads and grows. In summary, our experimental results indicate that the influence of primary fibroblast cells on SK-MEL-28 melanoma cell growth and spatial expansion in a two-dimensional circular barrier assay is minimal. To provide additional information about this apparent lack of interaction, we also calibrate a mathematical model to our experimental data.

In this work, we use our mathematical model to provide a novel analysis of experiments exploring potential interactions between fibroblast cells and melanoma cells. By first

estimating the cell diffusivity and cell proliferation rate for the primary fibroblast cells and SK-MEL-28 melanoma cells separately in monoculture, we find that the parameter estimates are consistent with previously published estimates for mouse fibroblast cells and other metastatic melanoma cell lines (Treloar *et al*. 2013; Treloar *et al*. 2014a). Therefore, we are confident in our estimates of the cell diffusivity and cell proliferation rate in monocultures because they are consistent with previously published data for similar experiments. Then, to address the question of whether cells in monoculture behave similarly, or differently, to cells in co-culture, we investigate whether the solution of the co-culture mathematical model, parameterised using estimates from the monoculture experiments, can genuinely predict the behaviour of the co-culture experiments. Since we find that a fixed choice of parameters, that is very similar to the estimates from the monoculture experiments, can predict both the spatial and temporal patterns of collective spreading in the two monoculture experiments, and all three co-culture experiments, we conclude that the spreading and growth patterns observed for primary fibroblast cells and SK-MEL-28 melanoma cells are not affected by growing them in monoculture or co-culture.

Our approach is to compare the spatial spreading of two different cell types in both monoculture and co-culture circular barrier assays to quantify the rates of cell migration and the rates of cell proliferation for each cell type. This approach is novel because most combined experimental and mathematical modelling studies focus on monoculture experiments alone (Kramer *et al*., 2013; Treloar *et al*., 2013). However, it is possible to explore other alternative experiments to further extend our work. This includes performing additional experiments to examine the rates of spatial spreading in different cell lines. For example, it could be of interest to repeat our work using other kinds of melanoma cell lines including cell lines from earlier stages of the disease, such as melanoma cells associated with the radial growth phase or the vertical growth phase (Haridas *et al*., 2016). This could be an important consideration because our current work focuses on examining potential interactions between fibroblast cells and SK-MEL-28 melanoma cells only. Since the SK-MEL-28 cell line is associated with the

metastatic phase (Fofaria and Srivastava, 2014; Haridas *et al*. 2016), it is possible that these cells have progressed beyond being influenced by fibroblasts. Alternatively, if our experiments and analysis were repeated using melanoma cells from earlier stages, it is conceivable that these melanoma cells might be more responsive to the presence of fibroblasts.

Other options to extend our work might involve incorporating further types of cells to make the co-culture experiments more realistic. For example, it is of interest to include both primary fibroblast cells and primary keratinocyte cells in a co-culture experiment with melanoma cell lines. However, this kind of extension is difficult because we would need to specifically identify three different cell types to understand how the three different subpopulations are spatially arranged. Therefore, we leave this extension for future consideration.

3.8 ACKNOWLEDGEMENTS

3.9 REFERENCES

1. Baraldi, M. M., Alemi, A. A., Sethna, J. P., Caracciolo, S., Porta, C. A. L. M., Zapperi, S., 2013. Growth and form of melanoma cell colonies. *Journal of Statistical Mechanics: Theory and Experiment*. 2013, P02032.

2. Byrne, H. M., 2010. Dissecting cancer through mathematics: from the cell to the animal model. *Nature Reviews Cancer*. 10, 221-230.

3. Cornil, I., Theodorescu, D., Man, S., Herlyn, M., Jambrosic, J., Kerbel, R. S., 1991. Fibroblast cell interactions with human melanoma cells affect tumor cell growth as a function of tumor progression. *Proceedings of National Academic Science. USA*. 88, 6028-6032.

4. Chapra, S. C., Canale, R. P., 1998. Numerical methods for engineers, third ed. McGraw-Hill, Singapore.

5. Dvorankova, B., Szabo, P., Kodet, O., Strnad, H., Kolar, M., Lacina, L., Krejci, E., Nanka, O., Sedo, A., Smetana, K. Jr., 2017. Intercellular crosstalk in human malignant melanoma. *Protoplasma*. 254, 1143-1150.

6. Erdei, E., Torres, S. M., 2010. A new understanding in the epidemiology of melanoma. *Expert Review of Anticancer Therapy.* 10, 1811-1823.

7. Faries, M. B., Ariyan, S., 2011. Current surgical treatment in melanoma. *Current Problems in Cancer*. 35: 173-184.

8. Flach, E. H., Rebecca, V. W., Herlyn, M., Smalley, K. S., Anderson, A. R. A., 2011. Fibroblasts contribute to melanoma tumor growth and drug resistance. *Molecular Pharmaceutics*. 8, 2039-2049.

9. Fofaria, N., Srivastava, S. K., 2014. Critical role of STAT3 in melanoma metastasis through anoikis resistance. *Oncotarget*. 5, 7051-7064.

10. Geller, A. C., Annas, G. D., 2003. Epidemiology of melanoma and nonmelnaoma skin cancer. *Seminars in Oncology Nursing*. 19, 2-11.

11. Goldstein, L. J., Chen, H., Bauer, R. J., Bauer, S. M., Velazquez, O. C., 2005. Normal human fibroblasts enable melanoma cells to induce angiogenesis in type I collagen. *Surgery*. 138, 439-449.

12. Haridas, P., McGovern, J. A., Kashyap, A. S., McElwain, D. L. S., Simpson, M. J., 2016. Standard melanoma-associated markers do not identify the MM127 metastatic melanoma cell line. *Scientific Reports*. 6, 24569.

13. Im, Y-S., Ryu, Y-K., Moon, E-Y., 2012. Mouse melanoma cell migration is dependent on production of reactive oxygen species under normoxia condition. *Biomolecules and Therapeutics*. 20, 165-170.

14. ImageJ, ImageJ User Guide: Research Services Branch, National Institute of Health. <https://imagej.nih.gov/ij/docs/guide/146-29.html> (April 2017).

15. Johnston, S. T., Simpson, M. J., McElwain, D. K. S., 2014. How much information can be obtained from tracking the position of the leading edge in a scratch assay? *Journal of the Royal Society Interface*. 11, 20140325.

16. Johnston, S. T., Shah, E. T., Chopin, L. K., McElwain, D. L. S., Simpson, M. J., 2015. Estimating cell diffusivity and cell proliferation rate by interpreting IncuCyte ZOOM™ assay data using the Fisher-Komogorov model. *BMC Systems Biology*. 9, 38.

17. Justus, C. R., Leffler, N., Ruiz-Echevarria, M., Yang, L. V., 2014. *In vitro* cell migration and invasion assays. *Journal of Visual Experiments*. 88, e51046.

18. Kalluri, R., Ziesberg, M., 2006. Fibroblasts in cancer. *Nature Reviews Cancer*. 6, 392-401.

19. Kramer, N., Walzl, A., Unger, C., Rosner, M., Krupitza, G., Hengstschlager, M., Dollznig, H., 2013. *In vitro* cell migration and invasion assays. *Mutation Research*. 752, 10-24.

20. Labrousse, A-L., Ntayi, C., Hornebeck, W., Bernard, P., 2004. Stromal reaction in cutaneous melanoma. *Critical Reviews in Oncology/ Hematology*. 49, 269-275.

21. Li, G., Satyamoorthy, K., Meier, F., Berking, C., Bogenrieder, T., Herlyn, M., 2003. Function and regulation of melanoma-stromal fibroblast interactions: when seeds meet soil. *Oncogene*. 22, 3162-3171.

22. Li, H., Fan, X., Houghton, J., 2007. Tumor microenvironment: the role of the tumor stroma in cancer. *Journal of Cellular Biochemistry*. 101, 805-815.

23. Liao, S., Deng, D., Zhang, W., Hu, X., Wang, W., Wang, H., Lu, Y., Wang, S., Meng, L., Ma, D., 2013. Human papillomavirus 16/18 E5 promotes cervical cancer cell proliferation, migration and invasion *in vitro* and accelerates tumor growth *in vivo*. *Oncology Reports*. 29, 95-102.

24. Marsh, T., Pietras, K., McAllister, S. S., 2013. Fibroblasts as architects of cancer pathogenesis. *Biochimica et Biophysica Acta.*1832, 1070-1078.

25. Melanoma Institute Australia. <https://www.melanoma.org.au/> (April 2017).

26. Ruiter, D., Bogenrieder, T., Elder, D., Herlyn, M., 2002. Melanoma–stroma interactions: structural and functional aspects. *Lancet Oncology*. 3, 35-43.

27. Simpson, M. J., Haridas, P., McElwain, D. L. S., 2014. Do pioneer cells exist? *PLoS ONE*. 9, e85488.

28. Schwartz, M. A., McRoberts, K., Coyner, M., Andarawewa, K. L., Frierson, H. F. Jr., Sanders, J. M., Swenson, S., Markland, F., Conaway, M. R., Theodorescu, D., 2008. Integrin agonists as adjuvants in chemotherapy for melanoma. *Clinical Cancer Research.* 14, 6193-6197.

29. Sneyd, M. J., Cox, B., 2013. A comparison of trends in melanoma mortality in New Zealand and Australia: the two countries with the highest melanoma incidence and mortality in the world. *BMC Cancer*. 13, 372.

30. Sriram, G., Bigliardi, P. L., Bigliardi-Qi, M., 2015. Fibroblast heterogeneity and its implications for engineering organotypic skin models *in vitro*. *European Journal of Cell Biology*. 94, 483-512.

31. Sugimoto, H., Mundel, T. M., Kieran, M. W., Kalluri, R., 2006. Identification of fibroblast heterogeneity in the tumor microenvironment. *Cancer Biology and Therapy*. 5, 1640-1646.

32. Treloar, K. K., Simpson, M.J., 2013. Sensitivity of edge detection methods for quantifying cell migration assays. *PLoS ONE*. 8, e67389.

33. Treloar, K. K., Simpson, M. J., Haridas, P., Manton, K. J., Leavesley, D. I., McElwain, D. L. S., Baker, R. E., 2013. Multiple types of data are required to identify the mechanisms influencing the spatial expansion of melanoma cell colonies. *BMC Systems Biology*. 7,137.

34. Treloar, K. K., Simpson, M. J., McElwain, D. L. S., Baker, R. E., 2014a. Are *in vitro* estimates of cell diffusivity and cell proliferation rate sensitive to assay geometry? *Journal of Theoretical Biology*. 356, 71-84.

35. Treloar, K. K., Simpson, M. J., Binder, B. J., McElwain, D. L. S., and Baker, R. E., 2014b. Assessing the role of spatial correlations during collective cell spreading. *Scientific Reports*. 4, 5713.

36. Xie, Y., Rizzi, S. C., Dawson, R., Lynam, E., Richards, S., Leavesley, D. I., Upton, Z., 2010. Development of a three-dimensional human skin equivalent wound model for investigating novel wound healing therapies. *Tissue Engineering. Part C-Methods*. 16, 1111-1123.

37. Ye, J., Wu, D., Wu, P., Chen, Z., Huang, J., 2014. The cancer stem cell niche: cross talk between cancer stem cells and their microenvironment. *Tumor Biology*. 35, 3945-3951.

38. Zhou, L., Yang, K., Andl, T., Wickett, R. R., Zhang, Y., 2015. Perspective of targeting cancer-associated fibroblasts in melanoma. *Journal of Cancer*. 6, 717-726.

3.10 SUPPLEMENTARY MATERIAL

3.10.1 Introduction

Here we describe, in detail, the method used to obtain the least-squares estimates of the cell diffusivity and cell proliferation rates in the two different monoculture experiments. The equation governing the monoculture experiments is the Fisher-Kolmogorov equation in radial coordinates for the density of cells $C(r, t)$, as a function of radial position, r, and time, t:

$$\frac{\partial C}{\partial t} = \frac{D}{r} \frac{\partial}{\partial r} \left(r \frac{\partial C}{\partial r} \right) + \lambda C \left(1 - \frac{C}{K} \right), \tag{1}$$

where D is the cell diffusivity, λ is the cell proliferation rate, and K is the carrying capacity. Since we use the same equation to model both the fibroblast monoculture experiments and the SK-MEL-28 melanoma monoculture experiments, we will use the same equation for the cell density without any subscripts. To estimate the carrying capacity density for both cell types, we set $K = 2.8 \times 10^{-3}$ cells/μm^2, since this is the maximum density of disks with diameter approximately 20 μm can be hexagonally packed in two-dimensions. We note that previous measurements of the diameter of both fibroblast cells and melanoma cells suggest that the cell diameter of both cell types is approximately 20 μm (Treloar *et al.* 2013; Treloar *et al.* 2014).

3.10.2 Estimating λ

Following the approach of Johnston *et al.* (2015), we note that in the central region of each monoculture experiment, where $r < 1425\,\mu$m, the cell density profile is approximately spatially uniform for all time, giving $\partial C/\partial r = 0$

locally. Therefore, in the central region of the monoculture experiments, Eq. (1) simplifies to the logistic equation:

$$\frac{d\hat{C}}{dt} = \lambda \hat{C} \left(1 - \frac{\hat{C}}{K} \right), \tag{2}$$

where we have used the $\hat{C}$ (t) notation to make it clear that we are dealing with the density of cells that is spatially averaged across the middle region of the expanding circular population, where $r < 1425$ μm. Eq. (2) has an exact solution, which can be written as:

$$\hat{C}(t) = \frac{K \hat{C}(0) e^{\lambda t}}{K + \hat{C}(0) (e^{\lambda t} - 1)}. \tag{3}$$

Therefore, if we focus on data from the central region of the monoculture experiments we can use Eq. (3) to estimate λ (Johnston *et al.* 2015). To obtain estimates of λ, we average the experimental cell density, C_{data} (r, t), across the central region, where $r < 1425$ μm to give $\hat{C}_{data}$ (t). We obtain averaged data by repeating the procedure for three experimental replicates, and averaging these results at three time points, $t = 0$, $t = 24$, and $t = 48$ hours. Using the averaged density at $t = 0$ as our initial condition, $\hat{C}(0)$, in Eq. (2), we calculate $\hat{C}(24)$ and $\hat{C}(48)$ for a range of values of λ. A measure of the discrepancy between the experimental data and the solution of the mathematical model, $E2(\lambda)$, is given by:

$$E^2(\lambda) = \left(\hat{C}_{\mathrm{data}}(24) - \hat{C}(24) \right)^2 + \left(\hat{C}_{\mathrm{data}}(48) - \hat{C}(48) \right)^2 . \qquad (4)$$

Fig. S3.1 (a) shows $E^2(\lambda_{SK})$ for SK-MEL-28 melanoma cells for a range of λ_{SK}. There is a clear minimum value of $E^2(\lambda_{SK})$, giving $\overline{\lambda}_{SK} \approx 0.04$ /hour. Fig. 1 (b) shows similar results for the fibroblast monoculture experiments, giving $\overline{\lambda}_{Fb} \approx 0.03$ /hour. Note that these estimates are obtained by first averaging the experimental data across the three experimental replicates and then minimising Eq. (4).

If we repeat this process using the experimental data from the three individual experimental replicates we can obtain a range of estimates of $\overline{\lambda}_{SK}$ and $\overline{\lambda}_{Fb}$, as shown in Table I. The advantage of working with the experiential replicates separately is that we now have a sensible way to estimate the variability in the proliferation rates by calculating the sample standard deviation. Using our estimate of the standard deviation, the variability in our estimates of the proliferation rate is $\overline{\lambda}_{SK} = 0.04 \pm 0.01$ /hour, and $\overline{\lambda}_{Fb} = 0.03 \pm 0.01$ /hour. Therefore, we conclude that the range of values of the proliferation rate is $0.03 \leq \overline{\lambda}_{SK} \leq 0.05$ /hour, and $0.02 \leq \overline{\lambda}_{Fb} \leq 0.04$ /hour.

3.10.3 Estimating D

Once we have found the best match for the proliferation rate, we can then find the best value for the diffusivity, D, in Eq. (1). We consider images of transects across the full width of the experiment, as described in the main document. Dividing the transect into subregions of width $w = 150\ \mu$m, we count the numbers of cells in each subregion to obtain a cell density for each subregion. Since the experiment is circular, we are interested in the cell density at each value of the radial coordinate, r.
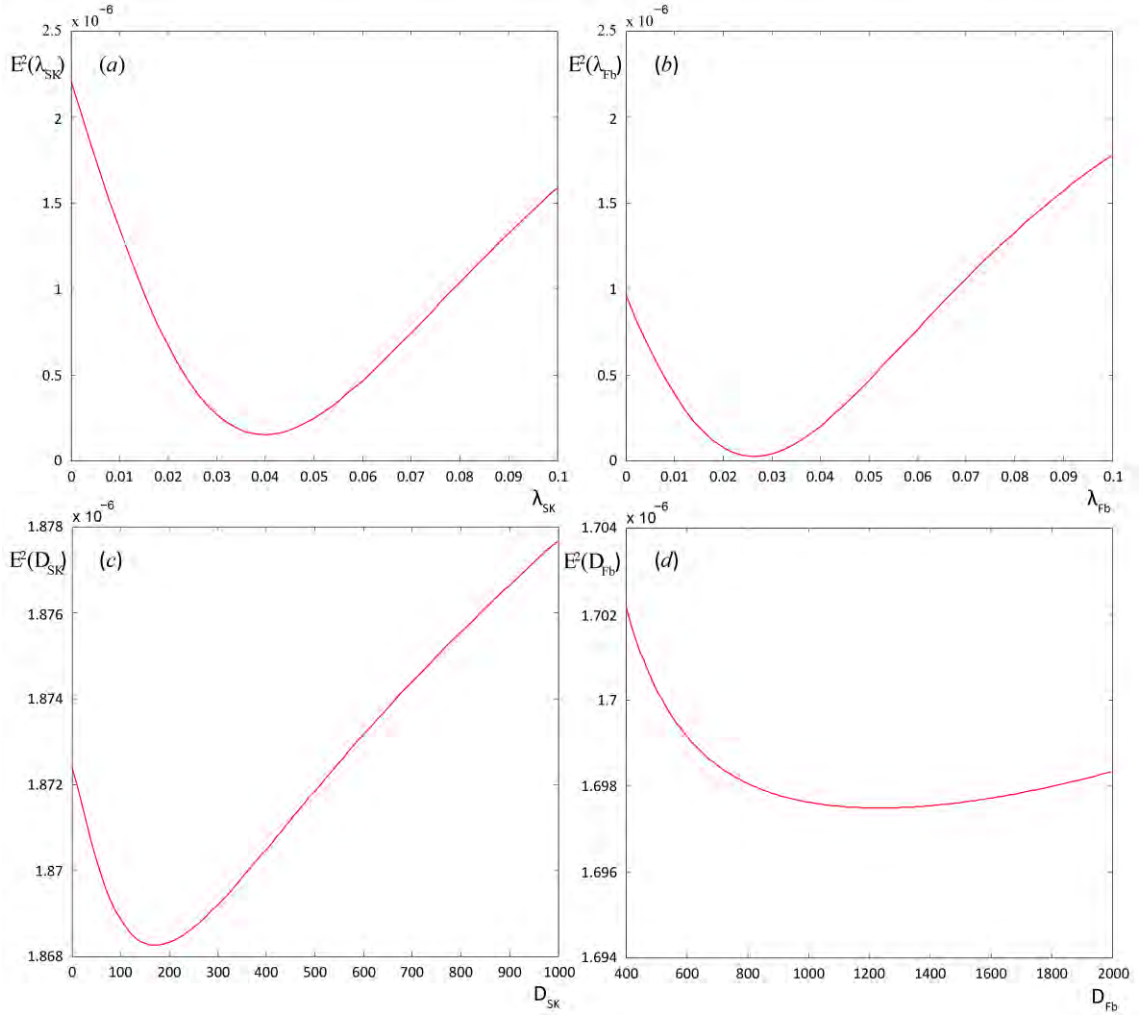
FIG. S3.1. Least-squares error between model and experimental data for (*a*) SK-MEL-28 melanoma cells for different values of λ_{SK}, (*b*) fibroblast cells for different values of λ_{Fb}, (*c*) SK-MEL-28 melanoma cells for different values of D_{SK}, and (d) fibroblast cells for different values of D_{Fb}. (*a*)–(*b*) are measured in units of /hour, while (*c*)–(*d*) are measured in units of μm^2 /hour. Note the different scales on both the horizontal and vertical axes.

Since each transect consists of two directions away from the centre of the experiment, we average the two estimates of cell density at each value of the radial coordinate, *r*, in both directions. This gives us an estimate of the cell density profile $C_{\text{data}}(r, t)$ at each value of the radial coordinate, r, in each

experimental replicate. Given these estimates from each experimental replicate, we then average the results across.

Time	Replicate	$\bar{\lambda}_{SK}$	$\bar{\lambda}_{Fb}$
	1	0.022	0.034
	2	0.016	0.008
24 hours	3	0.024	0.012
	1	0.052	0.032
	2	0.042	0.028
48 hours	3	0.054	0.028
Sample Mean		0.035	0.024
Sample Standard Deviation		0.015	0.010
Estimates using averaged data		0.040	0.026

TABLE S3.1: Estimated values for $\bar{\lambda}_{SK}$ and $\bar{\lambda}_{Fb}$ using single replicates (Rows 1–6) and averaged data (Row 9). The sample mean of the estimates from individual replicates is given in Row 7, and the sample standard deviation in Row 8. All values for $\bar{\lambda}_{SK}$ and $\bar{\lambda}_{Fb}$ are in units of /hour, and reported using two significant figures.

To estimate D we use the averaged density at $t = 0$ as our initial condition, $C(r, 0)$, in Eq. (1). Using the numerical solution, we calculate $C(r, 24)$ and $C(r, 48)$ for a range of D. An estimate of the least–squares error, $E^2(D)$, is calculated as:

$$E^2(D) = \frac{1}{N_C} \sum_{j=0}^{N_C-1} \left[(C_{\text{data}}(r, 24) - C(r, 24))^2 + (C_{\text{data}}(r, 48) - C(r, 48))^2 \right], \qquad (5)$$

where $r = jw$ is the radius if the centre of each subregion, $w = 150\,\mu$m is the subregion width, and $N_C = 30$ is the number of subregions. Estimates of $E^2(D_{SK})$, for a range of D_{SK}, are shown in Fig. S3.1(c). The minimum value of $E^2(D_{SK})$ corresponds to $\bar{D}_{SK} \approx 170\,\mu\text{m}^2$/hour, to two significant figures. Similarly, Fig. S3.1(d) shows $E^2(D_{Fb})$, for a range of D_{Fb}, giving $\bar{D}_{Fb} \approx 1200\,\mu\text{m}^2$/hour, to two significant figures.

We note that the shape of the curves in Fig. S3.1(a)-(b) are not the same as the shape of the curves in Fig. S3.1(c)-(d). In particular, the minima in Fig. S3.1(c)-(d) are not as clearly defined. However, we are still able to identify a minimum value using our averaged experimental data allowing us to provide estimates of $\bar{D}_{SK}$ and $\bar{D}_{Fb}$. Unlike our previous approach for estimating the uncertainty in the proliferation rate we are unable to apply the same approach by estimating the cell diffusivity for each experimental replicate. This is because the least-squares curves for each experimental replicate are complicated due to noise in the experimental data: we calculate the average cell density data across 19 subregions to find estimates for λ_{SK} and λ_{Fb}, but that size subregion does not provide sufficient spatial sensitivity to find estimates of $\bar{D}_{SK}$ and $\bar{D}_{Fb}$.

In summary we provide a range of estimates for the cell proliferation rates, we simply provide a point estimate of the cell diffusivities. Despite this, we note that our estimates of $\bar{D}_{SK}$ and $\bar{D}_{Fb}$ are very similar to estimates of the cell diffusivity of other metastatic melanoma cell lines (Treloar *et al*. 2013) and mouse fibroblast cells (Treloar *et al*. 2014), respectively.

3.10.4 *Quantifying the quality of match in the monoculture and co-culture assays*

In the main paper we claim that the quality of match between the experimental data and the solution of the mathematical model in the monoculture experiments is very similar to the quality of match for the co-

culture experiments. Here, we quantify the quality of match by calculating a measure of the least-squares error between the experimental data and the solution of the mathematical model for all experiments in Fig. 3.5 (main paper). The least-squares error is given by:

$$E^2(t) = \frac{1}{N_C} \sum_{j=0}^{N_C-1} (S_{\text{data}}(r, t) - S(r, t))^2,$$ (6)

where $r = jw$ is the radius of the centre of each subregion, $w = 150\,\mu$m is the subregion width, and $NC = 30$ is the number of subregions. Results in Table II shows the estimates of $E^2(t)$ for all results in Fig. 3.5. These results show that the quality of the match for the monoculture experiments at $t = 24$ hours, is practically indistinguishable from the quality of match for the three co-culture experiments. At $t = 48$ hours we see that the quality of match for the Fb monoculture experiments is practically indistinguishable from the quality of match for the three co-culture experiments. The quality of match for the SK monoculture experiments at $t = 48$ hours is less than the other experiments, but this match remains reasonable given the level of variability we observe amongst our experimental replicates.

	$E2(24)$	$E2(48)$
Fb monoculture	2.25×10^{-8}	3.22×10^{-8}
Co-culture 1	2.37×10^{-8}	3.38×10^{-8}
Co-culture 2	1.21×10^{-8}	8.11×10^{-8}
Co-culture 3	3.38×10^{-8}	9.87×10^{-9}
SK monoculture	1.12×10^{-8}	1.49×10^{-7}

TABLE S3.2: Least-squares error, $E2(t)$, for $t = 24$ hours and $t = 48$ hours, both monocultures and all three co-cultures. $E2(t)$ is defined in Eq. (6). In all cases, the parameter values are $\bar{\lambda}_{Fb} = 0.03$ /hour, $\bar{\lambda}_{SK} = 0.03$ /hour, $\bar{D}_{Fb} \approx 1200$ μm2/hour, and $\bar{D}_{SK} \approx 170$ μm2/hour.

Chapter 4: Quantitative comparison of the spreading and invasion of radial growth phase and metastatic melanoma cells in a three-dimensional human skin equivalent model

Statement of Contribution of Co-Authors
for Thesis by Published Paper

The following is the suggested format for the required declaration provided at the start of any thesis chapter which includes a co-authored publication.
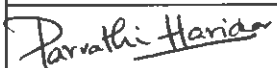
The authors listed below have certified that:

11. they meet the criteria for authorship in that they have participated in the conception, execution, or interpretation, of at least that part of the publication in their field of expertise;
12. they take public responsibility for their part of the publication, except for the responsible author who accepts overall responsibility for the publication;
13. there are no other authors of the publication according to these criteria;
14. potential conflicts of interest have been disclosed to (a) granting bodies, (b) the editor or publisher of journals or other publications, and (c) the head of the responsible academic unit, and
15. they agree to the use of the publication in the student's thesis and its publication on the QUT's ePrints site consistent with any limitations set by publisher requirements.

In the case of this chapter:

Haridas P, McGovern JA, McElwain DLS, Simpson MJ. (2017). Quantitative comparison of the spreading and invasion of radial growth phase and metastatic melanoma cells in a three-dimensional human skin equivalent model. *PeerJ*. 5: e3754

Published online 5 September 2017.

Contributor	Statement of contribution*
Parvathi Haridas *Parvathi Haridas* 29/05/2017	Designed experiments, performed all the laboratory experiments, analysed data, wrote the manuscript, prepared figures and/tables and reviewed drafts of the manuscript
Jacqui A. McGovern *signature*	Designed experiments, reviewed analysed data and reviewed drafts of the manuscript
D. L. Sean McElwain	Designed experiments, reviewed analysed data and reviewed drafts of the manuscript
Matthew J. Simpson	Designed experiments, reviewed analysed data and reviewed drafts of the manuscript

Principal Supervisor Confirmation

I have sighted email or other correspondence from all Co-authors confirming their certifying authorship.
(If the Co-authors are not able to sign the form please forward their email or other correspondence confirming the certifying authorship to the RSC).

Matthew J Simpson   *M Simpson*   10 | 11 | 2017

Name _____   Signature _____   Date _____

4.1 ABSTRACT

Background: Standard two-dimensional (2D) cell migration assays do not provide information about vertical invasion processes, which are critical for melanoma progression. We provide information about three-dimensional (3D) melanoma cell migration, proliferation and invasion in a 3D melanoma skin equivalent (MSE) model. In particular, we pay careful attention to compare the structure of the tissues in the MSE with similarly-prepared 3D human skin equivalent (HSE) models. The HSE model is identically prepared to the MSE model except that melanoma cells are omitted. Using the MSE model, we examine melanoma migration, proliferation and invasion from two different human melanoma cell lines. One cell line, WM35, is associated with the early phase of the disease where spreading is thought to be confined to the epidermis. The other cell line, SK-MEL-28, is associated with the later phase of the disease where spreading into the dermis is expected.

Methods: 3D MSE and HSE models are constructed using human de-epidermised dermis (DED) prepared from skin tissue. Primary fibroblasts and primary keratinocytes are used in the MSE and HSE models to ensure the formation of a stratified epidermis, with a well-defined basement membrane. Radial spreading of cells across the surface of the HSE and MSE models is observed. Vertical invasion of melanoma cells downward through the skin is also observed and measured using immunohistochemistry. All measurements of invasion are made at day 0, 9, 15 and 20, providing detailed time course data.

Results: Both HSE and MSE models are similar to native skin *in vivo*, with a well-defined stratification of the epidermis that is separated from the dermis by a basement membrane. In the HSE and MSE we find fibroblast cells confined to the dermis, and differentiated keratinocytes in the epidermis. In the MSE, melanoma cells form colonies in the epidermis during the early part of the experiment. In the later stage of the experiment, the melanoma cells in the MSE invade deeper into the tissues. Interestingly, both the WM35 and SK-MEL-28 melanoma cells eventually enter the dermis. However, these two cell lines invade at different rates, with the SK-MEL-28 melanoma cells invading faster than the WM35 cells.

Discussion: The MSE and HSE models are a reliable platform for studying melanoma invasion in a 3D tissue that is similar to native human skin. Interestingly, we find that the WM35 cell line, that is thought to be associated with radial spreading only, is able to invade into the dermis. The vertical invasion of melanoma cells into the dermal region appears to be associated with a localised disruption of the basement membrane. Presenting our results in terms of time course data, along with images and quantitative measurements of the depth of invasion extends previous 3D work that has often been reported without these details.

4.2   INTRODUCTION

Melanoma is a deadly form of skin cancer (Bertolotto, 2013; Weinstein *et al*., 2014) that is caused by the malignant transformation of melanocytes in the skin (Uong & Zon, 2010; Bertolotto, 2013; Liu, Peng & Tobin, 2013). Melanoma accounts for less than 10% of all skin cancers, however it is associated with 80% of skin cancer related deaths (Bandarchi *et al*., 2010; Bertolotto, 2013; Ramaraj & Cox, 2014; Leight *et al*., 2015; McCusker *et al*., 2017; Rivas *et al*., 2017). The early stage of a primary melanoma, where cancer cells are generally confined to the epidermis, is known as the radial growth phase (RGP) (Clark, 1991; Meier *et al*., 2000). Melanoma in the RGP is curable through surgical removal (Weinstock, 2000; Cummins *et al*., 2006). However, survival rates of patients with melanoma at a more advanced stage, where cancer cells have invaded vertically into the dermis, known as the vertical growth phase (VGP), is between 53-97 %. The five-year survival time for VGP melanoma depends on the stage of the disease. In comparison with VGP melanoma, survival rates of patients with metastatic melanoma, where cancer cells have moved into the blood stream and away from the primary location is between 15-75 %, depending on the stage of melanoma (Miller & Mihm, 2006; Sandru *et al*., 2014). The switch in progression, from radial spreading to vertical invasion is poorly understood (Hussein, 2004; Baruthio, Quadroni & Ruegg, 2008; Grahovac, Becker & Wells, 2013). Some cell lines are thought to be associated with the RGP (Bani *et al*., 1996; Cummins *et al*., 2006), whereas other cell lines are associated with more advanced stages of the disease (Fofaria & Srivastava, 2014; Tiwary *et al*., 2014). Thus, quantitative measurements of spreading and invasion of both RGP and metastatic cell lines in a 3D human skin model could help improve our understanding of melanoma progression, and the characteristics of both radial and vertical spreading.

Previous studies about the spreading of melanoma have focused on examining the spatial extent of population expansion, cell migration, cell proliferation, cell-to-cell adhesion and protein-expression on two-dimensional (2D) surfaces (Alexaki *et al*., 2010; Simpson *et al*., 2013; Treloar *et al*., 2014). These 2D studies are straightforward to perform and cost effective (Beaumont, Mohana-Kumaran & Haass, 2014; Johnston, Simpson & McElwain, 2014; Binny *et al*., 2016). Moreover,

2D models can be used for preliminary co-culture investigations to examine potential interactions between different cell types (Beaumont, Mohana-Kumaran & Haass, 2014; Haridas *et al*., 2017). This flexibility is very important for melanoma research as co-culture assays are more realistic than monoculture assays since co-cultures allow melanoma cells to interact dynamically with other relevant cells, such as fibroblasts and keratinocytes (Gaggioli & Sahai, 2007; Li, Fan & Houghton, 2007; Beaumont, Mohana-Kumaran & Haass, 2014; Sriram & Bigliardi-Qi, 2015).

Traditional 2D assays do not recreate a physiological environment similar to native human skin *in vivo* (Beaumont, Mohana-Kumaran & Haass, 2014). Perhaps the most obvious limitation of 2D experiments is that they cannot be used to quantify vertical invasion (Van-Kilsdonk *et al*., 2010; Vorsmann *et al*., 2013; Kramer *et al*., 2013; Taloni *et al*., 2014). To improve our understanding of the differences between radial and vertical invasion, it is of interest to make time course observations and measurements of the spreading and invasion of melanoma in a three-dimensional (3D) skin model (Brandner & Haass, 2013). Experimental studies focusing on melanoma spreading and invasion in 3D skin-based models have been described over the last 20 years. Table 4.1 compares key properties of some previous 3D skin-models using de-epidermised dermis (DED) to study melanoma progression and invasion. While other previous 3D models have been used, such as collagen-based models (Vorsmann *et al*., 2013), the brief review in Table 4.1 is restricted to those previous studies explicitly using 3D-DED models.

Previous Studies	Melanoma cell lines included			Comparison of MSE and HSE structure		Basement membrane marker	Proliferation marker	Migration marker	Melanoma marker	Measurements of invasion depth	Time course images
	RGP	VGP	Metastatic	Kc	Fb						
Bechetoille *et al.*, 2000	no	no	yes	yes	no	yes	no	yes	yes	no	no
Eves *et al.*, 2000	no	no	yes	yes	yes	yes	no	no	yes	no	no
Dekker *et al.*, 2000	yes	yes	yes	yes	no	yes	no	no	yes	no	no
Mac Neil *et al.*, 2000	no	no	yes	yes	yes	yes	no	no	yes	no	no
Eves *et al.*, 2003a	no	no	yes	yes	yes	yes	no	no	yes	yes	no
Eves *et al.*, 2003b	no	no	yes	yes	yes	yes	no	no	yes	yes	no
Dennhofer *et al.*, 2003	no	no	yes	no	no	no	no	no	yes	no	no
Marck *et al.*, 2005	no	no	yes	yes	yes	yes	no	no	yes	yes	no
Van-Kilsdonk *et al.*, 2008	no	no	yes	yes	no	yes	no	no	yes	no	no
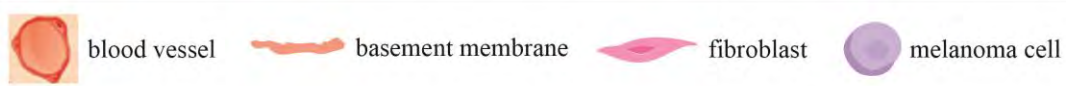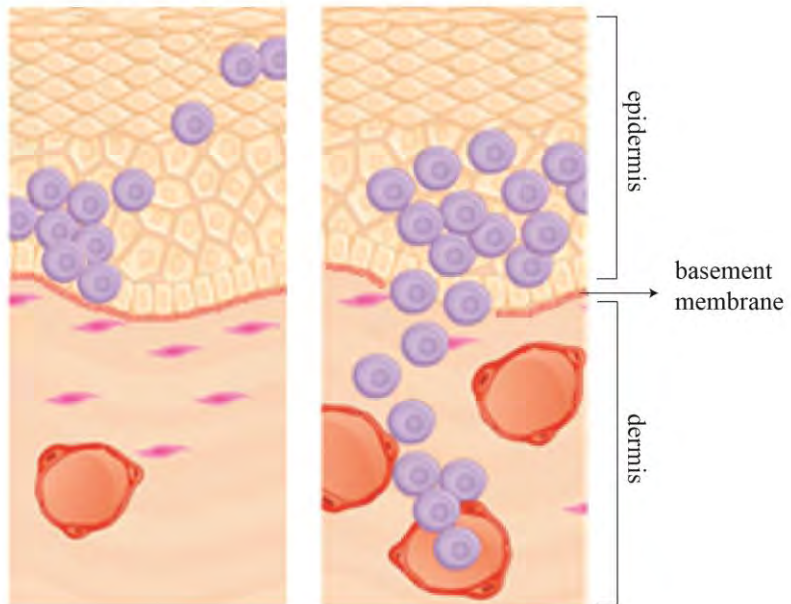
Yang, Sule-Suso & Sockalingum, 2008	no	no	yes	yes	yes	yes	no	no	yes	no	no
Van-Kilsdonk *et al*., 2010	no	no	yes	yes	no	yes	no	no	yes	no	no
Marques & Mac Neil, 2016	no	no	yes	yes	yes	yes	no	no	yes	yes	no
Current study	yes	yes	yes	yes	yes	yes	yes	yes	yes	yes	yes

Table 4.1: Key features of previous 3D-DED melanoma skin model studies. Key properties of previous studies using 3D-DED to establish HSE and MSE models. Kc indicates primary keratinocyte cells, and Fb indicates primary fibroblast cells.

There has been extensive research focusing on 3D melanoma migration and spreading using cell lines that are associated with the metastatic phase of melanoma progression (Damsky, Rosenbaum & Bosenberg, 2010; Finn, Markovic & Joseph, 2012; Tiwary *et al*., 2014). However, in this work we are also interested in the differences between: (i) radial migration, where melanoma cells are confined to the epidermis and associated with the early phase of melanoma progression; and (ii) vertical invasion that is associated with more advanced melanoma progression. Therefore, we quantitatively compare the vertical invasive properties of two melanoma cell lines in a 3D skin model as a function of time. In particular, we compare results from one cell line that is associated with the early RGP stage of melanoma progression with results from another cell line that is linked with a more advanced, metastatic stage of the disease. A schematic illustrating the key differences between RGP and metastatic stages of the disease are given in Fig. 4.1(*a*).
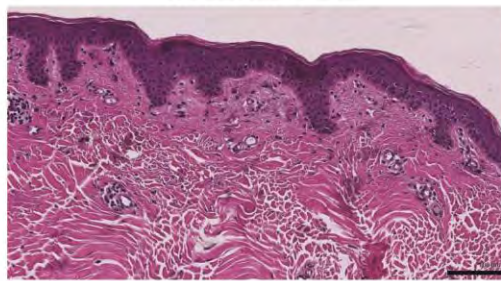
Radial growth phase   Metastatic phase

epidermis

basement
membrane

dermis

blood vessel   basement membrane   fibroblast   melanoma cell

(b)   (c)
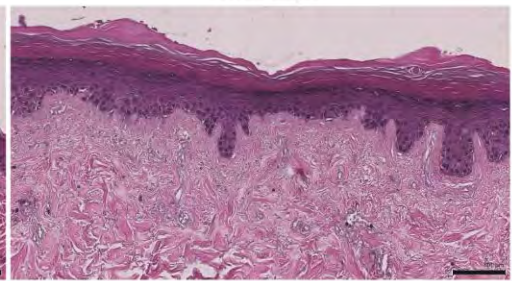
Human native skin   HSE: day 9

epidermis

dermis

Figure 4.1: Three-dimensional representation of melanoma progression. (*a*) Schematic representation of the RGP phase, associated with melanoma cells in the epidermal region only and the metastatic phase, associated with melanoma cells that move away from the primary site. The cells in the metastatic phase are able to cross the basement membrane, enter the dermis and move into the blood vessels. This illustration is adapted, with permission, from Zaidi, Day & Merlino, (2008). (*b*) and

(*c*) H&E staining of native human skin and HSE respectively, showing a well-defined epidermis and dermis. The scale bar corresponds to 100 μm.

VGP melanoma is an intermediate phase of the disease that is thought to be less aggressive than the metastatic phase (Hsu *et al*., 1998; Meier *et al*., 2000; Satyamoorthy *et al*., 2007). However, as RGP melanoma is generally thought to be confined to the epidermis, we think that the VGP phase is more aggressive than RGP. Therefore, in this study we compare RGP and metastatic cell lines only since we aim to investigate the differences between these phases and it is reasonable to assume that these differences will be more obvious by comparing the invasion of cells that are thought to be associated with the most aggressive phase of the disease with cells that are thought to be associated with a less aggressive phase of the disease. In addition, we anticipate that a cell line associated with the VGP would produce results that are intermediate between the RGP and metastatic results.

Overall, we hypothesise that our MSE model recreates both the spatial and temporal distribution of melanoma cells as observed in native human skin *in vivo*. Our approach is novel because this study extends previous 3D melanoma studies summarised in Table 4.1, as we compare results from RGP and metastatic cell lines, providing quantitative measurements of melanoma cell invasion in a time course.

Previous studies demonstrate particular protocols of DED to construct human skin equivalent (HSE) models (Xie *et al*., 2010; Fernandez *et al*., 2014; McGovern *et al*., 2016). These 3D skin models are established *in vitro* and resemble native human skin *in vivo* as shown in Figs. 4.1*b* and 1*c*. One of our aims in this study is to adapt this skin model and introduce melanoma cells to establish a sustainable melanoma skin equivalent (MSE) model and recreate the different stages of melanoma progression. The other primary aim is to make quantitative measurements of the depth of melanoma invasion as a function of time, and to use these measurements to examine differences between the two cell lines that we consider.

Two melanoma cell lines, WM35 (RGP) (Herlyn, 1990) and SK-MEL-28 (metastatic phase) (Carey *et al*., 1976) are grown in the MSE model over a period of 9, 15 and 20

days. We identify differences in behavior between the two cell lines, and in particular we quantify the vertical invasion of melanoma cells into the dermis over time. The conclusions facilitate an improved characterisation of MSE models, and the progression of RGP and metastatic phases of melanoma in realistic 3D environments, thereby extending previous 2D studies.

4.3 EXPERIMENTAL METHODS

4.3.1 Keratinocyte isolation and culture

Queensland University of Technology (QUT) human research ethics provides written approval for the skin samples to be used in this study (approval number: QUT HREC #1300000063; UnitingCare Health 2003/46). The samples come from patients undergoing abdominoplasty surgery and breast reduction surgery (Xie *et al*., 2010). Human keratinocyte cells are isolated from skin and cultured in full Green's medium following protocols described in Rheinwald & Green (1975), Dawson *et al*. (2006) and by Haridas *et al*. (2016). Primary keratinocyte cells are cultured at 37 °C, in 5% CO_2 and 95% air.

4.3.2 Fibroblast isolation and culture

Human fibroblast cells are isolated following protocols in Haridas *et al*. (2017). Primary fibroblast cells are cultured at 37 °C, in 5% CO_2 and 95% air.
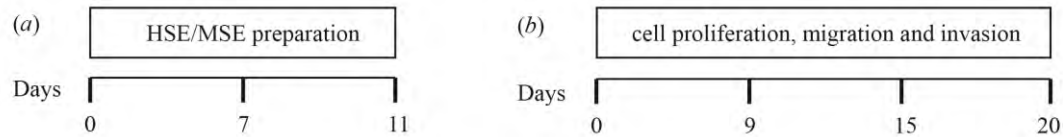
4.3.3 Melanoma cell culture

The human melanoma cell lines, WM35 and SK-MEL-28 are cultured as described in Haridas *et al*. (2016). WM35 melanoma cells are kindly donated by Professor Nikolas Haass (University of Queensland Diamantina Institute) and SK-MEL-28 melanoma cells are donated by Professor Brian Gabrielli (Mater Research Institute-University of Queensland). Cells are cultured at 37 °C, in 5% CO_2 and 95% air.

Both melanoma cell lines, WM35 and SK-MEL-28, are validated using short tandem repeat profiling (Cell Bank, Australia. January 2015). This means that the cell lines that we use are identical to the reference samples held in Cell Bank.

4.3.4   Establishing HSE and MSE

HSE models are established using the skin collected from donors undergoing elective plastic surgery. The protocol for establishing the HSE model is given in Figs. 2*a*-2*f*. These protocols are adapted from previous work (Fernandez *et al*., 2014; McGovern *et al*., 2016). The DED is prepared following protocols described by Chakrabarty *et al*. (1999) and Dawson *et al*. (2006). In brief, to construct the HSE model, sterile stainless steel rings (Aix Scientifics, Germany) with a diameter of 6 mm are placed on the papillary side of the DEDs in a 24 well tissue culture plate (Nunc®, Australia). Primary keratinocyte cells ($2x10^4$) and primary fibroblast cells ($1x10^4$) are seeded onto the DEDs in full Green's medium and incubated at 37 º C, in 5% CO_2 and 95% air for 2 days. Subsequently, the DEDs with cells, from now onwards referred to as HSE, is submerged in full Green's medium for 2 days. These HSEs are then cultured at an air-liquid interface on sterile stainless steel grids with full Green's medium for 9, 15 and 20 days. HSE is also collected at day 0, just before the DED is lifted to the air-liquid interface, as a reference sample.

Figure 4.2: HSE and MSE preparation.(*a*) Time frame for cell culture and DED preparation to construct HSE and MSE models. (*b*) Time intervals at which the HSE and MSE models are cultured and inspected. (*c*) Schematic of the circular barrier assay showing how cells are placed inside the barrier on a DED within a 24-well tissue culture plate. (*d*) DED with cells submerged in full Green's medium. (*e*)-(*f*) Schematic and image of the HSE and/or MSE models lifted to the air-liquid interface

on a sterile stainless steel grid with full Green's medium placed in a 6-well plate. Scale in (*f*) bar corresponds to 6 mm.

To construct the MSE models, we follow the same protocol for the HSE model, and include melanoma cells, WM35 ($5x10^3$) or SK-MEL-28 ($5x10^3$), in addition to primary keratinocyte ($2x10^4$) and primary fibroblast ($1x10^4$) cells on the individual DEDs. This protocol of adding all the cells together on DEDs is standard in all the previous DED studies summarised in Table 1. Experimental variability is assessed using triplicates for each cell line, and primary skin cells from three separate donors. This means that for each time point in our experiments we perform nine replicates, which accounts for biological and experimental variability. HSEs and MSEs are collected after day 0, 9, 15, and 20, and subjected to histological investigation.

4.3.5   MTT Assay

An MTT (3-(4,5-dimethylthiazol-2-yl)-2,5-diphenyltetrazolium bromide) (Thermo Scientific) assay is performed to check the viability of cells in the HSE and MSE models. HSE and MSEs collected on day 0, 9, 15 and 20 are submerged in 0.5 mg/ml w/v MTT solution and incubated at 37 $^{\circ}$ C, in 5% CO_2 and 95% air for 90 minutes. The metabolically active cells cleave the tetrazolium salt into an insoluble purple formazan dye. The purple colour indicates metabolically active cells on the HSE and MSE models and these are imaged using a stereo microscope (Nikon SMZ 800) fitted with a Nikon digital camera.

4.3.6   Histological Analysis

Haemotoxylin and eosin (H&E) staining is used to characterise the tissue structure in the HSE and MSE models. MTT stained HSE and MSEs are fixed using 10% neutral buffered formalin (United Biosciences, Australia), processed in an automated vacuum tissue processor (Thermo Scientific, USA) and embedded in paraffin wax. All samples are sectioned to 5 µm thickness using a microtome (Leica RM2245, Leica Microsystems, Australia). All HSE and MSE samples are first visually examined to see the spatial extent of the MTT positive region. Then, each sample is

divided using a sterile blade, through the centre of the MTT positive region. The two smaller samples of tissue are each embedded in paraffin wax. These smaller samples are then further sectioned into 5 µm thick tissue sections using a microtome. This procedure allows us to explore the depth of vertical invasion that is close to the centre of where the population of cells is initially placed in a circular barrier onto the DED. Furthermore, by examining the depth of vertical invasion in the various 5 µm thick sections, we can examine whether the depth of vertical invasion depends on the lateral position. In summary, we find that the patterns of vertical invasion appear to be independent of the lateral position. Overall, in each experiment, we examine approximately 80 to 120 sections that are 5 µm in thickness. This means that we examine the vertical invasion of melanoma cells within a region extending from the centre of the initial population to approximately 400 to 600 µm away from that centre.

Sections are first deparaffinised in 100% xylene and rehydrated in graded ethanol series of 100%, 90% and 70%, and followed by distilled water. These sections are incubated in Harris haematoxylin (HD Scientific, Australia) followed by differentiation with 1% acid alcohol, bluing with Scott's tap water solution and counterstaining with alcoholic eosin (HD Scientific). H&E stained sections are dehydrated in 90% and 100% ethanol, cleared with 100% xylene and mounted on coverslips using Pertex® mounting medium (Medite, Germany). All stained sections are imaged using an Olympus BX41 microscope fitted with an Olympus digital camera (Micropublisher, 3.3RTV, QImaging; Olympus, Q-Imaging, Tokyo, Japan).

4.3.7 Immunohistochemistry

Immunohistochemistry is performed on the paraffin-embedded (5 µm) sections. Paraffin embedded sections are deparaffinised and rehydrated as previously described in McGovern *et al*. (2013). HSE and MSE skin sections are subjected to heat-mediated antigen retrieval treatment using either sodium citrate buffer (pH 6.0) or EDTA buffer (pH 8.0) in a decloaking chamber (Biocare Medical, USA) as described in Table 2. All skin sections are washed in phosphate buffered saline followed by immunostaining using MACH 4™ Universal HRP polymer kit (Biocare Medical).

The temperature and time varies for each marker, as outlined in Table 2. The primary antibody for each protein is diluted in DaVinci Green diluent (Biocare Medical) to concentrations specified in Table 2, and these sections are incubated with the primary antibody for the time specified in Table 2. All the sections are finally counterstained using Gill's haematoxylin (HD Scientific), dehydrated, mounted and imaged as described in 'Histological Analysis'.

	Primary Antibody				Antigen Retrieval Method	
Antibody	Antibody type	Source	Dilution	Time and temperature	Buffer	Time and temperature
Collagen IV (Col IV)	Mouse	DKSH, Australia	1:50	1 hour, 37 °C	Sodium Citrate (pH6.0)	20 minutes, 80 °C
Ki-67	Mouse	Sigma Aldrich, Australia	1:100	1 hour, 37 °C	EDTA (pH8.0)	30 minutes, 90 °C
Loricrin	Rabbit	Dako, Australia	1:100	1 hour, 37 °C	EDTA (pH8.0)	5 minutes, 97 °C
S100	Rabbit	Dako, Australia	1:3000	1 hour, 37 °C	Sodium Citrate (pH6.0)	5 minutes, 95 °C
Vimentin	Rabbit	Thermo Scientific, Australia	1:800	12 – 24 hours, 4 °C	Sodium Citrate (pH8.0)	20 minutes, 80 °C

Table 4.2: Primary antibody protocols. Details of the primary antibodies and the antigen retrieval method used to detect the basement membrane (Col IV); terminal epidermal differentiation (Loricrin); migration (Vimentin); proliferation (Ki-67); and invasion (S100).

4.3.8 Image Analysis

We use ImageJ (Treloar & Simpson, 2013; Johnston, Simpson & McElwain, 2014; ImageJ, 2017) to measure the depth of melanoma cell invasion into the dermal region on the MSE models at different time points. The depth of melanoma invasion is taken to be the distance from the epidermal-dermal interface to the deepest region invaded by the melanoma cells, as shown in Figs. S4.1A-S4.1C.

4.4   RESULTS AND DISCUSSION

4.4.1   MTT assay of HSE and MSE

We first outline the MTT assay performed on both the HSE and MSE models. Results of the MTT assay, shown in Fig. 3, reveal radial expansion of the populations of cells on the HSE and MSE models over time. The purple colour on these images shows viable cells migrating radially away from the central region where the cells were originally located at day 0, as in Figs. 4.3*a*, 4.3*c* and 4.3*e*. By day 9, the cells have migrated radially to reach to the edge of the DED, as in Figs. 4.3*b*, 4.3*d* and 3*f*. This means that the population of cells in the HSE and MSE have spread radially, at least a distance of approximately 6 to 7 mm, over a period of 9 days as the purple colouration reaches the edge of the tissue. Consistent with this, we see that there are viable cells distributed right across the DED in both the HSE and MSE models after longer periods of time, shown in Fig. S4.2.
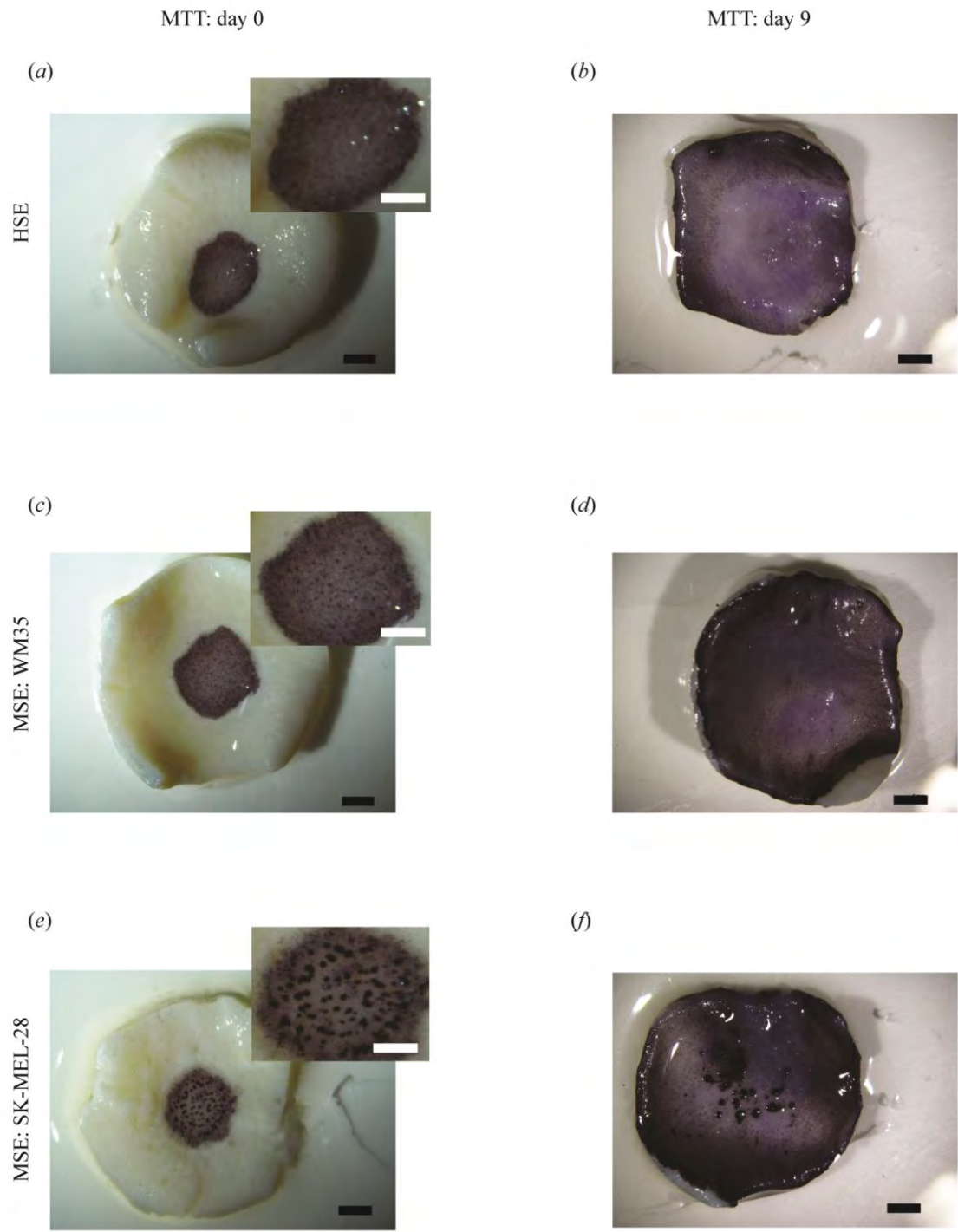
**Figure 4.3: MTT assay.** Experimental images of the MTT assay shows viable cells (purple) on the HSE (*a*)-(*b*). The MSE with WM35 melanoma cells is shown in (*c*)-(*d*). The MSE with SK-MEL-28 melanoma cells is shown in (*e*)-(*f*). Results in the left column are at day 0, and results in the right column are at day 9. The magnified central region of the HSE and MSE with melanoma cell colonies is shown in the

insets in (*a*), (*c*) and (*e*). Scale bars in the main image show 1 mm, whereas the scale bars in the insets show 3 mm.

An interesting result detected by the MTT assay is the formation of visually prominent colonies of cells in the central region of the MSE for the SK-MEL-28 cell line at day 0, as shown in the inset of Fig. 4.3*e* and also at day 9, as shown in Fig. 4.3*f*. Similarly, we also observe visually prominent colonies of cells in the central region of the MSE for the WM35 cell line at day 0, as shown in Fig. 4.3*c*. Previous 3D skin models of melanoma progression also report the formation of visually-distinct colonies of cells on the surface of the DED, and these colonies are presumably composed of melanoma cells (Dekker *et al*., 2000; Eves *et al*., 2000). Interestingly, we see that these distinct colonies of cells are no longer observed at day 15 or day 20 on the MSE with the SK-MEL-28 cell line, Fig. S2. Similarly, these distinct colonies of cells are no longer observed by day 9, 15 or 20 on the MSE with the WM35 cell line, Fig. 4.3*d* and Fig. S4.2. Since melanoma cells are thought to grow in colonies (Schwartz *et al*., 2008; Baraldi *et al*., 2013), a possible explanation for our observations is that the visually distinct dark purple colonies in the early period of the experiment could be groups of melanoma cells. As these colonies are not observed at later times, it is possible that these cells might have invaded deeper into the tissue, and are no longer present on the upper surface of the MSE. To confirm this conjecture, we now examine the distribution of different cell types within the HSE and MSE models. To do this we use histological analysis.

4.4.2 The HSE and MSE physiology resembles native human skin in vivo

The next aim in our study is to examine the tissue structure of the HSE and MSE models, and to compare the structure of the tissue in these models with the structure of native human skin *in vivo*. To investigate this, we perform histological analysis and describe our results in this section, Section 4.3.3. However, we also use immunohistochemistry to examine the spatial and temporal distribution of markers for cell migration, cell proliferation and cell invasion in Section 4.3.4. Since the main focus of this work is about cell migration, cell proliferation and cell invasion, we

choose to present all histological analysis about tissue structure in the Supplemental Information. However, we briefly describe the key points here.

Cross-sections through the HSE and MSE models are generated for H&E staining. Results at day 9, 15 and 20, showing HSE and MSE cross-sections, reveal morphological similarities to native human skin *in vivo*. In particular, we see the formation of distinct epidermal and dermal regions, Figs. S4.3B-S4.3D, Figs. S4.4B-S4.4D and Figs. S4.5B-S4.5D. These images show that keratinocytes stratify into well-defined layers: stratum basale; stratum granulosum; stratum spinosum; and stratum corneum, which are a characteristic of native human skin (Wikramanayake, Stojadinovic & Tomic-Canic, 2014) as shown in Figs. 1*b* and 1*c*, Figs. S4.3A-S4.3D, Figs. S4.4A-S4.4D and Figs. S4.5A-S4.5D. However, H&E staining in Fig. S4.3A, Fig. S4.4A and Fig. S4.5A, of HSE and MSE cross-sections at day 0, are consistent with the early stages of epidermal and dermal formation, which then matures with time. In summary, we observe mature stratification after 9 days, and this is consistent with previous investigations (Topping *et al*., 2006).

The basement membrane separates the epidermal and dermal compartments, and is a prominent feature of native human skin *in vivo* (Marinkovich *et al*., 1993; Golan *et al*., 2015). The basement membrane is particularly important in the context of melanoma progression because melanoma confined to the epidermal compartment can be successfully treated by surgical removal, whereas the prognosis for melanoma that has spread into the dermis is poor (Weinstock, 2000; Cummins *et al*., 2006; Bertolotto, 2013; Sandru *et al*., 2014). The positive immunohistological staining is obtained using the marker collagen IV (Col IV). Immunohistological examinations of the HSE and MSE cross-sections show positive staining of the basement membrane at day 9, 15 and 20, as shown in Figs. S4.3F-S4.3H, Figs. S4.4F-S4.4H and Figs. S4.5F-S4.5H. However, all cross-sections of the skin models at day 0 show minimal positive staining. This is consistent with the initial development of the basement membrane, as highlighted by the arrows in Fig. S4.3E, Fig. S4.4E and Fig. S4.5E.

We observe a weakly stained, mostly-continuous basement membrane in skin models constructed using WM35 cell lines at day 9, as shown in Fig S4.4F. Conversely, only intermittent Col IV staining is present in the MSE models with WM35 cells at day 15 and 20, as shown in Figs. S4.4G-S4.4H. Similarly, we observe intermittent Col IV staining in the MSE models with SK-MEL-28 cells at day 9, 15 and 20, as shown in Figs. S4.5F-S4.5H. Although the Col IV staining is relatively weak in these images compared to other staining results, we hypothesise that the Col IV staining results could be caused by melanoma cells disrupting the basement membrane and invading into the dermal region. Metastatic melanoma cells in particular are associated with dermal invasion *in vivo* by disturbing the basement membrane (Golan *et al*., 2015; Sandri *et al*., 2016). Therefore, this result further suggests that the MSE models recapitulates certain *in vivo* stages of melanoma progression *in vitro*.

Lastly, positive staining of the terminally differentiating epidermis confirms that both the HSE and MSE models constructed *in vitro* are similar to native human skin *in vivo*. The marker loricrin identifies terminally differentiating cells in the epidermis (Nithya, Radhika & Jeddy, 2015). Therefore, loricrin staining of HSE and MSE cross-sections, as shown in Figs. S4.3J-S4.3L, Figs. S4.4J-S4.4L and Figs. S4.5J-S4.5L, at day 9, 15 and 20, suggest that the epidermal structure in the HSE and MSE models is consistent with native human skin. However, results at day 0 from cross-sections of HSE and MSE models, shown in Fig. S4.3I, Fig. S4.4I and Fig. S4.5I, do not have any positive loricrin staining. Loricrin is known to be absent on non-stratified epithelium (Nithya, Radhika & Jeddy, 2015). Hence, the negative result at day 0 is probably due to the absence of the stratum corneum on day 0, which is consistent with an immature epidermis.

In summary, the loricrin staining suggests that the physiology of the HSE and MSE models is consistent with native skin. Furthermore, our findings show that HSE models have well-defined stratified epidermal and dermal regions that are separated by a basement membrane. This confirms that the *in vitro* HSE model is consistent with native human skin *in vivo*. In contrast, the MSE models do not always have a well-defined basement membrane. At early times in the experiments we see that the basement membrane is formed and present in the MSE model. However, at later

times, the basement membrane in the MSE model is partially absent. These differences between the MSE and HSE models suggest that the presence of melanoma cells in the MSE models might lead to disruptions in the basement membrane. Furthermore, we hypothesise that this disruption is associated with vertical invasion.

4.4.3   Proliferation, migration and invasion of melanoma cells on the MSE model

Certain key features of cancer progression, including melanoma, are thought to be the proliferation, migration and invasion of cancer cells (Hanahan & Weinberg, 2000). Therefore, we aim to explore the spatial and temporal distributions of these features in the HSE and MSE models. In particular, we use specific markers for cell migration, cell proliferation and cell invasion in our 3D models.

The MTT assay provides information about the radial spreading of cells across the MSE model. In addition to radial spreading, we also aim to observe and quantify the vertical invasion of melanoma cells, and in particular we wish to focus on cell lines that are associated with both the early and later stages of melanoma progression. RGP melanoma is generally associated with melanoma cells confined to the epidermal region of the skin (Clark, 1991; Meier *et al*., 2000). Previous experimental studies demonstrate that cells from the RGP are restricted above the intact basement membrane (Dekker *et al*., 2000; Meier *et al*., 2000). Hence we use WM35 melanoma cell lines that are derived from the RGP as this cell line represents the early phase of melanoma. VGP melanoma is associated with cells that enter and proliferate in the dermal region of the skin (Clark, 1991; Hsu *et al*., 1998; Zaidi, Day & Merlino *et al*., 2008). Cells from the VGP are thought to cross the basement membrane from the epidermis into the dermis (Hsu *et al*., 1998; Beaumont, Mohana-Kumaran & Haass, 2014). Additionally, metastatic melanoma cells not only invades into the dermis, but also have the ability to enter the blood stream and can therefore move far away from the primary site, to distant tissues (Clark, 1991; Zaidi, Day & Merlino *et al*., 2008). Cells derived from the metastatic phase are generally thought to be far more aggressive than cells from either the RGP or the VGP (Satyamoorthy *et al*., 2007). To examine these differences in our study we choose to focus on two cell lines: the

WM35 cell line is associated with the RGP, which is thought to be the less aggressive phase of melanoma; the other cell line that we examine is the SK-MEL-28 cell line, which is from the metastatic phase of melanoma, and is thought to be the more aggressive.

To make this comparison we examine data from the MSE with the WM35 melanoma cell line in Fig. 4.4, with results using the SK-MEL-28 cell line in Fig.4.5. Immunohistochemistry results in Fig. 4.4 and Fig. 4.5 indicate the migration, proliferation and invasion patterns of WM35 and SK-MEL-28 cell lines, respectively. We first identify actively proliferating cells in the MSE using the Ki-67 marker. Results in Figs. 4.4a-4.4d and Figs. 4.5a-4.5d highlight positively stained cells at day 0, 9, 15 and 20 for the WM35 and SK-MEL-28 cell lines, respectively. It is important to note that the Ki-67 marker identifies all proliferating cells, and does not distinguish between proliferating fibroblast cells, proliferating keratinocyte cells and proliferating melanoma cells. Therefore, additional information is required to distinguish between these different types of cells. Overall, we see that there are proliferative cells in both the epidermal and dermal regions of the tissue.
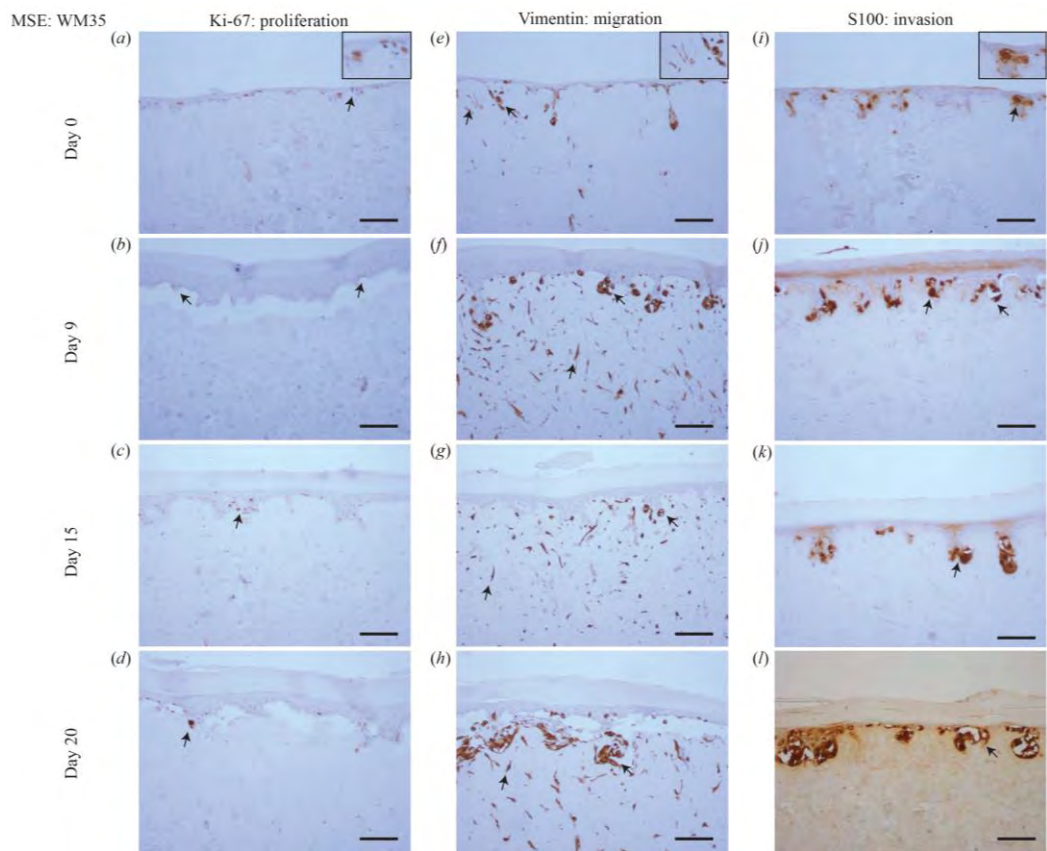
Figure 4.4: Proliferation, migration and invasion of skin cells and WM35 melanoma cells. (*a*)-(*d*) Proliferating cells (brown) highlighted by Ki-67 at day 0, 9, 15 and 20. (*e*)-(*h*) Migrating cells (brown) highlighted by vimentin. Dermal cells with elongated morphology are fibroblasts, and colonies of cells are migrating WM35 melanoma cells. (*i*)-(*l*) WM35 melanoma cells (brown) highlighted by S100 at day 0, 9, 15 and 20. Black arrows and inset images highlight positive staining. The scale bar in the main images shows 100 μm, and the width of the insets are approximately 75 μm.
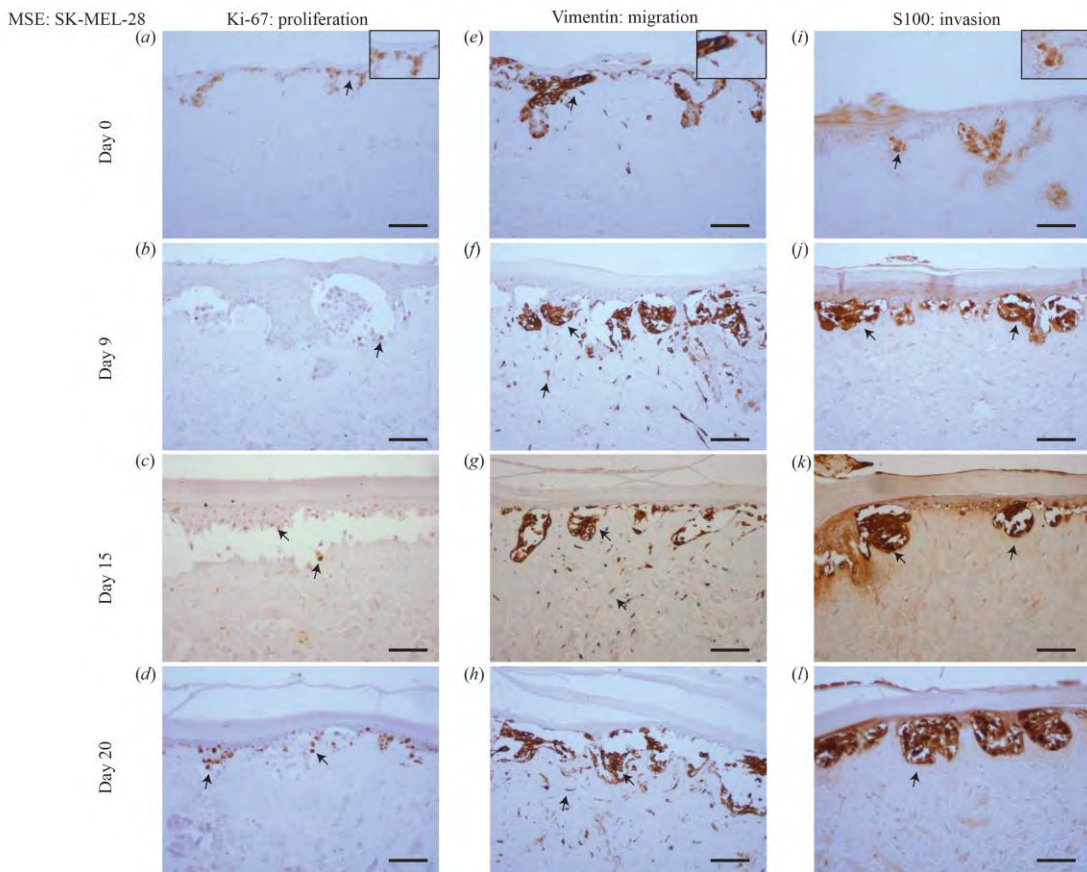
Figure 4.5: Proliferation, migration and invasion of skin cells and SK-MEL-28 melanoma cells. (*a*)-(*d*) Proliferating cells (brown) highlighted by Ki-67 at day 0, 9, 15 and 20. (*e*)-(*h*) Migrating cells (brown) highlighted by vimentin. Dermal cells with elongated morphology are fibroblasts, and colonies of cells are SK-MEL-28 melanoma cells. (*i*)-(*l*) SK-MEL-28 melanoma cells (brown) highlighted by S100 at day 0, 9, 15 and 20. Black arrows and inset images highlight positive staining. The scale bar in the main images shows 100 µm, and the width of the insets are approximately 75 µm.

Migrating cells in the MSE models are detected using the marker vimentin (Ivaska *et al*., 2007; Chernoivanenko, Minin & Minin, 2013; Liu *et al*., 2015). In this context, migration is referred to motile fibroblast cells and motile melanoma cells. It is challenging to identify the particular type of migrating cells using vimentin, as vimentin is expressed by most mesenchymal cell types (Goodpaster *et al*., 2008; Chernoivanenko, Minin &Minin, 2013). Since both fibroblasts and melanoma cell lines are mesenchymal (Goodpaster *et al*., 2008; Kim *et al*., 2013; Sriram &

Bigliardi-Qi, 2015) we expect that all melanoma and fibroblast cells will be positive for vimentin. To potentially distinguish between melanoma cells and fibroblast cells in the MSE models, we note that fibroblasts tend to be isolated and have an elongated cellular morphology (Sriram & Bigliardi-Qi, 2015). Furthermore, some of the vimentin positive cells appear to be arranged in colonies, and this is consistent with typical melanoma morphology (Schwartz *et al*., 2008; Kim *et al*., 2010; Baraldi *et al*., 2013). With this additional information, vimentin can be used to indicate the spatial distribution of fibroblasts, which appear to be only present in the dermal region, as shown in Figs. 4.4*e*-4.4*h* in the MSE with the WM35 melanoma cell line, and in Figs. 4.5*e*-4.5*h* in the MSE with the SK-MEL-28 melanoma cell line, at day 0, 9, 15 and 20. The fact that we tend to see fibroblast cells in the dermal region only provides further evidence that the MSE models resemble the HSE model, as shown in Fig. 4.6, as well as native human skin *in vivo* (Sriram & Bigliardi-Qi, 2015). Since fibroblast cells have migrated vertically downward, into the dermis, our MSE and HSE models also capture a key feature of native human skin, as fibroblasts are typically confined to the dermal region (Driskell & Watt, 2015). Note that in Fig. 4.6, all vimentin positive fibroblasts appear to be negative for S100. The fibroblasts are introduced into the DEDs along with keratinocyte cells and melanoma cells, which is 4 days before we collect our first results at the day 0 time point. We observe that there are more vimentin positive cells in the dermis on day 9 as shown in Fig. 4.6*f*, than on day 0, as shown in Fig. 4.6*e*. This indicates that the fibroblast cells have migrated vertically into the dermis. Vimentin positive melanoma cells, arranged in colonies, are detected in both the epidermal and dermal region of the MSE models, as shown in Figs. 4.4*e*-4.4*h* and Figs. 4.5*e*-4.5*h*, at day 0, 9, 15 and 20. All of the interpretations of the type of vimentin positive cells involve some subjective assessment of whether the cells are single, elongated or whether they appear to be arranged in colonies. To provide further information to distinguish between melanoma cells and fibroblast cells, we now use a specific marker for melanoma cells (Haridas *et al*., 2016).
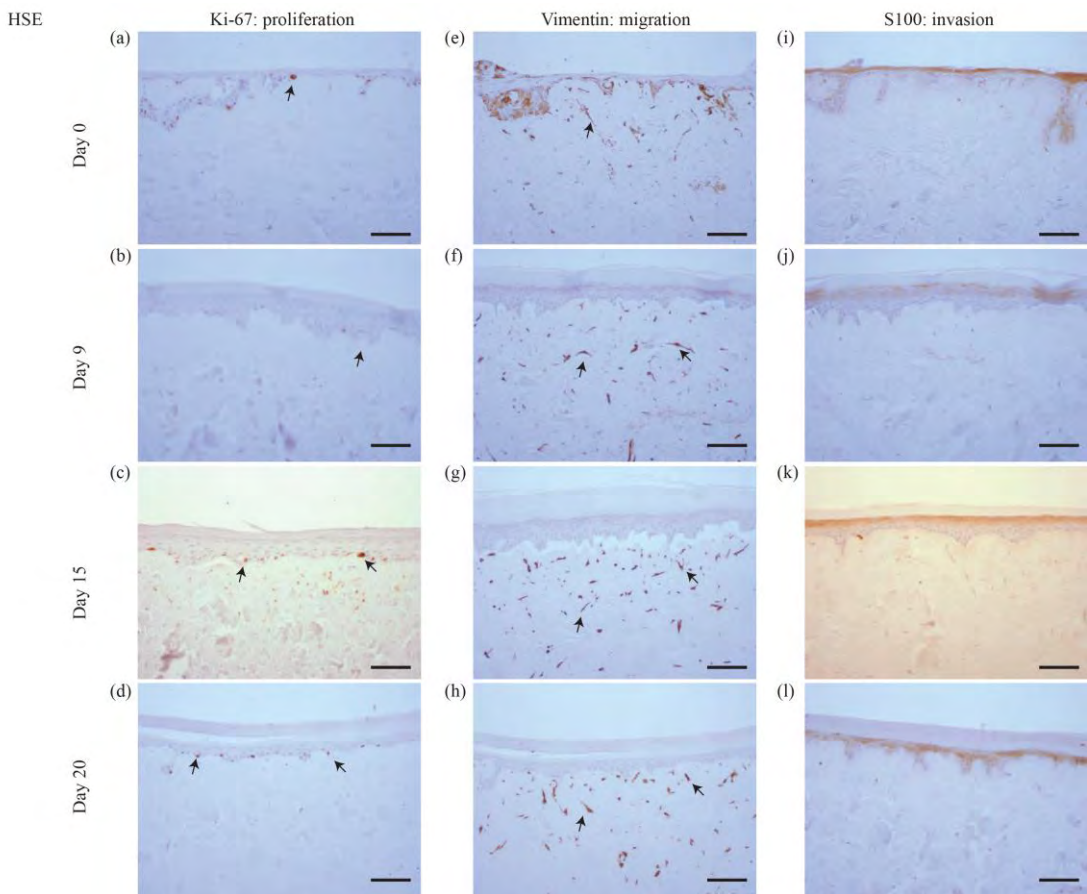
Figure 4.6: Proliferation, migration and invasion of skin cells. (*a*)-(*d*) Proliferating cells (brown) highlighted by Ki-67 at day 0, 9, 15 and 20. (*e*)-(*h*) Migrating fibroblast cells (brown) highlighted by vimentin. (*i*)-(*l*) No specific melanoma staining is highlighted by S100 at day 0, 9, 15 and 20. Black arrows and inset images highlight positive staining. Scale bar corresponds to 100 μm.

Vertical invasion of melanoma cells into the MSEs is detected by the marker S100. Invasion in this context refers to vertical spreading of melanoma cells into the dermis. Our previous studies show that S100 is a reliable marker that identifies both the WM35 and the SK-MEL-28 melanoma cell lines (Haridas *et al*., 2016; Haridas *et al*., 2017). Since the vimentin marker detects all elongated and motile cells in this MSE model, the inclusion of the S100 marker specifically allows us to distinguish melanoma cells from fibroblast cells. In both MSE models with the WM35 cell line and the SK-MEL-28 cell line, colonies of melanoma cells are present at day 0, 9, 15 and 20. Individual cells within these colonies are positively stained by S100. Smaller

colonies of melanoma cells are initially present near the upper surface of the MSE models, as shown in Fig. 4.4*i* and Fig. 4.5*i*. These melanoma colonies dramatically increase in size and number with time, and the melanoma colonies invade into the dermis after day 15 and 20, as shown in Figs. 4.4*k* and 4.4*l* for the WM35 melanoma cell line, and after day 9 in Figs. 4.5*j*-4.5*l* for the SK-MEL-28 melanoma cell line. It is important to note that on day 9, the WM35 melanoma cells are present only in the epidermal region. No S100 positive cells are present in the dermis. This observation, along with the Col IV staining of a mostly-continuous basement membrane at day 9, as shown in Fig. S4.4F, excludes the possibility of melanoma cells being trapped in the dermal region from the beginning of the experiment.

Comparing the size of the melanoma colonies over time in both MSE models shows that the colonies of SK-MEL-28 melanoma cells are larger than the colonies of WM35 melanoma cells. These differences are most evident at day 20, as shown by comparing the images in Fig. 4.4*l* and Fig. 4.5*l*. These results suggest that the SK-MEL-28 cell line is more aggressive than the WM35 melanoma cell line. This difference is consistent with the usual notion that the SK-MEL-28 melanoma cell line is associated with the later, more aggressive stage of the disease, whereas the WM35 melanoma cell line is associated with the early phase of melanoma progression. Also, it is possible that these immunohistochemistry results are consistent with the previous MTT results in Figs. 4.3*e* and 4.3*f* since the colonies of cells on the surface of the MSE model seem to disappear at later times. We initially observe colonies of cells, that we assume to be melanoma cells, on the surface of the MSE model on day 0 and day 9, as shown in Fig. 4.3*e* and Fig. 4.3*f*. It is reasonable to assume that these colonies are composed of SK-MEL-28 melanoma cells because there are no visible colonies on the equivalent HSE models at the same time points, as shown in Fig. 4.3*a* and Fig. 4.3*b*. These colonies are no longer visible on the MSE model after day 15, as shown in Fig. S4.2. Since we also observe S100 positive SK-MEL-28 cells moving vertically downward into the dermis over time, we believe that the MTT results of day 15 and day 20 are consistent with the S100 staining. That is, the eventual disappearance of the cell colonies on the surface of the MSE model could be a result of the melanoma cells moving deeper into the MSE tissue at later times.

To explore whether the differences in invasion of the two melanoma cell lines might be associated with any difference in cell size, we measure the size of WM35 and SK-MEL-28 cells, as shown in Fig. S4.6. These results show that the average size of both cell lines is approximately 10 μm. Therefore, the difference in invasion of the two cell lines is not attributed to any differences in cell size.

An interesting result from the MSE with the WM35 melanoma cell line is that we observe the invasion of small colonies of WM35 melanoma cells into the dermis at day 20, as shown in Fig. 4.4*l*. This result is interesting because WM35 melanoma cells are thought to be associated with the early phase of melanoma progression, where cells are believed to be limited to the epidermis (Gaggioli & Sahai, 2007). In Fig. 4.4*h* and Fig. 4.4*l* where WM35 melanoma cells are present in the dermis, we see intermittent staining of Col IV, suggesting that the basement membrane is somehow disrupted. In comparison, results in Fig. S4.4H where there are no melanoma cells present in the dermis, we see a more continuous Col IV staining, suggesting that the basement membrane is present and intact. These results, combined, are consistent with the notion that WM35 cells enter the dermis by somehow disrupting the basement membrane. While we have not investigated the mechanism by which the basement membrane is disrupted in detail, our conclusion that the WM35 cells appear to disrupt the basement membrane seems to be a plausible explanation of our results. Previous 3D studies suggest that cells from the early RGP are restricted in the epidermal region only (Dekker *et al*., 2000; Beaumont, Mohana-Kumaran & Haass, 2014). Therefore, our results are contradictory, suggesting that WM35 cells are able to breach the basement membrane and invade into the dermis in our MSE model.

Overall, these results showcase the successful establishment of a reliable and enduring MSE model that can be used to examine the migration, proliferation and invasion of melanoma cells from two different cell lines associated with RGP and metastatic stages of melanoma progression. However, in addition to providing qualitative information about the spatial and temporal distribution of different cell types in the MSE models, we also provide quantitative information about the invasion process.

4.4.4 Quantification of melanoma invasion

To further examine the differences in the invasion patterns associated with the WM35 and SK-MEL-28 melanoma cell lines, we measure the depth of cell invasion into the dermal region over time. The depth of invasion is taken to be the distance from the top of the dermis to the deepest region invaded by the melanoma cells, as shown in Figs. S4.1A-S4.1C. The invasion depth is measured in each experiment, at each time point, using ImageJ (ImageJ, 2017). Each measurement is repeated using three biological replicates for the DED, primary keratinocyte cells and primary fibroblast cells and the average depth is calculated by averaging the data across the three biological replicates performed in triplicates. Therefore, a total of nine individual data points are used to generate each averaged data point in Fig. 4.7.
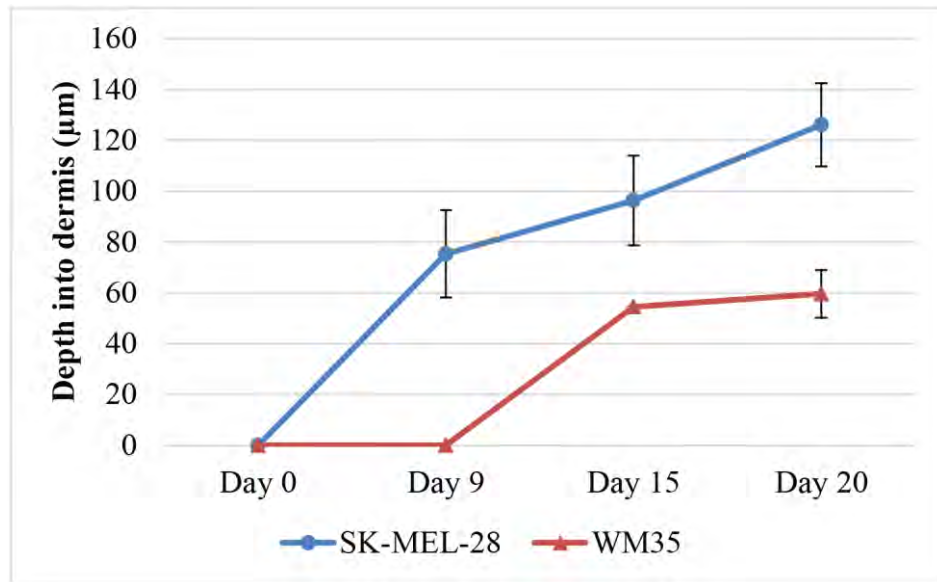
Figure 4.7: Quantification of melanoma cell invasion depth. Depth of melanoma invasion for the WM35 (red) and SK-MEL-28 (blue) cell lines. Data points show the average depth of invasion. The error bars measure the variability, as given by the sample standard deviation. In each case the sample mean and sample standard deviation is calculated using measurements from at least nine (n=9) identically prepared experiments.

Results in Fig. 4.7 show that the SK-MEL-28 melanoma cells invade earlier, deeper and faster than the WM35 melanoma cells. For example, at day 0 neither the SK-

MEL-28 nor the WM35 melanoma cells appear to be in the dermis, even with minimal basement membrane present. However, by day 9, the SK-MEL-28 melanoma cells have invaded into the dermis, whereas the WM35 melanoma cells are still contained within the epidermis. The slope of the curve for WM35 cells in Fig. 4.7 is steeper between day 9 and day 15. We believe that the initial difference of melanoma invasion between the cell lines, WM35 and SK-MEL-28 is not related to cell viability. We present all our results in a time course pattern, this allows identification of melanoma cells using S100, from day 0 until day 20. Melanoma positive cells observed in Fig. 4.4*i* and Fig. 4.5*i* reveal similar results regardless of whether the MSE is initialised with WM35 cells or SK-MEL-28 cells. This suggests that melanoma cells are viable during the first few days after co-culture. Note that the standard deviation of the invasion depth for WM35 cells is very small since there is very little variation in our measurements.

Previous research has measured the invasion of melanoma cells into the dermis (Eves *et al*., 2003a; Eves *et al*., 2003b; Marques and Mac Neil, 2016). These studies use a semi-quantitative measurement of cell counts, showing various metastatic melanoma cells invading the dermal region. It is interesting to note that our study of melanoma invasion using MSE models differs from previous approaches, as shown in Table 4.1. We use a simple method of visual analysis and measurement of melanoma cell invasion into the dermal region. Most importantly, we provide time course measurements of melanoma cell invasion.

In summary our results suggest that the WM35 and the SK-MEL-28 melanoma cell lines both exhibit invasive properties and have the ability to enter the dermis in our model. This is interesting because the WM35 melanoma cell line is thought to be associated with the early phase of melanoma progression where the cells are confined to the epidermis. We do, however, observe differences in the invasive properties of the two cell lines. For example, the WM35 cells appear to take a long duration of time to enter the dermis than the SK-MEL-28 cell. Our study does not explain why the WM35 cells take a longer period of time to enter the dermis. However, we anticipate that these differences could have many explanations. For example, the disruption of the basement membrane could be driven by some kind of chemical

signal, and the differences in the speed of invasion could be associated by differences in the production rates of such chemical signals. Exploring these ideas is a topic for future research. Overall, our qualitative observations and quantitative measurements suggest that the WM35 melanoma cell line is less invasive than the SK-MEL-28 melanoma cell line.

4.5   CONCLUSION

In summary, 3D skin model studies are more realistic, and more closely resemble native human skin *in vivo* than 2D studies. HSE skin models constructed using DED are used in many research areas including wound healing and burn studies (Topping *et al*., 2006; Xie *et al*., 2010; Monsuur *et al*., 2016). Since the physiological architecture of the HSE model is similar to native human skin *in vivo* it can be adapted to study melanoma proliferation, migration and invasion patterns. Melanoma has various phases of progression and 2D models are limited since 2D models cannot be used to study vertical invasion. In contrast, 3D skin-based melanoma models can be used to study vertical invasion, as well as exploring how melanoma cells interact with surrounding cells and tissues.

In this study we develop an *in vitro* MSE model using cell lines from early and late phases of melanoma. The MSE model incorporates ether WM35 melanoma cells or SK-MEL-28 melanoma cells, as well as primary keratinocytes and primary fibroblasts. Our MSE models are capable of examining melanoma progression for up to 20 days, which is the longest time point we have analysed. Collectively, our results suggest that MSE models constructed *in vitro* have similar tissue structure to native human skin. The melanoma cells in the MSE models proliferate, migrate and invade into the dermis as observed in native human skin *in vivo*. However, these two cell lines from the RGP and metastatic phase of melanoma lead to different patterns of invasion. Importantly, the MSE models enable quantitative measurements of the invasive process to be made, and allow us to quantitatively compare the progression of the two different cell lines.

Lastly, it could be of interest to extend this work by using cell lines associated with the VGP state of the disease in the MSE and comparing these additional results to our current study. Additionally the MSE could also be further developed as a pre-clinical platform to investigate the effects of anti-melanoma drugs. Both melanoma cell lines used in the current study have *BRAF* mutations (Smalley *et al*., 2008; Boussemart *et al*., 2014; Fofaria *et al*., 2015), hence these cell lines could possibly be targeted using a number of drugs such as vemurafnib, dabrafenib, trametinib, or a combination of either of these drugs (Jang & Atkins, 2013; Boussemart *et al*., 2014; Fofaria *et al*., 2015). The alteration in cell proliferation, cell invasion and colony formation, when melanoma cells are treated with these putative drugs could be examined in this MSE model.

4.6 ACKNOWLEDGEMENTS

4.7   REFERENCES

1. Alexaki VI, Javelaud D, Van-Kempen LCL, Mohammed KS, Dennler S, Luciani F, Hoek KS, Juarez P, Goydos JS, Fournier PJ, Sibon C, Bertolotto C, Verrecchia F, Saule S, Delmas V, Ballotti R, Larue L, Saiag P, Guise TA, Mauviel A. 2010. GL12-mediated melanoma invasion and metastasis. *Journal of the National Cancer Institute* 102:1148-1159.

2. Bandarchi B, Ma L, Navab R, Seth A, Rasty G. 2010. From melanocyte to malignant metastatic melanoma. *Dermatology Research and Practice* 2010:583748.

3. Bani MR, Rak J, Adachi D, Wiltshire R, Trent JM, Kerbel RS, Ben-David Y. 1996. Multiple features of advanced melanoma recapitulated in tumorigenic variants of early stage (radial growth phase) human melanoma cell lines: evidence for a dominant phenotype. *Cancer Research* 56:3075-3086.

4. Baraldi MM, Alemi AA, Sethna JP, Caracciolo S, Porta CALM, Zapperi S. 2013. Growth and form of melanoma colonies. *Journal of Statistical Mechanics-Theory and Experiment* 2013:p02032.

5. Baruthio F, Quadroni M, Ruegg C, Mariotti A. 2008. Proteomic analysis of membrane rafts of melanoma cells identifies protein patterns characteristic of the tumor progression stage. *Proteomics* 8:4733-4747.

6. Beaumont KA, Mohana-Kumaran N, Haass NK. 2014. Modelling melanoma *in vitro* and *in vivo*. *Healthcare* 2:27-46.

7. Bechetoille N, Haftek M, Staquet MJ, Cochran AJ, Schmitt D, Berthier-Vergnes O. 2000. Penetration of human metastatic melanoma cells through an authentic dermal-epidermal junction is associated with dissolution of native collagen IV and VII. *Melanoma Research* 10:427-434.

8. Bertolotto C. 2013. Melanoma: from melanocyte to genetic alterations and clinical options. *Scientifica* 2013:635203.

9. Binny RN, Haridas P, James A, Law R, Simpson MJ, Plank MJ. 2016. Spatial structure arising from neighbour-dependent bias in collective cell movement. *PeerJ* 4:e1689.

10. Brandner JM, Haass NK. 2013. Melanoma's connections to the tumour microenvironment. *Pathology* 45:443-452.

11. Boussemart L, Malka-Mahieu H, Girault I, Allard D, Hemmingsson O, Tomasic G, Thomas M, Basmadjian C, Ribeiro N, Thuaud F, Mateus C, Routier E, Kamsu-Kon N, Agoussi S, Eggermont AM, Desaubry L, Robert C, Vagner S. 2014. eIF4F is a nexus of resistance to anti-BRAF and anti-MEK cancer therapies. *Nature* 513:105-109.

12. Carey TE, Takahashi T, Resnick LA, Oettgen HF, Old LJ. 1976. Cell surface antigens of human malignant melanoma: mixed hemadsorption assays for humoral immunity to cultured autologous melanoma cells. *Proceedings of the National Academy of Sciences of the United States of America* 73:3278-3282.

13. Chakrabarty KH, Dawson RA, Harris P, Layton C, Babu M, Gould L, Phillips J, Leigh I, Green C, Freedlander E, Mac Neil S. 1999. Development of autologous human dermal-epidermal composites based on sterilized human allodermis for clinical use. *British Journal of Dermatology* 141:811-823.

14. Chernoivanenko IS, Minin AA, Minin AA. 2013. Role of vimentin in cell migration. *Russian Journal of Developmental Biology* 44:186-202.

15. Clark WH. 1991. Tumour progression and the nature of cancer. *British Journal of Cancer* 64:631-644.

16. Cummins DL, Cummins JM, Pantle H, Silverman MA, Leonard AL, Chanmugam A. 2006. Cutaneous malignant melanoma. *Mayo Clinic Proceedings* 81:500-507.

17. Damsky WE, Rosenbaum LE, Bosenberg M. 2010. Decoding melanoma metastasis. *Cancers* 3:126-163.

18. Dawson RA, Upton Z, Malda J, Harkin DG. 2006. Preparation of cultured skin for transplantation using insulin-like growth factor I in conjunction with insulin-like growth factor binding protein 5, epidermal growth factor, and vitronectin. *Tranplantation* 81:1668-1676.

19. Dekker SK, Van-Doorn R, Kempenaar J, Gruis NA, Vermeer BJ, Ponec M. 2000. Skin equivalent: an attractive model to evaluate early melanoma metastasis. *Melanoma Research* 10:127-140.

20. Dennhofer R, Kurschat P, Zirgrino P, Klose A, Bosserfoff A, Van-Muijen G, Krieg T, Mauch C, Hunzelmann N. 2003. Invasion of melanoma cells into the dermal connective tissue in vitro: evidence for an important role of cysteine proteases. *International Journal of Cancer* 106:316-323.

21. Driskell RR, Watt FM. 2015. Understanding fibroblast heterogeneity in the skin. *Trends in Cell Biology* 25:92-99.

22. Eves P, Layton C, Hedley S, Dawson RA, Wagner M, Morandini R, Ghanem G, Mac Neil S. 2000. Characterization of an *in vitro* model of human melanoma invasion based on reconstructed human skin. *British Journal of Dermatology* 142:210-222.

23. Eves P, Katerinaki E, Simpson C, Layton C, Dawson R, Evans G, Mac Neil S. 2003a. Melanoma invasion in reconstructed human skin is influenced by skin cells – investigation of the role of proteolytic enzymes. *Clinical and Experimental Metastasis* 20:685-700.

24. Eves P, Haycock J, Layton C, Wagner M, Kemp H, Szabo M, Morandini R, Ghanem G, Garcia-Borron JC, Jimenez-Cervantes C, Mac Neil S. 2003b. Anti-inflammatory and anti-invasive effects of α-melanocyte-stimulating hormone in human melanoma cells. *British Journal of Cancer* 89:2004-2015.

25. Fernandez TL, Lonkhuyzen DRV, Dawson RA, Kimlin MG, Upton Z. 2014. Characterization of a human skin equivalent model to study the effects of ultraviolet B radiation on keratinocytes. *Tissue Engineering Part C Methods* 20:588-598.

26. Finn L, Markovic SN, Joseph RW. 2012. Therapy for metastatic melanoma: the past, present, and future. *BMC Medicine* 10:23.

27. Fofaria NM, Srivastava SK. 2014. Critical role of STAT3 in melanoma metastasis through anoikis resistance. *Oncotarget* 5:7051-7064.

28. Fofaria NM, Frederick DT, Sullivan RJ, Flaherty KT, Srivastava SK. 2015. Overexpression of Mcl-1 confers resistance to BRAF^{v600E} inhibitors alone and in combination with MEK1/2 inhibitors in melanoma. *Oncotarget* 6:40535-40556.

29. Gaggioli C, Sahai E. 2007. Melanoma invasion – current knowledge and future directions. *Pigment Cell and Melanoma Research* 20:161-172.

30. Golan T, Messer AR, Amitai-Lange A, Melamed Z, Ohana R, Bell RE, Kapitansky O, Lerman G, Greenberger S, Khaled M, Amar N, Albrengues J, Gaggioli C, Gonen P, Tabach Y, Sprinzak D, Shalom-Feuerstein R, Levy C. 2015. Interactions of melanoma cells with distal keratinocytes trigger

metastasis via Notch signaling of inhibition of MITF. *Molecular Cell* 59:664-676.

31. Goodpaster T, Legesse-Miller A, Hameed MR, Aisner SC, Randolph-Habecker J, Coller HA. 2008. An immunohistochemical method for identifying fibroblasts in formalin-fixed, paraffin-embedded tissue. *Journal of Histochemistry and Cytochemistry* 56:347-358.

32. Grahovac J, Becker D, Wells A. 2013. Melanoma cell invasiveness is promoted at least in part by the Epidermal Growth Factor-like repeats of Tenascin-C. *The Journal of Investigative Dermatology* 133:210-220.

33. Hanahan D, Weinberg RA. 2000. The hallmarks of cancer. *Cell* 100:57-70.

34. Haridas P, McGovern JA, Kashyap AS, McElwain DLS, Simpson MJ. 2016. Standard melanoma-associated markers do not identify the MM127 metastatic melanoma cell line. *Scientific Reports* 6:24569.

35. Haridas P, Penington CJ, McGovern JA, McElwain DLS, Simpson MJ. 2017. Quantifying rates of cell migration and cell proliferation in co-culture barrier assays reveals how skin and melanoma cells interact during melanoma spreading and invasion. *Journal of Theoretical Biology* 423:13-25.

36. Herlyn M. 1990. Human melanoma: development and progression. *Cancer and Metastasis Reviews* 9:101-112.

37. Hsu MY, Shih DT, Meier FE, Belle PV, Hsu JY, Elder DE, Buck CA, Herlyn M. 1998. Adenoviral gene transfer of β3 integrin subunit induces conversion from radial to vertical growth phase in primary human melanoma. *American Journal of Pathology* 153:1435-1442.

38. Hussein MR. 2004. Genetic pathways to melanoma tumorigenesis. *Journal of Clinical Pathology* 57:797-801.

39. ImageJ, ImageJ User Guide: Research Services Branch, National Institute of Health. https://imagej.nih.gov/ij/docs/guide/146-29.html (accessed July 2017).

40. Ivaska J, Pallari HM, Nevo J, Eroksson JE. 2007. Novel functions of vimentin in cell adhesion, migration and signaling. *Experimental Cell Research* 313:2050-2062.

41. Jang S, Atkins MB. 2013. Which drug, and when, for patients with BRAF-mutant melanoma? *The Lancet. Oncology* 14:e60-e69.

42. Johnston ST, Simpson MJ, McElwain DLS. 2014. How much information can be obtained from tracking the position of the leading edge in a scratch assay? *Journal of the Royal Society Interface* 11:20140325.

43. Kim TK, Chen J, Li W, Zjawiony J, Miller D, Janjetovic Z, Tuckey RC, Slominski A. 2010. A new steroidal 5,7-diene derivative, 3β-hydroxyandrosta-5,7-diene-17β-carboxylic acid, shows potent anti-proliferative activity. *Steroids* 75:230-239.

44. Kim JE, Leung E, Baguley BC, Finlay GJ. 2013. Heterogeneity of expression of epithelial-mesenchymal transition markers in melanocytes and melanoma cell lines. *Frontiers in Genetics* 4:e97.

45. Kramer N, Walzl A, Unger C, Rosner M, Krupitza G, Hengstschlager M, Dolznig H. 2013. In vitro cell migration and invasion assays. *Mutation Research* 752:10-24.

46. Leight JL, Tokuda EY, Jones CE, Lin AJ, Anseth KS. 2015. Multifunctional bioscaffolds for 3D culture of melanoma cells reveal increased MMP activity and migration with BRAF kinase inhibition. *Proceedings of the National Academy of Sciences of the Unites States of America* 112:5366-5371.

47. Li H, Fan X, Houghton J. 2007. Tumor microenvironment: the role of the tumor stroma in cancer. *Journal of Cellular Biochemistry* 101:805-815.

48. Liu CY, Lin HH, Tang MJ, Wang YK. 2015. Vimentin contributes to epithelial-mesenchymal transition cancer cell mechanics by mediating cytoskeletal organization and focal adhesion maturation. *Oncotarget* 6:15966-15983.

49. Liu W, Peng Y, Tobin DJ. 2013. A new 12-gene diagnostic biomarker signature of melanoma revealed by integrated microarray analysis. *PeerJ* 1:e49.

50. Mac Neil S, Eves P, Richardson B, Molife R, Lorigan P, Wagner M, Layton C, Morandini R, Ghanem G. 2000. Oestrogenic steroids and melanoma cell interaction with adjacent skin cells influence invasion of melanoma cells in vitro. *Pigment Cell and Melanoma Research* 13:68-72.

51. Marck VV, Stove C, Bossche KVD, Stove V, Paredes J, Haeghen YV, Bracke M. 2005. P-cadherin promotes cell-cell adhesion and counteracts invasion in human melanoma. *Cancer Research* 65:8774-8783.

52. Marinkovich MP, Keene DR, Rimberg CS, Burgeson RE. 1993. Cellular origin of the dermal-epidermal basement membrane. *Developmental Dynamics* 197:255-267.

53. Marques CMdG, Mac Neil S. 2016. Use of a tissue engineered human skin model to investigate the effects of wounding and of an anti-inflammatory on melanoma cell invasion. *PLoS ONE* 11:e0156931.

54. Meier F, Nesbit M, Hsu M, Martin B, Belle P, Elder DE, Schaumburg-Lever G, Garbe C, Walz TM, Donatien P. 2000. Human melanoma progression in skin reconstructs: biological significance of bFGF. *The American Journal of Pathology* 156:193-200.

55. McGovern JA, Heinemann JR, Burke LJ, Dawson R, Parker TJ, Upton Z, Hooper JD, Manton KJ. 2013. Stratum basale keratinocyte expression of the cell-surface glycoprotein CDCP1 during epidermogenesis and its role in keratinocyte migration. *British Journal of Dermatology* 168:496-503.

56. McGovern JA, Meinert C, de Veer SJ, Hollier BG, Parker TJ, Upton Z. Attenuated kallikrein-related peptidase activity disrupts desquamation and leads to stratum corneum thickening in human skin equivalent models. *British Journal of Dermatology* 176:145-158.

57. McCusker JP, Dumontier M, Yan R, He S, Dordick JS, McGuinness DL. 2017. Finding melanoma drugs through a probabilistic knowledge gap. *PeerJ* 3:e106.

58. Miller AJ, Mihm MC. 2006. Melanoma. *The New England Journal of Medicine* 355:51-65.

59. Monsuur HN, Boink MA, Weijers EM, Roffel S, Breetveld M, Gefen A, van den Broek LJ, Gibbs S. 2016. Methods to study cell mobility during skin wound healing *in vitro*. *Journal of Biomechanics* 49:1381-1387.

60. Nithya S, Radhika T, Jeddy N. 2015. Loricrin- an overview. *Journal of Oral and Maxillofacial Pathology* 19:64-68.

61. Peinado H, Aleckovic M, Lavotshkin S, Matei I, Costa-Silva B, Moreno-Bueno G, Hergueta-Redondo M, Williams C, Garcia-Santos G, Ghajar CM, Niadori-Hoshino A, Hoffman C, Bdal K, Garcia BA, Callahan MK, Yuan J, Martins VR, Skog J, Kaplan RN, Brady MS, Wolchok JD, Chapman PB, Kang Y, Bromberg J, Lyden D. 2012. Melanoma exosomes educate bone

marrow progenitor cells toward a pro-metastatic phenotype through MET. *Nature Medicine* 18:883-891.

62. Pope JH, Morrison L, Moss DJ, Parsons PG, Regius MS. 1979. Human malignant melanoma cell lines. *Pathology* 11:191-195.

63. Ramaraj P, Cox JL. 2014. In-vitro effects of sex steroids on mouse melanoma (B16F10) cell growth. *CellBio* 3:60-71.

64. Rheinwald JG, Green H. 1975. Serial cultivation of strains of human epidermal keratinocytes: the formation of keratinizing colonies from single cells. *Cell* 6:331-343.

65. Rivas M, Rojas E, Calaf GM, Barberan M, Liberman C, Correa MDP. 2017. Association between non-melanoma and melanoma skin cancer rates, vimentin D and latitude. *Oncology Letters* 13:3787-3792.

66. Sandri S, Faiao-Flores F, Tiago M, Pennacchi PC, Massaro RR, Alves-Fernandes DK, Berardinelli GN, Evangelista AF, Vazquez VL, Reis RM, Maria-Engler SS. 2016. Vemurafenib resistance increases melanoma invasiveness and modulates the tumor microenvironment by MMP-2 upregulation. *Pharmacological Research* 111:523-533.

67. Sandru V, Voinea S, Panaitescu E, Blidaru A. 2014. Survival rates of patients with metastatic malignant melanoma. *Journal of Medicine and Life* 7:572-576.

68. Satyamoorthy K, DeJesus E, Linnenbach AJ, Kraj B, Kornreich DL, Rendle S, Elder DE, Herlyn M. 1997. Melanoma cell lines from different stages of progression and their biological and molecular analyses. *Melanoma Research* 7:S35-42.

69. Schwartz MA, McRoberts K, Coyner M, Andarawewa KL, Frierson HFJr, Sanders JM, Swenson S, Markland F, Conaway MR, Theodorescu D. 2008. Integrin agonists as adjuvants in chemotherapy for melanoma. *Clinical Cancer Research* 14:6193-6197.

70. Simpson MJ, Treloar KK, Binder BJ, Haridas P, Manton KJ, Leavesley DI, McElwain DLS, Baker RE. 2013. Quantifying the roles of ell motility and cell proliferation in a circular barrier assay. *Journal of the Royal Society Interface* 10:20130007.

71. Smalley KSM, Contractor R, Nguyen TK, Xiao M, Edwards R, Muthuswamy V, King AJ, Flaherty KT, Bosenburg M, Herlyn M, Nathanson KL. 2008. Identification of a novel sub-group of melanomas with KIT/cyclin dependent kinase-4 overexpression. *Cancer Research* 68:5743-5752.

72. Sriram G, Bigliardi-Qi M. 2015. Fibroblast heterogeneity and its implications for engineering organotypic skin models in vitro. *European Journal of Cell Biology* 94:483512.

73. Straume O, Sviland L, Akslen LA. 2000. Loss of nuclear p16 protein expression correlates with increased tumor cell proliferation (Ki-67) and poor prognosis in patients with vertical growth phase. *Clinical Cancer Research* 6:1845-1853.

74. Taloni A, Alemi AA, Ciusani E, Sethna JP, Zapperi S, La-Porta CA. 2014. Mechanical properties of growing melanocyte nevi and the progression to melanoma. *PLoS One* 9:e94229.

75. Tiwary S, Preziosi M, Rothberg PG, Zeitouni N, Corson N, Xu L. 2014. ERBB3 is required for metastasis formation of melanoma cells. *Oncogenesis* 3:e110.

76. Topping G, Malda J, Dawson RA, Upton Z. 2006. Development and characterisation of human skin equivalents and their potential application as a burn wound model. *Primary Intention* 14:14-21.

77. Treloar KK, Simpson MJ, Haridas P, Manton KJ, Leavesley DI, McElwain DLS, Baker RE. 2013. Multiple types of data are required to identify the mechanisms influencing the spatial expansion of melanoma cell colonies. *BMC Systems Biology* 7:137.

78. Treloar KK, Simpson MJ. 2013. Sensitivity of edge detection methods for quantifying cell migration assays. *PLoS ONE* 8:e67389.

79. Treloar KK, Simpson MJ, Binder BJ, McElwain DLS, Baker RE. 2014. Assessing the role of spatial correlations during collective cell spreading. *Scientific Reports* 4:5713.

80. Uong A, Zon LI. 2010. Melanocytes in development and cancer. *Journal of Cellular Physiology* 222:38-41.

81. Van-Kilsdonk JWJ, Wilting RH, Bergers M, van Muijen GNP, Schalkwijk J, van Kempen LCLT, Swart GWM. 2008. Attenuation of melanoma invasion

by a secreted variant of activated leukocyte cell adhesion molecule. *Cancer Research* 68:3671-3679.

82. Van-Kilsdonk JW, Bergers M, Van Kempen LC, Schalkwijk J, Swart GW. 2010. Keratinocytes drive melanoma invasion in a reconstructed skin model. *Melanoma Research* 20:372-380.

83. Vorsmann H, Groeber F, Walles H, Busch S, Beissert S, Walczak H, Kumls D. 2013. Development of a human three-dimensional organotypic skin-melanoma spheroid model for *in vitro* drug testing. *Cell Death and Disease* 4:e719.

84. Weinstein D, Leininger J, Hamby C, Safai B. 2014. Diagnostic and prognostic biomarkers in melanoma. *The Journal of Clinical and Aesthetic Dermatology* 7:13-24.

85. Weinstock MA. 2000. Early detection of melanoma *JAMA-Journal of the American Medical Association* 284:886-889.

86. Wikramanayake TC, Stojadinovic O, Tomic-Canic M. 2014. Epidermal differentiation in barrier maintenance and wound healing. *Advances in Wound Care* 3:272-280.

87. Xie Y, Rizzi SC, Dawson RA, Lynam E, Richards S, Leavesley DI, Upton Z. 2010. Development of a three-dimensional human skin equivalent wound model for investigating novel wound healing therapies. *Tissue Engineering Part C-Methods* 16:1111-1123.

88. Yang Y, Sule-Suso J, Sockalingum GD. 2008. Study of melanoma invasion by FTIR spectroscopy. *Progress in Biomedical Optics and Imaging-Proceedings of SPIE* 6859:68591U

89. Zaidi MR, Day C, Merlino G. 2008. From UV's to metastases: modelling melanoma initiation and progression in the mouse. *Journal of Investigative Dermatology* 128:2381-2391.

4.8   SUPPLEMENTARY INFORMATION

4.8.1   *Quantifying depth of melanoma cell invasion*

Images in Fig. S4.1 shows how melanoma invasion depth measurements are derived from MSE models at day 9, 15 and 20. SK-MEL-28 cells are detected using the marker S100 as shown in Fig. S4.1A-S4.1C. This allows visualisation of melanoma cells in the MSE model. The depth of melanoma cell invasion is taken as the distance from the top of the dermis to the deepest region invaded by the melanoma cells. We measure the depth of invasion at day 9, 15 and 20, using ImageJ software (https://imagej.nih.gov/ij/docs/guide/146-29.html). Each measurement is repeated using three biological replicates for the DED, primary keratinocyte cells and primary fibroblast cells and each experiment is performed in triplicates. Therefore, the average depth is calculated by averaging the data obtained from n=9 experimental results.
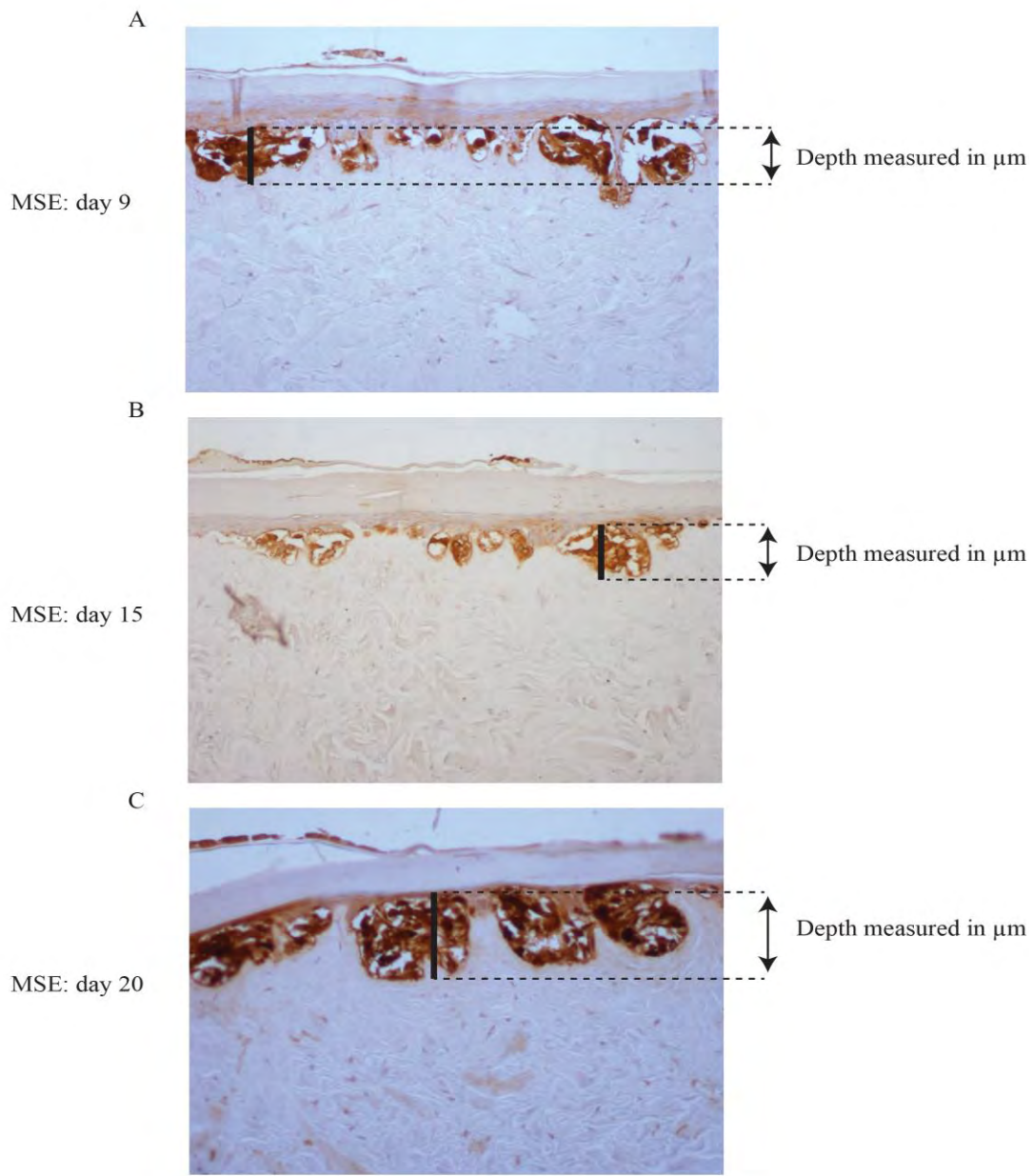
Figure S4.1: Quantifying depth of melanoma cell invasion. (A)-(C) MSE model with SK-MEL-28 melanoma cells (brown) highlighted by S100 at day 9, 15 and 20. The black arrows indicate the depth of melanoma cell invasion measured. Scale bar corresponds to 100 μm.

4.8.2 MTT assay

Viable cells (purple) are identified in the HSE model, MSE model with WM35 cells and MSE model with SK-MEL-28 cells using MTT assay. Images in Fig. S2 show MTT assay results obtained at day 15 and 20. These images reveal the radial

expansion of the total cell population on the HSE and MSE models imaged using a stereo microscope fitted with a Nikon digital camera.
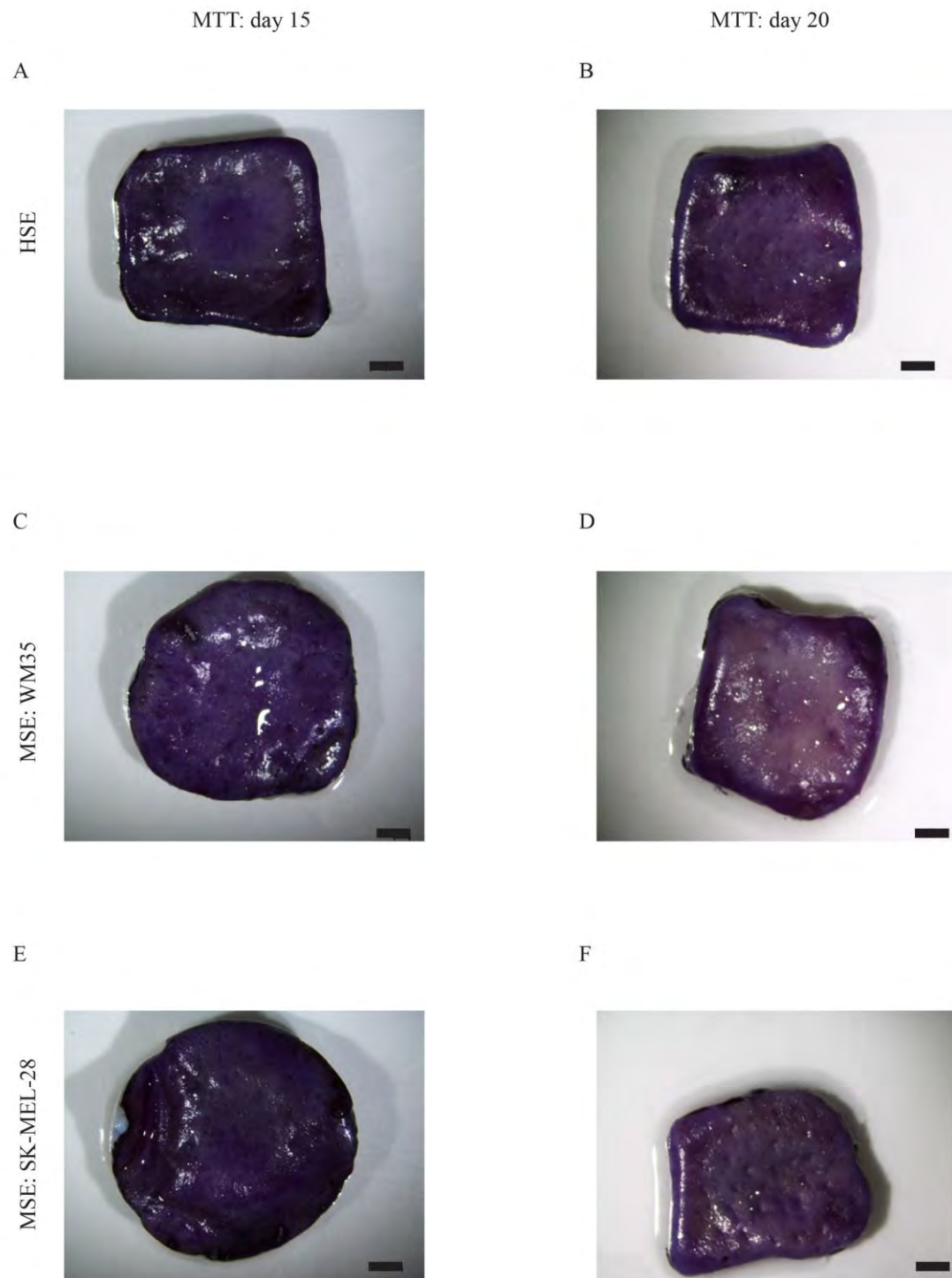
Figure S4.2: MTT assay. Experimental images of MTT assay shows viable cells (purple) on the HSE model (A) and (B).The MSE model with WM35 melanoma cells

is shown in (C) and (D).The MSE model with SK-MEL-28 melanoma cells is shown in (E) and (F). The results in the left column are at day 15, and the results in the right column are at day 20. Scale bar corresponds to 1 mm.

4.8.3   *Histological analysis of HSE model*

HSEs are first divided through the centre of the MTT positive region using a sterile blade and embedded in paraffin wax. The samples are then sectioned using a microtome into 5 µm thick tissue sections. To show the physiological similarities of the HSE model to native skin we perform H&E staining, basement membrane staining using Col IV, and terminally differentiating epidermal cell staining using Loricrin, on these tissue sections, as shown in Fig. S4.3. Staining is performed at day 0, 9, 15 and 20 and the results are imaged using Olympus BX41 microscope fitted with an Olympus digital camera.
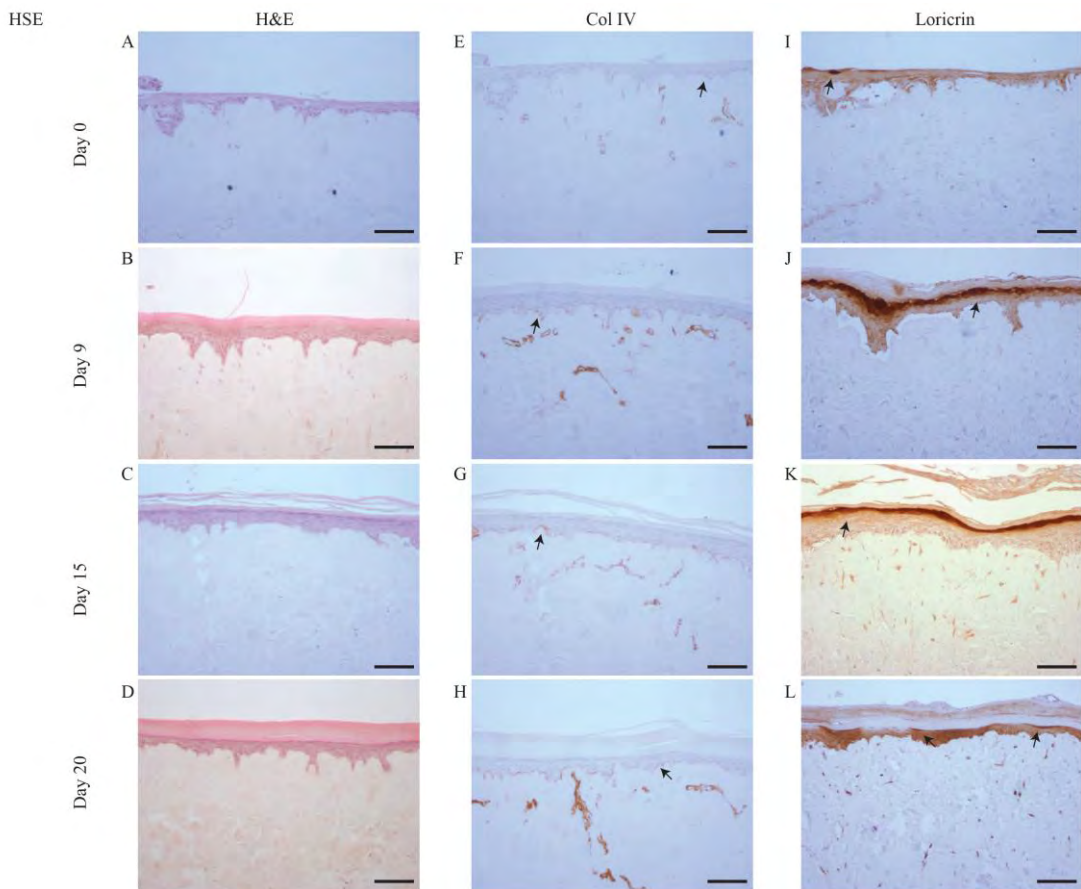
Figure S4.3: Histological analysis of HSE model.(A)-(D) H&E staining at day 0, 9, 15 and 20. (E)-(H) The basement membrane (brown) highlighted by collagen IV (Col IV) at day 0, 9, 15 and 20. (I)-(L) Terminally differentiating epithelial cells (brown) highlighted by loricrin at day 0, 9, 15 and 20. Black arrows indicate positive staining. Scale bar corresponds to 100 µm.

4.8.4   Histological analysis of MSE model with WM35 melanoma cells

MSE models with WM35 cells are first divided through the centre of the MTT positive region using a sterile blade and embedded in paraffin wax. The samples are then sectioned into 5 µm thick tissue sections. To show the physiological similarities of the MSE model to HSE and native skin we perform H&E staining, basement membrane staining using Col IV, and terminally differentiating epidermal cell staining using Loricrin, on these tissue sections, as shown in Fig. S4.4. Staining is performed at day 0, 9, 15 and 20 and the results are imaged using Olympus BX41 microscope fitted with an Olympus digital camera.
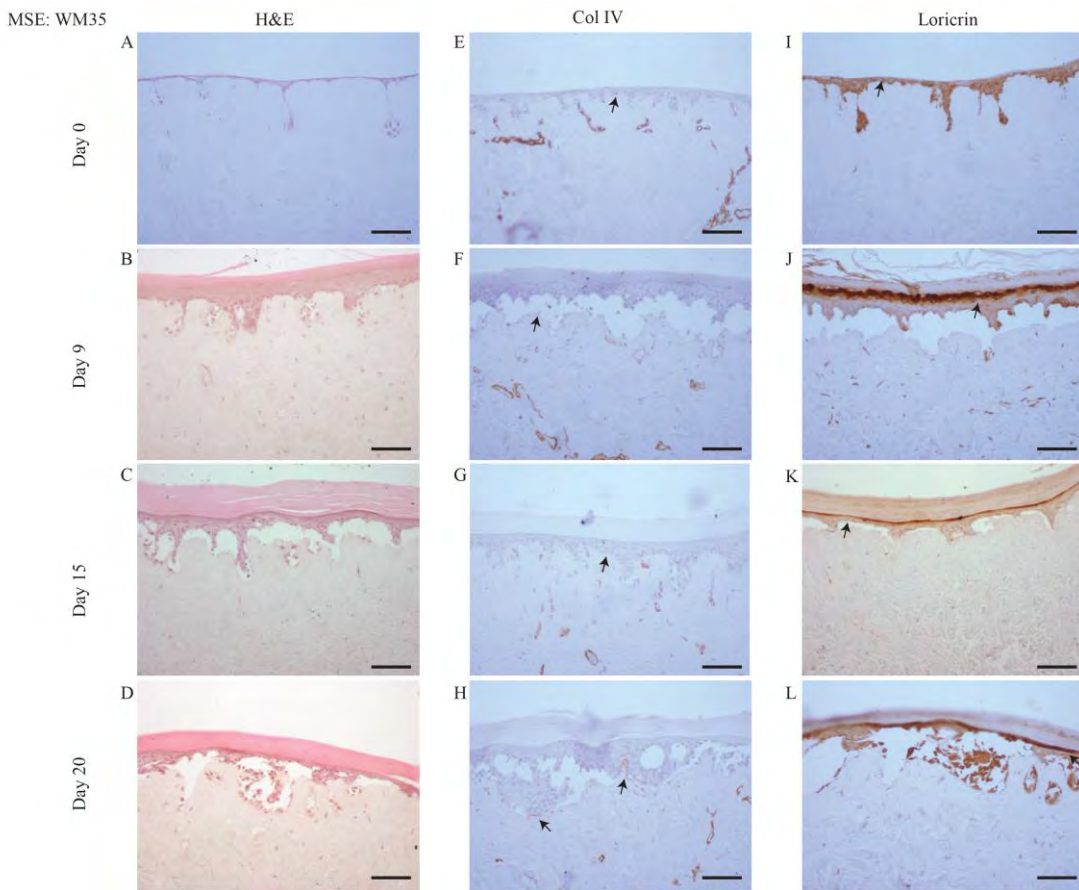
Figure S4.4: Histological analysis of MSE model with WM35 melanoma cells. (A)-(D) H&E staining at day 0, 9, 15 and 20. (E)-(H) The basement membrane (brown) highlighted by collagen IV (Col IV) at day 0, 9, 15 and 20. (I)-(L) Terminally differentiating epithelial cells (brown) highlighted by loricrin at day 0, 9, 15 and 20. Black arrows indicate positive staining. Scale bar corresponds to 100 μm.

4.8.5 Histological analysis of MSE model with SK-MEL-28 melanoma cells

MSE models with SK-MEL-28 cells are first divided through the centre of the MTT positive region using a sterile blade and embedded in paraffin wax. The samples are then sectioned into 5 μm thick tissue sections. To show the physiological similarities of the MSE model to HSE and native skin we perform H&E staining, basement membrane staining using Col IV, and terminally differentiating epidermal cell staining using Loricrin, on these tissue sections, as shown in Fig. S4.5. Staining is performed at day 0, 9, 15 and 20 and the results are imaged using Olympus BX41 microscope fitted with an Olympus digital camera.
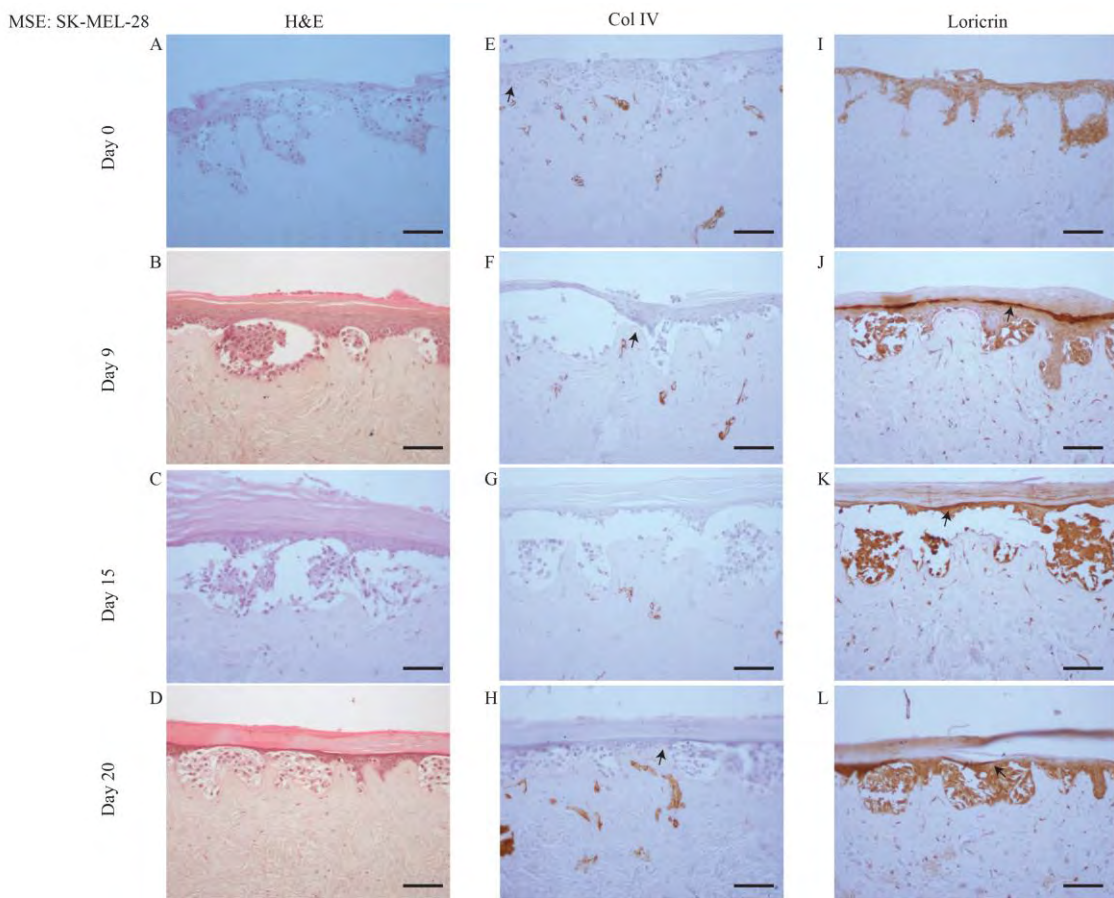
Figure S4.5: Histological analysis of MSE model with SK-MEL-28 melanoma cells. (A)-(D) H&E staining at day 0, 9, 15 and 20. (E)-(H) The basement membrane (brown) highlighted by collagen IV (Col IV) at day 0, 9, 15 and 20. (I)-(L) Terminally differentiating epithelial cells (brown) highlighted by loricrin at day 0, 9, 15 and 20. Black arrows indicate positive staining. Scale bar corresponds to 100 μm.

4.8.6 Estimating the size of melanoma cell lines

Images of melanoma cells are acquired using a brightfield microscope fitted with an Olympus digital camera. The size of each cell is measured using Leica LAS X software (http://www.leica-microsystems.com/applications/life-science/live-cell-imaging/). The average size of WM35 cells is approximately 9 μm and the average size of SK-MEL-28 cells is approximately 10 μm. These images show minimal differences between cell sizes for both melanoma cell lines. The average melanoma cell size is calculated using n=10 cells from each cell line.
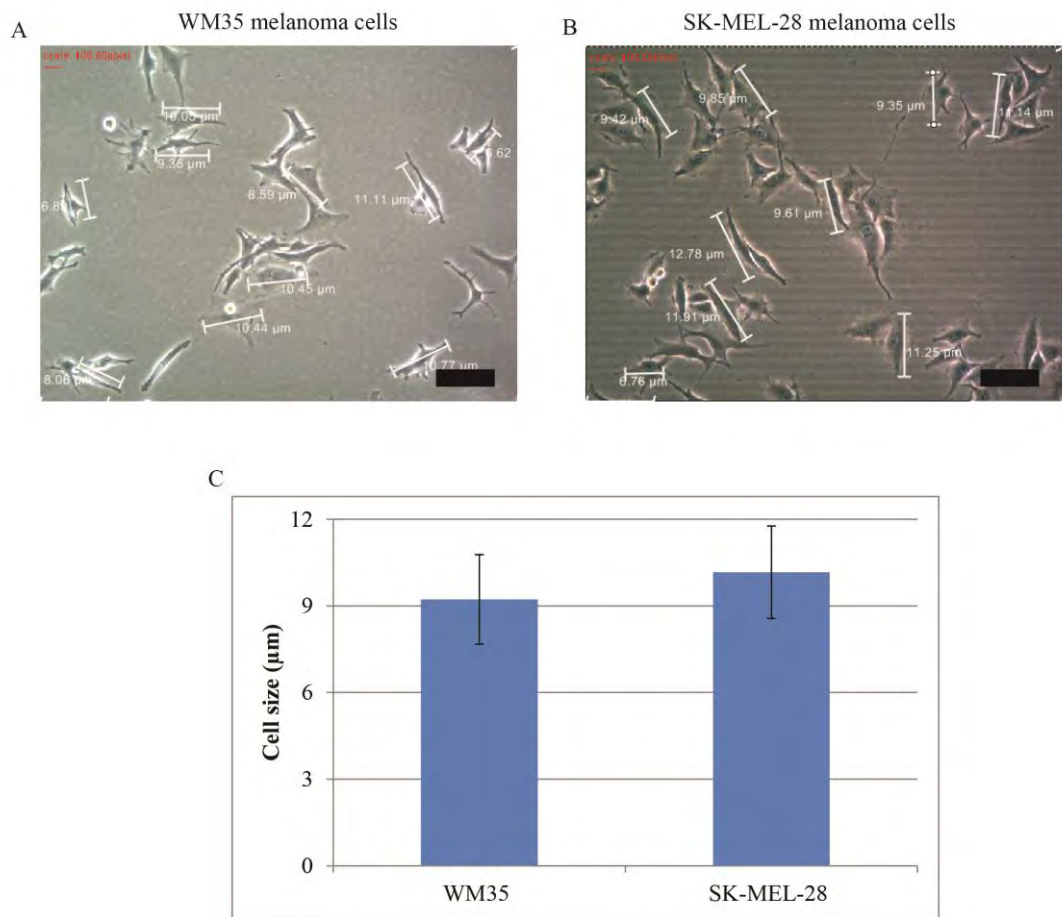
Figure S4.6: Estimating the size of melanoma cell lines. (A) and (B) Images of melanoma cells, WM35 and SK-MEL28, showing cell size measurements. The scale bar corresponds to 10 µm. (C) Graphical representation of averaged cell sizes for WM35 and SK-MEL-28 melanoma cells. Averaged cell size is calculated using measurements from n=10 cells for each cell line. The error bars measure the variability as given by the standard deviation.

Chapter 5: Three-dimensional experiments and individual based simulations show that cell proliferation drives melanoma nest formation in human skin tissue

Statement of Contribution of Co-Authors for Thesis by Published Paper
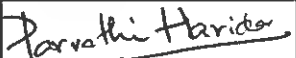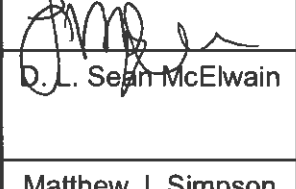
The following is the suggested format for the required declaration provided at the start of any thesis chapter which includes a co-authored publication.

The authors listed below have certified that:

16. they meet the criteria for authorship in that they have participated in the conception, execution, or interpretation, of at least that part of the publication in their field of expertise;
17. they take public responsibility for their part of the publication, except for the responsible author who accepts overall responsibility for the publication;
18. there are no other authors of the publication according to these criteria;
19. potential conflicts of interest have been disclosed to (a) granting bodies, (b) the editor or publisher of journals or other publications, and (c) the head of the responsible academic unit, and
20. they agree to the use of the publication in the student's thesis and its publication on the QUT's ePrints site consistent with any limitations set by publisher requirements.

In the case of this chapter:

Haridas P, Browning AP, McGovern JA, McElwain DLS, Simpson MJ. (2018). Three-dimensional experiments and individual based simulations show that cell proliferation drives melanoma nest formation in human skin tissue. *BMC Systems Biology*. 12:34
10.1186/s12918-018-0559-9

Contributor	Statement of contribution*
Parvathi Haridas *Parvathi Haridas* 29/05/2017	Conceived the study, designed experiments, performed all the laboratory experiments, analysed data, wrote the manuscript, prepared figures and/tables and reviewed drafts of the manuscript
Alex P. Browning	Designed experiments, performed mathematical simulations, analysed data and reviewed drafts of the manuscript
Jacqui A. McGovern	Designed experiments and reviewed drafts of the manuscript
D. L. Sean McElwain	Designed experiments and reviewed drafts of the manuscript
Matthew J. Simpson	Conceived the study, Designed experiments and reviewed drafts of the manuscript

Principal Supervisor Confirmation

I have sighted email or other correspondence from all Co-authors confirming their certifying authorship.
(If the Co-authors are not able to sign the form please forward their email or other correspondence confirming the certifying authorship to the RSC).

Matthew J Simpson

Name _____   Signature _____   Date 10 | 11 | 2017

5.1 ABSTRACT

Background: Melanoma can be diagnosed by identifying nests of cells on the skin surface. Understanding the processes that drive nest formation is important as these processes could be potential targets for new cancer drugs. Cell proliferation and cell migration are two potential mechanisms that could conceivably drive melanoma nest formation. However, it is unclear which one of these two putative mechanisms plays a dominant role in driving nest formation.

Results: We use a suite of three-dimensional (3D) experiments in human skin tissue and a parallel series of 3D individual-based simulations to explore whether cell migration or cell proliferation plays a dominant role in nest formation. In the experiments we measure nest formation in populations of irradiated (non-proliferative) and non-irradiated (proliferative) melanoma cells, cultured together with primary keratinocyte and fibroblast cells on a 3D experimental human skin model. Results show that nest size depends on initial cell number and is driven primarily by cell proliferation rather than cell migration.

Conclusions: Nest size depends on cell number, and is driven primarily by cell proliferation rather than cell migration. All experimental results are consistent with simulation data from a 3D individual based model (IBM) of cell migration and cell proliferation.

5.2 BACKGROUND

Clusters of melanoma cells, called *nests*, are a prominent feature of melanoma progression 1,2]. Identifying the presence and characteristics of melanoma nests in human skin is an important diagnostic tool [3,4]. Furthermore, nest size is an important characteristic because larger melanoma nests are associated with more aggressive melanoma [3]. Recent 3D experimental work by Wessels *et al.* [5] suggests that melanoma nest formation in Matrigel is driven by cell migration. However, nest formation might be different in human skin, where melanoma cells are in contact with other cell types [1,6]. We hypothesise that two different mechanisms could lead to nest formation: (i) cell proliferation, where clusters of melanoma cells are formed primarily through mitosis (Figure 5.1*a*); and (ii) cell migration, where clusters of adhesive melanoma cells form primarily through melanoma cell migration (Figure 5.1*b*). Cell migration occurs over a short time scale of hours, whereas cell proliferation takes place over a much longer time scale of days. Since our work is focused on the role of proliferation, we perform experiments over a period of four days so that we are able to observe and quantify the role of cell proliferation. This choice of experimental time scale means that our experimental observations do not resolve the details of cell migration, which would require a much finer time resolution in the experiments.
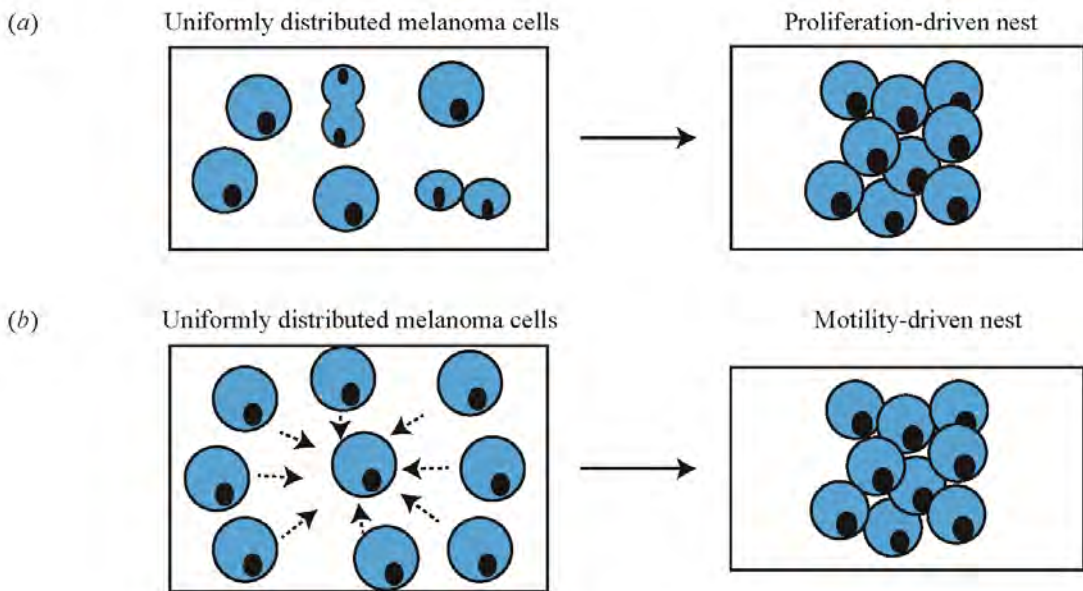
Figure 5.1: Mechanisms that drive melanoma nest formation. Schematics illustrating: (*a*) proliferation-driven nests; and (*b*) migration-driven nests. In both cases the schematic shows an initially-uniform distribution of cells that lead to the formation of a nest either by the action of proliferation (*a*) or migration (*b*).

We use a 3D human skin experimental model [7,8] to discriminate between these two conceptual models by performing a suite of experiments in which we systematically vary the initial density of proliferative melanoma cells placed on 3D human skin. This initial series of experiments allow us to examine the role of initial cell number in driving nest formation. All experiments are repeated using non-proliferative, gamma-irradiated melanoma cells. We find that higher initial numbers of melanoma cells lead to larger nests, and that cell proliferation leads to dramatically-larger nests. All experimental outcomes are consistent with a series of 3D simulations from an IBM [9]. These results provide insight into the mechanisms driving nest formation, showing that the mechanisms in 3D human skin are different to monoculture experiments performed in Matrigel.

5.3   RESULTS AND DISCUSSION

5.3.1   *Confirmation that irradiated melanoma cells do not proliferate and are capable of migrating in a two-dimensional barrier assay*

Experiments involving populations of proliferative melanoma cells are performed using non-irradiated SK-MEL-28 cells [10]. Experiments where melanoma cell proliferation is suppressed are performed using irradiated, but otherwise identical SK-MEL-28 cells [11,12]. The melanoma cells are gamma-irradiated to inhibit mitosis. It is possible that irradiation may have other impacts on cellular behaviour and could also influence DNA functioning [12,13].   We perform a series of live assays to show that irradiation does not affect the adherence or morphology of melanoma cells. These live cell assays involve placing populations of irradiated and non-irradiated melanoma cells on a two-dimensional tissue culture plate and making observations of cell numbers of a period of 24 hours [14]. Therefore, these assays provide quantitative information about whether the populations of melanoma cells are capable of proliferating. Results confirm that irradiated melanoma cells do not proliferate. Furthermore, these assays show that irradiation does not cause the cells to die and does not affect cell morphology [see Supplementary Material].

Two-dimensional (2D) barrier assays confirm that irradiated melanoma cells survive and migrate. Populations of irradiated melanoma cells are monitored over four days to confirm that irradiation does not impede the ability of cells to migrate. We use circular barrier assays to compare the spatial expansion of irradiated and non-irradiated melanoma cell populations. The leading edge of the spreading populations is detected using ImageJ [15], which also provides an estimate of the area occupied by the spreading population of cells. Since the spreading populations of cells maintain an approximately circular shape, we convert the estimates of area into an equivalent diameter and we report data in terms of the diameter of the spreading population. Results are obtained in triplicate. Images in Figure 5.2*a-b* show the increase in the diameter of the spreading cell populations for both irradiated and non-irradiated melanoma cells over four days. The upper row of images in Figure 5.2*a-b,* show increased spatial expansion of the population of non-irradiated cells compared to the population of irradiated melanoma cells in the lower row. Since irradiated melanoma cells do not proliferate, we expect that the size of the expanding

population of irradiated cells will be smaller than the size of the expanding population of non-irradiated cells [16]. However, the area occupied by the population of irradiated melanoma cells increases over the four-day period, and this increase is due to cell migration alone. To confirm these visual observations, we also quantify the spatial spreading of irradiated and non-irradiated melanoma cell populations.
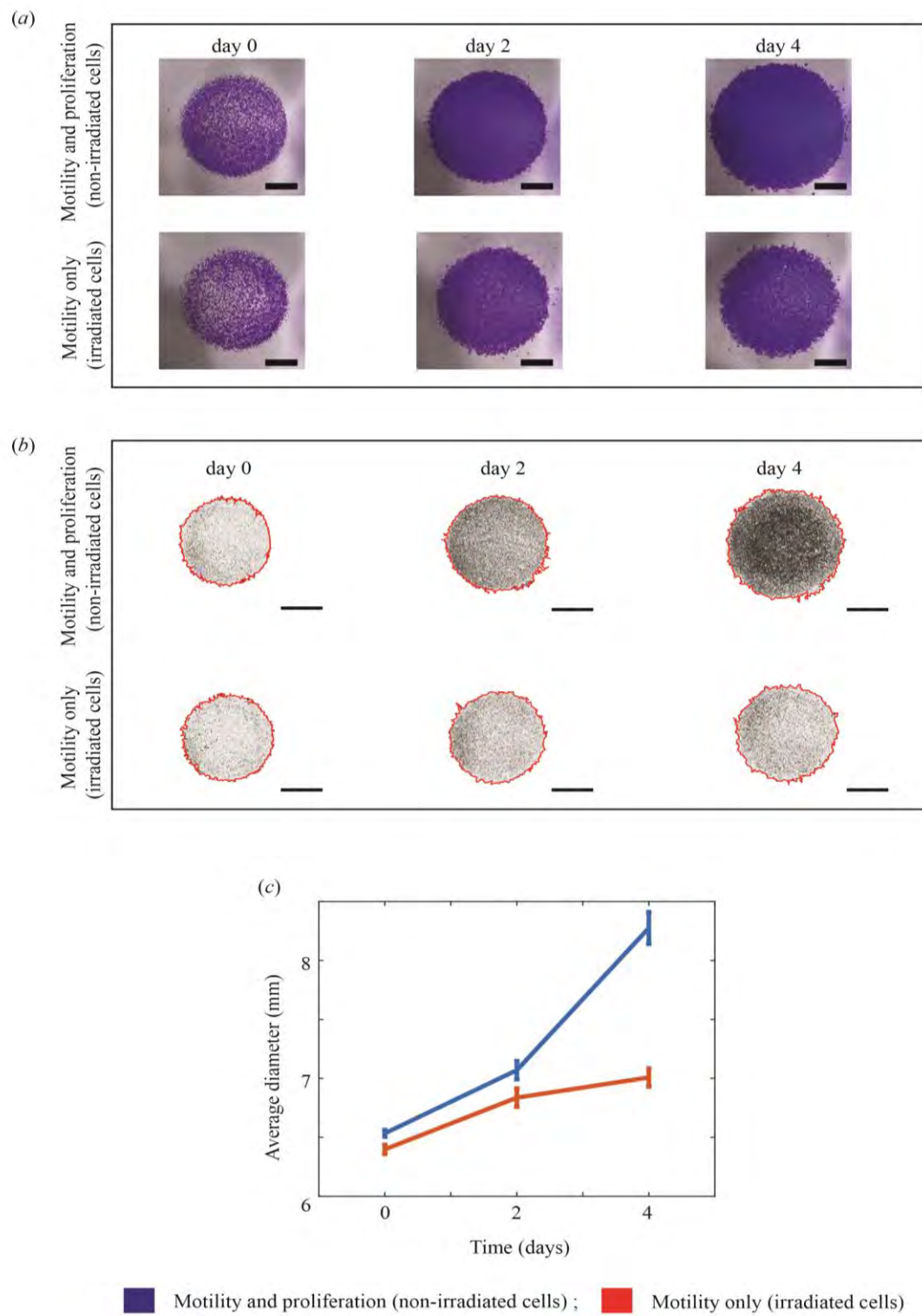
Figure 5.2: Two-dimensional spatial expansion of irradiated and non-irradiated melanoma cell monocultures. (*a*) Experimental images show barrier assays initialised with approximately 10000 melanoma cells. The upper row of images show non-irradiated (proliferative) melanoma cells, and the lower row shows irradiated (non-proliferative) melanoma cells. The images show the spreading of cell

populations at zero, two and four days, respectively. The scale bar is 2 mm in each image. (*b*) Experimental images from (*a*) analysed by ImageJ. Results show the position of the leading edge of the spreading population (red) superimposed on images of the spreading populations. The upper row of images corresponds to non-irradiated melanoma cells, and the lower row of images show irradiated melanoma cells. The images show the spreading of cell populations at zero, two and four days, respectively. The scale bar in each image is 3 mm. (*c*) Data shows the average diameter of the spreading populations as a function of time (n=3). All data generated using non-irradiated melanoma cells is in blue, and data generated using irradiated melanoma cells is in red. Plots in (*c*) also show the variability. The error bars correspond to the sample standard deviation (n=3).

Data in Figure 5.2*c* shows the increase in diameter of both irradiated and non-irradiated melanoma cell populations over four days. At all times considered, the average diameter of the irradiated cell population is less than the average diameter of the non-irradiated cell population. This is expected because the irradiated melanoma cells do not proliferate, and it is known that proliferative populations of cells expand and invade the surrounding empty space faster than non-proliferative populations of cells [9,16]. Most importantly, the experiments initialised with irradiated melanoma cells show an increase in the diameter of the spreading population, confirming that irradiation does not prevent migration. All experiments are performed in triplicate and the averaged results are presented. We now use both, irradiated and non-irradiated melanoma cells in 3D experiments to identify the mechanism that drives melanoma nest formation.

5.3.2   *Identifying the dominant mechanism driving melanoma nest formation*

Nests of melanoma cells are well-characterised histological features of melanoma progression. Early identification of these nests is critical for successful melanoma treatment. However, in addition to examining the presence of melanoma nests, it is important to identify the biological mechanisms that lead to nest formation as this information might be relevant to the development of new drugs. To examine these pathways we use a 3D experimental skin model.

Irradiated and non-irradiated melanoma cells are cultured with primary keratinocytes and primary fibroblasts in the 3D experimental skin model for four days. From this point we refer to keratinocyte and fibroblast cells as *skin* cells. All cells are initially placed onto the 3D experimental skin model as a monolayer, as uniformly as possible. MTT (3-(4,5-dimethylthiazol-2-yl)-2,5-diphenyltetrazolium bromide) assays highlight the metabolic activity of all cells, and show the spatial extent and spatial structure of cells on the top surface of the 3D experimental skin model. Images in Figure 5.3*a-b* show prominent dark purple clusters on the surface of some 3D experimental skin models. Control studies, where 3D experiments are constructed without melanoma cells, show a complete absence of nests [see Supplementary Material 1] suggesting that the dark purple clusters in Figure 5.3*a-b* are melanoma nests. We make the natural assumption that higher densities of metabolically active cells are associated with darker purple colouration.
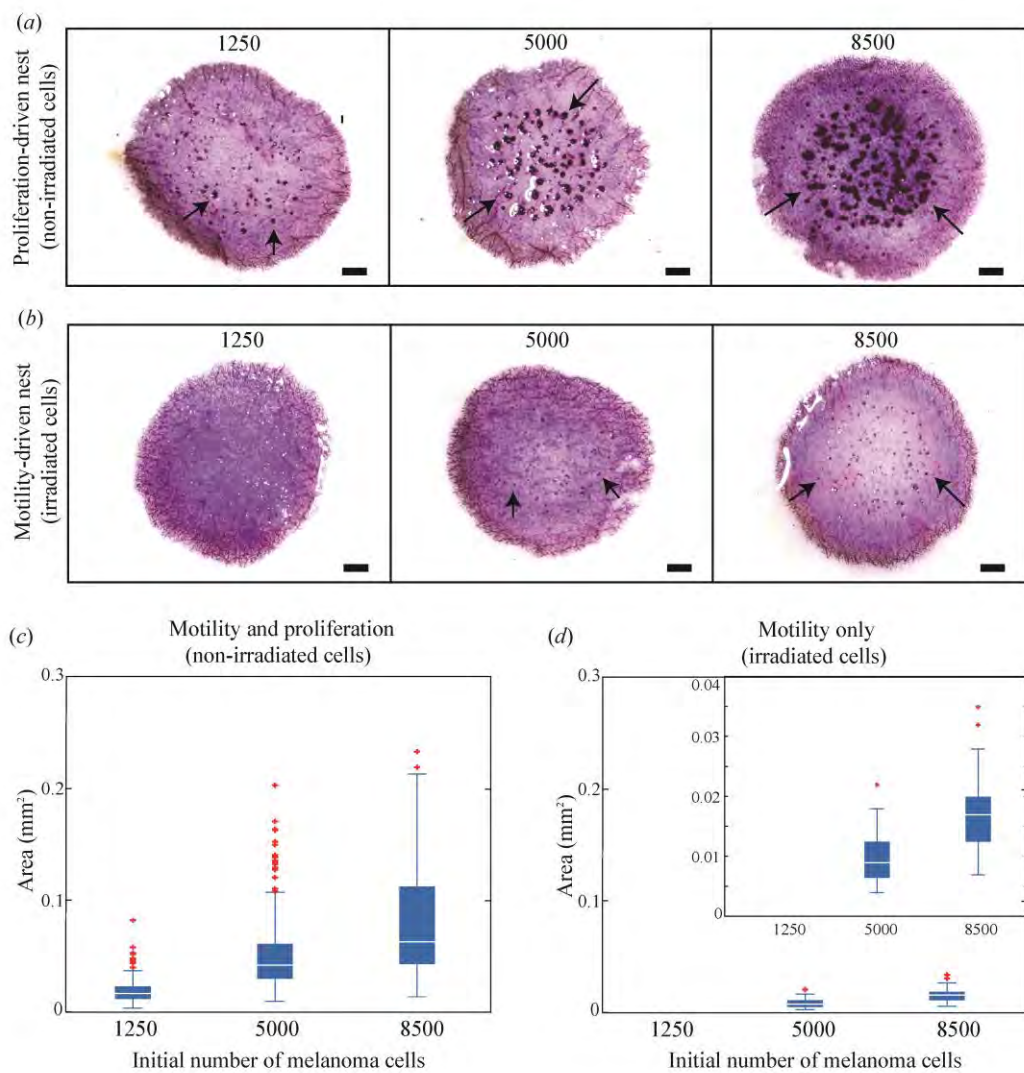
Figure 5.3: Proliferation drives melanoma nest formation. (*a*) MTT assays show all metabolically active cells (light purple) on the surface of the 3D experimental skin model initialised with different numbers of proliferating melanoma cells, as indicated. (*b*) Equivalent results with irradiated melanoma cells. Melanoma nests are in dark purple (arrows). Scale bars are 1 mm. (*c*)-(*d*) Box plots showing nest area as a function of initial number of melanoma cells. Inset in (*d*) shows details in the range 0-0.045 mm^2.

Images in Figure 5.3*a* show that larger nests are associated with higher initial numbers of melanoma cells. To quantify this we measure the area of individual nests using ImageJ [15], and data in Figure 5.3*c* confirms our visual observation. Interestingly, larger initial numbers of melanoma cells lead to a smaller number of larger nests [see Additional file 2]. This is consistent with smaller sized nests coalescing into a smaller number of larger nests over time. These results suggest smaller nests might coalescence into larger nests over time. To confirm this conjecture we would need to analyse our experiments using time-lapse imaging. Since our results show that cell number plays a critical role, we now examine the role of proliferation by suppressing mitosis.

We examine the role of cell proliferation by constructing 5.3*d* experimental skin models with irradiated melanoma cells. Images in Figure 5.3*b* show that this leads to the formation of dramatically smaller nests. To quantify our results, the area of individual nests is measured using ImageJ [15] [see Supplementary Material 2]. Data in Figure 5.3*d* shows a similar trend to data in Figure 5.3*c* as the nest area increases with initial cell number. However, comparing results in Figure 5.3c-d shows that proliferation plays a dominant role in nest formation. For example, experiments initialised with 8500 proliferative melanoma cells leads to a median nest area of 0.15 mm^2, whereas the median nest area is just 0.027 mm^2 when proliferation is suppressed. These measurements of nest area do not provide direct estimates of the number of cells present in each nest. However, it is reasonable to assume that larger nests contain more cells than smaller nests.

Our results are different to previous 3D studies that show melanoma nests are formed by cell migration [5]. We anticipate that the difference in our outcome could be due to: (i) differences between the melanoma cell lines used; (ii) the interaction of melanoma cells with the surrounding skin cells in the 3D experiments; or, (iii) differences in the material used to construct the 3D model described in [5] and the 3D model used in this study. Since our experiments are performed in 3D materials derived from human skin, and our experiments involve culturing melanoma cells together with primary human skin cells, we feel that our results are more realistic than examining nest formation in monoculture experiments in Matrigel. We now

perform immunohistochemistry to confirm that irradiated melanoma cells survive in the 3D experimental human skin model over a period of four days.

5.3.3 *Irradiated melanoma cells survive in a 3D experimental skin model*

Here, we perform a series of experiments using a specific melanoma marker to provide additional evidence that nests observed on the 3D experimental human skin models are clusters of melanoma cells, and that irradiated melanoma cells survive in a 3D environment over four days. The 3D experimental skin models are constructed using both irradiated and non-irradiated melanoma cells. Vertical cross-sections through the 3D experimental skin models initialised with melanoma cells are stained using S100, which is a reliable melanoma cell marker [17]. Both irradiated and non-irradiated melanoma cells are found in the 3D experimental skin model after four days. Images in Figure 5.4*a-f* show positive S100 staining of melanoma cells. In particular, Figure 5.4*b,d,f* show positive S100 staining of irradiated melanoma cells after four days. This immunostaining confirms that irradiation does not alter the antigen properties of melanoma cells for this marker, and the irradiated melanoma cells survive in a 3D experimental skin model for four days. Our experimental results use skin cells and skin dermis from one donor. Additional results using cells and dermis from two other donors show little variability between them.
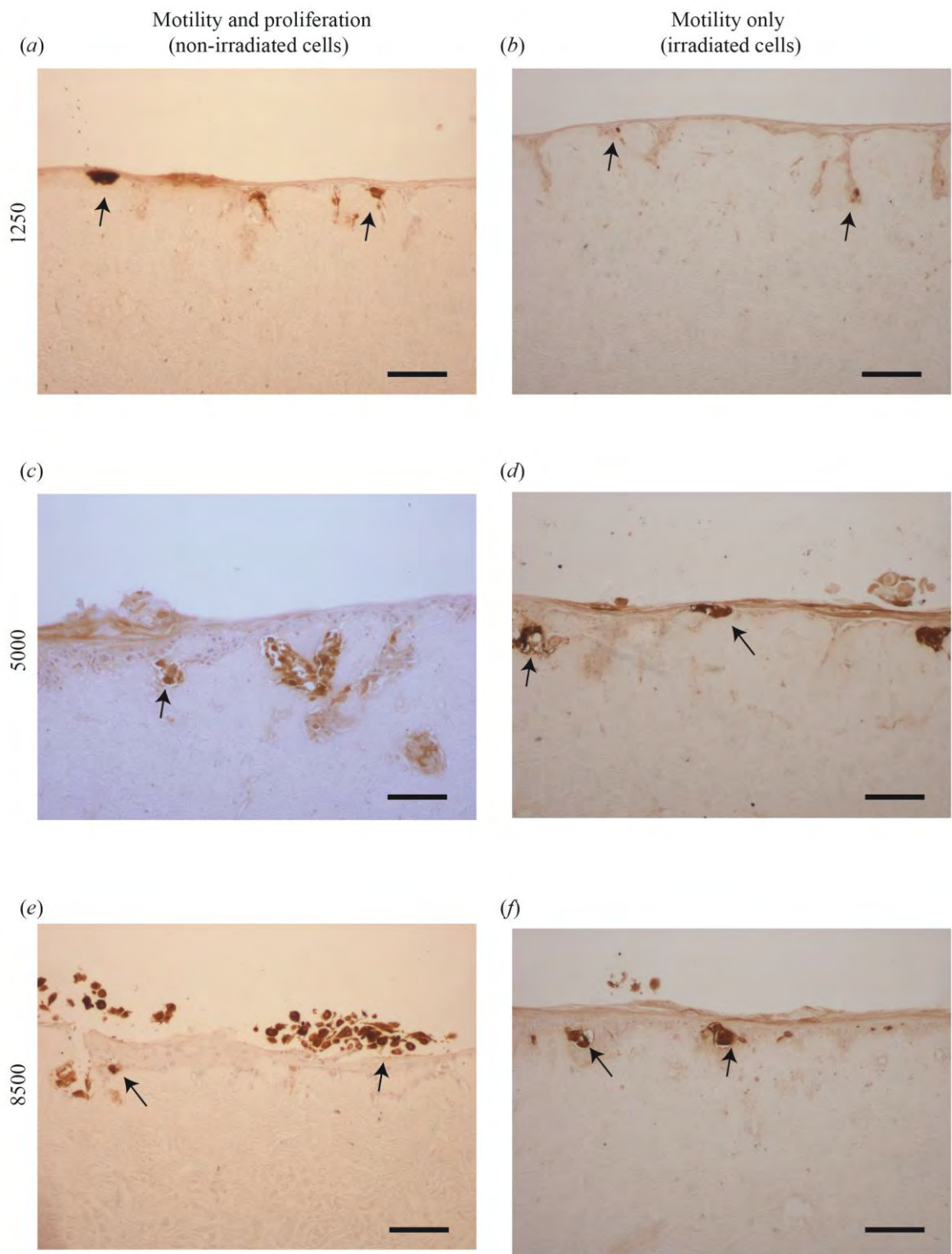
Figure 5.4: Irradiated and non-irradiated melanoma cells survive in 3D experimental skin models. S100 identifies melanoma cells (brown), and the arrows indicate positive staining. (*a*), (*c*) and (*e*) Cross-sections through 3D experimental skin models initialised with 1250, 5000 and 8500 non-irradiated melanoma cells, as indicated. (*b*), (*d*), and (*f*) Cross-sections through 3D experimental skin models

initialised with 1250, 5000 and 8500 irradiated melanoma cells, respectively. Scale bar in each image is 100 μm.

5.3.4   *Variability between skin samples*

We now examine whether there is any important variability in our results between skin samples from different donors.   To examine this we perform additional experiments using dermis and primary skin cells from three different donors, which we denote as donor A, donor B and donor C. We show MTT assays on the 3D experimental skin models initialised with non-irradiated and irradiated melanoma cells in Figure 5.5. The upper row of images in Figure 5.5*a-c* show 3D experimental skin models initialised with 1250, 5000 and 8500 non-irradiated melanoma cells, respectively. In each case, we see that larger nests are associated with higher initial number of melanoma cells. A similar trend is observed for the images in the lower row of images in Figure 5.5*a-c* where the experiments are initialised with an equivalent number of irradiated melanoma cells. However, regardless of whether we consider results from donor A, donor B or donor C, we always see that nest formation is dramatically reduced when we consider irradiated, non-proliferative melanoma cells.
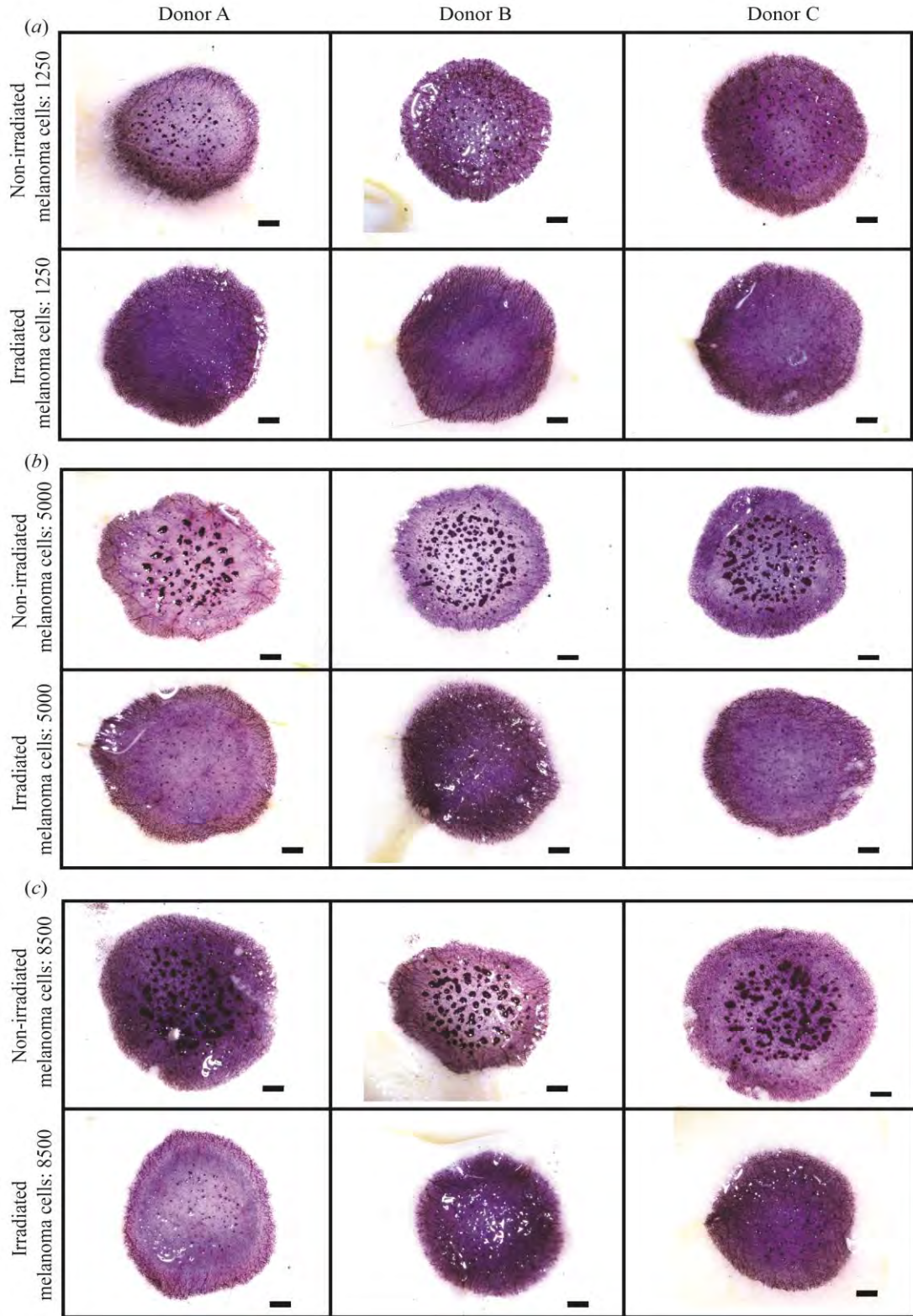
Figure 5.5: Donor variability in 3D experimental skin models with melanoma cells. Experimental images show metabolically active cells (light purple) on the 3D experimental skin model after four days. The skin models are constructed using primary skin cells and dermis from three different donor samples denoted A; B; and

C. The scale bars are 1 mm. The melanoma nests are shown in dark purple. In each set of subfigures, (*a*)-(*c*), the images in the upper row show experiments initialised with 1250, 5000 and 8500 non-irradiated melanoma cells, respectively. In each set of subfigures, (*a*)-(*c*), the images in the lower row show experiments initialised with 1250, 5000 and 8500 irradiated melanoma cells, respectively.

Visual inspection of the images in Figure 5.5 suggests that the size, shape and number of individual nests does vary slightly between the three donors. However, the influence of the initial cell number and the action of cell proliferation on nest formation remains consistent between the skin samples from the three different donors. That is, larger initial numbers of cells produces larger nests, and the action of cell proliferation leads to dramatically larger nests. To provide additional evidence we also measure the area of individual nests on skin samples from all donors using ImageJ [15]. Data provided [see Supplementary Material 2] confirm that the relationship between initial cell number and the action of cell proliferation holds for all three donor samples.

The nests on the 3D experimental skin model initialised with 1250 irradiated melanoma cells are very small. Most experimental replicates of this particular experiment do not lead to any visually observable nests, as shown in the lower row of images in Figure 5.5*a*. Therefore, data for nest area in these experiments is omitted [see Supplementary Material 2]. We now use an IBM to verify our experimental outcomes.

5.3.5   *Modelling melanoma nest formation using an individual based model*

To corroborate our experimental findings, we use a random walk-based IBM to simulate the key features of the experiments. The IBM describes the spatial distribution of simulated cells on a 3D square lattice [18]. We use a 3D lattice of cross section 3 mm × 3 mm, and depth 2 mm, to represent the central region of each experimental 3D skin model (Figure 5.6*a*). The lattice spacing is 20 μm. Simulated cells are called *agents*. We consider non-adhesive skin agents (green, Figure 5.6*b*)

and adhesive melanoma agents (blue, Figure 5.6*b*). Note that the domain shown in Figure 5.6*b* is a small subregion within the overall domain so that we visualise just the upper portion of the lattice where the majority of agents are located.
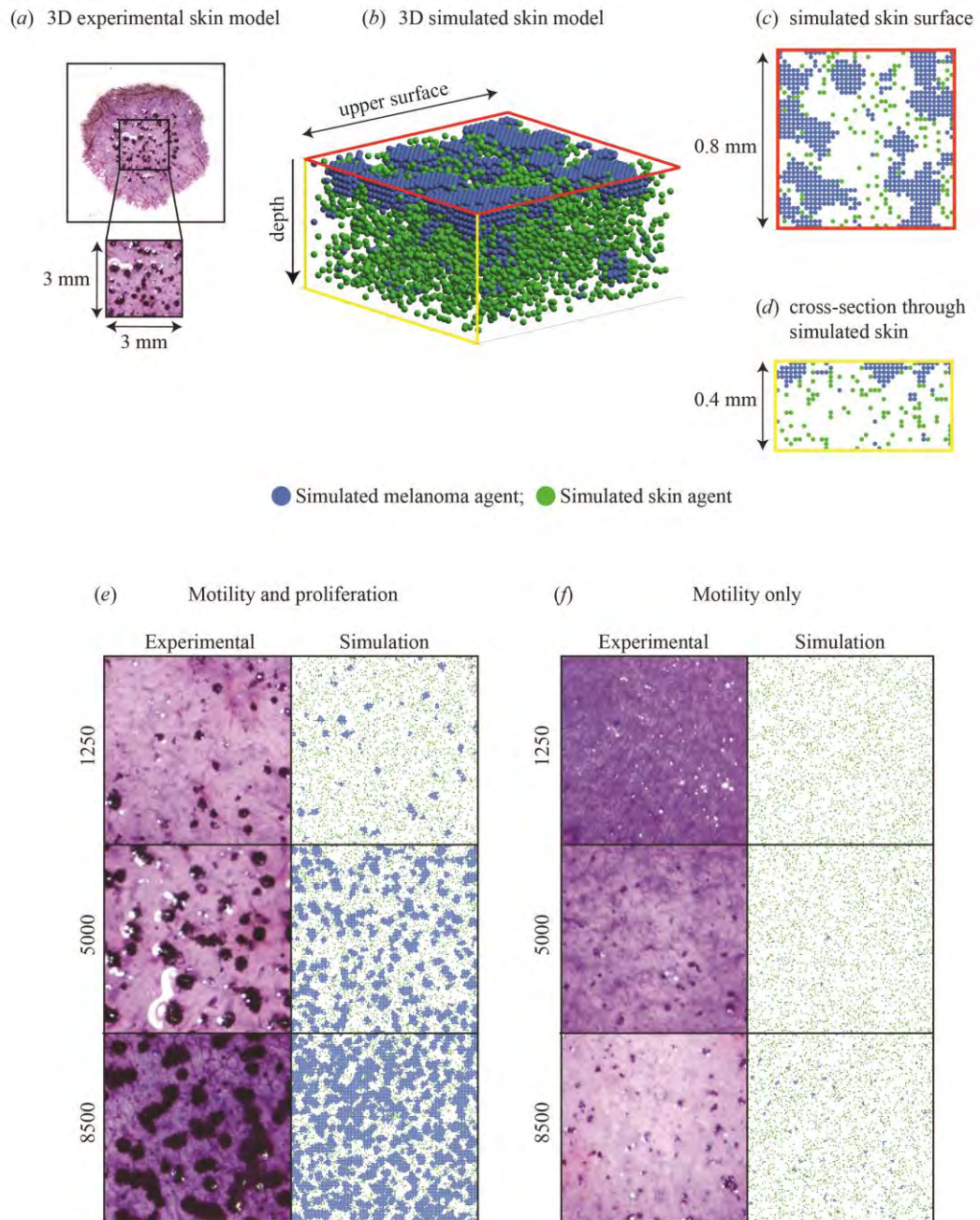
Figure 5.6: IBM simulations corroborate experiments. (*a*) Experimental image showing all metabolically active cells (light purple) on a 3D experimental skin model initialised with 5000 proliferating melanoma cells. The magnified 3 mm × 3 mm region shows melanoma nests (dark purple). (*b*) Sub-region of the 3D simulated skin model with simulated skin agents (green) and simulated melanoma agents (blue). The dimension of the upper surface is 0.8 mm × 0.8 mm, and the depth is 0.4 mm. (*c*) Upper surface of the simulated skin model. (*d*) Cross-section through the simulated skin model. (*e*)-(*f*) Experimental and simulated nests initiated with varying numbers

of melanoma cells, as indicated, and an equivalent density of simulated melanoma agents, respectively. Results in (*e*) correspond to non-irradiated (proliferative) melanoma cells/agents. Results in (*f*) correspond to irradiated (non-proliferative) melanoma cells/agents. Images in (*e*)-(*f*) have dimensions 3 mm × 3 mm, and the depth is 2 mm. IBM parameters are $\tau = 0.01$ h; $\Delta = 20$ μm; $P_p^{(m)} = 0.0004$; $P_m^{(m)} = 0.0075$; $P_p^{(s)} = 0.00025$; $P_m^{(s)} = 0.0075$; and $q = 0.7$. Simulations with suppressed melanoma proliferation use $P_p^{(m)} = 0.0$.

It is well-known that it can be difficult to quantitatively calibrate stochastic IBMs to match complicated experimental data precisely [19,20]. Therefore we simply use parameters in the IBM that are adapted from previous work [9,21]. These previous studies report estimates of the proliferation rate of SK-MEL-28 melanoma cells, the proliferation rate of primary human fibroblast cells, the cell diffusivity of SK-MEL-28 melanoma cells and the cell diffusivity of primary human fibroblast cells [21]. We make a reasonable assumption that the proliferation rate and cell diffusivity of keratinocyte cells are the same as the proliferation rate and the cell diffusivity of the fibroblast cells, respectively. Our estimate of the strength of cell-to-cell adhesion is also adapted from a previous study where this parameter was determined using a series of two-dimensional barrier assays with a metastatic melanoma cell line [9]. This approach of using previously-reported parameter estimates allows us to focus on understanding the roles of the key underlying biological features, such as the role of cell migration and cell proliferation, without being distracted by the secondary task of obtaining precise parameter estimates. We achieve this by using previously determined parameter estimates and simply comparing simulation results where melanoma cell proliferation is present, with simulation results where melanoma cell proliferation is suppressed.

We initialise the IBM simulations to precisely mimic the way that cells are placed onto the upper surface of the 3D skin in the experiments. To initialise the simulations we randomly place a particular number of skin and melanoma agents onto the surface of the 3D lattice. The initial number of agents in each subpopulation is chosen to match to the initial cell density in the experiments. Figures 5.6*b-d* show smaller sub-regions of the 3D simulated skin to visualise the distribution of agents on

the 3D lattice as clearly as possible. Results in Figure 5.6*b-c* show that the IBM predicts the formation of clusters of adhesive melanoma agents on the surface of the 3D lattice. Results in Figure 5.6*d* shows how the IBM predicts the downward movement of both skin and melanoma agents. Figure 5.6*d* shows that skin agents move deeper into the 3D lattice than the melanoma agents, while nests of melanoma agents tend to remain on the surface. Overall, the spatial arrangement of skin and melanoma agents in the IBM (Figure 5.6*b-d*) is similar to the spatial arrangement of cells in the 3D experiments (Figure 5.3-5.4) [6].

To explore the role of initial melanoma cell number in nest formation, IBM results in Figure 5.6*e* show that nests form on the surface of the 3D lattice, and that the trends in simulated nest area are qualitatively similar to those in the corresponding experiments. Therefore, the simulation outcomes in Figure 5.6*e* confirm that initial melanoma cell number is an important factor in driving nest formation. We also explore the role of cell proliferation by repeating the simulations in Figure 5.6*e* without any melanoma agent proliferation. Simulation results in Figure 5.6*f* are comparable to the corresponding experimental results, as we observe similar trends in nest size and morphology. In conclusion, similar to the experiments, our 3D simulation results indicate that melanoma nest formation is driven by initial melanoma cell number, and that the presence of melanoma proliferation leads to dramatically-larger nests.

In addition to qualitatively visualising the trends in Figure 5.6, we also use the IBM results to quantitatively examine trends in simulated nest size. Boxplots in Figure 5.7 show data quantifying the size of nests predicted using the IBM under four different conditions. We measure the area of individual nests in the IBM using the Image Region Analyzer in MATLAB [22]. For model realisations where nests are not clearly defined we adjust the image manually by increasing the separation between neighbouring nests so that the Image Region Analyzer accurately measures nests separately. We exclude extremely small nests that are composed of less than four agents.
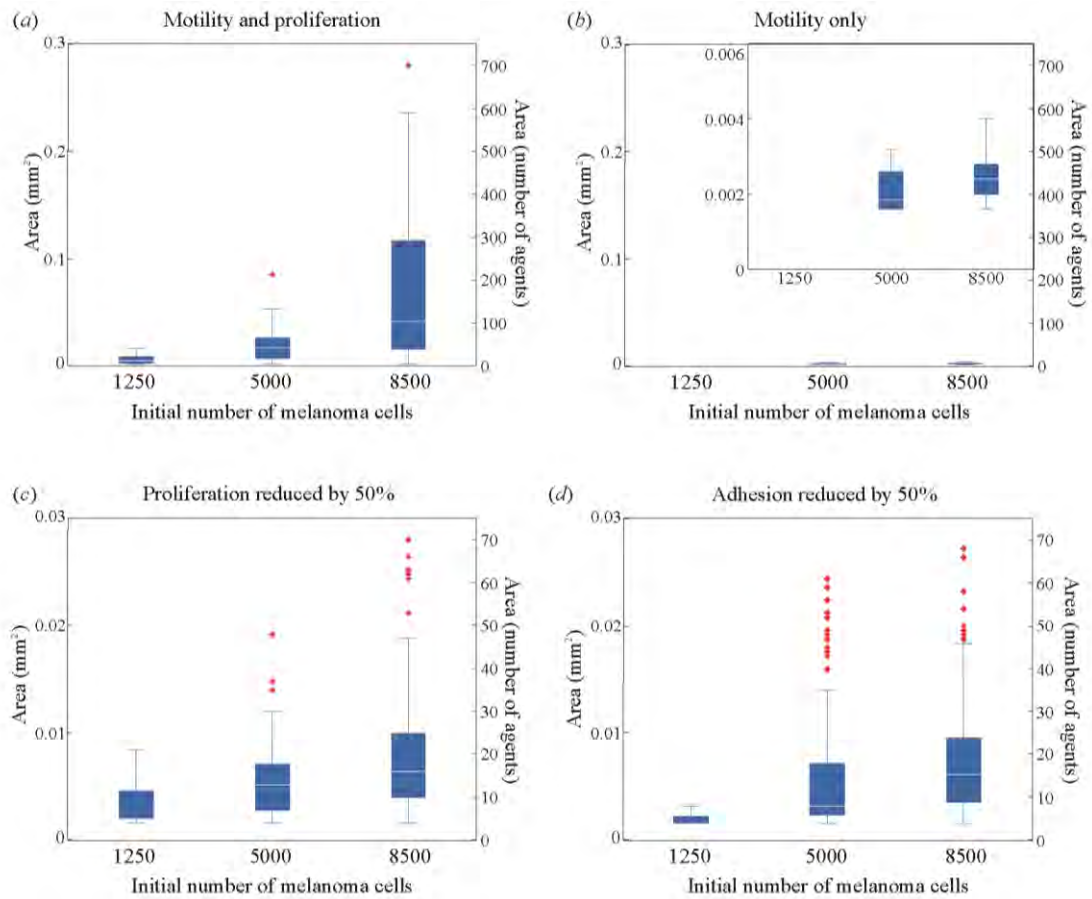
Figure 5.7: Mathematical model confirms trends in nest formation data and predicts new results. Box plots of nest size, assuming the area of each melanoma agent is 20 × 20 = 400 μm2, for a typical realisation of the IBM for (*a*) proliferative melanoma agents; (*b*) non-proliferative melanoma agents; (*c*) proliferative melanoma agents where the proliferation rate is reduced by 50%; and, (*d*) proliferative melanoma agents where adhesion strength is reduced by 50%. In each case, outliers are indicated by red crosses. Results in (*a-b*) confirm the trends in Figs. 5.3*c-d* and 5.6*e-f*. Note the difference in the vertical scale in (*c-d*) compared to (*a-b*)

Results in Figure 5.7*a* confirm that larger initial number of melanoma agents leads to larger simulated nests. Results in Figure 5.7*b* show that suppressing proliferation in the IBM leads to dramatically smaller nests. These results in Figure 5.7*a-b* correspond to the experimental results in Figure 5.3c-d. Both the boxplots in Figure 5.3*c-d* and Figure 5.7*a-b* report nest area in the same units, therefore this is a direct comparison of the experimental observation and the prediction of the computational model.

In addition to using the IBM to replicate the experimental results, it is also straightforward to adjust the parameters in the IBM to make some simple predictions that have not been experimentally validated. Additional results in Figure 5.7*c* show the distribution of simulated nest size when the proliferation rate of melanoma cells is reduced by half. Noting the difference in the vertical scale in Figure 5.7*a* and Figure 5.7*b*, we see that reducing the proliferation rate of melanoma cells by half leads to a reduction in simulated nest size by a factor of ten. Similarly, additional results in Figure 5.7*d* show the distribution of simulated nest size when the strength of cell-to-cell adhesion for the melanoma cells is reduced by half. Again, noting the difference in vertical scale in Figure 5.7*a* and Figure 5.7*d* shows that reducing the strength of melanoma adhesion by half reduces the size of simulated nests be a factor of ten.

5.4   CONCLUSION

Our combined experimental and simulation findings demonstrate that cell proliferation plays the dominant role in melanoma nest formation. While it is well-accepted that proliferation is important in the latter stages of tumour growth [23] and in the spatial spreading of cell populations [24], our work shows that proliferation is vitally important at the very earliest stages of melanoma progression. As far as we are aware, our work if the first to use a 3D experimental human skin model incorporating irradiated and non-irradiated melanoma cells and shows that cell proliferation is the dominant mechanism that drives melanoma nest formation.

Our results, pointing to the importance of cell proliferation, are interesting for a number of reasons: (i) previous monoculture experiments report that melanoma nests are formed by cell migration in Matrigel [5]. One potential explanation for this difference is that the Matrigel experiments are very different to our experiments since we study nest formation on 3D human tissues where melanoma cells are in contact with skin cells; (ii) some previous mathematical models of cluster/nest formation focus on cell migration only, e.g. [25], whereas we find that cell proliferation plays the most important role; and (iii) our findings about the importance of cell proliferation in melanoma progression are consistent with the fact that many promising melanoma drugs aim to suppress proliferation [26,27,28].

Our suite of experimental results can be extended in many ways. For example, one limitation of our work is that we group the keratinocytes and fibroblast cells together, and refer to these cells as skin cells. It would be interesting to repeat our work and use specific markers to differentiate between these two populations of skin cells [29]. Another interesting extension of our experimental work could be to examine nest formation in 3D experiment using a mixture of irradiated and non-irradiated melanoma cells. This condition could mimic a partial reduction in proliferation, whereas our results correspond to a total inhibition of melanoma cell proliferation. Additionally in these experiments, cell proliferation can be blocked using drug treatments, such as mitomycin-C or some other commercially available proliferation inhibitor. Another relevant extension could be to perform a series of 3D skin experiments where the melanoma cells are treated so that they are non-migratory but maintain their ability to proliferate. Finally, it could also be interesting to repeat the 3D skin experiments as described here, and to image the formation of nests on a much shorter timescale that is comparable to the timescale of cell migration. If we had access to such time course data, it might then be possible to compare this kind of transient data from the experiment with transient information from a mathematical model [30].

Our suite of modelling results can also be extended in many ways. In this work we choose to work with a relatively simple mathematical model that represents just the key processes of interest, namely a population of motile, proliferative and adhesive melanoma cells, and a population of motile and proliferative skin cells. This model

is parameterised using previously-determined parameter estimates [9,21]. While our model is useful in that it can both recapitulate our experimental results as well as generating new predictions that could be verified or challenged in future experimental studies, it would also possible to repeat all our simulation results using a more complicated mathematical model. For example, other modelling approaches such as continuous-space lattice-free models [31] or discrete models with force potentials between agents [32] could also be used in this context. While it is always tempting to use a more complicated mathematical model that incorporates additional biological detail, this approach is limited in that using more complex models requires additional parameters. We avoid this situation by always working with the simplest possible mathematical model that describes just the key features of interest.

5.5 METHODS

5.5.1 *Keratinocyte isolation and culture*

Queensland University of Technology (QUT) human research ethics obtained written approval for the skin samples to be used in this study (approval number: QUT HREC #1300000063; UnitingCare Health 2003/46). Skin samples are collected from patients undergoing elective plastic surgery. Human keratinocyte cells are isolated from skin and cultured in full Green's medium containing DMEM with Ham's F12 (Thermo Scientific, Australia) in a 3:1 v/v ratio, 10% FCS, 2 mM L-glutamine, 50 U/ml of penicillin, 50 μg/ml of streptomycin, 180 mM adenine (Sigma Aldrich, Australia), 1 μg/ml insulin, 0.1 μg/ml cholera toxin (Sigma Aldrich), 0.01% non-essential amino acid solution (Thermo Scientific), 5 μg/ml transferrin (Sigma Aldrich), 0.2 μM triiodothyronine (Sigma Aldrich), 0.4 μg/ml hydrocortisone (Sigma Aldrich) and 10 ng/ml human recombinant EGF (Thermo Sceientific) following protocols described previously [17,33]. Primary keratinocyte cells are cultured at 37 ºC, in 5% CO_2 and 95% air.

5.5.2 Fibroblast isolation and culture

Human fibroblast cells are isolated following protocols in Haridas *et al*. [15]. Primary fibroblast cells are cultured at 37 °C, in 5% CO_2 and 95% air.

5.5.3 Melanoma cell culture

The human melanoma cell line SK-MEL-28 is cultured as described in Haridas *et al*. [17]. SK-MEL-28 melanoma cells are kindly donated by Professor Brian Gabrielli (Mater Research Institute-University of Queensland). Cells are cultured at 37 °C, in 5% CO_2 and 95% air.

A batch of SK-MEL-28 melanoma cells is irradiated to prevent cell proliferation. Approximately $1x10^7$ melanoma cells are gamma-irradiated using a Gammacell 40 research irradiator (Australia) at approximately 0.8 Gy/minute for one hour resulting in a cumulative dose of 50 Gy. We refer to these non-proliferative cells as *irradiated* melanoma cells, and the proliferative cells as *non-irradiated* melanoma cells.

Identification of SK-MEL-28 cells is validated using short tandem repeat profiling (Cell Bank, Australia. January 2015).

5.5.4 Barrier assay

We perform circular barrier assays to observe and measure the spreading of populations of irradiated and non-irradiated melanoma cells. The protocol from Simpson *et al*. [16] is followed. Briefly, sterile stainless steel silicon barriers (Aix Scientific, Germany) are carefully placed in a 24-well tissue culture plate with 0.5 ml growth medium. The tissue culture plate containing cells is incubated for one hour at 37 °C, in 5% CO_2 and 95% air. Viable cell suspensions of 20000 cells/100 µl of irradiated and non-irradiated melanoma cells are carefully introduced into the barriers to ensure an even distribution of cells. The tissue culture plates containing cell suspensions are incubated for a further two hours to allow cells to attach to the plate. The barriers are removed and the cell layers are washed with serum-free medium (culture medium without foetal calf serum) and replaced with fresh growth medium.

Plates are then incubated at 37 °C, in 5% CO_2 and 95% air for zero, two and four days. We replace the growth medium after two days to replenish the nutrients. Each assay is performed in triplicate.

5.5.5 Crystal violet staining

We use the staining technique described by Simpson *et al*. [14] to analyse the barrier assays. In brief, cell monolayers are washed with phosphate buffered saline (PBS; Thermo Scientific, Australia) and fixed using 10% neutral buffered saline (United Biosciences, Australia) for 20 minutes at room temperature. The fixed cells are stained using 0.01% v/v crystal violet (Sigma Aldrich, Australia) in PBS for 20 minutes at room temperature. Excess crystal violet stain is removed using PBS, and the plates are air-dried. Images of irradiated and non-irradiated cell populations are acquired using a Nikon SMZ 800 stereo microscope fitted with a Nikon digital camera.

5.5.6 Establishing 3D experimental skin model with melanoma cells

We establish 3D experimental skin models using the skin collected from donors undergoing elective plastic surgery. The protocol for establishing the 3D skin equivalent model with melanoma cells is adapted from previous work [7]. In brief, sterile stainless steel rings (Aix Scientifics) with a radius of 3 mm are placed on the papillary side of the de-epidermised dermis in a 24-well tissue culture plate (Nunc®, Australia). We refer to the de-epidermised dermis as *dermis*. Single cell suspensions of primary keratinocyte cells (20000), primary fibroblast cells (10000) and non-irradiated melanoma cells (1250; 5000; 8500), are seeded onto the dermis in full Green's medium as uniformly as possible, and incubated at 37 °C, in 5% CO_2 and 95% air for two days. We refer to the primary keratinocyte and fibroblast cells as *skin cells*. Subsequently, the stainless steel rings are removed and the dermis containing cells is submerged in full Green's medium for a further two days. After this four-day pre-culture period, the spatial distribution of cells in the 3D experimental skin model is analysed. We also perform a series of equivalent experiments using irradiated melanoma cells.

All experiments are performed in triplicate. Furthermore, all experiments are repeated using primary skin cells and dermis from three separate donors to account for variability between different donors.

5.5.7 MTT Assay

An MTT (Thermo Scientific) assay is performed to check the metabolic activity of cells on the 3D experimental skin models. These assays are imaged with a stereo microscope (Nikon SMZ 800) fitted with a Nikon digital camera. We follow the protocol from Haridas *et al*. [7].

5.5.8 Immunohistochemistry on 3D experimental skin models with melanoma cells

We use immunohistochemistry to identify melanoma cells in the 3D experimental skin models. 10% neutral buffered formalin (United Biosciences, Australia) is used to fix the 3D experimental skin models. The tissue is divided through the centre of the MTT positive region using a sterile blade. The two smaller pieces of tissue are processed and embedded in paraffin. These samples are sectioned into 5 μm thick sections using a microtome. These sections are de-paraffinised, rehydrated and then subjected to heat-mediated antigen retrieval treatment using sodium citrate buffer (pH 6.0) in a decloaking chamber (Biocare Medical, USA) at 95 °C for 5 minutes. Skin sections are washed in PBS followed by immunostaining using the MACH 4™ Universal HRP polymer kit (Biocare Medical). The primary antibody S100 (Dako, Australia) is diluted in DaVinci Green diluent (Biocare Medical) at 1:3000, and these sections are incubated with the primary antibody for one hour at room temperature. Positive immunoreactivity is visualized using 3,3-diaminobenzidine (DAB; Biocare Medical) and then counterstained with using Gill's haematoxylin (HD Scientific, Australia). The sections are dehydrated, and mounted on coverslips using Pertex® mounting medium (Medite, Germany). All stained sections are imaged using an Olympus BX41 microscope fitted with an Olympus digital camera (Micropublisher, 3.3RTV, QImaging; Olympus, Q-Imaging, Tokyo, Japan).

5.5.9 IBM Simulation Methods

We use a 3D lattice-based IBM, with adhesion between some agents, to describe the 3D experiments. In the IBM, cells are treated as equally sized spheres, and referred to as *agents*. These agents are restricted to reside on a 3D square lattice, with no more than one agent per site. The lattice spacing, Δ, represents the approximate size of each simulated agent, or the minimum spacing between agents. Here, we set $\Delta =$ 20 µm to match previous measurements [21]. We use a 3D lattice of dimension, 3 mm $\times$ 3 mm, and depth 2 mm, to represent the central region of each experimental skin model. This means that the number of lattice sites is $150 \times 150 \times 100$. We choose the depth of the domain so that agents in the simulation never touch the bottom of the domain during the simulations. The parameters in the simulation model are adapted from previous studies [21]. Since we use the 3D lattice to represent the central region of the tissue, where cells are initialised uniformly across the surface, we apply periodic boundary conditions along all vertical boundaries. Since cells cannot leave the skin through the upper or lower surfaces, we apply no flux conditions on the upper and lower horizontal boundaries of the 3D lattice. We choose the depth of the 3D lattice to be large enough so that the agents never touch the bottom boundary of the lattice on the time scale of the simulations we consider.

To initialise simulations, we randomly place a particular number of simulated skin agents, $N^{(s)}(0)$, and a particular number of simulated melanoma agents, $N^{(m)}(0)$, onto the surface of the lattice. When the IBM is initialised we take care to ensure that no more than one agent occupies each lattice site. We always choose the initial number of agents in each subpopulation to match the equivalent initial density of cells in the experimental skin model. In the experiments, the initial populations of cells are uniformly placed inside a disc of radius 3 mm, whereas in the IBM the initial populations of agents are uniformly placed inside a square subregion of side length 3 mm. We set the initial number of skin agents to be $N^{(s)}(0)= 9549$ to match the initial experimental population of 30,000 skin cells distributed in a disc of radius 3 mm. We vary the initial number of simulated melanoma agents to be $N^{(m)}(0)= 398$, 1592 or 2706, to match the initial density of melanoma cells. This initial experimental density corresponds to 1250, 5000 and 8500 melanoma cells distributed in a disc of radius 3 mm. To match the experiments, the IBM simulations are run for four days.

At any time, t, there are $N(t)=N^{(m)}(t)+N^{(s)}(t)$ agents on the lattice. In each discrete time step, of duration τ, we use a random sequential update method [34] to simulate motility and proliferation events. The algorithm involves executing two sequential steps:

1. $N(t)$ agents are selected one at a time, with replacement and given the opportunity to move to a nearest neighbour lattice site with probability $P_m^{(s)}$ $\in[0,1]$ and $P_m^{(m)} \in[0,1]$. Here we can specify different motility probabilities for the skin cells and the melanoma cells, and this is important because previous work has shown that fibroblast cells are more motile than melanoma cells [21]. If the chosen agent is a melanoma agent, we incorporate adhesion into the model by examining the occupancy of the 26 nearest lattice sites in the 3D Moore neighbourhood. We count the number of those sites occupied by melanoma agents, a [18]. Potentially motile melanoma agents then attempt to move with a modified probability, $P_m^*= (1 - q)^a$, which accounts for adhesion between neighbouring melanoma agents. The parameter q controls the strength of melanoma-melanoma agent adhesion, with $q=0$ corresponding to no adhesion, and increasing q leading to increased adhesion [18]. Setting $q=1$ corresponds to maximal adhesion, and this would prevent any motility of melanoma agents that are in contact with other melanoma agents. We do not include any adhesion between skin agents as fibroblast cells are known to be mesenchymal and act as individuals rather than being strongly affected by adhesion [16]. If a movement event is successful, the agent attempts to move to a nearest neighbour lattice site from the six sites in the 3D von Neumann neighbourhood. To simulate crowding effects, potential motility events that would place an agent on an occupied site are aborted.

2. $N(t)$ agents are selected one at a time, with replacement and given the opportunity to proliferate with probability $P_p^{(s)} \in[0,1]$ and $P_p^{(m)} \in[0,1]$. Again, this framework allows us to specify different proliferation probabilities for the skin cells and the melanoma cells [18,21]. If a proliferation event is successful, a daughter agent is placed at a randomly chosen nearest site from

the six sites in the 3D von Neumann neighbourhood. To simulate crowding effects, we abort the proliferation event if all six nearest neighbouring sites are occupied. In all cases where a proliferation event is successful, a proliferative melanoma agent will produce a daughter melanoma agent, and a proliferative skin agent will produce a daughter skin agent.

The parameters in the IBM are Δ, τ, $P_m^{(s)}$, $P_m^{(m)}$, $P_p^{(s)}$ $P_p^{(m)}$ and q. These IBM parameters are related to the cell proliferation rates ($\lambda^{(s)} = P_p^{(s)}/\tau$, $\lambda^{(m)} = P_p^{(m)}/\tau$) and cell diffusivities ($D^{(s)} = P_m^{(s)} \Delta^2/(6\tau)$, $D^{(m)} = P_m^{(m)} \Delta^2/(6\tau)$).

5.6   ACKNOWLEDGEMENTS

5.7   REFERENCES

1. Beaumont KA, Mohana-Kumaran N, Haass NK. Modeling melanoma *in vitro* and *in vivo*. Healthcare. 2014;2:27-46. doi: 10.3390/healthcare2010027

2. Meier F, Nesbit M, Hsu M, Martin B, Belle PV, Elder DE, Schaumburg-Lever G, Garbe C, Walz TM et al. Human melanoma progression in skin reconstructs: biological significance of bFGF. Am J Pathol. 2000;156:193-200. doi: 10.1016/S0002-9440(10)64719-0

3. Balu M, Kelly KM, Zachary CB, Harris RM, Krasieva TB, Konig K, Durkin AJ, Tromberg BJ. Distinguishing between benign and malignant melanocytic nevi by in vivo multiphoton microscopy. Cancer Res. 2014;74:2688-2697. doi:10.1158/0008-5472.CAN-13-2582

4. Urso C, Rongioletti F, Innocenzi D, Batolo D, Chimenti S, Fanti PL, Filotico R, Gianotti R, Lentini M, Tomasini C, et al. Histological features used in the diagnosis of melanoma are frequently found in benign melanocytic naevi. J Clin Pathol. 2005;58:409-412. doi: 10.1136/jcp.2004.020933

5. Wessels D, Lusche DF, Voss E, Kuhl S, Buchele EC, Klemme MR, Russell KB, Ambrose J, Sol BA, Bossler A et al. Melanoma cells undergo aggressive coalescence in a 3D Matrigel model that is repressed by anti-CD44. PLoS ONE. 2017;12:e0173400. doi: 10.1371/journal.pone.0173400

6. Eves P, Layton C, Hedley S, Dawson RA, Wagner M, Morandini R, Ghanem G, Mac Neil S. Characterization of an *in vitro* model of human melanoma invasion based on reconstructed human skin. Brit J Dermatol. 2000;142:210-222. doi: 10.1046/j.1365-2133.2000.03287.x

7. Haridas P, McGovern JA, McElwain DLS, Simpson MJ. Quantitative comparison of the spreading and invasion of radial growth phase and metastatic melanoma cells in a three-dimensional human skin equivalent model. PeerJ. 2017;**5**:e3754. doi: 10.7717/peerj.3754

8. MacNeil S, Eves P, Richardson B, Molife R, Lorigan P, Wagner M, Layton C , Morandini R, Ghanem G. Oestrogenic   steroids   and   melanoma   cell interaction with adjacent skin cells influence invasion of melanoma cells *in vitro*. Pigm   Cell   Melanoma   Res.   2000;13:68-72.   doi: 10.1034/j.1600-0749.13.s8.13.x

9. Treloar KK, Simpson MJ, Haridas P, Manton KJ, Leavesley DI, McElwain DLS, Baker RE. Multiple types of data are required to identify the mechanisms influencing the spatial expansion of melanoma cell colonies. BMC Syst Biol. 2013;7:137. doi: 10.1186/1752-0509-7-137

10. Carey TE, Takahashi T, Resnick LA, Oettgen HF, Old LJ. Cell surface antigens of human malignant melanoma: mixed hemadsorption assays for humoral immunity to cultured autologous melanoma cells. P Natl Acad Sci USA. 1976;73:3278-3282. doi:10.1073/pnas.73.9.3278

11. Deacon DH, Hogan KT, Swanson EM, Chianese-Bullock KA, Denlinger CE, Czarkowski AR, Schrecengost RS, Patterson JW, Teague MW, Slingluff Jr CL. The use of gamma-irradiation and ultraviolet-irradiation in the preparation of human melanoma cells for use in autologous whole-cell vaccines. BMC Cancer 2008;8:360. doi: 10.1186/1471-2407-8-360

12. Todorovic D, Petrovic I, Todorovic M, Cuttone G, Ristic-Fira A. Early effects of gamma rays and protons on human melanoma cell viability and morphology. J Microsc-Oxford. 2008;232:517-521. doi: 10.1111/j.1365-2818.2008.02151.x

13. Lahtz C, Bates SE, Jiang Y, Li AX, Wu X, Hahn MA, Pfeifer GP. Gamma irradiation does not induce detectable changes in DNA methylation directly following exposure of human cells. PLoS ONE. 2012;7:e44858. doi: 10.1371/journal.pone.0044858

14. Warne DJ, Baker RE, Simpson MJ. Optimal quantification of contact inhibition in cell populations. Biophys J 2017;113:1920-1924. doi: 10.1016/j.bpj.2017.09.016

15. Schneider CA, Rasband WS, Eliceiri KW. NIH image to ImageJ: 25 years of image analysis. Nat Methods. 2017;9:671-675. doi:10.1038/nmeth.2089

16. Simpson MJ, Treloar KK, Binder BJ, Haridas P, Manton KJ, Leavesley DI, McElwain DLS, Baker RE. Quantifying the roles of cell motility and cell proliferation in a circular barrier assay. J R Soc Interface. 2013;10:20130007. doi: 10.1098/rsif.2013.0007

17. Haridas P, McGovern JA, Kashyap AS, McElwain DLS, Simpson MJ. Standard melanoma-associated markers do not identify the MM127

metastatic melanoma cell line. Sci Rep. 2016;6:24569. doi: 10.1038/srep24569

18. Simpson MJ, Towne C, McElwain DLS, Upton Z. Migration of breast cancer cells: understanding the roles of volume exclusion and cell-to-cell adhesion. Phys Rev E. 2010;82:041901. doi: 10.1103/PhysRevE.82.041901

19. Read MN, Alden K, Rose LM, Timmis J. Automated multi-objective calibration of biological agent-based simulations. J R Soc Interface. 2016;13:20160543. doi: 10.1098/rsif.2016.0543

20. Browning AP, McCue SW, Binny RN, Plank MJ, Shah ET, Simpson MJ. Inferring parameters for a lattice-free model of cell migration and proliferation using experimental data. J Theor Biol. 2018;437:251-260. doi: 10.1016/j.jtbi.2017.10.032

21. Haridas P, Penington CJ, McGovern JA, McElwain DLS, Simpson MJ. Quantifying rates of cell migration and cell proliferation in co-culture barrier assay reveals how skin and melanoma cells interact during melanoma spreading and invasion. J Theor Biol. 2017;423:13-25. doi: 10.1016/j.jtbi.2017.04.017

22. Image Acquisition Toolbox Documentation R2017b. In: Mathworks. [https://au.mathworks.com/help/images/calculate-region-properties-using-image-region-analyzer.html] Accessed 17 Jan 2018.

23. Gerlee P. The model muddle: in search of tumor growth laws. Cancer Res. 2013;73:2407-2411 doi: 10.1158/0008-5472.CAN-12-4355

24. Vo BN, Drovandi CC, Pettitt AN, Simpson MJ. Quantifying uncertainty in parameter estimates for stochastic models of collective cell spreading using Approximate Bayesian Computation. Math Biosci. 2015;263:133-142. doi: 10.1016/j.mbs.2015.02.010

25. Green JEF, Waters SL, Whiteley JP, Edelstein-Keshet L, Shakesheff KM, Byrne HM. Non-local models for the formation of hepatocyte-stellate cell aggregates. J Theor Biol. 2010;267:106-120. doi: 10.1016/j.jtbi.2010.08.013

26. Chan KS, Koh CG, Li HY. Mitosis-targeted anti-cancer therapies: where they stand. Cell Death Dis. 2012;3:e411. doi:10.1038/cddis.2012.148

27. Ramaraj P. *In vitro* inhibition of human melanoma (BLM) cell growth by progesterone receptor antagonist RU-486 (Mifprestone). J Caner Ther. 2016;7:1045-1058. doi: 10.4236/jct.2016.713101

28. Lai X, Friedman A. Combination therapy for melanoma with BRAF/MEK inhibitor and immune checkpoint inhibitor: a mathematical model. BMC Syst Biol. 2017;11:70. doi: 10.1186/s12918-017-0446-9

29. Krtolica A, Solorzano CO, Lockett S, Campisi J. Quantification of epithelial cells in coculture with fibroblasts by fluorescence image analysis. Cytometery. 2002;49:73-82. doi: 10.1002/cyto.10149

30. Simpson MJ, Landman KA, Hughes BD, Fernando AE. A model for mesoscale patterns in motile populations. Physica A. 2010;389:1412-1424. doi: 10.1016/j.physa.2009.12.010

31. Bruna M, Chapman SJ. Diffusion of finite-size particles in confined geometries. Bull Math Biol. 2014;76:947-982. doi: 10.1007/s11538-013-9847-0

32. Matsiaka OM, Penington CJ, Baker RE, Simpson MJ. Continuum approximations for lattice-free multi-species models of collective cell migration. J Theor Biol. 2017;422:1-11. doi: 10.1016/j.jtbi.2017.04.009

33. Dawson RA, Upton Z, Malda J, Harkin DG. Preparation of cultured skin for transplantation using insulin-like growth factor I in conjunction with insulin-like growth factor binding protein 5 epidermal growth factor, and vitronectin. Transplantation. 2006;81:1668-1676. doi: 10.1097/01.tp.0000226060.51571.89

34. Chowdhury D, Schadschneider A, Nishinari K. Physics of transport and traffic phenomena in biology: from molecular motors and cells to organisms. Phys Life Rev. 2005;2:318-352. doi: https://doi.org/10.1016/j.plrev.2005.09.001

5.8 SUPPLEMENTARY MATERIAL - 1

This document provides additional information to support the results and discussion in the main manuscript. Here, we describe the experimental protocols in detail. We follow these protocols to obtain the results discussed in the main manuscript. Further, we disclose results from additional experiments. These outcomes supplement the overall findings documented in the main manuscript.

5.8.1 Methods

5.8.1.1 Live cell assay

We perform a live cell assay to study the morphological and behavioural differences between irradiated and non-irradiated melanoma cells. Melanoma cell suspensions of 5000/ml and 10000/ml, are cultured using growth medium in wells of a 24-well tissue culture plate. The diameter of each well is 15.6 mm. The tissue culture plate containing cells is placed on the stage of a live cell imaging microscope (Leica DMi8, Australia) housed within an incubation chamber at 37 °C, in 5% CO_2 and 95% air. Cells are monitored over 24 hours, and images are captured at t=0, 12 and 24 hours.

5.8.1.2 Establishing 3D experimental skin model with melanoma cells and control skin model without melanoma cells

We construct 3D experimental skin models following protocols in the main manuscript. We also construct control 3D experimental skin models following the same protocol except that melanoma cells are omitted.

5.8.2 Results

5.8.2.1 Confirmation that irradiated melanoma cells do not proliferate

The melanoma cells are gamma-irradiated to inhibit mitosis. We perform a live assay to provide evidence that irradiation does not change adherence or morphology, and to

confirm that irradiated melanoma cells do not proliferate. Two initial densities of melanoma cells are used in this experiment. The assay is initialised with either 5000 or 10000 irradiated melanoma cells/0.5 ml growth medium, in a 24-well tissue culture plate. Equivalent experiments with non-irradiated melanoma cells are performed in triplicate. The assay is monitored for 24 hours in optimal growth conditions. Images are captured at t=0, 12 and 24 hours. The images in Figure S1A-F show that the irradiated melanoma cells have no change in adherence or morphology when compared to non-irradiated melanoma cells.

To confirm that irradiation prevents mitosis we count the total number of cells in each field of view, as a function of time, in the three experimental replicates. Figure S1G shows that non-irradiated melanoma cells proliferate as we see an increase in average cell number over 24 hours. However, the average cell number for experiments with irradiated melanoma cells remains constant over 24 hours (Figure S1H) confirming that the irradiated melanoma cells do not proliferate. Furthermore, the fact that the average number of irradiated melanoma cells remains constant with time suggests that there is no cell death. This shows that the melanoma cells survive gamma-irradiation.
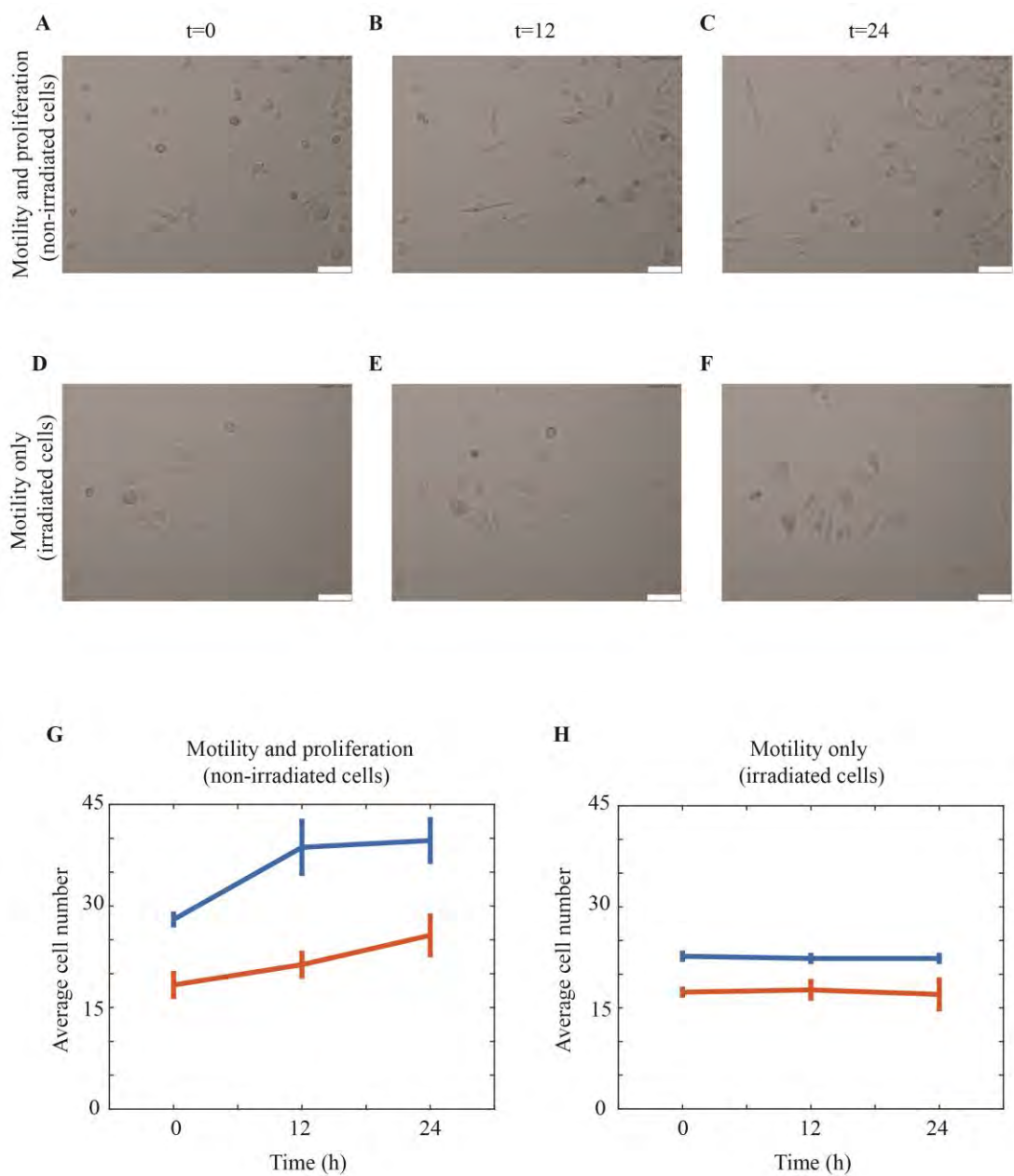
Figure S5.1: Live cell assay of non-irradiated and irradiated melanoma cells. Melanoma cells are cultured in a 24-well tissue culture plate, at approximately 10000 cells/0.5 ml growth medium. Sub-regions of size 0.92 mm × 0.69 mm are imaged. The images show: (A-C) non-irradiated melanoma cells; and (D-F) irradiated melanoma cells. The images correspond to t=0, 12 and 24 hours, respectively. The scale bar in each image is 100 μm. Plots show the average cell number (n=3) for: (G) non-irradiated melanoma cells; and (H) irradiated melanoma cells, as a function of time. We count the total number of cells in each field of view, as a function of time, in the three experimental replicates to calculate the average cell number. In both (G)

and (H), the data points corresponding to experiments initialised with 10000 melanoma cells is in blue, and experiments initialised with 5000 melanoma cells is in red, respectively.

5.8.2.2 Absence of nests on control 3D experimental skin models

To provide evidence that nests are composed of melanoma cells on the 3D experimental skin model, we perform a set of control experiments. We construct control 3D experimental skin models in exactly the same way as the main experiments except that we omit melanoma cells. Therefore, the only cells present in the control experiments are the primary skin cells. The metabolic activity of all cells on the control 3D experimental skin models is observed using an MTT assay. Results for the control experiments are compared to the MTT assays performed on 3D skin models initialised with non-irradiated melanoma cells. In this case, we use a 3D skin model initialised with 5000 non-irradiated melanoma cells. The MTT assay highlights the metabolic activity of all cells on the surface of both 3D experimental skin models in purple (Figure S5.2). Results in Figure S5.2A show a complete absence of nests, while Figure S5.2B shows clear dark purple nests. This suggests that the dark purple staining on the 3D experimental skin model initialised with melanoma cells are clusters of melanoma cells.
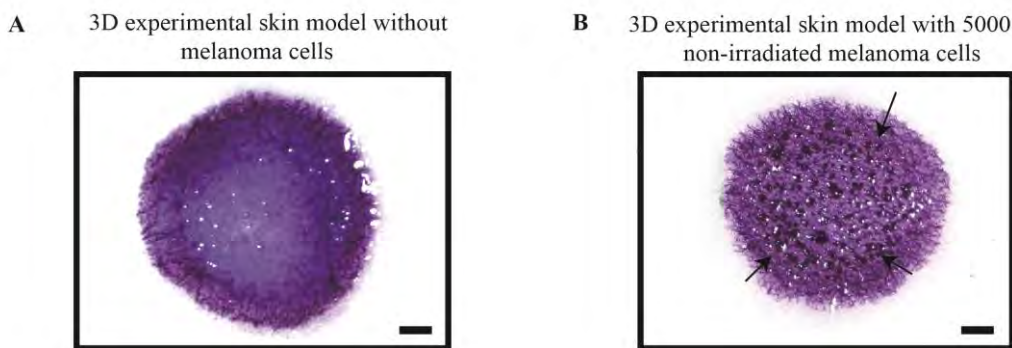
Figure S5.2: Nest formation is absent on the 3D skin model without melanoma cells. Images show metabolically active cells (light purple) on: (A) 3D experimental skin model without melanoma cells; and (B) 3D experimental skin model initialised with 5000 irradiated melanoma cells. Nests (dark purple) in (B) are indicated (arrows). The scale bar in each image is 1 mm.

5.8.2.3 Conclusion

These additional results confirm that irradiation does not alter melanoma cell morphology, adherence to substrate or their ability to migrate. Further, these additional results confirm that the dark purple nests on the 3D experimental skin model are clusters of melanoma cells.

NEST AREA (mm²): EXPERIMENTS USING IRRADIATED MELANOMA CELLS

Initial cell number: 1250	Initial cell number: 5000			Initial cell number: 8500		
	DONOR A	*DONOR B*	*DONOR C*	*DONOR A*	*DONOR B*	*DONOR C*
	0.016	0.012	0.006	0.032	0.028	0.021
	0.007	0.009	0.018	0.022	0.020	0.010
	0.009	0.013	0.015	0.018	0.020	0.019
	0.007	0.013	0.014	0.010	0.015	0.010
	0.005	0.013	0.014	0.013	0.020	0.007
	0.007	0.010	0.014	0.010	0.017	0.019
	0.009	0.008	0.012	0.021	0.025	0.015
	0.006	0.012	0.005	0.009	0.020	0.010
nest area below detectable limit	0.011	0.009	0.014	0.010	0.020	0.020
	0.005	0.007	0.007	0.014	0.026	0.013
	0.005	0.010	0.006	0.017	0.022	0.015
	0.006	0.017	0.006	0.010	0.010	0.013
	0.012	0.013	0.009	0.020	0.035	0.017
	0.009	0.009	0.007	0.014	0.020	0.010
	0.005	0.006	0.004	0.015	0.026	0.019
	0.005	0.008	0.012		0.017	0.013
	0.007	0.015	0.011			0.012
	0.012	0.013	0.009	**AVERAGE**	**AVERAGE**	**AVERAGE**
	0.011	0.022	0.009	**0.016**	**0.021**	**0.014**
	0.009	0.012	0.006			
	0.014		0.007	**MEDIAN**	**MEDIAN**	**MEDIAN**
			0.005	**0.014**	**0.020**	**0.013**
			0.004			
	AVERAGE	**AVERAGE**	**AVERAGE**			
	0.008	**0.012**	**0.009**			
	MEDIAN	**MEDIAN**	**MEDIAN**			
	0.007	**0.012**	**0.009**			

NEST AREA (mm²): EXPERIMENTS USING NON-IRRADIATED MELANOMA CELLS								
Initial cell number: 1250			Initial cell number: 5000			Initial cell number: 8500		
DONOR A	DONOR B	DONOR C	DONOR A	DONOR B	DONOR C	DONOR A	DONOR B	DONOR C
0.045	0.029	0.018	0.080	0.045	0.080	0.181	0.036	0.460
0.037	0.022	0.020	0.088	0.086	0.130	0.095	0.094	0.123
0.022	0.014	0.029	0.070	0.076	0.032	0.202	0.042	0.266
0.016	0.024	0.028	0.089	0.044	0.029	0.785	0.054	0.138
0.012	0.049	0.083	0.062	0.044	0.051	0.038	0.114	0.186
0.034	0.029	0.023	0.062	0.099	0.031	0.189	0.129	0.213
0.029	0.029	0.046	0.050	0.038	0.043	0.233	0.152	0.329
0.026	0.026	0.017	0.087	0.060	0.067	0.201	0.035	0.319
0.035	0.022	0.013	0.052	0.108	0.047	0.258	0.050	0.199
0.045	0.023	0.010	0.041	0.129	0.051	0.213	0.033	0.144
0.035	0.020	0.008	0.032	0.078	0.066	0.121	0.045	0.129
0.053	0.022	0.017	0.103	0.077	0.042	0.176	0.024	0.123
0.026	0.023	0.024	0.057	0.036	0.057	0.571	0.038	0.098
0.048	0.018	0.018	0.053	0.136	0.051	0.814	0.048	0.088
0.036	0.014	0.029	0.034	0.081	0.021	0.302	0.097	0.040
0.022	0.022	0.014	0.053	0.065	0.031	0.077	0.045	0.069
0.030	0.020	0.021	0.036	0.171	0.029	0.083	0.219	0.147
0.019	0.021	0.010	0.053	0.121	0.102	0.175	0.027	0.076
0.024	0.023	0.014	0.095	0.048	0.135	0.170	0.317	0.152
0.020	0.017	0.026	0.051	0.066	0.111	0.049	0.265	0.089
0.022	0.022	0.022	0.053	0.032	0.084	0.094	0.113	0.109
0.049	0.017	0.024	0.023	0.024	0.089	0.048	0.316	0.082
0.022	0.012	0.020	0.069	0.044	0.063	0.022	0.164	0.089
0.014	0.015	0.038	0.141	0.032	0.163	0.059	0.138	0.054
0.012	0.041	0.020	0.051	0.049	0.094	0.061	0.165	0.086
0.022	0.022	0.014	0.133	0.057	0.107	0.051	0.101	0.073
0.034	0.025	0.020	0.128	0.061	0.069	0.073	0.025	0.045
0.015	0.020	0.010	0.150	0.051	0.039	0.073	0.027	0.081
0.010	0.019	0.010	0.085	0.045	0.041	0.059	0.036	0.073
0.015	0.020	0.020	0.139	0.078	0.045	0.051	0.358	0.082
0.012	0.015	0.026	0.069	0.051	0.038	0.059	0.041	0.094
0.009	0.031	0.013	0.079	0.078	0.059	0.071	0.044	0.062
0.019	0.019	0.024	0.150	0.019	0.038	0.058	0.024	0.069
0.022	0.009	0.010	0.109	0.059	0.031	0.072	0.030	0.085
0.013	0.010	0.014	0.121	0.045	0.026	0.089	0.028	0.059
0.020	0.012	0.013	0.092	0.053	0.047	0.036	0.054	0.059
0.026	0.017	0.012	0.041	0.036	0.020	0.044	0.027	0.066
0.033	0.025	0.018	0.017	0.075	0.035	0.062	0.032	0.086
0.020	0.018	0.013	0.032	0.051	0.032	0.041	0.035	0.079
0.054	0.012	0.020	0.048	0.048	0.032	0.051	0.042	0.067
0.059	0.014	0.018	0.068	0.030	0.029	0.091	0.044	0.076

0.026	0.022	0.014	0.028	0.043	0.035	0.044	0.070	0.059
0.022	0.018	0.038	0.084	0.047	0.041	0.092	0.049	0.032
0.035	0.024	0.020	0.028	0.034	0.032	0.032	0.036	0.056
0.014	0.009	0.028	0.011	0.017	0.047	0.031	0.028	0.082
0.034	0.012	0.017	0.071	0.031	0.045	0.028	0.023	0.044
0.017	0.012	0.018	0.020	0.057	0.061	0.026	0.015	0.073
0.022	0.018	0.012	0.067	0.050	0.039	0.017	0.053	0.026
0.036	0.038	0.014	0.087	0.054	0.037	0.026	0.141	0.065
0.025	0.029	0.020	0.019	0.042	0.036	0.030	0.138	0.077
0.032	0.024	0.023	0.019	0.032	0.056	0.047	0.084	0.061
0.025	0.010	0.017	0.055	0.153	0.043	0.041	0.057	0.052
0.022	0.012	0.013	0.028	0.075	0.033	0.040	0.130	0.042
0.014	0.011	0.010	0.045	0.083	0.039	0.046	0.051	0.040
0.023	0.019	0.008	0.063	0.071	0.041	0.055	0.047	0.042
0.017	0.022	0.017	0.028	0.076	0.046	0.045	0.068	0.078
0.017	0.021	0.024	0.089	0.084	0.024	0.043	0.047	0.042
0.020	0.014	0.018	0.057	0.029	0.026	0.049		0.046
0.024	0.012	0.029	0.058	0.066	0.031	0.063		
0.017	0.013	0.014	0.076	0.032	0.025	AVERAGE	AVERAGE	AVERAGE
0.009	0.021	0.021	0.203	0.025	0.032	0.118	0.083	0.101
0.013	0.009	0.010	0.102	0.057	0.036			
0.012	0.011	0.014	0.051	0.039	0.034			
0.010	0.008	0.026	0.055	0.039	0.036	MEDIAN	MEDIAN	MEDIAN
0.012	0.007	0.022	0.041	0.017	0.026	0.059	0.048	0.078
0.016	0.012	0.022	0.042	0.059	0.031			
0.012	0.009	0.018	0.058	0.054	0.028			
0.017	0.009	0.024	0.039	0.034	0.025			
0.012	0.008	0.009	0.028	0.061	0.023			
0.012	0.013	0.012	0.164	0.049	0.045			
0.010	0.008	0.012	0.015	0.028	0.034			
0.012	0.005	0.018	0.019	0.021	0.043			
0.017	0.008		0.022	0.062	0.031			
0.022			0.029	0.020	0.032			
0.014			0.045	0.032	0.030			
0.014			0.025	0.051	0.028			
0.012			0.046	0.015	0.028			
0.014			0.044	0.031	0.029			
0.015			0.048	0.037	0.032			
0.010			0.034	0.067	0.031			
AVERAGE	AVERAGE	AVERAGE	0.021	0.048	0.042			
0.023	0.018	0.020	0.018	0.043	0.026			
			0.028	0.070	0.026			
MEDIAN	MEDIAN	MEDIAN	0.012	0.054	0.039			
0.020	0.018	0.018	0.018	0.015	0.032			
			0.057	0.023	0.020			
			0.020	0.014	0.032			

0.032	0.043	0.043
0.029	0.030	0.040
0.033	0.014	0.013
0.015	0.020	0.031
0.031		0.033
0.061		0.024
0.037		0.026
		0.026
		0.021
		0.026
		0.031
		0.035
		0.035
		0.020
		0.020
AVERAGE	AVERAGE	AVERAGE
0.059	0.054	0.043

MEDIAN	MEDIAN	MEDIAN
0.051	0.048	0.035

Chapter 6: Conclusion and Future Work

6.1.1   Summary and Conclusion

Melanoma is a complex disease that has therapeutic challenges (Liu *et al*., 2014; Chen & Robinson 2017). Disease relapse combined with the ineffectiveness of melanoma medications presses the need for novel, alternate treatment options (Waggle *et al*., 2011; Chen & Robinson 2017). New treatments require an improved understanding of the cause of melanoma development and progression. Thus, it is important to understand the underlying mechanisms that drive the progression of melanoma which still remains unclear. The rationale for this project is to construct 2D and 3D model systems which reliably showcase the early and late phase of melanoma as well as characterise the key features of the disease progression such as, cell migration, cell proliferation and cell invasion by extending previous research studies. This project is designed with four separate but closely linked aims that are investigated and resulted in published manuscripts. The outcomes from these individual studies are detailed in the preceding chapters and summarised below.

To investigate particular phases of melanoma progression we use cell lines associated with each stage of the disease. In this thesis we use: (i) radial growth phase (RGP) associated with WM35 cell line (Herlyn 1990); (ii) vertical growth phase (VGP) associated with WM793 cell line (Herlyn *et al*., 1985); (iii) metastatic cell lines, MM127 (Pope *et al*., 1979) and SK-MEL-28 (Carey *et al*., 1976). As we will be using these cell lines throughout the entire project, we first aim to identify a reliable melanoma-associated marker to detect each melanoma cell line. We attempt to detect the melanoma cells using individual markers. The melanoma-associated markers, S100, HMB-45, Melan-A, MITF and tyrosinase are commonly used and are previously reported to identify melanoma cells (Eves *et al*., 2003a; Viray *et al*., 2013; Zand *et al*., 2016).

We also use an array of 2D experimental techniques such as immunofluorescence, Western blotting and quantitative reverse transcription – polymerase chain reaction (qRT-PCR) to ensure a thorough detection of the melanoma-associated marker expressions.

Collectively, the findings of this study provides evidence that standard melanoma-associated markers detects all the melanoma cell lines examined in this study except MM127 cells. Alternatively, SK-MEL-28 is another metastatic cell line that can be accurately detected using all the melanoma-associated markers and is therefore used in further studies throughout this project. Hence we choose to omit MM127 cell line from prospective projects. Furthermore, the remaining melanoma cell lines, apart from MM127, used in this study are identified using the melanoma-associated marker S100 suggesting S100 to be a reliable marker. These results concur with previous research by Viray *et al*. (2013) where their study suggests S100 to be a sensitive marker for melanoma cells. Ordonez *et al*. (2014) and Foth *et al*. (2016) suggest the use of a mutli marker panel to detect melanoma cells hence, alternate markers or a combination of the alternate markers could be used to detect the MM127 melanoma cell line.

At the conclusion of the first aim of this project we are confident that we have identified a reliable melanoma marker that can be used to identify three different melanoma cell lines from different stages of the disease. Thus, we extend previous monoculture investigations around melanoma cell migration and melanoma cell proliferation using 2D barrier assays. However, the main extension from previous research investigations such as Justus *et al*. (2014); Gallinaro *et al*. (2013); and Treloar *et al*. (2013); is the use of co-cultures instead of a single population of cells. This 2D co-culture displays a more relevant environment to human skin, where melanoma cells are surrounded by skin cells like fibroblasts. We hypothesise that the rates at which these heterogeneous cell populations proliferate and migrate might be different to when the monocultures of fibroblast and melanoma cells are cultured in isolation. To investigate our hypothesis we perform a series of barrier assays using varying densities of heterogeneous cell populations and monocultures of both cell types. We inhibit cell proliferation to accurately quantify cell migration. The spatial and temporal spreading patterns of cell populations are further quantified using partial differentiation equations. Overall, our results provide evidence that the dermal fibroblasts do not influence the migratory pattern of the melanoma cells in 2D models. Here, we are successful in extending previous studies by using 2D co-culture models, however our results do not concur with previous research that report fibroblasts promote melanoma growth (Li *et al*., 2007; Sriram *et al*., 2015; Flach *et al*., 2011). Additionally, experimental results in this chapter are verified using mathematical models that provide a novel

analysis of co-culture interactions, as well as the spatial spreading patterns of both, monocultures and co-cultures. Further, using melanoma cell lines associated to other stages of the disease such as RGP or VGP, could result in an alternate outcome. This is mainly because the melanoma cell lines associated to these phases could still be under the control of the surrounding dermal fibroblasts as opposed to metastatic melanoma cell lines. However, a more realistic 3D model is required to further study these cell-cell and cell-substrate interactions.

Melanoma cell invasion is the primary cause for the spread of the disease (Martin *et al*., 2013; Xu *et al*., 2013). Melanoma cells divide and invade into tissues causing metastases (Xu *et al*., 2013). Most of the *in vitro* melanoma research data are obtained using 2D assays. Although these 2D assays provide a wealth of preliminary information, they cannot be used to assess melanoma invasion patterns (Beaumont *et al*., 2014). There are limited models that accurately represent the human skin environment, *in vitro*. In order to study the behaviour of melanoma cells in a physiologically relevant context, we further extend our research by using a 3D human skin equivalent (HSE) model. Here, we adapt the 3D HSE model to construct a 3D melanoma skin equivalent (MSE) model, through the addition of melanoma cells, and investigate the invasion patterns of the early and late phase melanoma.

The 3D MSE model consists of keratinocytes, fibroblasts and melanoma cell lines WM35 (RGP) or the SK-MEL-28 (metastatic), on a de-epidermised human skin dermis substrate. The protocol to construct the 3D MSE models is also adapted from previous 3D melanoma modelling studies (Eves *et al*., 2000; Dekker *et al*., 2000). The 3D MSE model with melanoma cells are cultured for 9, 15 and 20 days. VGP representative cells are not included as we anticipate that invasion results would remain intermediate between those obtained from the most aggressive metastatic phase and least aggressive RGP phases of the disease. Hence, we focus our study on the two different phases of melanoma.

The physiology of the 3D MSE models are similar to native human skin as well as results from previous studies; displaying a well-defined epidermis and dermis regions across all the time-points (9, 15 and 20 days) examined in this study (Eves *et al*., 2003). Further, the spatial expansion of melanoma cells is also observed at the above mentioned time-points.

Most importantly, visually distinct colonies of cells, commonly referred to as nests are observed on the surface of both the MSE models, with the WM35 and SK-MEL-28 cell lines. These nests are anticipated to be melanoma cells as the skin models without melanoma cells do not show these colonies of cells and previous *in vitro* models report similar nest formations (Eves *et al*., 2000; Dekker *et al*., 2000).

As the main focus of our study is to explore the invasion patterns of the melanoma cells, we use S100 to reliably detect melanoma cells, previously shown to identify WM35 and SK-MEL-28 in Chapter 2. In our 3D MSE model the aggressive SK-MEL-28 cells invade into the dermis at day 9 as reported by previous research studies. (Satyamoorthy *et al*., 1997; Hsu *et al.*, 1998; Meier *et al*., 2000). Hence, our results concur with the literature and previous research. However, it is interesting to note that the melanoma colonies of WM35 cells are able to breach the basement membrane and invade into the dermis in our 3D MSE model, observed at day 15 and 20. The WM35 melanoma cell line is generally known to be confined to the epidermal region (Clark 1991; Meier *et al*., 2000). Our results contradict literature and previous studies like (Beaumont, *et al*., 2014; Dekker *et al*., 2000) that show RGP cells to be restricted to the epidermis. Additionally, we quantify differences in the invasion patterns associated with the WM35 and SK-MEL-28 melanoma cell lines by measuring the depth of melanoma cell invasion into the dermal region over time using an approach different from previous studies (Eves *et al*., 2003b; Eves *et al*., 2003a; Marques & Mac Neil 2016).

To conclude, the results from this study demonstrate the successful establishment of a reliable and reproducible 3D MSE model that can be used to examine the invasion of melanoma cells from two different cell lines associated with the melanoma progression. Here, we provide qualitative information about the spatial and temporal distribution of different cell types in the MSE models and quantitative information about the invasion process.

Since melanoma cells in the 3D MSE models proliferate, migrate and invade into the dermis as in native human skin *in vivo*, we use this 3D model to further investigate another important aspect of melanoma progression, which is melanoma nest formation. This aspect of melanoma cell clustering is previously highlighted and detailed in the

findings in our study summarised in Chapter 4. Early identification of melanoma nests is critical for effective melanoma treatment (Garbe *et al*., 2016). However, effective treatment for metastatic melanoma remains a challenge. Therefore, it is imperative to identify the biological mechanisms that lead to nest formation. In this study we decipher the dominant mechanism that drives nest formation.

We use the 3D MSE model to discriminate between cell proliferation and cell migration, the two potential mechanisms that drive melanoma nest formation, by performing a suite of experiments. In this study we systematically vary the initial density of proliferative melanoma cells and non-proliferative melanoma cells on the 3D MSE model. Additionally, we also explore the role of initial cell number in these experiments. Collectively, our results show that higher initial number of melanoma cells lead to larger nests, and that cell proliferation leads to dramatically-larger nests. These series of experimental outcomes are consistent with a series of 3D mathematical simulations. Our results contradict previous melanoma coalescing studies in Matrigel by Wessel *et al*. (2017) who demonstrate cell migration to drive melanoma nest formation. However, our experiments are performed using melanoma cells cultured together with primary human skin cells, creating a more realistic *in vitro* human skin model than previous studies that examine nest formation using monocultures of melanoma cells. Alternatively, the duration of the experiments could be another interesting factor that affects melanoma nest formation. Our experiments are conducted for longer periods of time than Wessels *et al*. (2017). Overall our results suggest that targeting melanoma cell proliferation would result in reduced nest formation. Our findings concur with recent studies that report melanoma-related drugs and therapies target the altered gene or related protein preventing melanoma cell division finally inhibiting the disease metastasis (Hu *et al*., 2016; Kaluzki *et al*., 2016; Meierjohann *et al*., 2017).

6.1.2   *Future Work*

The results presented in this thesis demonstrate the use of a reliable 3D model to study melanoma progression. Although these findings are important in their respective manner they open multiple research avenues that warrant further investigation.

In Chapter 2 we conclude by omitting the metastatic cell line MM127 from our project. This cell line is used in melanoma research (Chenevix-Trench *et al*., 1990; Cozzi *et al*., 2006). Although we use five different melanoma-associated markers in this study, the use of additional sensitive melanoma markers like SOX 10, Chondroitin sulfate proteoglycan 4 (CSPG4) and Mel-CAM (Weinstein *et al*., 2014; Willis *et al*., 2015) could potentially identify MM127. Furthermore, since studies suggest the use of multiple markers to accurately identify melanoma cells, it is possible that a combination of melanoma-associated markers such as: Mel-CAM + S100; PMEL17 + Melan A (MART-1) + tyrosinase; as suggested by Ordonez *et al.* (2014) and Foth *et al.* (2016) could identify MM127. Identifying a suitable marker would broaden the range of studies within which MM127 can be used.

Further, in Chapter 3 our approach to explore the spatial spreading of co-cultures is limited to the use of only fibroblasts and melanoma cells. The inclusion of keratinocytes would not only make the 2D co-culture model more relevant to the human skin but also might change the outcome of this experiment. Literature suggests that keratinocytes promote melanoma cell invasion and migration, hence including these cells in the co-culture model could result in an alternate outcome (Chung *et al*., 2011; Muller *et al*., 2016). Additionally this work can further be extended using different melanoma cell lines from the RGP and VGP stages of the disease. For example it would be interesting to observe results using cell lines previously used like, RGP associated in our 3D MSE model (Dekker *et al*., 2000). Additionally, repeating these experiments using the melanoma cell lines from the earlier stages would also address whether the metastatic cells have progressed to a stage beyond being influenced by fibroblasts. The cells associated to the RGP or VGP phase of melanoma could potentially be influenced by fibroblasts and may show altered migration and proliferation patterns.

Our findings in Chapters 4 and 5 are interestingly different to previous research studies like Dekker *et al*. (2000) where the RGP associated cells do not enter the dermal compartment and Wessels *et al*. (2016) who report that migration drives melanoma nest formation. Our 3D MSE model described in these chapters provide a strong foundation for future work in melanoma progression. Firstly, this work can be extended by using

other RGP cell lines to confirm our current results and note if the other RGP associated cell lines invade into the dermal region. Further, incorporating cell lines from the VGP stage into our 3D MSE model would strengthen the concept that this 3D model recapitulates all the stages of melanoma progression. Additionally, the invasion pattern of other cell types associated with the different phases of melanoma can also be quantified.

Secondly, the 3D MSE models can be used to explore the interaction of melanoma cells with the surrounding cells and tissues. For example, the disruption of the basement membrane in the 3D MSE model could be driven by some kind of proteolytic enzyme released from either the melanoma cells or the surrounding host cells. The degradation of the basement membrane by proteolytic enzymes such as MMPs are considered essential for melanoma invasion and metastasis (Katerinaki *et al*., 2003). Our investigations can extend previous studies that mainly report these results using cell lines that are associated to the metastatic phase of melanoma (Katerinaki *et al*., 2003; Eves *et al*., 2003a; Marques & Mc Neil 2016). The 3D MSE model comprises of three cell types, hence it would be interesting to investigate the secretions and enzymatic activity for each cell type as well as the different melanoma cell lines associated with each stage of the disease. This can be achieved by using both 2D and 3D model systems. Also, the differences in the speed of invasion could be associated with the type of melanoma cells included in the study and the rate at which these enzymes are secreted. Identifying these enzymes and associating them with the respective stage of the disease will produce relevant information that could potentially be used for diagnostic or treatment purposes.

Thirdly, the 3D MSE model has potential to translate basic cellular research to clinical applications. As drugs cannot be tested on humans due to ethical constraints there is need for reliable 3D models. The MSE model can be further developed by investigating the effects of anti-melanoma drugs as described in Tsai *et al*. (2008) and Lee *et al*. (2010) who use collagen gels in their 3D models. Similarly, using the MSE model we can investigate the influence of anti-melanoma drugs on the size of nests. For example, since the melanoma cell lines WM35 and SK-MEL-28 used in this thesis have *BRAF* mutations they can be targeted using anti-melanoma drugs like vemurafnib and or dabrafenib (Boussemart *et al*., 2014). Introducing the 3D MSE model into the pre-clinical testing

repertoire of anti-melanoma drugs could increase their success rate in the actual clinical trials.

Lastly, the *in vivo* environment in human tissue, where melanoma cells proliferate, migrate and invade is more complex than our *in vitro* 3D MSE model. Currently there are 3D skin models with either endothelial cells or Langerhans cells (Broek *et al*., 2017). Therefore, this 3D MSE model can be used as a basis to construct a more complex environment integrating other cell types such as immune cells as well as endothelial cells into the model. This could open possibilities to study immunotherapies for melanoma treatments. Further, this model can be used as a foundation to host other cancers, in particular other skin related cancers such as basal cell carcinoma and squamous cell carcinoma.

6.1.3   Concluding Remarks

The overall findings of this thesis addresses several underlying key features of melanoma progression. We have quantified independent roles of melanoma cell motility and melanoma cell proliferation in heterogeneous populations. In particular, we have developed a 3D MSE model to study the progression of the disease and have provided evidence to show that initial cell density and proliferation are important parameters that drive melanoma nest formation. Lastly, this thesis demonstrates how the combination of experimental investigations along with the mathematical models can provide indispensable information. The mathematical models not only aid in extrapolating data from experiments providing detailed information about cell migration and cell proliferation but also re-confirm series of experimental results. In conclusion, the findings from this thesis provide a deeper understanding about melanoma progression. A revised illustration of the disease progression based on the outcomes from this thesis is shown in (Figure 6.1). These results warrant further investigation.
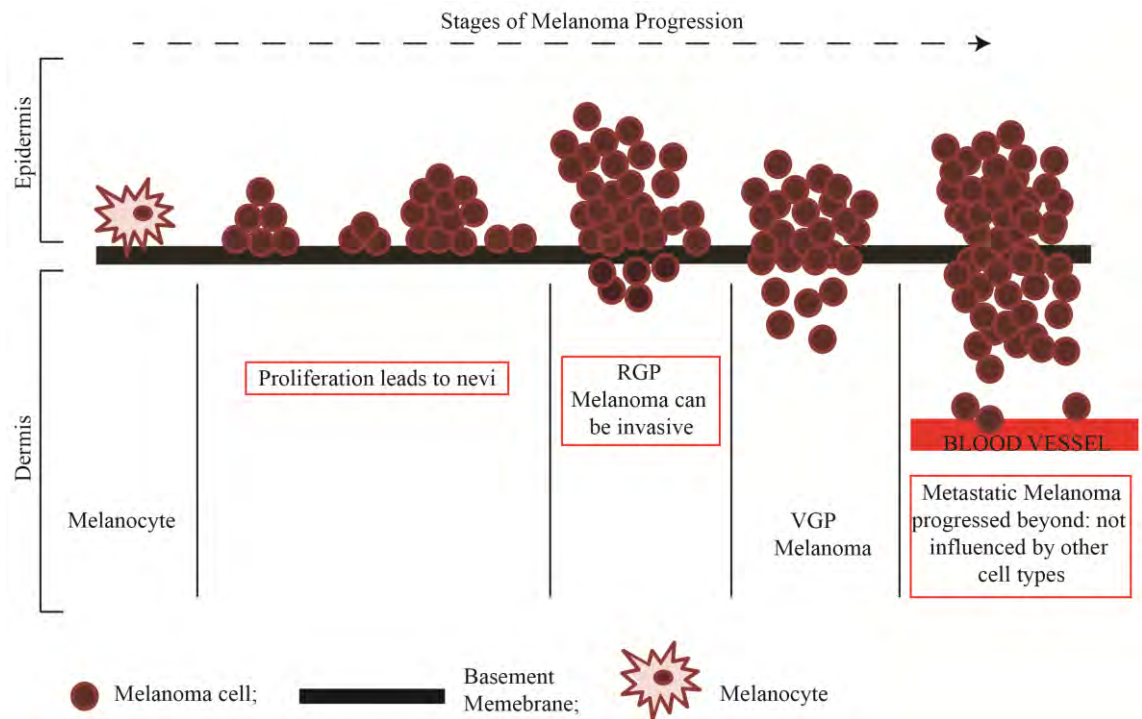
Figure 6.1: *Potential re-classification of melanoma progression.* The schematic illustrates melanoma progression showing the localisation of nevi and clusters of melanoma cells. The key outcomes of this thesis is highlighted in red boxes.

Efforts to explore how the 3D MSE model can be carried forward to further our understanding of melanoma progression will also provide better insights into effective treatment options for this fatal disease.

6.2 REFERENCES

1. Beaumont KA, Mohana-Kumaran N, Haass NK. 2014. Modelling melanoma *in vitro* and *in vivo*. *Healthcare* 2: 27-46.

2. Boussemart L, MalkaMahieu H, Girault I, Allard D, Hemmingsson O, Tomas ic G, Thomas M, Basmadjian C, Ribeiro N, Thuaud F, Mateus C, Routier E, KamsuKon N, Agoussi S, Eggermont AM, Desaubry L, Robert C, Vagner S. 2014. eIF4F is a nexus of resistance to anti-BRAF and anti-MEK cancer therapies. *Nature*. 513: 105-109.

3. Broek van den LJ, Bergers LIJC, Reijnders CMA, Gibbs S. 2017. Progress and future prospectives in skin-on-chip development with emphasis on the use of different cell types and technical challenges. *Stem Cell Reviews*. 13: 418-429.

4. Carey TE, Takahashi T, Resnick LA, Oettgen HF, Old LJ. 1976. Cell surface antigens of human malignant melanoma: mixed hemadsorption assays for humoral immunity to cultured autologous melanoma cells. *Proceedings of the National Academy of Sciences of the United States of America*.73: 3278-3282.

5. Chen S, Robinson A. 2017. New approaches to melanoma treatment: checkpoint inhibition with novel targeted therapy. *Clinical Research in Dermatology*. 4: 1-4.

6. Chenevix-Trench G, Martin NG, Ellem KAO. 1990. Gene expression in melanoma cell lines and cultured melanocytes: correlation between levels of c-src-1, c-myc and p53. *Oncogene*. 5: 1187–1193.

7. Cozzi SJ, Parsons PG, Ogbourne SM. 2006. Induction of senescence in diterpene ester-treated melanoma cells via protein kinase c- dependent hyperactivation of the mitogen-activated protein kinase pathway. *Cancer Research*. 66: 10083–10091.

8. Clark WH. 1991. Tumour progression and the nature of cancer. *British Journal of Cancer*. 64: 631-644.

9. Dekker SK, Van-Doorn R, Kempenaar J, Gruis NA, Vermeer BJ, Ponec M. 2000. Skin equivalent: an attractive model to evaluate early melanoma metastasis. *Melanoma Research*. 10:127-140.

10. Eves P, Layton C, Hedley S, Dawson RA, Wagner M, Morandini R, Ghanem G, Mac Neil S. 2000. Characterization of an *in vitro* model of human

melanoma invasion based on reconstructed human skin. *British Journal of Dermatology.* 142:210-222.

11. Eves P, Katerinaki E, Simpson C, Layton C, Dawson R, Evans G, Mac Neil S. 2003a. Melanoma invasion in reconstructed human skin is influenced by skin cells – investigation of the role of proteolytic enzymes. *Clinical and Experimental Metastasis.* 20:685-700.

12. Eves P, Haycock J, Layton C, Wagner M, Kemp H, Szabo M, Morandini R, Ghanem G, Garcia-Borron JC, Jimenez-Cervantes C, Mac Neil S. 2003b. Anti-inflammatory and anti-invasive effects of α-melanocyte-stimulating hormone in human melanoma cells. *British Journal of Cancer.* 89:2004-2015.

13. Flach EH, Rebecca VW, Herlyn M, Smalley KSM, Anderson ARA. 2011. Fibroblasts contribute to melanoma tumour growth and drug resistance. *Molecular Pharmaceutics*. 8:2039-2049.

14. Foth M Wouters J, Chaumont C, Dynoodt P, Gallagher WM. 2015. Prognostic and predictive biomarker in melanoma: an update. *Expert Review of Molecular Diagnosis*. 16:223-237.

15. Garbe C, Peris K, Hauschild A, SaiagP, Middleton M, Bastholt L, Grob JJ, Malvehy J, Newton-Bishop J, Strtigos A *et al*., 2016. Diagnosis and treatment of melanoma. European consensus-based interdisciplinary guideline – Update 2016. *European Journal of Cancer*. 63:201-217.

16. Herlyn M, Thurin J, Balaban G, Bennicelli JL, Herlyn D, Elder DE, Bondi E, Guerry D, Nowell P, Clark WH, Koprowski H. 1985. Characteristics of cultured human melanocytes isolated from different stages of tumor progression. *Cancer Research.*45:5670-5676.

17. Herlyn M. 1990. Human melanoma: development and progression. *Cancer and Metastasis Reviews*. 9: 101-112.

18. Hsu MY, Shih DT, Meier FE, Belle PV, Hsu JY, Elder DE, Buck CA, Herlyn M. 1998. Adenoviral gene transfer of β3 integrin subunit induces conversion from radial to vertical growth phase in primary human melanoma. *American Journal of Pathology.* 153:1435-1442.

19. Hu X, Jiang F, Bao Q, Qian H, Fang Q, Shao Z. 2016. Compound 13, an α1-selective small molecule activator of AMPK, potently inhibits melanoma cell proliferation. *Tumor Biology*. 37:1071-1078.

20. Kaluzki I, Hrgovic I, Hailemariam-Jahn T, Doll M, Kleemann J, Valesky EM, Kippenberger S, Kaufmann R, Zoeller N, Meissner M. 2016. Dimethylfumarate inhibits melanoma cell proliferation via p21 and p53 induction and bcl-2 and cyclin B1 downregulation. *Tumor Biology* 37:13627–13635.

21. Katerinaki E, Evans GS, Lorigan PC, and MacNeil S. 2003. TNF-α increases human melanoma cell invasion and migration in vitro: the role of proteolytic enzymes. *British Journal of Cancer*. 89: 1123–1129.

22. Lee JT, Li L, Brafford PA, van den Eijnden M, Halloran MB, Sproesser K, Haass NK, Smalley KS, Tsai J, Bollag G, Herlyn M. 2010. PLX4032, a potent inhibitor of the B-Raf V600E oncogene, selectively inhibits V600E-positive melanomas. *Pigment Cell and Melanoma Research*. 23:820–827.

23. Li, G., Satyamoorthy, K., Meier, F., Berking, C., Bogenrieder, T., Herlyn, M., 2003. Function and regulation of melanoma-stromal fibroblast interactions: when seeds meet soil. *Oncogene*. 22:3162-3171.

24. Liu Y, Sheikh MS. 2014. Melanoma: molecular pathogenesis and therapeutic management. *Molecular Cell Pharmacology*. 6:228.

25. Martin TA, Ye L, Sanders AJ, Lane J, Jiang WG. Cancer invasion and metastasis: molecular and cellular perspective. In: Madame Curie Bioscience Database [Internet]. Austin (TX): Landes Bioscience; 2000-2013. Available from: https://www.ncbi.nlm.nih.gov/books/NBK164700/

26. Marques CMdG, Mac Neil S. 2016. Use of a tissue engineered human skin model to investigate the effects of wounding and of an anti-inflammatory on melanoma cell invasion. *PLoS ONE.* 11: e0156931.

27. Meier F, Nesbit M, Hsu M, Martin B, Belle P, Elder DE, Schaumburg-Lever G, Garbe C, Walz TM, Donatien P. 2000. Human melanoma progression in skin reconstructs: biological significance of bFGF. *The American Journal of Pathology.* 156:193-200.

28. Meierjohann S. 2017. Crosstalk signaling in targeted melanoma therapy. *Cancer and Metastasis Reviews*. 36:23-33.

29. Ordonez NG. 2014. Value of melanocytic-associated immunohistochemical markers in the diagnosis of malignant melanoma: a review and update. *Human Pathology*. 45: 191-205.

30. Pope JH, Morrison L, Moss DJ, Parsons PG, Mary SR. 1979. Human malignant melanoma cell lines. *Pathology.* 11: 191-195.

31. Satyamoorthy K, DeJesus E, Linnenbach AJ, Kraj B, Kornreich DL, Rendle S, Elder DE, Herlyn M. 1997. Melanoma cell lines from different stages of progression and their biological and molecular analyses. *Melanoma Research.* 7: 35-42.

32. Sriram G, Bigliardi PL, Bigliardi-Qi M. 2015. Fibroblast heterogeneity and its implications for engineering organotypic skin models *in vitro*. *European Journal of Cell Biology*. 94:483-512.

33. Tsai J, Lee JT, Wang W, Zhang J, Cho H, Mamo S, Bremer R, Gillette S, Kong J, Haass NK. *et al*., 2008. Discovery of a selective inhibitor of oncogenic B-Raf kinase with potent antimelanoma activity. *Proceedings of the National Academy of Science USA*. 105:3041–3046.

34. Viray H, Bradley WR, Schalper KA, Rimm DL, Rothberg BEG. 2013. Marginal and joint distributions of S100 HMB-45 and Melan-A across a large series of cutaneous melanomas. *Archives of Pathology and Laboratory Medicine.* 137:1063-1073.

35. Wagle N. Emery C, Berger MF, Davis MJ, Sawyer A, Pochanard P, Kehoe SM, Johannessen CM, Mac Conaill LE, Hahn WC, Meyerson M, Garraway LA. 2011. Dissecting therapeutic resistance to RAF inhibition in melanoma by tumor genomic profiling. *Journal of Clinical Oncology*. 29:3085-3096.

36. Weinstein D, Leininger J, Hamby C, Safai B. 2014. Diagnostic and prognostic biomarkers in melanoma. *The Journal of Clinical and Aesthetic Dermatology*. 7:13-24.

37. Wessels D, Lusche DF, Voss E, Kuhl S, Buchele EC, Klemme MR, Russell KB, Ambrose J, Sol BA, Bossler A *et al*. 2017. Melanoma cells undergo aggressive coalescence in a 3D Matrigel model that is repressed by anti-CD44. *PLoS ONE*. 12:e0173400.

38. Willis BC, Johnson G, Wang J, Cohen C. 2015. SOX10: a useful marker for identifying metastatic melanoma in sentinel lymph nodes. *Applied Immunohistochemistry and Molecular Morphology*. 23: 109-112.

39. Xu P, Zhang XX, Miao C, Fu Ziyi, Li Z, Zhang G, Zheng M, Liu Y, Yang L, Wang T. 2013. Promotion of Melanoma Cell Invasion and Tumor Metastasis

by Microcystin-LR via Phosphatidylinositol 3-Kinase/AKT Pathway. *Environmental Science and Technology*. 47:8801-8808.

40. Zand S, Buzney E, Duncan LM, Dadras SS.2016. Heterogeneity of metastatic melanoma: correlation of MITF with its transcriptional targets MLSN1, PEDF, HMB-45, and MART-1. *American Journal of Clinical Pathology*. 146:353-360.